ADVANCED STEEL CONSTRUCTION

An International Journal

Volume 20 Number 1

March 2024

CONTENTS

Copyright © 2024 by :
The Hong Kong Institute of Steel Construction
Website: *http://www.hkisc.org*
ISSN 1816-112X
Science Citation Index Expanded, Materials Science Citation Index and ISI Alerting
Cover: A Steel Ferris wheel in Harbin, China. Photo@ Liu Yao-Peng
e-copy of IJASC is free to download at "www.ascjournal.com" in internet and mobile apps.

ADVANCED STEEL CONSTRUCTION

VOL.20, NO.1 (2024)

ADVANCED STEEL CONSTRUCTION

an International Journal

ISSN 1816-112X

Volume 20 Number 1 *March 2024*

Editors-in-Chief

S.L. Chan, *The Hong Kong Polytechnic University, Hong Kong, China*

W.F. Chen, *University of Hawaii at Manoa, USA*

R. Zandonini, *Trento University, Italy*

ISSN 1816-112X

Science Citation Index Expanded, Materials Science Citation Index and ISI Alerting

Advanced Steel Construction
an international journal

EDITORS-IN-CHIEF

Asian Pacific, African and organizing Editor
S.L. Chan
The Hong Kong Polyt. Univ., Hong Kong, China

American Editor
W.F. Chen
Univ. of Hawaii at Manoa, USA

European Editor
R. Zandonini
Trento Univ., Italy

ASSOCIATE EDITORS

Y.P. Liu
The Hong Kong Polyt. Univ., Hong Kong, China

S.W. Liu
The Hong Kong Polyt. Univ., Hong Kong, China

INTERNATIONAL EDITORIAL BOARD

F.G. Albermani
Central Queensland Univ., Australia

I. Burgess
Univ. of Sheffield, UK

F.S.K. Bijlaard
Delft Univ. of Technology, The Netherlands

R. Bjorhovde
The Bjorhovde Group, USA

M.A. Bradford
The Univ. of New South Wales, Australia

D. Camotim
Technical Univ. of Lisbon, Portugal

C.M. Chan
Hong Kong Univ. of Science & Technology, Hong Kong, China

T.H.T. Chan
Queensland Univ. of Technology, Australia

T.M. Chan
The Hong Kong Polyt. Univ., Hong Kong, China

Z.H. Chen
Tianjin Univ., China

S.P. Chiew
Nanyang Technological Univ., Singapore

W.K. Chow
The Hong Kong Polyt. Univ., Hong Kong, China

G.G. Deierlein
Stanford Univ., California, USA

L. Dezi
Univ. of Ancona, Italy

D. Dubina
The Politehnica Univ. of Timosoara, Romania

R. Greiner
Technical Univ. of Graz, Austria

L. Gardner
Imperial College of Science, Technology and Medicine, UK

Y. Goto
Nagoya Institute of Technology, Japan

L.H. Han
Tsinghua Univ. China

S. Herion
University of Karlsruhe, Germany

G.W.M. Ho
Ove Arup & Partners Hong Kong Ltd., Hong Kong, China

B.A. Izzuddin
Imperial College of Science, Technology and Medicine, UK

J.P. Jaspart
Univ. of Liege, Belgium

S. A. Jayachandran
IIT Madras, Chennai, India

S.E. Kim
Sejong Univ., South Korea

S. Kitipornchai
The Univ., of Queensland, Australia

D. Lam
Univ. of Bradford, UK

H.F. Lam
City Univ. of Hong Kong, Hong Kong, China

G.C Li
Shenyang Jianzhu Univ., China

G.Q. Li
Tongji Univ., China

J.Y.R. Liew
National Univ. of Singapore, Singapore

E.M. Lui
Syracuse Univ., USA

Y.L. Mo
Univ. of Houston, USA

J.P. Muzeau
CUST, Clermont Ferrand, France

D.A. Nethercot
Imperial College of Science, Technology and Medicine, UK

Y.Q. Ni
The Hong Kong Polyt. Univ., Hong Kong, China

D.J. Oehlers
The Univ. of Adelaide, Australia

J.L. Peng
Yunlin Uni. of Science & Technology, Taiwan, China

K. Rasmussen
The Univ. of Sydney, Australia

J.M. Rotter
The Univ. of Edinburgh, UK

C. Scawthorn
Scawthorn Porter Associates, USA

P. Schaumann
Univ. of Hannover, Germany

Y.J. Shi
Tsinghua Univ., China

G.P. Shu
Southeast Univ. China

L. Simões da Silva
Department of Civil Engineering, University of Coimbra, Portugal

J.G. Teng
The Hong Kong Polyt. Univ., Hong Kong, China

G.S. Tong
Zhejiang Univ., China

K.C. Tsai
National Taiwan Univ., Taiwan, China

C.M. Uang
Univ. of California, USA

B. Uy
University of Western Sydney, Australia

M. Veljkovic
Univ. of Lulea, Sweden

F. Wald
Czech Technical Univ. in Prague, Czech

Y.C. Wang
The Univ. of Manchester, UK

Y.L. Xu
The Hong Kong Polyt. Univ., Hong Kong, China

D. White
Georgia Institute of Technology, USA

E. Yamaguchi
Kyushu Institute of Technology, Japan

Y.B. Yang
National Taiwan Univ., Taiwan, China

Y.Y. Yang
China Academy of Building Research, Beijing, China

B. Young
The Univ. of Hong Kong, Hong Kong, China

X.L. Zhao
Monash Univ., Australia

X.H. Zhou
Chongqing University, China

Z.H. Zhou
The Hong Kong Polyt. Univ., Hong Kong, China

S.Y. Zhu
The Hong Kong Polyt. Univ., Hong Kong, China

R.D. Ziemian
Bucknell Univ., USA

Cover: A Steel Ferris wheel in Harbin, China. Photo @Liu Yao-Peng
e-copy of IJASC is free to download at "www.ascjournal.com" in internet and mobile apps.

General Information
Advanced Steel Construction, an international journal

Aims and scope

The International Journal of Advanced Steel Construction provides a platform for the publication and rapid dissemination of original and up-to-date research and technological developments in steel construction, design and analysis. Scope of research papers published in this journal includes but is not limited to theoretical and experimental research on elements, assemblages, systems, material, design philosophy and codification, standards, fabrication, projects of innovative nature and computer techniques. The journal is specifically tailored to channel the exchange of technological know-how between researchers and practitioners. Contributions from all aspects related to the recent developments of advanced steel construction are welcome.

Disclaimer. No responsibility is assumed for any injury and / or damage to persons or property as a matter of products liability, negligence or otherwise, or from any use or operation of any methods, products, instructions or ideas contained in the material herein.

Subscription inquiries and change of address. Address all subscription inquiries and correspondence to Member Records, IJASC. Notify an address change as soon as possible. All communications should include both old and new addresses with zip codes and be accompanied by a mailing label from a recent issue. Allow six weeks for all changes to become effective.

The Hong Kong Institute of Steel Construction
HKISC
c/o Department of Civil and Environmental Engineering,
The Hong Kong Polytechnic University,
Hunghom, Kowloon, Hong Kong, China.
Tel: 852- 2766 6047 Fax: 852- 2334 6389
Email: *ceslchan@polyu.edu.hk* Website: *http://www.hkisc.org/*
ISSN 1816-112X
Science Citation Index Expanded, Materials Science Citation Index and ISI Alerting
Copyright © 2024 by:
The Hong Kong Institute of Steel Construction.

ISSN 1816-112X

Science Citation Index Expanded, Materials Science Citation Index and ISI Alerting

EDITORS-IN-CHIEF

Asian Pacific, African and organizing Editor
S.L. Chan
The Hong Kong Polyt. Univ., Hong Kong, China
Email: ceslchan@polyu.edu.hk

American Editor
W.F. Chen
Univ. of Hawaii at Manoa, USA
Email: waifah@hawaii.edu

European Editor
R. Zandonini
Trento Univ., Italy
Email: riccardo.zandonini@ing.unitn.it

Advanced Steel Construction
an international journal

VOLUME 20 NUMBER 1 March 2024

Technical Papers

Advanced Steel Construction – Vol. 20 No. 1 (2024) 1–11
DOI:10.18057/IJASC.2024.20.1.1

INVESTIGATION ON BEHAVIOR OF STEEL CABLES SUBJECT TO LOCALIZED FIRE IN LARGE-SPACE BUILDINGS

Xiu-Shu Qu [1], Yu-Xiang Deng [1] and Guo-Jun Sun [2, *]

[1] *School of Civil and Transportation Engineering, Beijing University of Civil Engineering and Architecture, Beijing,100044,China*
[2] *Faculty of Architecture, Civil And Transportation Engineering, Beijing University of Technology, Beijing 100124, PR China*
* *(Corresponding author: E-mail: sunny2369@163.com)*

ABSTRACT

Pre-tensioned steel cable is a crucial load-bearing component of steel structure, the fire behavior of which affects the overall performance of the structure. However, it presently lacks research and fire safety design method to consider steel cable members subject to localized large-space building fire. In this paper, the mechanical behavior of normal steel strand cable and full-locked steel cable under large-space building fire is investigated, to provide guidance for the fire safety design of steel cable. Firstly, the numerical model of temperature field of steel cables subject to large-space building fire was established and verified with the test results. Secondly, based on the verified temperature field model, the sequential thermal-mechanical coupling numerical model was established to study the fire behavior of steel cable, including temperature field, temperature gradient, failure mechanism, internal force and contact stress. Thirdly, the numerical method was adopted for the parametric analysis on the fire resistance of steel cables, considering the effect of temperature-field model, non-uniform fire, load ratio and span of steel cable. The following conclusions are obtained: 1) The average temperature can be taken to simplify the transverse temperature field due to the small amplitude of transverse temperature gradient of steel cable section; 2) Because of the size effect of steel wire, the overall temperature of normal steel strand cable is higher than that of full-locked steel cable under the same conditions of same nominal diameter and fire conditions, and the damage occurs earlier than that of full-locked steel cable under fire.

ARTICLE HISTORY

Received: 8 December 2022
Revised: 8 June 2023
Accepted: 27 August 2023

KEYWORDS

Fire in large-space building;
Steel cable;
Failure mechanism;
Fire resistance

Copyright © 2024 by The Hong Kong Institute of Steel Construction. All rights reserved.

1. Introduction

Spatial cable-truss structure is a widely used large-space steel structure. At present, in addition to focusing the static or dynamic properties of cable-truss structure, people begin to pay attention to the influence of length errors, structural layout optimization, construction forming optimization on the performance of cable-truss structure [1][2][3][4]. With the development of urban construction, the fire accidents occur more and more frequently in buildings. Scholars have started to focus on the phenomenon of a decline in the overall load-bearing capacity of large-space steel structure caused by cable rupture under fire, which can result in the further progressive collapse of whole steel structures. The studies [5][6] show the high-temperature environment caused by fire has a negative effect to reduce the material strength of steel cables, affecting the load distribution of overall structure, the evaluation of the fire-resistant capacity of steel cable members in engineering design practice is important. Thus, it is essential to study the fire behavior of steel cables subject to localized fire in large-space buildings, providing research basis to develop the fire safety protection standards for steel cable.

In the early 1950s, Frank Day et al. [7] conducted a preliminary elevated temperature test on the prestressed steel wires used for concrete components. Gales et al. [8] and Hou et al. [9] studied the mechanical performance of prestressed steel wires with different strength under high temperature. It was found that the additional prestress loss caused by high-temperature creep under fire impacts significantly on the fire-resistant limit of structure. Sun et al. [10] investigated the mechanical behaviors of Z-shape steel wire under elevated temperature, the modified two-stage Ramberg-Osgood model of which was proposed to present the constitutive relationship. With the further researches were conducted, the studies of the fire behaviors of prestress steel cables are focused. Zong et al. [11], Kotsovinos et al. [12], Du et al. [13][14][15] and Sun et al. [16][17][18] carried out the steady-state tests of the steel cables with different strength, including normal steel strand cable, stainless steel cable, parallel wire cable, etc., concentrating on the fire behaviors of material including the stress-strain relationship at elevated temperature, the reduction laws of mechanical properties and the high-temperature creep. Du et al. [19] conducted the post-fire tensile tests on Grade 1670 steel wire, the fitting equations of post-fire mechanism performance for the steel wire were proposed. Sun et al. [20], Fontanari et al. [21][22] conducted transient thermal simulations on normal steel strand cables, steel wire ropes and parallel wire cables subject to ISO-834 fire, the mechanical behavior and the temperature field of which under continuous temperature history were studied comprehensively.

At present, the studies of the fire behaviors of steel cables mostly concentrate on the steady-state heating study or the transient thermal study based on the ISO-834 fire. However, the investigations on the fire behaviors of steel cables subject to large-space building fire in transient heating condition are not fully carried out. In this paper, the numerical method is used to analyze the temperature field and the tensile fracture mechanism of steel cables under the large-space building fire, to reveal the thermo-mechanical behaviors of normal steel strand and full-locked steel strand, including failure mode and redistribution of internal force in fire. Furthermore, the parametric study on the fire resistance is performed to clarify the main factors that affect the fire-resistant capacity of steel cables in the large-span fire condition.

2. Setup and validation of numerical models

2.1. Development of thermal FE model

2.1.1. Temperature-field model for fire in large-space building

The ISO-834 curve recommended by the specification "Code for fire safety of steel building structures" (GB 51249-2017) [23] is mainly appropriate to indoor fire scene of small space, but not applicable to the fire scene in which the steel cable components subject to the large-space building fire. The literature [24] was referred in this paper, and the temperature-time curve applied to the fire behavior investigation on steel cable was introduced to depict the large-space fire:

$$\mathrm{T(x,H,t)} = \mathrm{T_g(0)} + \mathrm{T_g^{max}}(1 - 0.8\mathrm{e^{-\gamma t}} - 0.2\mathrm{e^{-0.1\gamma t}}) \cdot \mathrm{K_{sm}} \tag{1}$$

$$T_g^{max} = (20Q + 80) - (0.4Q + 3)H + (52Q + 598) \times 10^2/A_{sp} \tag{2}$$

$$K_{sm} = \beta + (1 - \beta)e^{(D/2-x)/7} \tag{3}$$

$$D = 2\sqrt{A_q/\pi} \tag{4}$$

Where $T(x,H,t)$ is the air temperature (℃) when the calculation location is x (m) from the fire source center and H (m) from the ground; T_g^{max} is the maximum air temperature; Q (MW)is the heat release rate; A_{sp} (m^2) is the floor area; A_q (m^2) is the fire area; γ is the factor of fire growth type; K_{sm} is the factor for regression ratio of maximum air temperature; β is the shape factor related to space height and the floor area.

2.1.2. Thermal FE model setting

The FE software Abaqus is used to analyze the thermal behavior of steel cable under the large-space fire. The unit DC3D8 was applied as the heat transfer element for the model. The thermal boundary conditions of thermal radiation and convective heat transfer were respectively set on the surface element of steel cables, and a closed-cavity radiation condition was established on the surface

element of inner steel wires. In reference to European specification [25], the convective heat transfer coefficient was taken as $25W{\cdot}m^{-2}{\cdot}K^{-1}$, the Stefan-Boltzmann constant was set as $5.67\times10^{-8}w/(m^2\cdot K^4)$, the surface heat emission was set as 0.8. In reference to the European specification [26], the cavity heat emission was taken as 0.8; the initial ambient temperature was 20℃. In the process of thermal simulation, the thermal contact resistance between steel wires was ignored, and the interaction between the steel wires was simulated by the "tie-boned" contact.

2.1.3. Thermal parameters of materials

The density of steel was taken as $7850\,kg\cdot m^{-3}$. In reference to the European specification [27], the thermal conductivity of steel λ_s ($W\cdot(m^2\cdot℃)^{-1}$) was taken as $\lambda_s=52.57-1.541\times10^{-2}T_S-2.155\times10^{-5}{T_S}^2$, and the specific heat capacity c_s ($J\cdot(kg\cdot℃)^{-1}$) was taken as $c_s=470+20\times10^{-2}T_S+38\times10^{-5}{T_S}^2$, where T_{st} (℃) is the temperature of steel material.

In reference to the specification [23], when verifying the thermal FE model, the equivalent thermal conductivity of non-swelling fire protection coating λ_i ($W\cdot(m^2\cdot℃)^{-1}$) and the equivalent thermal resistance of intumescent fire protection coating R_i ($(m^2\cdot℃)\cdot W^{-1}$) were taken as follows:

$$\lambda_i=\frac{d_i}{\frac{5\times10^{-5}}{(\frac{T_S-T_{S0}}{t_0}+0.2)^2-0.044}\times\frac{F_i}{V}} \tag{5}$$

$$R_i=\frac{5\times10^{-5}}{\left(\frac{T_S-T_{S0}}{t_0}+0.2\right)^2}\times\frac{F_i}{V} \tag{6}$$

Where $\frac{F_i}{V}$ is shape factor of cross-section of steel cable with fire protection coating; T_{s0} (℃) is initial temperature of steel cable before heating; T_s (℃) is average temperature of steel cable; t_0 (s) is the time of the temperature of steel cable reaching average temperature.

2.2. Development of mechanical finite element

2.2.1. Mechanical FE model setting

In the finite element analysis, the unit C3D8R was adopted as the element of mechanical analysis. In terms of mechanism, the interaction between steel wires was simulated by the general contact, in which the tangential friction coefficient was taken as 0.3 and 'hard contact' was applied for the normal contact simulation. In the setting of the boundary conditions at both ends of the steel cable, it was assumed that the steel cable was completely constrained to the anchoring devices. Thus, the displacement boundary condition of the unloaded end of the steel cable was set to be completely fixed, and that of the loaded end was only released the displacement degree of freedom that was consistent with the loading direction.

2.2.2. Mechanical parameters of material

It is essential to fully take account of deterioration of material, thermal creep and thermal expansion when the steel cable is under the fire conditions. In referrence to the test results of the literature [15], the stress-strain relationship for steel at elevated temperature is adopted as follows:

$$\sigma=\begin{cases}E\varepsilon & ,0\leqslant\varepsilon\leqslant\varepsilon_{\mathrm{pp},\theta}\\ f_{\mathrm{pu},\theta}-\left(a_1e^{-(\varepsilon/a_2)}+a_3\right) & ,\varepsilon_{\mathrm{pp},\theta}<\varepsilon\leqslant\varepsilon_{\mathrm{pt},\theta}\\ b_1\varepsilon^2+b_2\varepsilon+b_3 & ,\varepsilon_{\mathrm{pt},\theta}<\varepsilon<\varepsilon_{\mathrm{pu},\theta}\\ 0 & ,\varepsilon\geqslant\varepsilon_{\mathrm{pu},\theta}\end{cases} \tag{7}$$

Where the coefficients a_1,a_2,a_3,b_1,b_2,b_3 are the factors fitting the regression formula, the specific values refer to the literature [15]; σ (MPa) is the stress of steel wires; ε is the strain of steel wires; E (MPa) is the elastic modulus of steel wires at elevated temperature; $\varepsilon_{\mathrm{pu},\theta}$ is the rupture strain at elevated temperature; $\varepsilon_{\mathrm{pp},\theta}$ is the proportional limit strain at elevated temperature; $\varepsilon_{\mathrm{pt},\theta}$ is the limit strain for yield strength at elevated temperature.

In reference of the literature [28], the thermal expansion coefficient is acquired as follows:

$$\varepsilon_{\mathrm{th}}=1.87\times10^{-9}\times T^2+1.22\times10^{-5}\times T-3.14\times10^{-4} \tag{8}$$

$$\alpha_{\mathrm{T}}=\frac{\mathrm{d}\varepsilon_{\mathrm{th}}}{\mathrm{d}T}=3.74\times10^{-9}\times T+1.22\times10^{-5} \tag{9}$$

Where $\varepsilon_{\mathrm{th}}$ is the strain caused by thermal expansion; α_{T} is the thermal expansion coefficient; T (℃) is the temperature of steel wires, ranging from 20℃~800℃.

The thermal creep coefficient of steel cables at elevated temperature is calculated as follows:

$$\varepsilon_{\mathrm{cr}}=\frac{c_1}{c_3+1}\sigma^{c_2}t^{c_3+1}\mathrm{e}^{-\frac{c_4}{T}}+c_5\sigma^{c_6}\mathrm{e}^{-\frac{c_7}{T}} \tag{10}$$

Where $\varepsilon_{\mathrm{cr}}$ is the creep strain at elevated temperature; c_1~c_7 are the regression parameters in reference of the literature [28]; t (min) is the heat up time.

2.3. Validation of FE model

To verify the FE model in analysis of the fire behavior of steel cables, the thermal FE model was established, and its simulated results were compared with the test result of the specimens with fire protection reported by the literature [29]. In the thermal FE model, the mesh division of the specimen with the non-swelling fire protection coating and the specimen with the intumescent fire protection coating is presented in Fig.1. Fig.21 shows the comparative results of the simulation and the test, where Δ (mm) denotes the distance from the checkpoint to the surface of the steel cable, d (mm) denotes the thickness of the fire protection, D (mm) denotes the diameter of the steel cable.

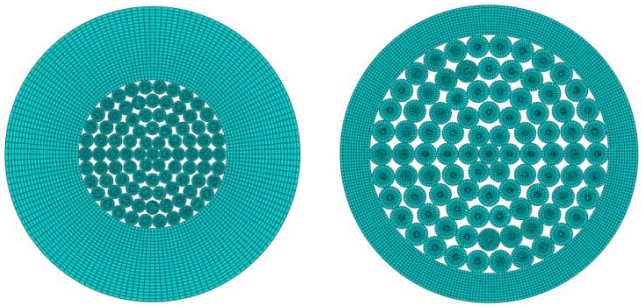

(a) Non-swelling fire protection coating (b) Intumescent fire protection coating

Fig. 1 Mesh division of specimens

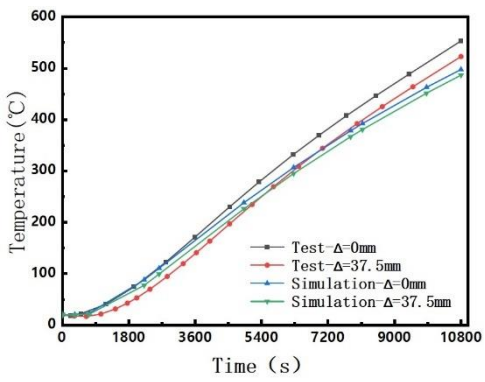

(a) d=50mm, D=75mm

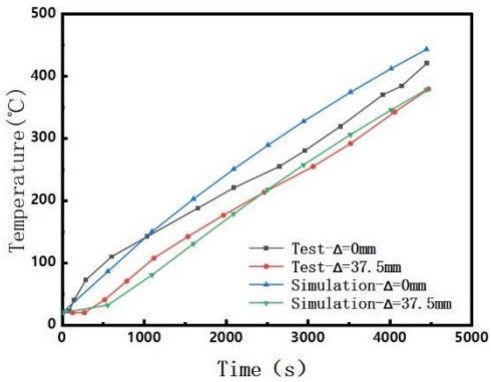

(b) d=10mm,D=75mm

Fig. 2 Time-temperature curve of specimens

The simulation result of the specimen with the non-swelling fire protection coating shown in Fig.2 (a) was nearly consistent with the experimental result, while the simulation result of the specimen with the intumescent fire protection coating shown in Fig.2 (b) had a certain error. The reason for the difference in the fitting degree of the two species is that, the actual thermal conductivity of non-swelling fire protection coating is relatively stable in heat up time, changing little over the elevated temperature. Therefore, the temperature field of the specimen with the non-swelling fire protection coating can be well simulated by adopting the equivalent thermal conductivity of the non-swelling fire protection coating in reference to the specification [23]. However, the thickness of the intumescent fire protection coating changes dramatically during the thermal expansion phase, and the actual thermal conductivity of which varies greatly over the elevated temperature [30]. Thus, the simulation deviation exists in the temperature of the specimen surface, approaching to 5%~10% during the thermal expansion phase, when the actual thermal resistance of the intumescent fire protection coating is replaced by the equivalent thermal resistance in reference to the specification [23]. Though the deviation existed in the simulation, it was still generally within a reasonable range, the numerical model can still be adopted as the reference for subsequent analysis.

3. Fire behavior of steel cable in large-space fire

3.1. Specimen design

The normal steel strand cable and the full-locked steel cable were chosen as the study specimen in this paper. The diameter of the round steel wire used in the specimens was 7 mm. The height of the Z-shape steel wire was 7 mm and the area was 51.32 mm^2. The diameter of the steel cable was 35 mm. The length was 2500 mm. The second layer of twist angle was 7.2° and the third layer of which was 14.4°. The type of the steel cable was 1×19.

The numerical simulation of monotonic tension at room temperature was carried out on the steel cables. The ultimate break force of the normal steel strand cable was 1264.07 KN, and the ultimate break force of the full-locked steel cable was 1459.96 KN. In the simulation, the load ratio was 0.7.

3.2. Parameters of uniform and non-uniform fire distribution

In this section, the fire scenario is simulated according to the temperature-field model of the large-space building fire stated in Section 1.1. Equation (1) ~ (4) indicates the meaning of physical parameters in the large-space building fire model, including floor area A_{sp}, position height H, heat release rate Q, factor of fire growth type γ, effective diameter of the fire source D and regression ratio of the fire K_{sm}. In this paper. The large-space building refers to the building space with a floor area of no less than 500 m^2 and a space height of no less than 4 m [31]. The setting parameters of the uniform and non-uniform fire distribution within the definition of large-space building were set as follows: The floor area A_{sp} was 500; the position height H was 6 m; the heat release rate Q was 25 MW; the factor of fire growth type γ was 0.004.

For the uniform fire condition, the effective diameter of the fire source was 2500 mm, covering the longitudinal span of the steel cable; for the non-uniform fire condition, the effective diameter of the fire source was 1000 mm, and the non-uniform fire was set below the median part, the regression ratio of the fire K_{sm} was taken as 0.6. The detail arrangement of the fire source under the non-uniform and the uniform fire distribution are presented in Fig.3.

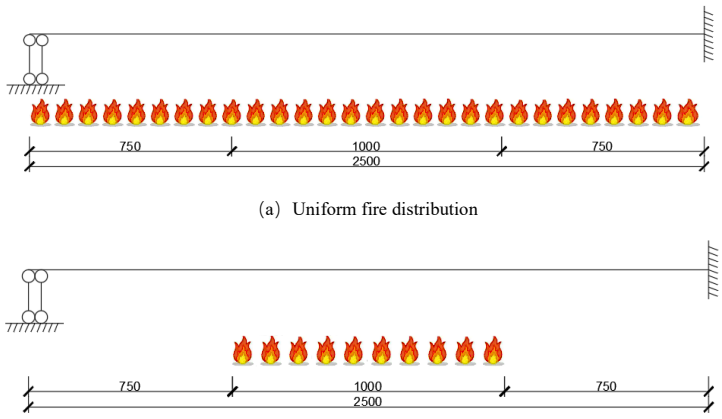

(a) Uniform fire distribution

(b) Non-uniform fire distribution

Fig. 3 Arrangement of fire source

3.3. Judging criteria of fire resistance

In the simulation, the judging criteria of the fire resistance of steel cable was adopted in reference to the literature [15]. The total strain of the mechanical element of the steel cable is composed of mechanical strain, thermal creep strain and thermal expansion under the thermo-mechanical coupling condition. As the total strain reaching the failure criterion of its rupture strain or the element achieving ultimate strength at elevated temperature, it is judged that the steel cable loses the fire-resistant capacity, reaching the fire resistance. The element of the FE model in the analysis should be checked by the following criterion:

$$\sigma_{p,\theta} \le f_{pt,\theta} \tag{10}$$

or

$$\varepsilon_{total} \le \varepsilon_{pu,\theta} \tag{11}$$

Where $\sigma_{p,\theta}$ is the total stress of the element at elevated temperature; $\varepsilon_{pu,\theta}$ is the rupture strain of steel wire at elevated temperature; ε_{total} is the total strain of the element; $f_{pt,\theta}$ is the ultimate strength of steel wire at elevated temperature.

3.4. Analysis of temperature field of steel cable

Under both the non-uniform fire and the uniform fire distribution conditions, the temperature fields of the two types of the steel cables were analyzed for 180 min. In the uniform fire condition, both the center and the surface of the steel cables were taken as the temperature measuring points, the layouts of which are presented in Fig.4 (a)(b). For the non-uniform fire condition, the measuring positions of temperature arranged along the longitudinal span of steel cable are presented in Fig.4 (c), where the center of cross section was taken as the temperature measuring point.

3.4.1. Temperature field

Under the uniform fire condition, the temperature field of the transverse sections and the temperature development of the measuring points are presented in Fig.5 (a)(b); under the non-uniform fire condition, the temperature development of the longitudinal measuring points of the steel cables is presented in Fig.6. It can be seen from Fig.5 and Fig.6, under the two types of the fire conditions, the transverse temperature and the longitudinal temperature of the normal steel strand cable was higher than that of the full-locked steel cable. At the measuring position Z6, the peak temperature for the normal steel strand cable was 588.5°C, and the peak temperature of the full-locked steel cable was 468.14°C; at the measuring position Z1, the peak temperature of the normal steel strand cable was 509.67°C, and that of the full-locked steel cable was 388.37°C. It indicated that the strength deterioration of the normal steel strand cable occurred earlier than that of the full-locked steel cable.

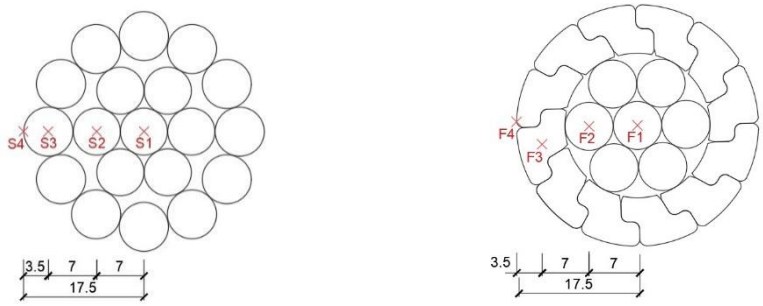

(a) Transverse section of normal steel strand cable (b) Transverse section of full-locked steel cable

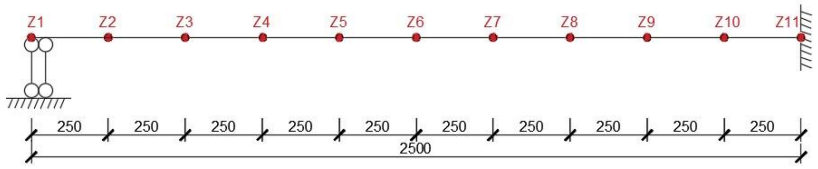

(c) Longitudinal measuring position

Fig. 4 Layout of temperature measuring position

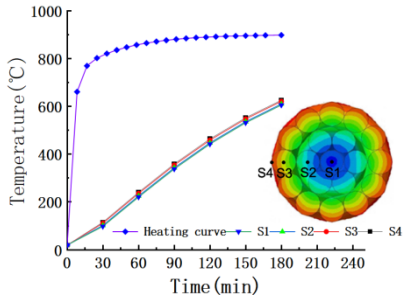

(a) Normal steel strand cable

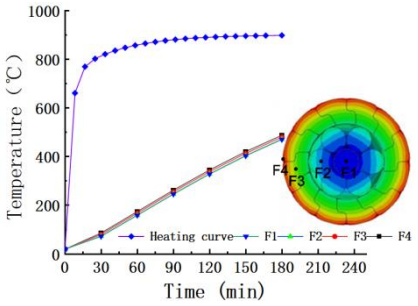

(b) Full-locked steel cable

Fig. 5 Transverse temperature field of steel cable under uniform fire

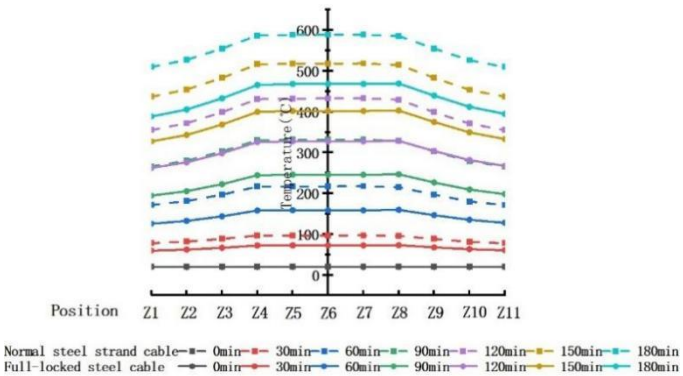

Fig. 6 Longitudinal temperature field of steel cable under non-uniform fire

To reveal the difference of the temperature field between the two types of the steel cables, the temperature measuring points at the same position of the two steel cables were compared. Under the uniform fire, the measuring points S4 and F4, S1 and F1 were taken in comparative analysis, Fig.7 (a) shows the comparative result. Under the non-uniform fire condition, the measuring points Z6 at fire position and the measuring points Z1~Z3 at non-fire position were compared, Fig.7(b) shows the comparative result.

As shown in Fig.7, for the two types of fire conditions, the temperature of the normal steel strand cable was higher than that of the full-locked steel cable, and the temperature difference continued to expand with time. In the condition of uniform fire, the peak temperature difference between the surfaces of the two types of steel cables was 138.30 degrees; under the non-uniform fire, the peak temperature difference between the two was 122.05 °C. Moreover, the temperature difference of the two steel cables decreased with the distance from the measuring point to the fire resource increased. The reason for this phenomenon is that, under the condition of the same section diameter, the geometric curvature of the third layer of steel wires of the normal steel strand cable is higher than that of the full-locked steel cable, there is the size effect leading to more heat absorption during the heating process [20].

At the same time, due to the steel ration of the full-locked steel cable higher than steel ration of the normal steel strand cable, the temperature development of the full-locked steel cable in the longitudinal direction lagged that of the normal steel strand cable.

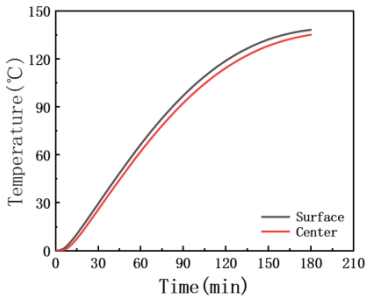

(a) Uniform fire condition

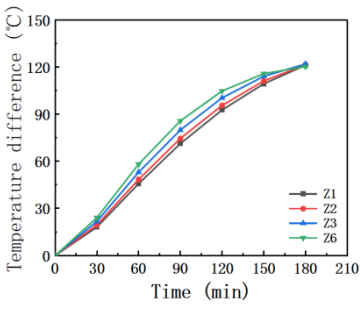

(b) Non-uniform fire condition

Fig. 7 Comparison of temperature field of steel cables

3.4.2. Temperature gradient

The transverse temperature gradient was obtained by calculating the temperature difference between the measuring points S4 and S1, F4 and F1, while the longitudinal temperature gradient was acquired by calculating the temperature difference of the center wires of the two types of the steel cables at the measuring point Z6 and Z1. Fig.8 shows the results of the temperature gradient .

As shown in Fig.8 (a)(b), under both the uniform fire and the non-uniform fire, the peak value of the transverse temperature gradient of the two types of the steel cables was small, the normal steel strand cable was 22℃, and the full-locked steel cable was 17℃. It shows that the extent of the stress redistribution caused by the transverse temperature gradient is low. To simplify the calculation in fire design, it is recommended that the transverse temperature field can be simplified by taking the average temperature of the section. However, as shown in Fig.8 (c), the peak value of the longitudinal temperature gradient was large, the normal steel strand cables was 81℃, and the full-locked steel cable was 79℃, which cannot be ignored in fire design.

There was the large difference between the longitudinal temperature gradient and the transverse temperature gradient. This is mainly because the heating rate of the non-fire part of the steel cable is much smaller than that of the fire part, and there is a lag in the longitudinal transfer of heat flux from the higher temperature area to the lower temperature area along the cable length. In the example, the temperature hysteresis phenomenon of the non-fire part tends to be more obvious with the increase of the distance from the fire part.

It is noted that Fig.8 shows the descending period of the temperature gradient when the steel cables were in the later stage of the heat up time. The reason is the thermal conductivity λ_s decreases and the specific heat capacity c_s increases when the temperature increases, so the rate of temperature increment of the steel cables declines with the heat up time. While during the process of heat transfer from high temperature position to low temperature position, the thermal lag behavior exists between the surface and the center of the transverse section, and also exists between the longitudinal measuring point Z6 and Z1. The temperature-elevation rate of the measuring point with relatively higher temperature first declines compared with the measuring point with lower temperature, and therefore the temperature gradient decreases during the later stage of the heating process.

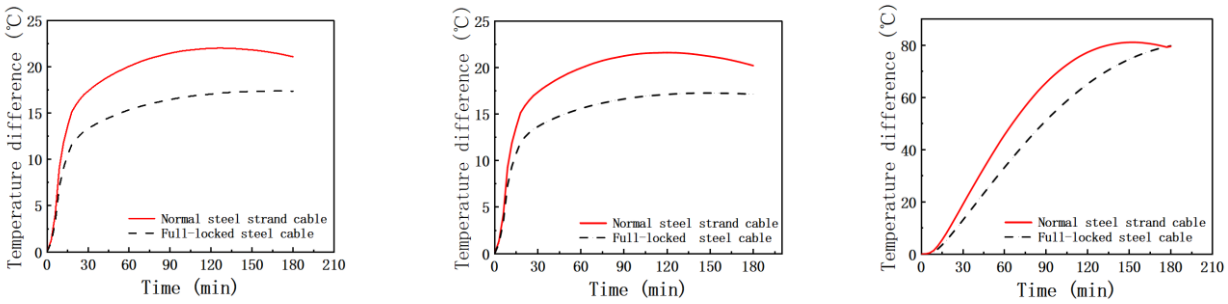

(a) Transverse gradient in uniform fire (b) Transverse gradient in non-uniform (c) Longitudinal gradient in non-uniform

Fig. 8 Temperature gradient of steel cables

3.5. Mechanism analysis of steel cable

3.5.1. Damage development and mode

Fig.9 shows the damage locations and modes of the steel cables under uniform fire and non-uniform fire conditions. It can be found that the steel cables mainly experienced three stages of necking, spiral decoupling and breakage when working in a fire environment.

In the stage of necking, the first layer and the second layer of steel wires entered the yield stage, the deformation development of the steel wires was accelerated. The necking phenomenon was intensified with the elevated temperature.

In the stage of spiral decoupling, all the steel wires entered the plastic stage, and the deformation of the steel wires developed rapidly. The torsional moment produced in the inner part of the steel cables caused the second and the third layer of steel wires to spread out to different extent.

In the stage of breakage, when the steel cable was subject to the uniform fire, the center steel wire firstly ruptured at the position where the necking phenomenon occurred near the end of the steel cable, then was pulled out. When the steel cable was subject to the non-uniform fire, the center steel wire firstly ruptured near the boundary of the fire position and the non-fire position. The second and the third layer of steel wires were broken almost at the same time, leading to the transmission path of the internal force was cut off totally and the inner torsional moment disappeared. Thus, the phenomenon that the steel wires spread out cannot be observed.

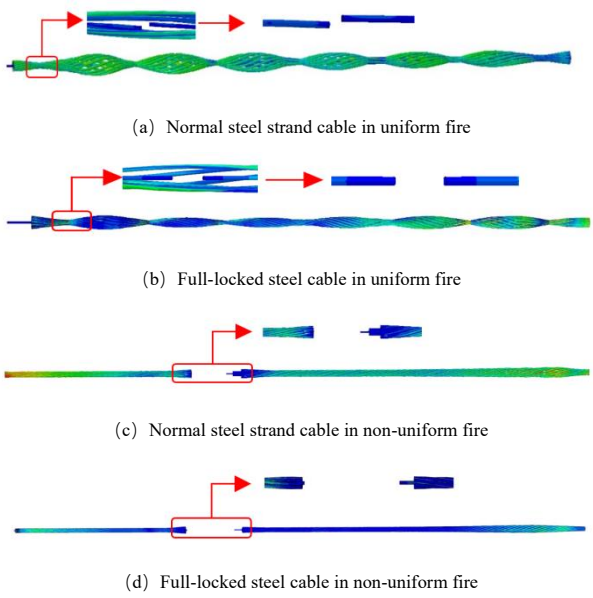

(a) Normal steel strand cable in uniform fire

(b) Full-locked steel cable in uniform fire

(c) Normal steel strand cable in non-uniform fire

(d) Full-locked steel cable in non-uniform fire

Fig. 9 Damage location and mode of steel cable under large-space fire

3.5.2. Axial deformation and fire resistance

As shown in Fig. 10, the axial displacement-time curves of the steel cables under the two fire conditions are acquired. In the uniform fire condition, the fire resistance of the normal steel strand cable was 77.18 min, and that of the full-locked steel cable was 98.98 min. In the non-unform fire condition, the fire resistance of the normal steel strand cable was 80.20 min, and that of the full-locked steel cable was 101.90 min.

The axial deformation of the steel cables was in a growing trend in the heating process, but the deformation rate of which was changing. In the heating period of 20 ~ 40 min, the axial displacement of the steel cable increased rapidly, this is because, in this period, the steel cables are in the necking stage, the first and the second layer of steel wires entered the plastic state, causing the axial deformation rate of the steel cables increases.

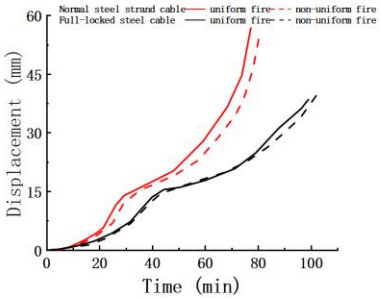

Fig. 10 Axial displacement-time curves of steel cables

3.5.3. Energy analysis

According to the energy conservation, the external work done by the tensile force loaded on the steel cable is mainly converted into the internal strain energy, the internal energy mainly caused by thermal expansion and the friction energy dissipation (energy dissipated by overcoming friction between the steel wires). The relevant data of the overall external work, friction energy dissipation and internal strain energy of the steel cables were directly extracted in the post-processing program of Abaqus. The internal non-strain energy mainly caused by thermal expansion was obtained by subtracting the internal strain energy and friction energy dissipation from the external work of the steel cables.

Fig.11 presents the variation curves of the proportion of the internal strain energy to the external work and the variation curves of the proportion of the internal non-strain energy mainly caused by thermal expansion to the external work during the heating process under different fire conditions.

As shown in Fig.11, thermal expansion primarily caused the deformation development of the steel cables during the early stage of heating; while in the middle and late period of heating, stress deformation mainly caused the deformation development. The reason is that, during the early stage of the heating process, the extent of material strength deterioration is low. With the elevation of temperature, the extent of the deterioration is gradually deepened, so that the axial displacement increases over time. During the middle and late period of heating process, the temperature-elevation rate of the steel cables gradually decreases, leading to the development of thermal expansion deformation slows down.

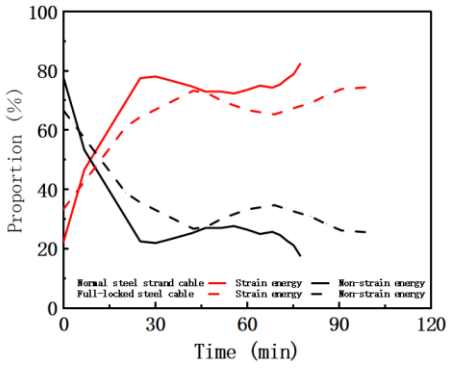

(a) Unform fire condition

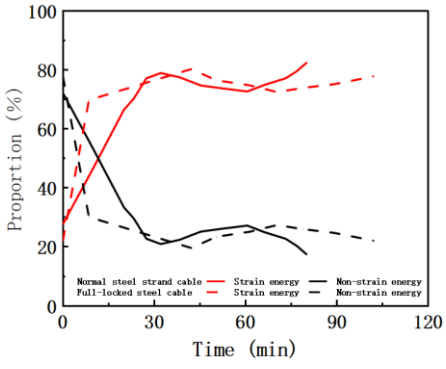

(a) Non-uniform fire condition

Fig. 11 Contribution analysis of axial deformation of steel cables

3.5.4. Internal force development of steel wires

Fig.12 shows the development of the average internal force of the steel wires at the mid-span position under the uniform fire. Fig.13 shows the internal force development of the steel wires at the boundary of the fire position and the non-fire position under the non-uniform fire.

Fig.12 and Fig.13 show that the average internal force of the first two layer of steel wires increased and then declined, while the average internal force of the third layer of steel wires decreased first, then increased and finally destroyed.

It indicated the internal force was redistributed in the steel cables under the fire condition. The reason is that, during the early stage of the heat up time, compared with the first two layer of steel wires, the third layer of steel wires exposed directly to the high-temperature environment has deeper extent of material strength deterioration and thermal expansion deformation, and the tensile stiffness of which is lower due to the larger twist angle. Thus, in this stage, the tensile force loaded on the steel cables is mainly borne by the first two layer of steel wires. When the steel cables enter the necking stage, the first two layer of the steel wires begin to deform plastically, causing the tensile stiffness decreases sharply. And at this moment, the internal force starts to transfer from the first two layer of steel wires to the third layer of steel wires.

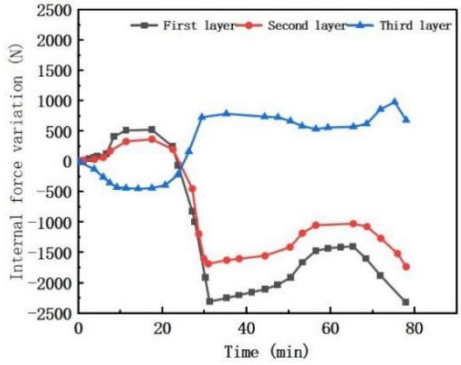

(a) Normal steel strand cable

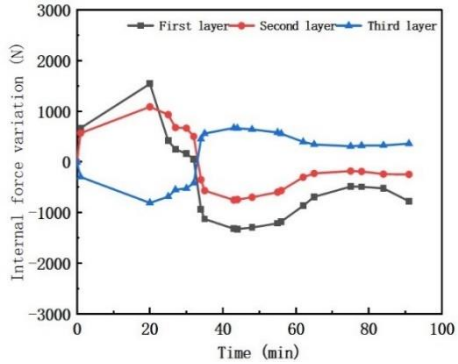

(b) Full-locked steel cable

Fig. 12 Development of average internal force of steel cable in uniform fire

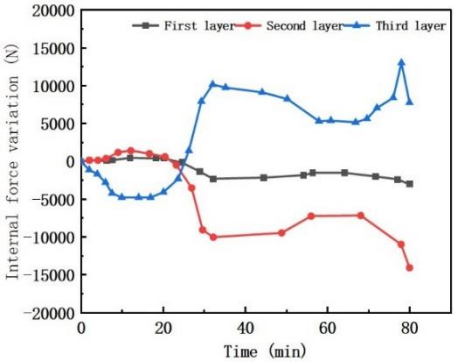

(a) Normal steel strand cable

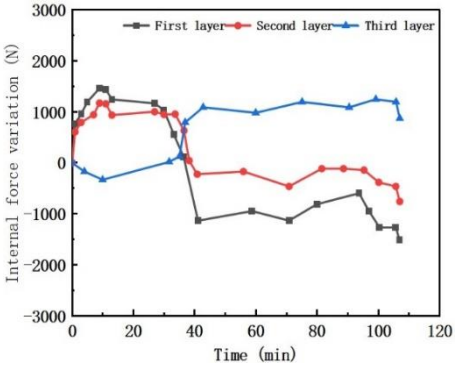

(b) Full-locked steel cable

Fig. 13 Development of average internal force of steel cable in non-uniform fire

3.5.5. Contact stress development

Taking the mid-span section of the steel cables under the uniform fire as the object, where the contact stress during the heat up time was analyzed. Fig.14 shows the arrangement of the contact points of the section.

Fig.15 shows the development of the contact stress over time. Overall, the contact stress of the steel wires declined over time, especially the contact relationships between A33, B33, A21 and B21 were the most sensitive. This is because as the temperature rises, due to the spiral decoupling of the steel wires, the deformation of the transverse section gradually increases, causing the overall contact stress between the steel wires decreases over time.

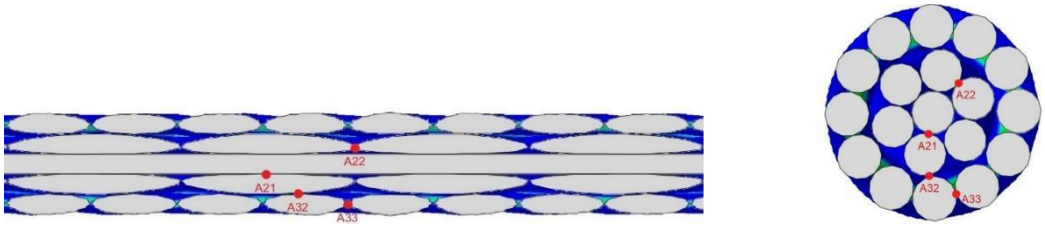

(a) Y-Z section and transverse section of normal steel strand cable

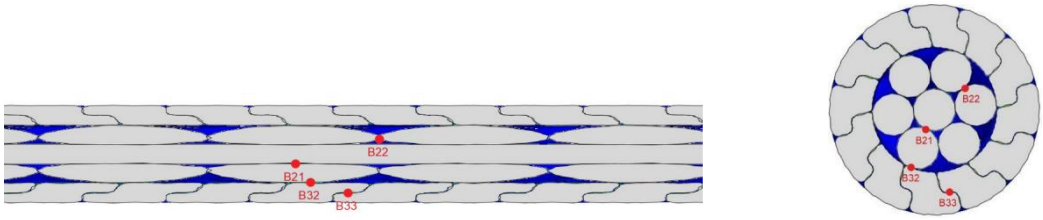

(b) Y-Z section and transverse section of full-locked steel cable

Fig. 14 Arrangement of contact points between steel wires

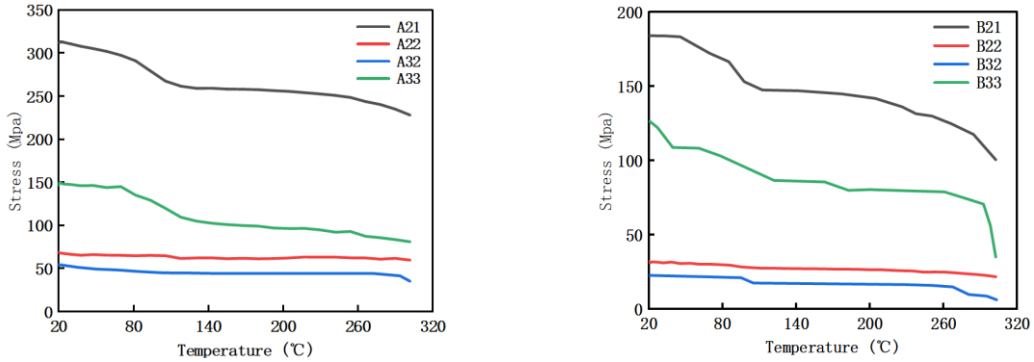

(a) Normal steel strand cable (b) Full-locked steel cable

Fig. 15 Stress-temperature curves of steel cables

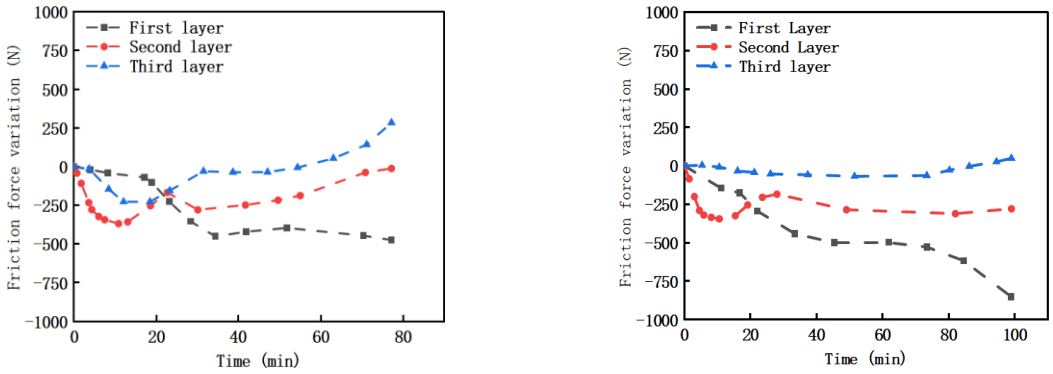

(a) Normal steel strand cable (b) Full-locked steel cable

Fig. 16 Variation of average resultant force of friction of steel cables

Taking the steel cables under the uniform fire as the object , the average resultant force of friction between each layer of steel wire was analyzed. Fig.16 shows the variation of the average resultant force of friction.

Fig.16 shows that the average resultant force of friction of the normal steel strand cable and the full-locked steel cable was much smaller than the contact stress of the steel cables, which indicated that the friction contributed little to the force transmission inside the steel cable. With the increase of time, the average resultant force of friction of the first two layer of steel wires presented a decreasing trend in general. Combined with the phenomenon that the contact stress decreased with the elevated temperature, it indicated that the contact relationship of the steel wires had been weakened in general. In addition, as the internal force of the first two layer of steel wires was transferred to the third layer of steel wires over time, the average resultant force of friction of the third layer of steel wire declined with time.

4. Parametric analysis of steel cable in large-space fire

In this section, the numerical investigation of 41 normal steel cables was carried out. The parametric analysis of the fire-resistant capacity and the deformation development of the normal steel cable was performed.

4.1. Effect of temperature-field model for large-space fire

The parametric investigation on the fire-resistant capacity of the steel cable was conducted under the large-space building fire condition, including the parameters of floor area, position height of steel cable, fire grow type and heat release rate, and the numerical examples for which are shown in Table 1. In Table 1, the non-uniform level η denotes the ratio of the span of the unburned part to the total span of the steel cables. When the non-uniform level η is 0, it indicates the steel cable is uniformly subject to fire along the whole span. In addition, in reference to the literature [6], the parameter of load ratio in Table 1 denotes the ratio of the horizontal tension to the ultimate break force of the steel cable after the design load is applied at room temperature. In this section, the ultimate break force of the numerical examples is 1253.36 KN, and the other geometric parameters not given in Table 1 are consistent with the FE model of the normal steel strand cable stated in section 2.1.

Table 1
Numerical examples for parametric analysis of temperature-field model

Specimen	Floor area A_{sp}（mm²）	Position height H（m）	Factor of fire growth type γ	Fire release rate Q（MW）	Non-uniform level η	Load ratio R	Span L（m）
RF-0	500	6	0.004	25	0	0.3	15
Area-1	1000	6	0.004	25	0	0.3	15
Area-2	3000	6	0.004	25	0	0.3	15
Area-3	6000	6	0.004	25	0	0.3	15
Height-1	500	11	0.004	25	0	0.3	15
Height-2	500	16	0.004	25	0	0.3	15
Height-3	500	21	0.004	25	0	0.3	15
Height-4	500	26	0.004	25	0	0.3	15
Growth-1	500	6	0.001	25	0	0.3	15
Growth-2	500	6	0.002	25	0	0.3	15
Growth-3	500	6	0.003	25	0	0.3	15
Power-1	500	6	0.003	12	0	0.3	15
Power-2	500	6	0.003	14	0	0.3	15
Power-3	500	6	0.003	16	0	0.3	15
Power-4	500	6	0.003	19	0	0.3	15
Power-5	500	6	0.003	22	0	0.3	15

4.1.1. Floor area

As shown in Fig.17, in the condition of remaining other parameters unchanged, when the building area rose from 500 m² to 6000 m², the fire resistance rose from 141 min to 455 min. The lag phenomenon of the axial deformation development of the steel cable was deepened when the floor area increased, and the fire resistance increased in nonlinear tendency. This is because as the floor area increases, the ambient temperature of the large-space building decreases in nonlinear tendency, causing the lagging development of the material strength deterioration, the thermal creep and the axial deformation caused by thermal expansion.

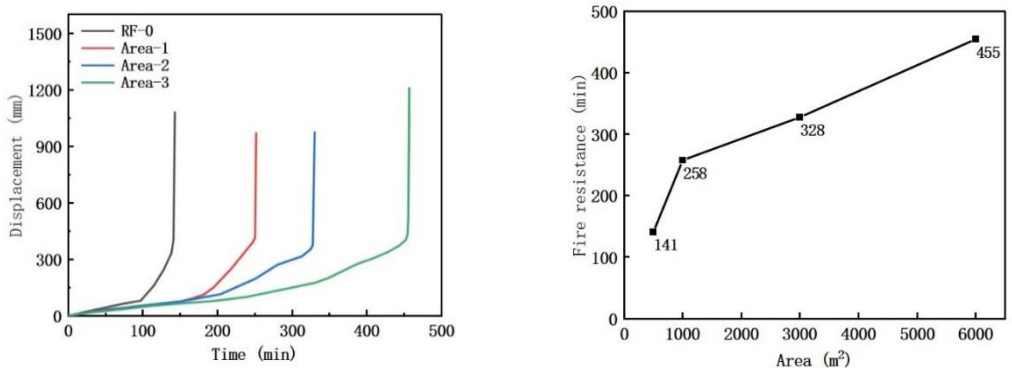

(a) Effect on axial deformation (b) Effect on fire resistance

Fig. 17 Parametric analysis of floor area on steel cable

4.1.2. Position height

As shown in Fig.18, in the condition of remaining other parameters unchanged, when the position height increased from 6m to 26m, the fire resistance rose from 141 min to 341 min. The lagging phenomenon of axial deformation development of the steel cable was deepened when the position height of the steel cables increased, leading to the higher fire resistance.

This is because according to the temperature-field model for large-space fire, the greater position height leads to the lower elevated temperature of the steel cable, which causes the lagging development of the material strength deterioration, the thermal creep and the axial deformation caused by thermal expansion under the same heat up time.

4.1.3. Fire growth type

As shown in Fig.19, in the condition of remaining other parameters unchanged, the fire resistance declined from 187 min to 141 min, as the fire growth type rose from 0.001 to 0.004. During the early stage of the heat up process, the fire growth type had little difference in the deformation development, but the difference in the deformation development gradually became larger over time. As the fire growth rate increased, the fire resistance of the steel cable presented a nonlinear downward trend. Compared to the other parameters, the increase of the fire growth type had little influence on the downward trend of the fire resistance.

4.1.4. Heat release rate

As shown in Fig.20, in the condition of remaining other parameters unchanged, when the heat release rate rose from 14 MW to 25 MW, the fire resistance decreased from 434 min to 141 min. As the heat release rate of the steel cables increasing, the fire resistance of the steel cables reduced over time, and the difference in the deformation development was greater. The heat release rate of the fire had the significant effect on the fire resistance.

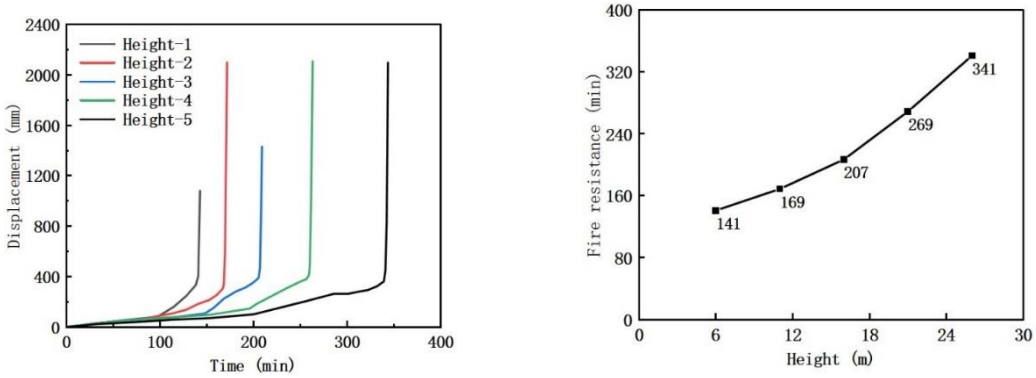

(a) Effect on axial deformation (b) Effect on fire resistance

Fig. 18 Parametric analysis of position height of steel cable

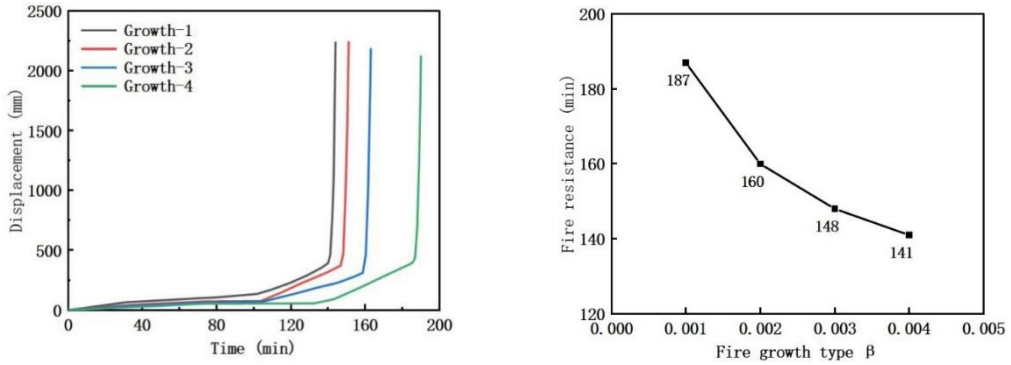

(a) Effect on axial deformation (b) Effect on fire resistance

Fig. 19 Parametric analysis of fire growth

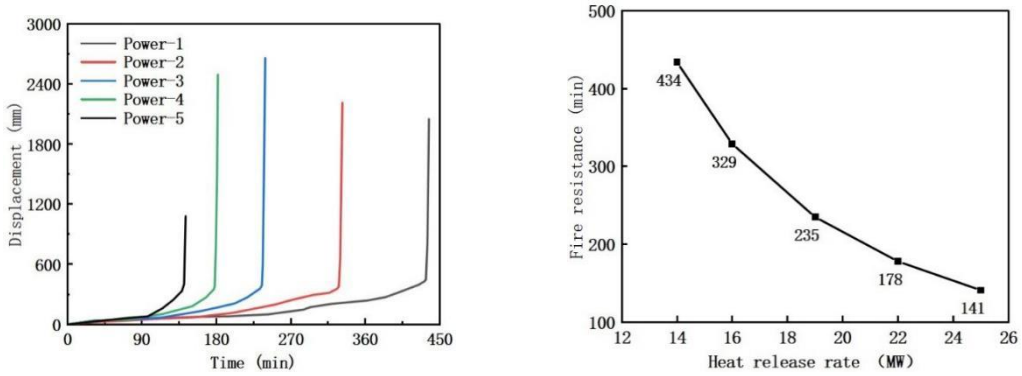

(a) Effect on axial deformation (b) Effect on fire resistance

Fig. 20 Parametric analysis of heat release rate of fire

4.2. Non-uniform level of fire and fire source location

The parameter of non-uniform level of fire is set ranging from 0~0.8, and the non-uniform fire is located at the mid-span and the end of steel cable. As the non-uniform fire is located at the mid-span, the non-uniform fire extends from the middle to both ends of the steel cable; as the non-uniform fire is located at the end of the steel cable, the non-uniform fire extends from the one end to the other end. In addition, for the other parameters, the floor area is 500 m^2; the position height is 6 m; the factor of fire growth type is 0.004; the load ratio is 0.3; the fire release rate is 25 MW; the span is 15 m.

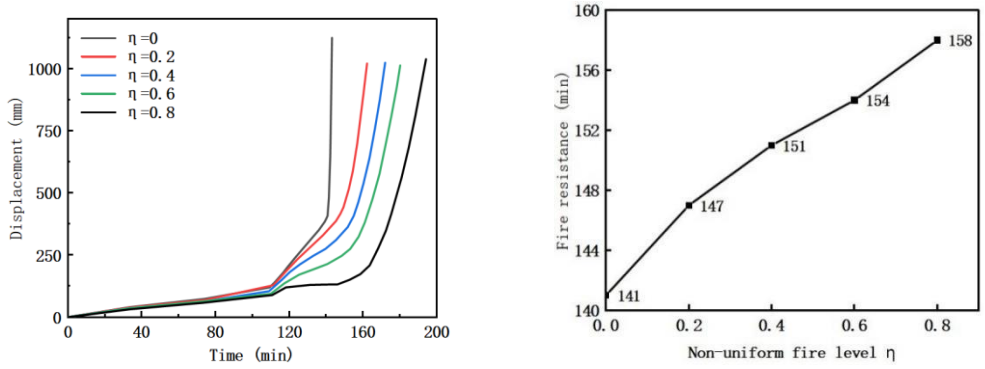

(a) Effect on axial deformation (b) Effect on fire resistance

Fig. 21 Parametric analysis of non-uniform level of fire at mid-span of steel cable

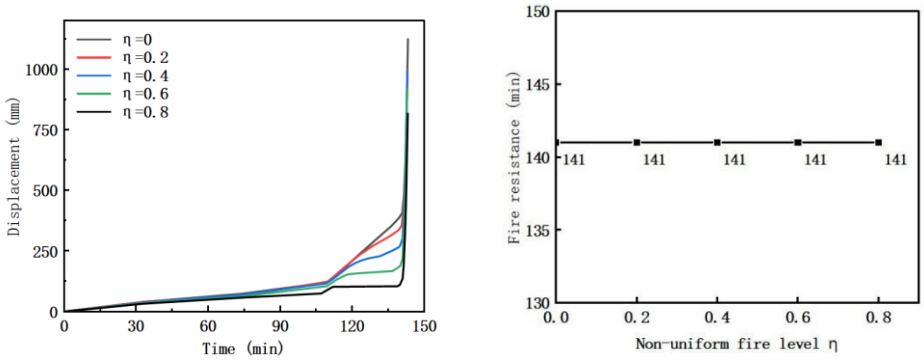

(a) Effect on axial deformation (b) Effect on fire resistance

Fig. 22 Parametric analysis of non-uniform level of fire at end of steel cable

Fig.21 and Fig.22 show the effect of non-uniform level of fire and fire source location on the deformation and the fire resistance.

Fig.21 shows that, when the fire was set at the mid-span, with the increase of the non-uniform level, the deformation of the steel cable was smaller and the fire resistance was higher. The reason is that the increasing continuous area of the steel cable causes more heat absorption under the non-uniform fire condition, which makes the accumulated axial deformation due to thermal expansion and thermal creep larger. Thus, the strain of the steel wire reaches the rupture strain early, and the fire resistance decreases.

As shown in Fig. 22, when the fire source was set at the end of the steel cable, with the increase of the non-uniform level, the deformation of the steel cable was smaller, but the fire resistance did not change. The reason is the damage of the specimens with fire at the end is induced by the fact that the first layer of steel wires at the loading end reaches the rupture strain first, and breaks at the necking part near the end, which is different from the failure mode when the steel cable is subject to the fire source located under the mid-span. It indicates the failure pattern of the steel cable is mainly related to the location of fire source.

4.3. Load ratio

The parameter of load factor is set ranging from 0.2~0.7. The non-uniform level of fire is set as 0. For the other parameters, the floor area is 500 m^2; the position height is 6 m; the factor of fire growth type is 0.004; the fire release rate is 25 MW; the span is 15 m.

As shown in Fig.23, in the condition of remaining other parameters unchanged, the fire resistance decreased from 158 min to 87 min, as the load ratio rose from 0.2 to 0.7. As the load ratio increasing, the deformation was larger and the fire resistance declined in nonlinear tendency, indicating that the parameter of load ratio greatly affects the fire behavior of the steel cables.

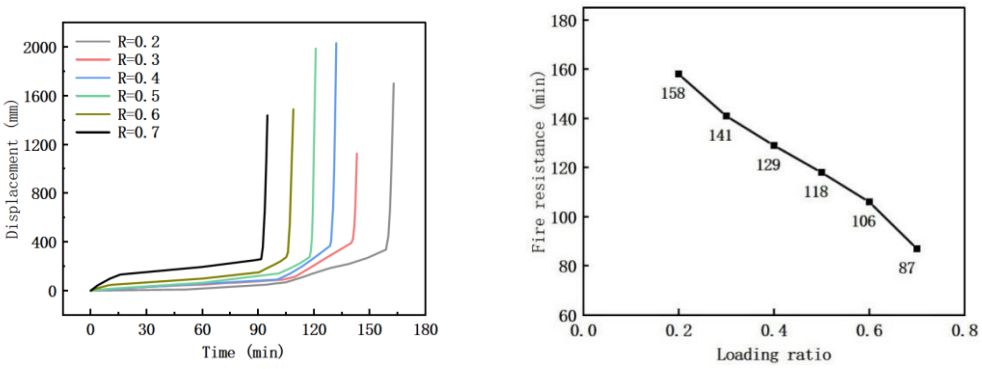

(a) Effect on axial deformation (b) Effect on fire resistance

Fig. 23 Parametric analysis of load ratio

4.4. Span

The parameter of fire source location is set under the mid-span and the end of steel cable. The non-uniform fire level is set ranging from 0~0.8. The span is set ranging from 15 ~35 m. In addition, the floor area is 500 m^2; the position height is 6 m; the factor of fire growth type is 0.004; the fire release rate is 25 MW ;the load ratio is 0.3. Fig. 24 shows the parametric analysis result.

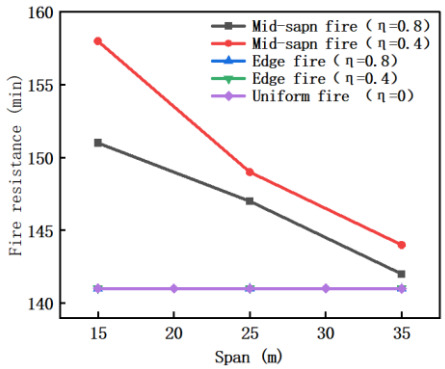

Fig. 24 Parametric analysis of span under different fire conditions

According to Fig.24, the fire resistance of the specimens subject to the edge fire is the same as that of the specimens subject to uniform fire, which is 141 min. When the end part of the steel cables was directly exposed to fire, the specimen was damaged earlier than when the mid-span position was exposed to fire. This phenomenon is consistent with the conclusion pointed out in the literature [6], in which the effect of the non-uniform level of fire on the fire resistance of steel cable was studied. When the end part of the steel cable subject to fire, the fire resistance is independent of the parameter of span and non-uniform level of fire. The uniform fire condition of the steel cable can be taken as the unfavorable working condition in the fire safety design to ensure the reliability of steel cable.

Moreover, it can be found that when the mid-span of the steel cable was subject to fire resource, the fire resistance decreased in nonlinear tendency with the increase of span. And the fire resistance increased as the non-uniform level of fire increased, but with the increase of the span, the influence of the non-uniform level of fire on the fire resistance was weakened.

5. Conclusion

This paper numerically analyzes the fire behavior of the normal steel strand cable and the full-locked steel cable under the large-space building localized fire. The following conclusions for providing fire safety design guidance of steel cable can be drawn:

(1) In the uniform fire condition, the peak temperature difference between the normal steel strand cable and the full-locked steel cable is 138.80 °C, while in the non-uniform fire condition, the maximum temperature difference is 122.05°C. It indicates that the outer surface geometric curvature of the full-locked steel cable is smaller than the outer surface geometric curvature of the normal steel strand cable, which causes that the full-locked steel cable needs to absorb more heat. Therefore, the overall temperature of the normal steel strand cable is higher than that of the full-locked steel cable.

(2) In the fire safety design, it is suggested that the average temperature can be used to simplify the temperature field of the steel cable when calculating the transverse temperature of section, due to the small temperature gradient amplitude of the steel cables(the transverse temperature gradient of normal steel strand cable is 22 °C, and that of the full-locked cable is 17 °C). However, the longitudinal temperature gradient amplitude of the two types of steel cables is large (the longitudinal temperature gradient of normal steel strand cable is 81 °C, and that of the full-locked steel cable is 79 °C), which cannot be ignored in fire safety design.

(3) In the condition of remaining other parameters unchanged, when the floor area increases from 500 m^2 to 6000 m^2, the fire resistance of the steel cable rises from 141 min to 455 min ; when the position height increases from 6m to 26m, the fire resistance rises from 141 min to 341 min; when the fire growth type rises from 0.001 to 0.004, the fire resistance decreases from 187 min to 141 min; when the heat release rate rises from 14 MW to 25 MW, the fire resistance decreases from 434 min to 141 min; as the load ratio increases from 0.2 to 0.7, the fire resistance decreases from 158 min to 87 min. The effect extent of the parameter in the model on the steel cable is as follows: heat release rate, position height of steel cable, floor area, fire growth type. In addition, the parameter of load ratio greatly affects the fire resistance.

(4) The influence of non-uniform level of fire and span on the fire resistance of the steel cable is related to the fire location. When the fire location is at the end of the steel cable, the non-uniform level of fire and the span have no effect on the fire resistance. When the fire location is only at the mid-span of the steel cable, the non-uniform level of the mid-span fire increases from 0 to 0.8, the fire resistance of the steel cable increases from 141 min to 158 min. In the condition of remaining other parameters unchanged, the fire resistance decreases with the increasing span, the span factor greatly affects on the fire resistance.

(5) The influence of span on the fire resistance under different fire conditions is analyzed, including the fire conditions of non-uniform fire at the mid-span of steel cable, non-uniform fire at the span end and uniform fire. It is found that the uniform fire condition can be regarded as the most unfavorable fire condition of the steel cable in the fire safety design.

Notations

λ_s-Thermal conductivity of steel
λ_i- Equivalent thermal conductivity of non-swelling fire protection coating
R_i- Equivalent thermal resistance of intumescent fire protection coating
H- Position height
T_g^{max}-Maximum air temperature
Q- Heat release rate
A_{sp}- Floor area
A_q- Fire area
γ- Factor of fire growth type
K_{sm}- Factor for regression ratio of maximum air temperature
β- Shape factor dependent on the floor area and space height
C_s- Specific heat capacity
T_{st}- Temperature of steel material
σ- Stress of steel wires
ε- Strain of steel wires
E- Elastic modulus of steel wires
$\varepsilon_{pp,\theta}$- Proportional limit strain at elevated temperature
$\varepsilon_{pt,\theta}$- Limit strain for yield strength at elevated temperature
$\varepsilon_{pu,\theta}$- Rupture strain at elevated temperature
ε_{th} – Thermal expansion strain
α_T- Thermal expansion coefficient
T- Temperature of steel wires
ε_{cr}- Creep strain at elevated temperature

Acknowledgments

The investigation was supported by the General Program of National Natural Science Foundation of China (52278136), and the General Program of National Natural Science Foundation of China (52378118).

Reference

[1] J. Lu, S.D. Xue, X. Y. Li, Experiment study on the influences of length errors of cables and struts on spatial cable-truss structure without inner ring cables [J]. Adv. Steel Constr. 19(2) (2023) 112-120.
[2] J. Lu, S.D. Xue, X.Y. Li, Q. Liu, Study on static and dynamic experiment of spatial cable-truss structure without inner ring cables based on grid-jumped layout of struts [J]. Adv. Steel Constr. 18(4) (2022) 783-792.
[3] J. Lu, S.D. Xue, X. Y. Li, M. Dezhkam, Segmented assembly construction forming method without brackets of spatial cable-truss structure without inner ring cables [J]. Adv. Steel Constr. 18(3) (2022) 687-698.
[4] J. Lu, X. Y. Li, S.D. Xue, R.J Liu, M. Dezhkam, Study on force mechanism of cable-truss frame and jumped layout of annular crossed cable-truss structure [J]. Adv. Steel Constr. 17(3) (2022) 243-252.
[5] A.L. Zhang, W.J. Rao, W.L. Cui, Stability analysis of pre-stress loss on suspend-dome structure under fire hazard [J]. J. Beijing Uni. Technol. 8 (36) (2010) 1044-1051 (in Chinese). doi:10.11936/bjutxb2010081044.
[6] Y. Du, J.Y. Richard Liew, H. Zhang, G.Q. Li, Pre-tensioned steel cables exposed to localized fires [J]. Adv. Steel Constr. 14(2) (2018) 206-226. Doi: 10.18057/IJASC.2018.14.2.5.
[7] M.F. Day, E.A. Jenkinson, A.I. Smith, Effect of elevated temperatures on high-tensile-steel wires for prestressed concrete [J]. Proc. Inst. civ. Eng. 16 (5) (1960) 55-70. https://doi.org/10.1680/iicep.1960.11781.
[8] J. Gales, L.A. Bisby, T. Strafford, New parameters to describe high-temperature deformation of prestressing steel determined using digital image [J].Correlation, Struct. Eng. Int. 22 (4) (2012) 476–486. https://doi.org/10.2749/ 101686612X13363929517730.
[9] X.M. Hou, W.Z. Zheng, V. Kodur, H.Y. Sun. Effect of temperature on mechanical properties of prestressing bars [J].Constr. Build. Mater. 61 (6) (2014) 24-32. https://doi.org/10.1016/j.conbuildmat.2014.03.001.
[10] G.J. Sun, Z.H. Li, J.Z. Wu, J.Y. Ren, Investigation of steel wire mechanical behavior and collaborative mechanism under high temperature [J]. J. Constr. Steel Res.188 (2022) 107039. https://doi.org/10.1016/j.jcsr.2021.107039.
[11] Z. Zong, D. Jiang, J. Zhang, Study of the mechanical performance of grade 1860 steel wires at elevated temperatures [J]. Mater. Res. Innov. 19 (suppl.5) (2015), S5.1175-S5.1181. http://dx.doi.org/10.1179/1432891714Z.0000000001273.
[12] P. Kotsovinos, A. Atalioti, N. McSwiney, F. Lugaresi, G. Rein, A.J. Sadowski, Analysis of the thermo-mechanical response of structural cables subject to fire [J]. Fire Technol. (2019) 1–29, https://doi.org/10.1007/s10694-019-0.
[13] Y. Du, J.Z. Peng, J.Y. Richard Liew, G.Q. Li, Mechanical properties of high tensile steel cables at elevated temperatures [J]. Constr. Build. Mater. 182 (2018) 52-65. https://doi.org/10.1016/j.conbuildmat.2018.06.012.
[14] Y. Du, H.H. Qi, J. Jiang, J.Y. Richard Liew, G.Q. Li, Mechanical properties of 1670 MPa parallel wire strands at elevated temperatures [J]. Constr. Build. Mater. 263 (2020) 120582. https://doi.org/10.1016/j.conbuildmat.2020.120582.
[15] Y. Du, J.Y. Richard Liew, J. Jiang, G.Q. Li, Improved time-hardening creep model for investigation on behavior of pre-tensioned steel strands subject to localized fire [J]. Fire Saf. J. 116 (2020) 103191. https://doi.org/10.1016/j.firesaf.2020.103191.
[16] G.J. Sun, J. Yuan, S.D. Xue, Y. Yang, M. Mensinger, Experimental investigation of the mechanical properties of zinc-5% aluminum-mixed mischmetal alloy-coated steel strand cables [J]. Constr. Build. Mater. 233 (2020) 117310.
[17] G.J. Sun, X.H. Li, J.Z. Wu, R.H. Chen, G.N. Chen, Deformation of stainless steel cables at elevated temperature [J]. Eng. Struct. 211 (2020) 110498. https://doi.org/10.1016/j.engstruct.2020.110498.
[18] G.J. Sun, S. Xiao, X.S. Qu, Thermal–mechanical deformation of Galfan-coated steel strands at elevated temperatures [J]. J. Constr. Steel Res. 180 (2021) 106574. https://doi.org/10.1016/j.jcsr.2021.106574.
[19] E.F. Du, X.B. Hu, Z. Zhou, Q. Li, X. Lyu, Y.Q. Tang, Experimental investigation on mechanical properites of Grade 1670 steel wires under and after elevated temperature [J]. Adv. Steel Constr. 19(1) (2023) 9-16.
[20] Y. Du, Y.K. Sun, J. Jiang, G.Q. Li, Effect of cavity radiation on transient temperature distribution in steel cables under ISO834 fire [J]. Fire Saf. J. 104 (2019) 79-89. https://doi.org/10.1016/j.firesaf.2019.01.002.
[21] V. Fontanari, M. Benedetti, B.D. Monelli, F. Degasperi, Fire behavior of steel wire ropes: Experimental investigation and numerical analysis [J]. Eng. Struct. 84 (2015) 340-349. http://dx.doi.org/10.1016/j.engstruct.2014.12.004.
[22] V. Fontanari, M. Benedetti, B.D. Monelli, Elasto-plastic behavior of a Warrington-Seale rope: Experimental analysis and finite element modeling [J]. Eng. Struct. 82 (2015) 113-120. http://dx.doi.org/10.1016/j.engstruct.2014.10.032.
[23] GB 51249-2017, Code Fires Safety Steel Building Structures [S]. China Planning Press, Beijing, 2017.
[24] G.Q. Li, Y. Du, A new temperature-time curve for fire-resistance analysis of structures [J]. Fire Saf. J. 54 (2012) 113-120. http://dx.doi.org/10.1016/j.firesaf.2012.07.004.
[25] EN 1991-1-2, General actions-actions on structures exposed to fire, European Committee for Standardization [S]. Brussels, 2002.
[26] J.R. Welty, G.L. Rorrer, C.E. Wicks, C.E. Wicks. Fundamentals of momentum, heat, and mass transfer, fifth ed. [M]. Wiley, State of New Jersey, 2008.
[27] R. M. Lawson , G. M. Newman, PUB 080 Fire Resistant Design Of Steel Structures: A Handbook To Bs 5950: Part 8 [S]. The Steel Construction Institute, Ascot,1990.
[28] H. Zhou, Y. DU, G.Q. Li, J.Y. Richard Liew, X.C. Wang, Experimental study on thermal expansion and creep properties of pre-stressed steel strands at elevated temperature [J]. Eng. Mech. 35(06) (2018) 123-131. (in Chinese). Doi: 10.6052/j.issn.1000-4750.2017.02.0155
[29] G.Y. Wang, Y.D. Meng, R.J. Liu, Liu Werihua. An experimental research on the fire resistance of steel cable structures and its finite element analysis [J]. J. Build. Struct. :1-8[2022-09-16]. (in Chinese). DOI:10.14006/j.jzjgxb.2021.0563.
[30] L.L. Wang, G.Q. Li, Y.Y. Xu, W.H. Wang, Insulating properties of intumescent coating for steel element under different fire conditions [J]. J. Build. Mater. 19 (02) (2016), 267-273+279. (in Chinese). doi:10.3969/j. issn.1007-9629.2016.02.010.
[31] G.Q. Li, P.J. Wang . Advanced Analysis and Design for Fire Safety of Steel Structures [M]. Advanced Topics in Science and Technology in China, Zhejiang, 2013.

Advanced Steel Construction – Vol. 20 No. 1 (2024) 12–20
DOI:10.18057/IJASC.2024.20.1.2

RESIDUAL LIFE PREDICTION AND DESIGN CORRECTION METHOD OF CORRODED CIRCULAR STEEL TUBES BASED ON TIME-VARYING RELIABILITY

Zhi-Wei Zhang [1], Hua-Jie Wang [1, *], Hong-Liang Qian [1], Xiao-Fei Jin [2], Qiu Feng [1, 3] and Feng Fan [3]

[1] *Department of Civil Engineering, Harbin Institute of Technology at Weihai, Weihai 264209, China*
[2] *China Construction First Group Corporation Limited, Beijing 100161, China*
[3] *School of Civil Engineering, Harbin Institute of Technology, Harbin 150090, China*
** (Corresponding author: E-mail: huajie_wang@hit.edu.cn)*

ABSTRACT

Current research on the effects of corrosion on the safety of steel members is primarily focused on the degradation of the ultimate bearing capacity, and there is a lack of research on the reliability-based service life assessment. In this paper, a modified reliability function and an uncertainty model for each parameter considering the effects of corrosion are established based on the reliability analysis method of the GB50068-2018 design specification. The effects of the corrosive environment category, wall thickness, and slenderness ratio on the time-varying reliability of axially compressed round tubes are analyzed. The results indicate that an increase in the corrosion duration and the environmental category can cause a decrease in the reliability index of the component, and the smaller the wall thickness, the faster the corrosion-related degradation of the reliability index. However, with the increase of the slenderness ratio, the corrosion-related degradation of the reliability index gradually decreases. In the end, a residual life prediction method and a design correction method for corroded components based on the reliability index are proposed. Moreover, the values of the corrosion life and corrosion coefficient of circular steel tubes for different environmental categories, slenderness ratios, and thicknesses are determined. This paper provides a technical reference for the residual life prediction and full life design of round steel tubes considering local corrosion.

ARTICLE HISTORY

Received: 15 January 2023
Revised: 31 May 2023
Accepted: 27 August 2023

KEYWORDS

Local corrosion;
Round steel tubes;
Reliability;
Durability;
Residual life prediction

Copyright © 2024 by The Hong Kong Institute of Steel Construction. All rights reserved.

1. Introduction

As the service life of a large number of steel structures progresses, durability issues[1-3] related to corrosion problems come to the fore[4,5]. However, there are no operational assessment and design correction methods that take into consideration the development and effects of corrosion under different environments. Therefore, it is of high importance to conduct research on this issue.

Previous studies [6-8] have paid extensive attention to the effects of corrosion on the durability of reinforced concrete structures, focusing on characteristics including the corrosion development rate, surface crack length and width, and stray currents.

In contrast, there is a distinct lack of research on the durability of steel structures after corrosion, with available studies focusing mainly on the degradation of the load bearing capacity of components. A number of scholars have shown that corrosion has a non-negligible effect on the load-bearing capacity and structural safety of steel components. For example, Khedmati et al. [9] derived a semi-empirical equation based on a finite element model to predict the relationship between the axial compressive bearing capacity and the corrosion of circular steel tubes. Zhang et al.[10] analyzed the axial bearing capacity of irregularly corroded tubes and presented a recommended engineering assessment method. Wu et al [11] used an outdoor cycling spray and found that the corrosion duration had a strong effect on the ultimate bearing capacity of the specimens and a small effect on their stiffness. Jie et al [12] used hemispherical notches to simulate pitting damage and performed and analyzed the effect of small corrosion points on the fatigue performance of cross-shaped joints. Yang et al [13] investigated the performance degradation of offshore sheet pile walls using a corrosion model that could approximate the actual conditions.

It should be noted that the above studies mainly concern the degradation of the carrying capacity rather than the change in the failure probability. However, most of the current design codes [14-16] are based on the reliability theory and do not take into account the effect of corrosion on design [17,18]. In response to this conflict between research and design, Lin et al [19] employed the Monte Carlo method to analyze the uncertainty of pitting corrosion in submarine pipelines. Their study revealed that the uncertainty of the corrosion process is crucial to the study of corrosion effects. Ma et al. [20] calculated the failure probability of corroded pipelines based on the critical and working pressures. Zelmati et al. [21] concluded that the reliability of gas transmission steel pipelines was reduced by 40% when the defect length of the pipeline increased to 55 mm. While the loading form considered in the above studies is internal pressure, the main loading form for circular tubes in spatial structures is axial pressure[22,23].

In view of the above limitations, this paper takes the axially compressed circular steel tubes in spatial steel structures as the research object. In the analysis of the reliability indices, the effect of corrosion is taken into account. On the basis of the existing liability function, the uncertainty of the generation and effect of local corrosion are taken into consideration. The variation trend of the reliability index of corroded axially compressed circular steel tubes under different load combinations is analyzed. Finally, based on the reliability index requirements, the residual life of steel tubes under different corrosion environments and the corrosion coefficient value for structural design modification are determined.

2. Reliability calculation model

2.1. Reliability function

According to GB50068-2018 [24], the basic variables to be considered when calculating the reliability index of a structure include the material strength K_M, geometric dimensions K_G, resistance calculation mode K_P, effect calculation mode K_B, and action effect S. The action effect in the reliability function can be divided into the constant load effect S_G, live load effect S_{LR}, and wind load effect S_W. Using these essential variables, the reliability function can be obtained, when the corrosion effect is not taken into account.

$$Z = R - S = K_P R(K_M, K_G) - K_B(S_G + S_{LR} + S_W) \tag{1}$$

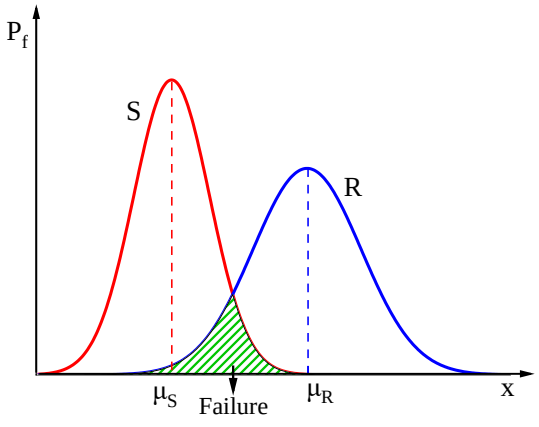

Fig. 1 Uncertainty of corrosion effect

As illustrated in Fig. 1, both the resistance R of the structure and the action S of the load are stochastic in nature. When the resistance R is larger than the effect S (Z>0), the structure is in a safe state; when the resistance R is smaller than the effect S (Z<0), the structure is in a failure state; and when the resistance R is equal to the effect S (Z=0), the structure is in a marginal state. The green area in Fig. 1 is the probability of the failure state.

When the corrosion effect is taken into consideration, K_C is introduced to represent the resistance degradation caused by corrosion; thus, the modified function becomes:

$$Z = K_P K_C R(K_M, K_G) - K_B(S_G + S_{LR} + S_W) \tag{2}$$

For axially compressed components, the resistance is related to the material strength f, the cross-sectional area A_n, and the stability coefficient φ. The action effect can be considered according to the provisions of the load sub-factor in GB50009-2012 [25]. As a result, the resistance and effect of corrosion can be determined by:

$$R_d = \varphi A_d f_d \tag{3}$$

$$S_d = \gamma_0(\gamma_G S_{GK} + \gamma_{LR} S_{LRK} + \psi\gamma_W S_{WK}) \tag{4}$$

where the subscripts k and d denote the standard and design values, respectively, S_{GK} is the standard value of the constant load effect, S_{LRK} is the standard value of the live load effect, S_{WK} is the standard value of the wind load effect, γ is the load sub-factor, ψ is the combined value factor, and γ_0 is the structural importance factor, which is taken as 1.

In the design of building structures, when the components are in the ultimate state, the design value of the resistance is equal to that of the load effect, which can be expressed as:

$$R_d = S_d \tag{5}$$

Consequently, when φ, A_d, and f_d are known, the load effect design value S_d can be determined, and the standard load effect value generated by each load can be determined according to the load ratio relationship commonly used in engineering practice. Subsequently, the relationship between the standard value of each load, its mean value, and its variation coefficient is used; that is, the probability distribution pattern of each load is obtained. The specific process of the above reliability index calculation can be found in the literature [26-28].

Taking the corrosion effects into consideration, the equation of state for axially compressed round steel tubes can be further expressed as:

$$Z = K_P K_C K_G K_M R - K_B(S_G + S_{LR} + S_W) \tag{6}$$

where K_C is the bearing capacity reduction factor due to corrosion. To determine the reasonable value of K_C, experimental and numerical simulation studies were performed in our previous work [29]. The factors considered in the study included the dimensions of the steel tubes and the size of local corrosion, as well as the location of random corrosion. A comparison of the experimental and simulation results is illustrated in Fig. 2.

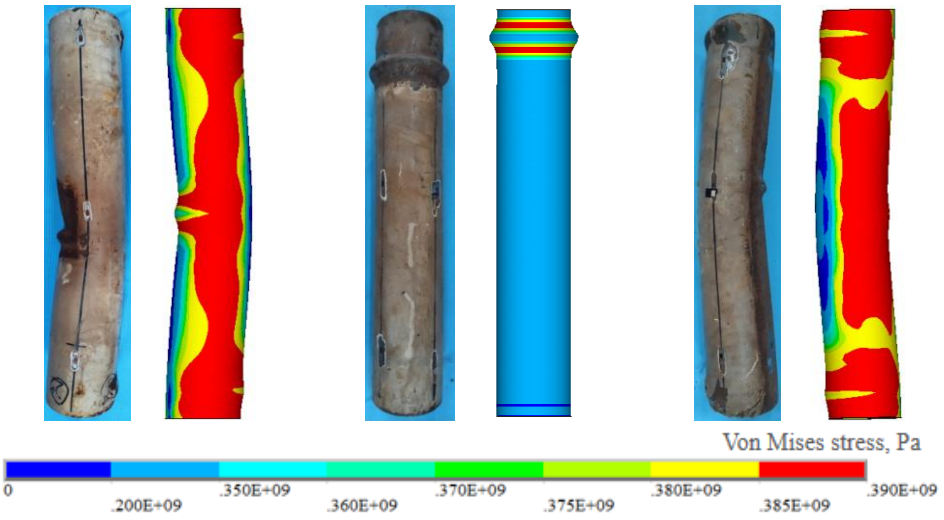

Fig. 2 Comparison of experimental and simulation results

Under the protective effect of the external coating, it has been determined that the main form of corrosion of steel members is localized corrosion. Based on the experimentally validated model, the reduction factor K_C for locally-corroded round steel tubes was determined by parametric analysis using the following equation [30]:

$$K_C = \begin{cases} 0.01*(-19*D_C + 19*H_C^2 - 13H_C - 7*L_C - 109D_C*H_C) + 1 & \lambda < 70 \\ 0.01*(-34*D_C + 22*H_C^2 - 22H_C + 0.08*\lambda - 17*L_C - 62D_C*H_C) + 1 & 150 \geq \lambda \geq 70 \end{cases} \tag{7}$$

where λ is the slenderness ratio of the tube, H_C is the circumferential ratio of corrosion, L_C is the axial ratio of corrosion, and D_C is the depth ratio of corrosion.

2.2. Calculation method

The Monte Carlo method was utilized for random sampling, and according to the law of large numbers, when the number of samples is substantially large, the probability value obtained statistically after random sampling is equal to the actual probability value. A more detailed description of the Monte Carlo method and its application in corrosion prediction can be found in the literature [19, 31].

For an in-service building structure, the failure probability is about 10^{-5}, and then, when the sampling number is 10^7, it can be guaranteed that the error is less than 20% with a confidence level of 95% [26, 32]. Consequently, the number of samples used in the subsequent study of this paper was $3*10^7$, and when the failure probability has been determined, the corresponding reliability index can be deduced from the standard normal distribution. The reliability index calculation results can be found in Section4.

3. Uncertainty of parameters

3.1. Load and resistance uncertainty

A large number of engineering applications and measurements have indicated that there is significant randomness and variability in both load and resistance. The uncertain statistical parameters of loads according to the provisions of "Unified Standard for Reliability Design of Building structures" GB50068-2018 [4], "Code for load of Building structures" GB50009-2012 [25], and "Technical Specification for Spatial Grid structures" JGJ7-2010 [33] are shown in Table 1.

On the other hand, the uncertainty regarding the structural resistance to load mainly includes the effect of several aspects, such as the geometric dimension uncertainty K_G introduced above, the uncertainty of the material properties K_M, and that of the resistance calculation model K_P. The uncertainties of each parameter for mild steel [34, 35] are listed in Table 2.

Table 1
Load uncertainty

	Mean/standard value	Variation coefficient	Distribution type
Constant load	1.06	0.07	Normal distribution
Live load	0.644	0.233	Extreme value type I distribution
Wind load	0.908	0.193	Extreme value type I distribution
Snow load	1.14	0.225	Extreme value type I distribution
Effect calculation model	1.0	0.05	Normal distribution

Table 2
Resistance uncertainty

	Mean/standard value	Variation coefficient	Distribution type
Wall thickness	1.0	0.05	Normal distribution
Diameter	1.0	0.03	Normal distribution
Yield strength	1.19	0.096	Normal distribution
Young's modulus	1.02	0.01	Normal distribution
Resistance calculation model	1.0	0.05	Normal distribution

3.2. Corrosion uncertainty

In addition to the aforementioned uncertainties, corrosion of steel structures occurs inevitably with the progress of service life. The reaction process and speed of corrosion are also associated with strong randomness. Based on the specification "Corrosion of Metals and Alloys—Corrosivity of Atmospheres— Classification, Determination and Estimation" ISO 9223:2012 [36], the relationship between corrosion amount depth and time can be expressed as follows:

$$d_t = \begin{cases} \gamma_{corr} t^n & t < 20 \\ \gamma_{corr}(20^n + n(20^{n-1})(t-20)) & t \geq 20 \end{cases} \quad (8)$$

where t is the duration of the corrosion process, d_t is the corrosion volume of the t^{th} year (mm), γ_{corr} is the corrosion volume of the metal in the first year, and n is the environmental characteristic parameter of the metal in the corrosion model. It reflects the inhibitory effect of corrosion products on the corrosion rate. Taking a value less than 1, its distribution can be simplified to a normal distribution with a mean value of 0.523 and a standard deviation of 0.026 [37-39].

The corrosion environment can be divided into 6 categories [36]. Among them, C5 has a wide range of corrosion rate, which here has been divided into C5A and C5B. The corrosion rate range for each category in the first year and the corresponding environment type are given in Table 3.

Table 3
Corrosion environment category

Category	One year after exposure		Reference environment case
	Loss of weight ($g \cdot m^2$)	Loss of thickness (μm)	
C1 Very low	<10	<1.3	Atmospheric environments with very low levels of pollution and very short periods of humidity, e.g., deserts, Antarctica, etc.
C2 Low	10-200	1.3-25	Atmospheres with low pollution levels in rural areas or terminals with low humidity levels
C3 Medium	200-400	25-50	Moderately polluted urban and industrial atmospheres or low-pollution areas in the temperate subtropics
C4 High	400-650	50-80	Highly polluted urban and industrial areas, medium salinity coastal areas, or swimming pools
C5 Very high	650-1100	80-140 (C5A)	Highly polluted industrial environments, high salinity seaside areas, or tropical or subtropical seaside industrial environments
	1100-1500	140-200 (C5B)	
CX Extreme	>1500	>200	Specific marine environments, e.g., tropical offshore environments, or production spaces with almost permanent condensation

In addition to the corrosion rate, it is also necessary to take the uncertainty of the corrosion area size into consideration. Through statistical analysis of corrosion observation data[26,27], the probability distribution patterns of the corrosion annular size, longitudinal size, and depth ratio have been determined (Table 4).

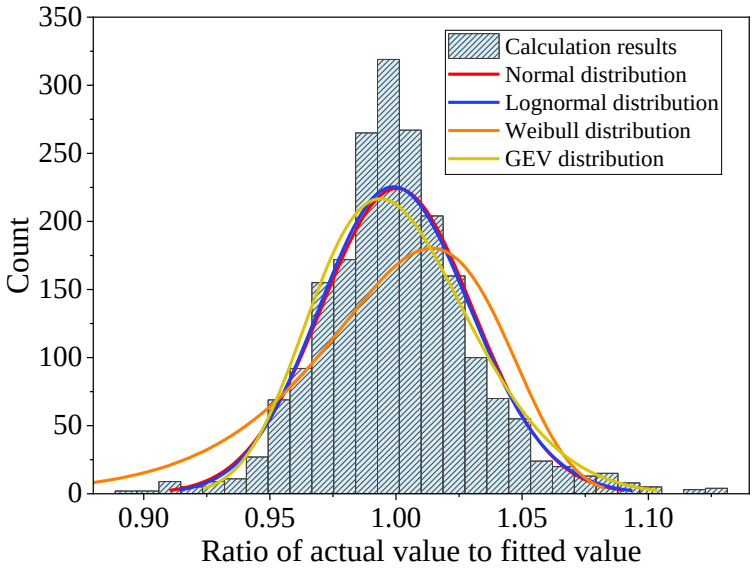

Fig. 3 Corrosion effect uncertainty

Table 4
Corrosion size uncertainty

Corrosion size direction	Corrosion size-to-depth ratio		
	Mean value	Standard deviation	Distribution type
Circumferential	150	25	Normal distribution
Longitudinal	550	70	Normal distribution

The uncertainty of the simplified calculation method of the corrosion effect (Eq. 7) should also be taken into consideration. The deviation of the simplified calculation method can be obtained by dividing the results of the finite element model calculation with those of the simplified calculation. Based on the data reported in the literature [30], Figure 3 exhibits the deviation distribution of the calculation method. The distribution of the corrosion effect calculation model resembled that of normal distribution. Using a normal distribution with a mean of 1 and a standard deviation of 0.03 to describe the actual and fitted values, the uncertainty of the corrosion effect calculation model can be suitably amplified, making the calculation results slightly biased toward safety.

The above analysis takes into account the stochastic process of the corrosion area expansion and corrosion depth deepening with the increase of the structure service time. In the first year of service of the structure, the member surface exhibits a small exposure to corrosion, which can be probably attributed to bumping or accidental abrasion of the coating during the transportation of the member[40, 41]. During the subsequent service period, the local corrosion corresponding to the initial exposure is gradually aggravated, which is consistent with the assumption made in the reliability analysis of this paper.

4. Time-varying reliability index calculation

4.1. Loading conditions considered

In engineering design, it is necessary to consider the typical loads for the reliability level analysis of structural members. For the purposes of this paper, three most common forms of load combinations were selected (Table 5). The slenderness ratio is controlled within 150 [14]. The numerical relationships between different load effects on structures are not constant and correspond to a variety of reliability indices. However, relevant studies [42-44] have reported that, when the ratio between variable and constant loads is taken as 0.5 and that between wind or snow loads and variable loads is taken as 0.7, the calculated reliability indices are similar to those obtained by the weighted combination of different load effects. Thus, the above values were used in this study.

Table 5
Selection of load combinations

Condition	Considered loads	Expression [25]
1	Constant load; live load	$1.3S_G+1.5S_{LR}$
2	Constant load; live load; wind load	$1.3S_G+1.5(S_{LR}+0.6S_W)$
3	Constant load; wind load; snow load	$1.3S_G+1.5(S_W+0.6S_N)$

4.2. Effect of corrosion duration and environmental category

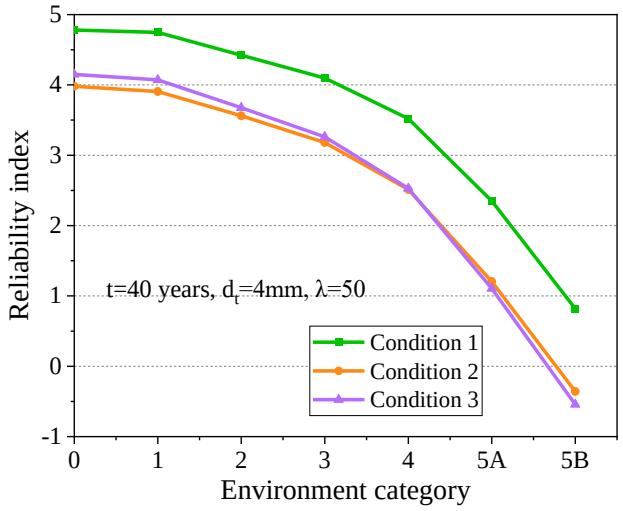

Fig. 5 Reliability index as a function of the environment category

The duration of the corrosion process and the environmental category determine the corrosion depth. According to Fig. 4, when the other factors remained unchanged, the reliability index of an axially compressed circular steel tube changed with increasing corrosion time. It should be noted that d denotes the original wall thickness of the steel tube and λ is its slenderness ratio. It can be observed that with the progress of service time, the reliability index of the circular steel tube under axial compression exhibited a downward trend, indicating that the failure possibility increased gradually. Moreover, the change trend of the reliability index was basically the same under the different load combinations. The curve of the relationship between reliability index and corrosion time was smooth; thus, the index was calculated every 5 years in order to reduce the calculation cost.

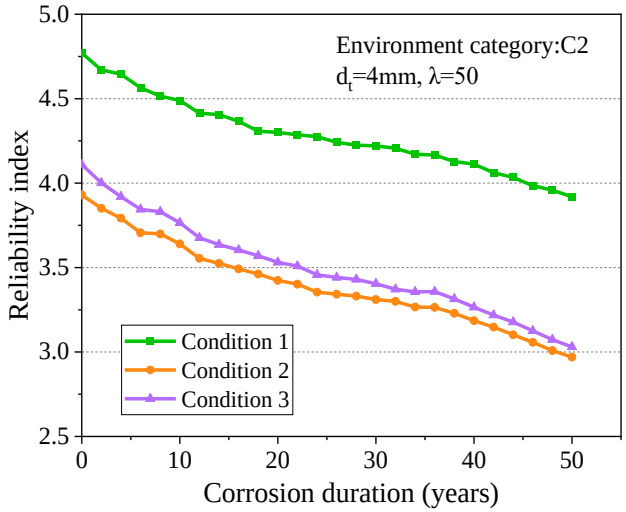

Fig. 4 Reliability index as a function of the corrosion duration

Fig. 5 depicts the reliability index of the axially compressed round steel tube under different corrosive environment categories. It can be observed that, as the corrosive environment category increased, the reliability index of the component exhibited a decreasing trend. When the corrosive environment category was between C1-C3, the change in the reliability index was small, while when it was between C4 and C5, the reliability index decreased sharply.

To better understand the effect of different corrosion environments and corrosion duration on the reliability index, Fig. 6 demonstrates the relationship between the reliability index, the corrosion rate, and the corrosion duration. It can be seen that, as the corrosion time and harshness of the environment increase, the reliability index decreased significantly. When the corrosive environment category was C1, the reliability index after 50 years of corrosion for a steel tube with 4 mm wall thickness and slenderness ratio of 50 was 3.71. When the environment category was C2, the corresponding reliability index decreased slightly to 3.45, while the reliability indices under the C3 and C4 category corrosive environments were 2.97 and 2.23, respectively. The reliability index for the steel tube in the extremely corrosive environment (C5B) decreased to 1.28 after 50 years, and the failure probability of the component was more than 50% with significant structural risk.

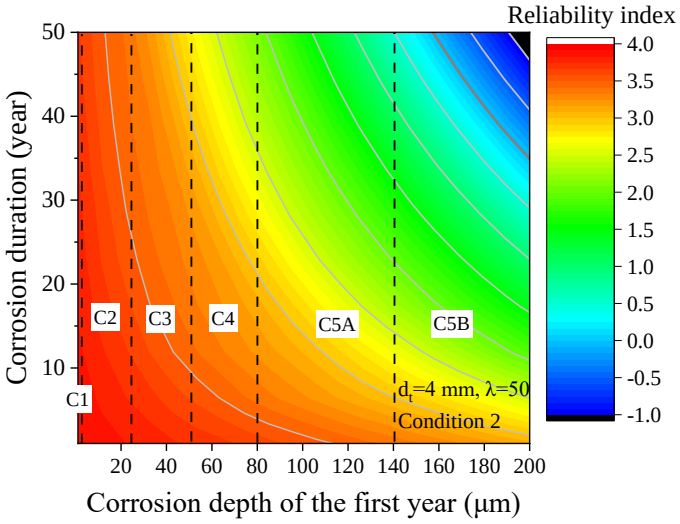

Fig. 6 Reliability index under different corrosion rate and corrosion duration

4.3. Effect of steel tube wall thickness and slenderness ratio

The corrosion depth ratio D_C in Eq. (7) denotes the ratio of the wall thickness loss to the original wall thickness of the steel tube; thus, in addition to the corrosion depth, the effect of the wall thickness of the steel tube should also be taken into consideration. In Fig. 7, it can be observed that, when the wall thickness of circular steel tubes is small, the corrosion can easily cause serious reliability index degradation; however, when the wall thickness is larger, the effect of corrosion is relatively weak. Therefore, in the follow-up parametric analysis, it is necessary to make a more detailed parameter division for steel tubes with small wall thickness.

In Fig. 8, it can be observed that the reliability index of the steel tube increased with the increase of the slenderness ratio. When the slenderness ratio was larger than 70, the effect of corrosion on the reliability index decreased with increasing slenderness ratio. This phenomenon can be attributed to that, with the increase of the slenderness ratio, the initial bending phenomenon of large-slenderness steel tubes becomes increasingly apparent, and the effect of local defects and centroid deviation induced by corrosion on the bearing capacity becomes weaker. Based on the calculation results, when summarizing the reliability index under different conditions, the slenderness ratio can be simply classified into five regions, i.e., less than 40, 40-70, 70-100, 100-130, and 130-150.

5. Residual life expectancy

5.1. Design goals of the GB50068-2018 specification

Currently, the limit state design method based on the probability theory and expressed in terms of sub-factors is commonly used in structural design codes. In GB50068-2018 [19], the reliability requirements of the structure are divided into different security levels according to the possible consequences of structural damage. The corresponding lower limit values of the reliability indices are listed in Table 6.

Table 6
Reliability indices of structural components

Damage Type	Security Level		
	Level I	Level II	Level III
Ductile damage	3.7	3.2	2.7
Brittle damage	4.2	3.7	3.2

Ductile damage means that the structural elements undergo obvious deformation or other precursors prior to damage, while brittle damage is associated with no obvious deformation or other precursors prior to damage. Most of the structures are commonly designed based on security level II, and the damage of steel structures is generally considered to be ductile damage [14]; thus, the lower limit for the reliability index in the design corresponding to this study was $\beta_0 = 3.2$.

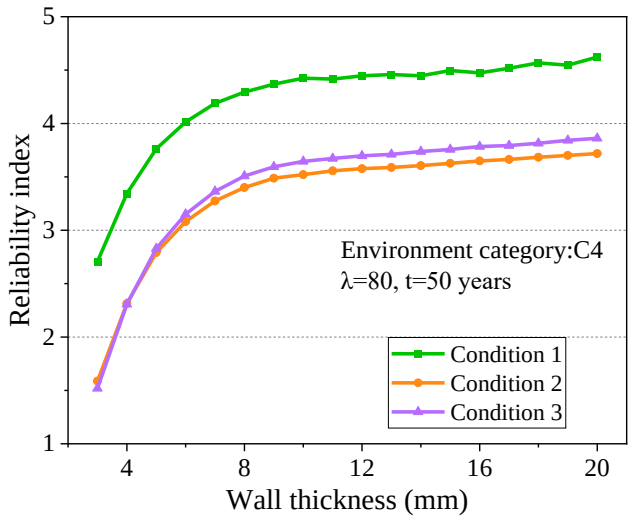

Fig. 7 Reliability index as a function of the wall thickness

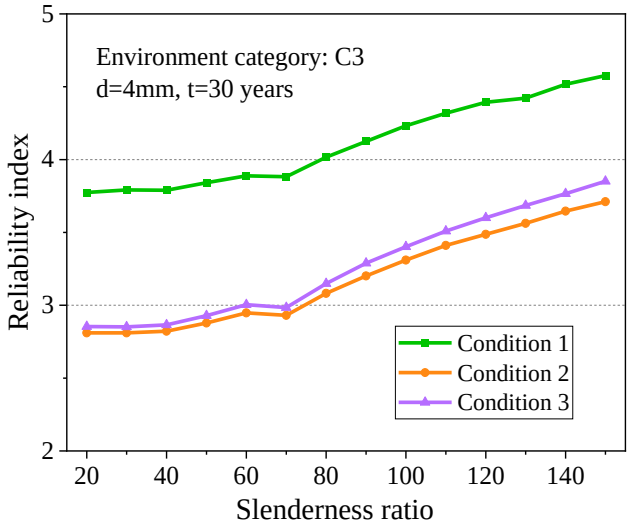

Fig. 8 Reliability index as a function of the slenderness ratio

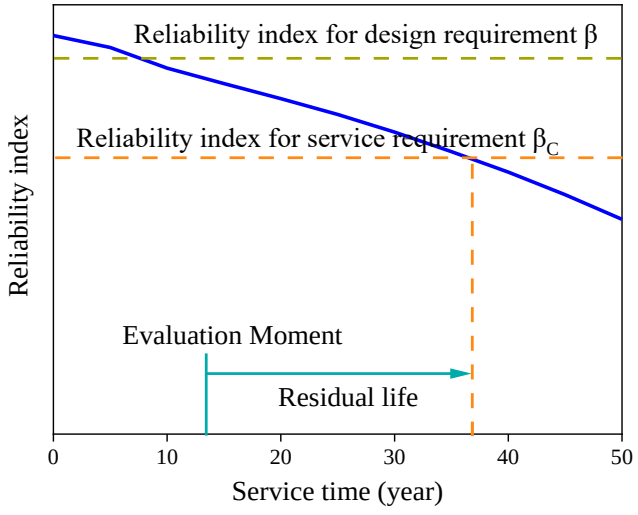

Fig. 9 Relationship between reliability index and remaining life

5.2. Residual life prediction

It should be highlighted that the remaining life of a structural member based on reliability theory is not the time remaining until the structure is destined to fail or be destroyed. In fact, under the reliability theory, just as no structure is completely safe and never likely to fail, no structure is 100% destined to fail. The safety of a structural component is related to a certain probability, and the prediction of its residual life is also based on a certain reliability index, i.e., the end of service life is considered to have been reached when the reliability index of the structure is below a certain level. This reliability index can be called the reliability index for the service requirement β_C, which corresponds to the corrosion duration called the ultimate corrosion duration T_C. For the assessment of in-service structures, the residual life of the members under the reliability index for the service requirement β_C can be determined by subtracting the ultimate corrosion duration from the elapsed in-service time. The relationship between the indicators and the residual life is presented in Fig. 9.

According to the above analysis, determining the reliability index for the service requirement β_C and calculating its corresponding ultimate corrosion duration T_C are the core elements of determining the residual life. Currently, there is no unified conclusion on the reliability index of the endurance limit state, and the design codes [14] provide only a recommended value of 1.0-2.0 for the reliability index of the first type of endurance limit state, e.g., cover damage, steel bar rust, etc. Nevertheless, for the other type of durability limit state, which is directly related to the bearing capacity and structural safety of members, there is no suggestion regarding the appropriate reliability index value. Considering that the problems caused by the third category of durability problems are more severe, the reliability index value of 1.0-2.0 may be on the low side. To meet the safe use requirements of the structure, this paper suggests that β_C should be taken according to the lower security level (Table 1). For instance, for ductile damage members with security level 1, the β_C needs to be designed for ductile damage members with security level 2. Therefore, the β_C corresponding to the ultimate corrosion duration of second-class ductile damage components needs to be used, which is 2.7 (Table 6).

Through linear interpolation of the reliability index, the ultimate corrosion duration T_C of round steel tube components under different corrosion conditions can be determined.

Under C1 and C2 corrosion environments, the reliability index of all components is higher than the value of β_C after 50 years, and the lowest value is 3.15; thus, the T_C can be considered to be more than 50 years. This is mainly due to that the reliability indices specified in the codes are "lower limit values", i.e., any structural calculation results should be higher than this value. After several revisions of the relevant codes, the reliability index for the initial design of the structure is now significantly higher than the target reliability index (3.2). In addition, the code indicates that the current reliability index is high in order to leave room for "environmental factors" [24]. Tables 7 to 10 lists the ultimate corrosion duration of steel tubes in the C3, C4, C5A, and C5B corrosion environments, respectively. It can be found that the severity of the corrosive environment can significantly affect the ultimate corrosion duration T_C. Furthermore, when the wall thickness or slenderness ratio is increased, the ultimate corrosion duration will increase as well, indicating that the structural members can withstand longer corrosion times on the premise of ensuring safety.

Table 7
Ultimate corrosion duration in C3 type corrosive environment

Slenderness ratio	Wall thickness (mm)								
	3	4	5	6	8	10	12	14	16
15-40	41.8	50+	50+	50+	50+	50+	50+	50+	50+
40-70	46.3	50+	50+	50+	50+	50+	50+	50+	50+
70-100	48.6	50+	50+	50+	50+	50+	50+	50+	50+
100-130	50+	50+	50+	50+	50+	50+	50+	50+	50+
130-150	50+	50+	50+	50+	50+	50+	50+	50+	50+

Table 8
Ultimate corrosion duration in C4type corrosive environment

Slenderness ratio	Wall thickness (mm)								
	3	4	5	6	8	10	12	14	16
15-40	19.8	31.9	44.5	50+	50+	50+	50+	50+	50+
40-70	23.1	35.4	47.4	50+	50+	50+	50+	50+	50+
70-100	31.3	40.2	50+	50+	50+	50+	50+	50+	50+
100-130	40	50+	50+	50+	50+	50+	50+	50+	50+
130-150	44	49	50+	50+	50+	50+	50+	50+	50+

Table 9
Ultimate corrosion duration in C5A type corrosive environment

Slenderness ratio	Wall thickness (mm)								
	3	4	5	6	8	10	12	14	16
15-40	8	11.4	18.5	25	39.1	50+	50+	50+	50+
40-70	9.9	15.6	21.9	27.4	43.5	50+	50+	50+	50+
70-100	13.9	19.1	26.4	36.3	48	50+	50+	50+	50+
100-130	18.3	27.5	34.8	46.4	50+	50+	50+	50+	50+
130-150	21.1	32.8	42.8	50+	50+	50+	50+	50+	50+

Table 10
Ultimate corrosion duration in C5B type corrosive environment

Slenderness ratio	Wall thickness (mm)								
	3	4	5	6	8	10	12	14	16
15-40	4.1	6.8	9.4	13.6	22	32.1	42.8	50+	50+
40-70	5.4	8.7	12.3	17	25.6	34.8	46.3	50+	50+
70-100	8.2	11.5	15.4	22.2	33	41.3	49.5	50+	50+
100-130	10.5	20.9	21.8	27.7	39.5	50+	50+	50+	50+
130-150	11.9	20.3	26.8	32.4	48.5	50+	50+	50+	50+

6. Design correction

6.1. Suggestions for design corrections

According to Eqs. (6)-(8), the limit state design expressions for structural members contain various sub-factors, the values of which are determined by the code values regarding the reliability indicators. These reflect the acceptable level of the risk posed by structural failure. However, these reliability indicators and sub-factors do not take the effect of corrosion into account. When the bearing capacity of structural members is degraded due to corrosion, the reliability index is likely to no longer meet the corresponding reliability index requirement at the time of design, which means that the structural failure risk exceeds the acceptable level.

To tackle this problem, the corrosion coefficient γ_C is introduced into the structural design to consider the bearing capacity degradation and the reliability index decrease induced by corrosion. Accordingly, the load-bearing capacity limit state can be re-written as:

$$\gamma_C \varphi A_d f_d = \gamma_0 (\gamma_G S_{GK} + \gamma_{LR} S_{LRK} + \psi \gamma_W S_{WK}) \quad (9)$$

By introducing a corrosion factor γ_C lower than 1, the cross-sectional area required in the design phase of the structure will be increased, enhancing its ability to resist loads. There is a correlation between the corrosion coefficient γ_C and the corrosion time of components, which, in this study, is conservatively determined as the design life of 50 years for ordinary houses and structures. Moreover, its calculation process takes into account the increase in the wall thickness in order to reduce the impact of corrosion. A trial algorithm was adopted to gradually reduce the value of γ_C and calculate the reliability index

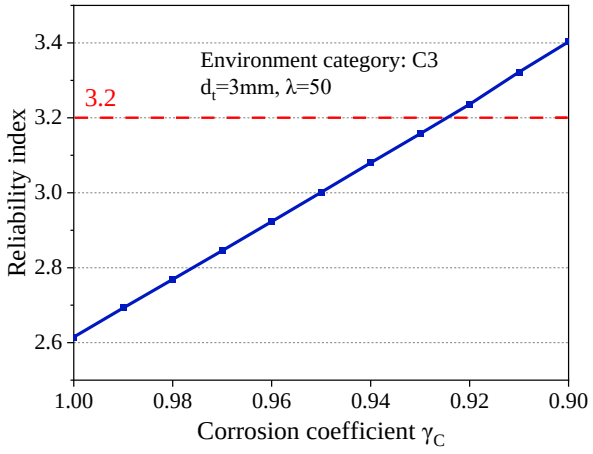

Fig. 10 Reliability index as a function of the corrosion coefficient

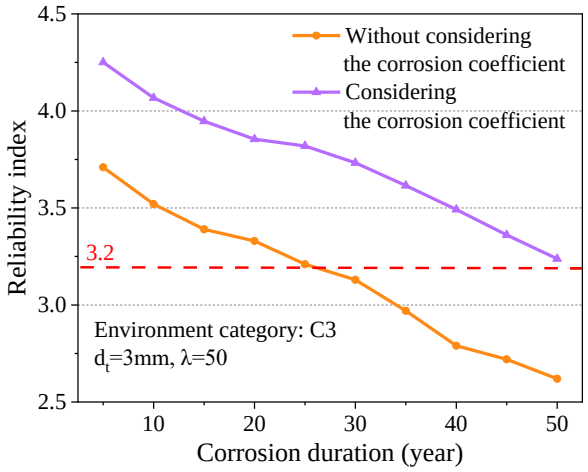

Fig. 11 Corrected reliability index

of the corresponding case until this becomes greater than or equal to the value of 3.2 taken from the specification. It should be noted that this value is taken considering the structural safety. This paper has been relatively conservative to use the reliability index for the design requirement at the limit state of the bearing capacity as the target.

Fig. 10 plots the reliability index of the structural members for a 50-year corrosion duration as a function of the corrosion coefficient γ_C. Fig. 11 illustrates the trend of the reliability index of the member after correcting the corrosion factor. The analysis results indicated that, by introducing the corrosion factor, the reliability indices of the steel members during the entire service period are greater than the required reliability index, which can guarantee the safety of the structure.

6.2. Corrosion coefficient value

Tables 11 to 14 list the corrosion coefficient γ_C values which can meet the reliability index requirements of the design code after trial calculations. In practice, the cross-sectional area A_0 obtained without taking the corrosion effect into consideration should be divided by the corrosion coefficient γ_C to determine the cross-sectional area A_1 that satisfies the corrosive environment. Subsequently, the wall thickness of the steel tube should be re-selected according to the new cross-sectional area (Fig. 12). The above adjustment process provides sufficient safety margins for steel members in harsh corrosive environments and meets the current structural design requirements. It should be clarified again that, for steel members in the C1 and C2 environments, the reduction of the load capacity due to corrosion is negligible (see Section 5.2); therefore, no adjustment to the cross-section is required.

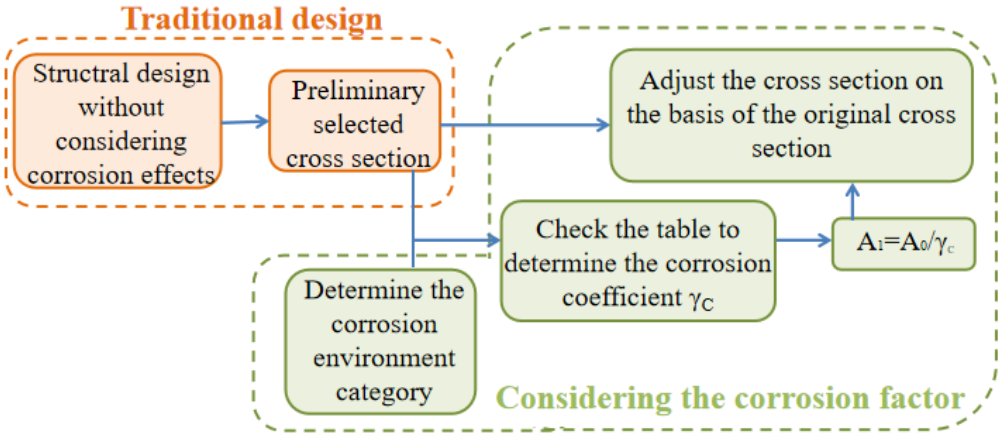

Fig. 12 Consideration of corrosion effects in the structural design process

Table 11
Corrosion factors for C3 type corrosive environment

Slenderness ratio	Wall thickness (mm)								
	3	4	5	6	8	10	12	14	16
15-40	0.91	0.96	0.98	0.99	1	1	1	1	1
40-70	0.91	0.97	0.99	1	1	1	1	1	1
70-100	0.94	0.99	1	1	1	1	1	1	1
100-130	0.99	1	1	1	1	1	1	1	1
130-150	1	1	1	1	1	1	1	1	1

Table 12
Corrosion factors for C4 type corrosive environment

Slenderness ratio	Wall thickness (mm)								
	3	4	5	6	8	10	12	14	16
15-40	0.82	0.88	0.91	0.95	0.98	1	1	1	1
40-70	0.82	0.88	0.93	0.96	1	1	1	1	1
70-100	0.84	0.91	0.95	0.99	1	1	1	1	1
100-130	0.89	0.95	1	1	1	1	1	1	1
130-150	0.92	0.98	1	1	1	1	1	1	1

Table 13
Corrosion factors for C5A type corrosive environment

Slenderness ratio	Wall thickness (mm)								
	3	4	5	6	8	10	12	14	16
15-40	0.68	0.76	0.81	0.85	0.93	0.94	0.96	0.98	0.99
40-70	0.68	0.77	0.81	0.86	0.93	0.95	0.97	0.99	1
70-100	0.7	0.77	0.82	0.86	0.95	0.97	0.99	1	1
100-130	0.74	0.81	0.87	0.92	0.97	1	1	1	1
130-150	0.75	0.84	0.92	0.95	0.99	1	1	1	1

Table 14
Corrosion factors for C5B type corrosive environment

Slenderness ratio	Wall thickness (mm)								
	3	4	5	6	8	10	12	14	16
15-40	0.58	0.67	0.72	0.77	0.84	0.88	0.91	0.94	0.96
40-70	0.58	0.68	0.72	0.77	0.84	0.88	0.92	0.94	0.97
70-100	0.61	0.68	0.74	0.77	0.85	0.92	0.96	0.98	1
100-130	0.62	0.71	0.78	0.81	0.9	0.95	0.99	1	1
130-150	0.65	0.73	0.81	0.86	0.92	0.98	1	1	1

7. Conclusions

In this paper, the time-varying reliability of corroded round steel tubes has been systematically analyzed. Moreover, a method for predicting the residual bearing capacity of members based on the time-varying reliability and a steel tube design correction method have been thoroughly investigated. The following main conclusions can be drawn.

1) A reliability function considering the effect of corrosion was established and the process of local corrosion development under coating protection was considered. Based on the Monte Carlo method, the effects of corrosion duration, corrosion environment category, wall thickness, and slenderness ratio on the reliability index of corroded tubes were analyzed. The reliability indices of various types of round steel tubes under different environmental categories and corrosion durations were determined.

2) Based on the time-varying reliability analysis considering corrosion, a method for predicting the residual life of corroded round steel tubes was proposed, which takes the reliability index for the service requirement β_C into consideration. Furthermore, the ultimate corrosion durations were given for structural evaluation.

3) To meet the requirements regarding the expected reliability indices for round steel tubes in corrosive environments, it has been proposed to modify their cross-section based on the corrosion coefficients. Finally, tables for consulting the corrosion coefficients that can facilitate the engineering design have been provided.

Acknowledgment

This work was financially supported by the National Natural Science Foundation of China (Grant No. 51308154), the Science Foundation of Shandong Province (Grant No. ZR2019MEE047), and the China Construction Group Science and Technology Project (Grant No. CSCEC-2020-Z-35).

Reference

[1] Ning J, Lin T, Liu S, et al. Three-dimensional pipeline element formulation for global buckling analysis of submarine pipelines with sleeper[J]. Marine Structures, 2023, 90: 103428.
[2] Kumar A, Roy K, Uzzaman A, et al. Finite element analysis of unfastened cold-formed steel channel sections with web holes under end-two-flange loading at elevated temperatures[J]. Advanced Steel Construction, 2021, 17(3): 231-242.
[3] Zhiwei Z, Huajie W, Hongliang Q, Feng Q, Xiaofei J, Feng F. Comparative analysis and applicability of corrosion test methods for construction steel components. Case Studies in Construction Materials, 2023, 18:e02034.
[4] Lisheng L; Houlin F; Yongqiang Z; Xinran X; Experimental Study on the Overall Stability

of Corroded H-Shaped Steel Beams [J]. Buildings, 2022, 12.
[5] Wang Y, Shenoi R, Wharton A, et al. Ultimate strength analysis of aged steel-plated structures exposed to marine corrosion damage: A review[J]. Corrosion Science, 2014.
[6] Goyal A, Pouya H S, Ganjian E, et al. A Review of Corrosion and Protection of Steel in Concrete[J]. ARABIAN JOURNAL FOR SCIENCE AND ENGINEERING, 2018(6):1-21.
[7] Hu J, Zhang S, Chen E, et al. A review on corrosion detection and protection of existing reinforced concrete (RC) structures[J]. Construction and Building Materials, 2022(28): 325.
[8] Fang X, Pan Z, Chen A. Phase field modelling of concrete cracking for non-uniform corrosion of rebar[J]. Theoretical and Applied Fracture Mechanics, 2022.
[9] Khedmati M R, Nazari M, Khalaj A. Numerical Investigation Into Ultimate Strength and Buckling Behavior of Locally Corroded Steel Tubular Members[C]. ASME 2012 31st International Conference on Ocean, Offshore and Arctic Engineering. 2012.
[10] Zhiwei Z, Yu G, Huajie W, et al. A sub-region-based method for evaluating regularly and irregularly corroded steel tubes under axial compression[J]. Structures. 2023.
[11] Wu Z, Wei Y, Wang X, et al. Orthogonal test study on the axial compression mechanical properties of locally corroded round steel pipe members[J]. Engineering Mechanics, 2020(4).(in Chinese)
[12] Jie Z Y, Wang W J, Zhuge P, et al. Fatigue properties of inclined cruciform welded joints with artificial pits[J]. Advanced Steel Construction, 2021, 17(1): 20-27.
[13] Yang Y, Ouyang W, Liu K, et al. Efficient numerical algorithms for assessing the mechanical performance of corroded offshore steel sheet piles[J]. Ocean Engineering, 2022, 266: 112776.
[14] GB 50017-2017, Code for design of steel structures[S], 2017.(in Chinese)
[15] ANSI/AISC 360-16, Specification for Structural Steel Buildings [S], 2016.
[16] UNI EN 1993-1-1 : 2014, EUROCODE 3 - DESIGN OF STEEL STRUCTURES - PART 1-1: GENERAL RULES AND RULES FOR BUILDINGS
[17] Dehghani A, Aslani F. A review on defects in steel offshore structures and developed strengthening techniques[J]. Structures, Elsevier, 2019, 20: 635-657.
[18] Adedipe O, Brennan F, Kolios A. Review of corrosion fatigue in offshore structures: Present status and challenges in the offshore wind sector[J]. Renewable and Sustainable Energy Reviews, 2016, 61: 141-154.
[19] Lin T, Huang W, Liu S, et al. An Investigation on the Effect of Random Pitting Corrosion on the Strength of the Subsea Pipeline Using Monte Carlo Method[J]. Available at SSRN 4424885.
[20] Ma S, Wang B, Su H, et al. Residual life calculation of corroded pipelines based on Monte Carlo method[J]. Total Corrosion Control,2019,33(11):40-43.(in Chinese)
[21] Zelmati D, Ghalloudj O, Amirat A. Correlation between defect depth and defect length through a reliability index when evaluating of the remaining life of steel pipeline under corrosion and crack defects[J]. Engineering Failure Analysis, 2017:171-185.
[22] Yu Z , Lu C , Zhong Y. Performance-Based Analysis of Single-Layer Cylindrical Steel Reticulated Shells in Fire[J]. Applied Sciences, 2020, 10(9):3099.
[23] Guibo Nie, Chen-xiao Zhang, Xu-dong Zhi, Junwu Dai. Damage quantification, damage limit state criteria and vulnerability analysis for single-layer reticulated shell. Thin-Walled Structures, 2017, 120:378-385.
[24] GB 50068-2018, Unified standard for reliability design of building structures [S], 2018.(in Chinese)
[25] GB50009-2012, Load code for design of building structures [S], 2012. (in Chinese)
[26] Liu H, Lu J, Chen Z. Residual behavior of welded hollow spherical joints after exposure to elevated temperatures[J]. Journal of Constructional Steel Research, 2017, 137: 102-118.
[27] Lemaire M. Structural reliability[M]. John Wiley & Sons, 2013.
[28] Chaves I A, Melchers R E. Extreme value analysis for assessing structural reliability of welded offshore steel structures[J]. Structural safety, 2014, 50: 9-15.
[29] Wang H , Zhang Z , Qian H , et al. Effect of local corrosion on the axial compression behavior of circular steel tubes[J]. Engineering Structures, 2020, 224:111205.
[30] Zhang Z, Wang H, Qian H, et al. Parameter sensitivity analysis and evaluation method of axial compression bearing capacity of corroded circular steel tubes[J]. Thin-Walled Structures, 2021, 163(4):107699.
[31] Chen L, Liu S W, Zhang J Z, et al. Efficient algorithm for elastic buckling of corroded I-section steel members with Monte Carlo simulation[J]. Thin-Walled Structures, 2022, 175: 109216.
[32] Zhongwei Z, Lumeng T, Ni Z, et al. Shear capacity of H-shaped steel beam with randomly located pitting corrosion[J]. Applied Ocean Research, 2021, 115: 102851.
[33] JGJ7-2010, Technical specification for space structures [S], 2010. (in Chinese)
[34] Asgarian B, Ordoubadi B. Effects of structural uncertainties on seismic performance of steel moment resisting frames[J]. Journal of Constructional Steel Research, 2016, 120: 132-142.
[35] Chu Yanfeng. Structural steel properties tests and parameter estimation of Q345GJ [D]. Chongqing University, 2008. (in Chinese)
[36] ISO 9223:2012, Corrosion of metals and alloys — Corrosivity of atmospheres [S], 2012.
[37] Melchers R E. Corrosion uncertainty modelling for steel structures[J]. Journal of Constructional Steel Research, 1999, 52(1): 3-19.
[38] Cinitha A, Umesha P K, Iyer N R. An overview of corrosion and experimental studies on corroded mild steel compression members[J]. KSCE Journal of Civil Engineering, 2014, 18(6): 1735-1744.
[39] Cole I S. The Atmosphere Conditions and Surface Interactions[M]. Springer Netherlands, 2016.
[40] Motojima S, Kohno M. Corrosion and abrasion resistivities to sea water and whirled sea sand of TiN-coated stainless steel[J]. Thin Solid Films, 1986, 137(1): 59-63.
[41] Zhongwei Z, Qian Y, Xiangyang J, et al. Influence of corrosion location on compression capacity of WHSJs[J]. Journal of Engineering Mechanics-ASCE, 2020, 146(5): 04020023.
[42] Ayyub B M. Uncertainty modeling and analysis in civil engineering[M]. CRC Press, 1997.
[43] Zhao Yuanzheng. Research on mechanical properties and reliability analysis of 6082-T6 aluminum alloy deflected and bent members[D]. Harbin Institute of Technology, 2020. (in Chinese)
[44] Chan S L. Non-linear behavior and design of steel structures[J]. Journal of Constructional Steel Research, 2001, 57(12): 1217-1231.

Advanced Steel Construction – Vol. 20 No. 1 (2024) 21–29
DOI:10.18057/IJASC.2024.20.1.3

ANALYSIS OF THE DYNAMIC MECHANISM OF SQUARE TUBULAR T-JOINTS WITH CHORD FLANGES SUBJECTED TO IMPACT LOADING

Peng Deng [1, 2], Dong-Song Chang [2], Xiu-Long Chen [3], Zhong-Yi Zhu [4, *] and Raheel Asghar [2]

[1] *Shandong Provincial Key Laboratory of Civil Engineering Disaster Prevention and Mitigation, Shandong University of Science and Technology, Qingdao 266590, China*

[2] *College of Civil Engineering and Architecture, Shandong University of Science and Technology, Qingdao 266590, China*

[3] *School of Civil Engineering, Southeast University, Nanjing, China*

[4] *Beijing Institute of Architectural Design, Beijing 100055, China*

** (Corresponding author: E-mail: Zhuzhongyi0719@163.com)*

ABSTRACT

This study examines the dynamic mechanical properties of square tubular T-joints with impact loads acting on the chord surface in the joint area. The study first verified the failure modes and behaviors of the specimens under a brace axial force and impact, respectively, where the simulation results demonstrated good agreement with the experimental results. A total of 138 square hollow section tubular T-joint finite element models were divided into T1, T2, and T3 groups based on different tube diameter ratios. The failure modes, displacement-time history curves, and impact force-time history curves were obtained. The results revealed that the joint deformation modes were primarily characterized by significant local indentation at the impact site and junction of the chord and brace, as well as a certain degree of deformation at both ends of the chord. Within a certain range, the preloaded axial force could mitigate the development of plastic deformation, whereas an increased ratio of the drop hammer length to chord diameter exacerbated it. Finally, theoretical analysis was simplified by defining the plastic element set, and the energy dissipation coefficient ψ was proposed to evaluate the impact resistance of square tubular T-joints by analyzing the specific energy changes in the intersecting region (E_I) and at the ends of the chord (E_e).

ARTICLE HISTORY

Received: 29 April 2023
Revised: 31 May 2023
Accepted: 27 August 2023

KEYWORDS

Square tubular T-joint;
Impact loading;
Preloading axial force;
Energy dissipation

Copyright © 2024 by The Hong Kong Institute of Steel Construction. All rights reserved.

1. Introduction

Square hollow sections (SHS) [1–3] are widely used in architecture, bridges, and other long-span structures because of their excellent performance in bending and torsion. The key to connecting all parts of the steel tube component as a whole is the joint, which plays a critical role in the transmission load of the structure. However, owing to the significant disparity between the transverse stiffness of the chord and axial stiffness of the brace, the chord surface near the brace/chord intersection tends to fail [4], leading to local or overall damage to the structure. Tube members may be subjected to various impact loads during their service life (e.g., earthquakes, explosions, or collisions resulting from dropped objects). Currently, studies of scenarios in which the load acts directly on the end of the brace represent simplified analytical models that do not fully correspond to actual structural loading conditions. Consequently, research on the joint response to the load acting on the tubular surface is essential in evaluating the overall response of tubular structures.

Numerical analytical models are crucial in studying the impact performance of tube joints, and reasonable selection of the constitutive model significantly influences the calculation accuracy. Experiments have demonstrated that the mechanical properties of steel, such as the yield stress, ultimate strength, and elongation of the material, differ significantly under dynamic loading from those under static loading, and these properties change under different deformation rates, particularly the strain rate effect [5]. With an increase in the strain rate, the lower and upper limits of the yield strength increase, but the fracture strength decreases [6]. Different material constitutive relationships have been developed to describe accurately the mechanical properties of steel under dynamic loads. The Cowper–Symonds [7] model, which is based on the ideal rigid-plastic model, reflects the relationship between the ratio of the dynamic to the static yield stress, and this model is widely used to predict the strength growth of metals. The Johnson–Cook [8] constitutive model, which is suitable for large strains and high strain rates, reflects the strain-hardening effect of materials and describes their stress flow. A comparison of these models reveals that the Cowper–Symonds model considers the effect of the strain rate on the mechanical properties of steel by introducing the strain rate factor; thus, the model involves fewer parameters and has better applications for topical research.

According to the basic concept of a structure, the structure's mechanical response varies with changes in the load position, and this difference has been studied by researchers. Chen and Shen [9] investigated the dynamic behavior of 226 steel pipes fully clamped at both ends. The results showed that the dented area presented a symmetrical distribution when the load acted on the mid-span, whereas an asymmetrical distribution emerged at one-quarter span and near the supports impact locations. For these types of impact issues, the energy dissipation has been further studied [10], where the failure thresholds were determined to be 655, 395, and 290 J at the mid-span, one-quarter span, and near the supports, respectively. Shen et al. [11] showed that the circumferential stress of a pipe near the end support easily caused the pipeline to buckle on the bottom surface, resulting in shear sliding at the impact location, whereas an impact position at the one-quarter span was susceptible to shear damage at the support [9]. Interestingly, by combining the behavior of axial compression, Al-Thairy et al. [13] found that the plastic-hinge location was not significantly affected by the impact position and was always close to the mid-span, particularly under a large axial load. Regarding the dynamic performance of tubular joint members subjected to impacts, owing to the stress formed by the brace pressure on the chord, it is worth further exploring the impact of the load on the surface of the chord.

Compared with the resistance mechanism of circular tubes, the performance of square tubes is more complicated [12–15]. Square tubes are formed by connecting four steel plates, where the deformation in any plate affects the characteristics of the two adjacent plates [2]. Gupta et al. [16] divided the four steel plates constituting a square tube into horizontal and vertical arms and found that when a static load acted uniformly in the transverse in-plane direction, the middle height of the two vertical arms initially formed hinges, after which second-stage hinges were formed at the four corners. Bin et al. [17] performed hemispherical indenter impact analyses at the mid-span and one-quarter span positions of a rectangular hollow section (RHS) tube with both ends fully clamped. The results indicated that plastic hinges were mainly formed at the indenter impact position and the support, and accompanied by an asymmetric deformation mode when the impact was along the width direction of the upper flange. Furthermore, Bin et al. [18] revealed that the peak force value of the upper flange of the RHS was always constant, even at different impact positions, as the local indentation of the tube could be attributed to the deformation and failure characteristics of the plate. In other words, similar local plastic deformation occurred at the onset of failure. Additionally, the action of the corner in SHS structures should not be ignored. Zhao et al. [19] found that the average tensile yield strength of the corner coupons was 16.8% higher than that of the flat coupons. Shao et al. [4] also revealed that the enhancement effect was beneficial to the transverse stiffness of the chord, increasing the load-bearing capacity of tubular joints, and the larger the corners of the SHS (within a certain

range), the better the strength of the structure [20]. In addition, a reasonable design of the rounded-corner geometry could also significantly improve the energy absorption capacity [21]. Thus, the mechanical behaviors of the corners and plates result in an SHS that differs from a circular hollow section (CHS).

In this study, commercial ABAQUS software was used to perform independent numerical modeling of the static loading [22] and impact tests [23] of SHS T-joints, and the numerical results were compared with experimental curves to verify the feasibility of the finite element (FE) model. Then, 138 FE models of SHS T-joints were developed, including three static specimens and 135 specimens with impact loads acting on the surface of the chord. The three static specimens were used to obtain the ultimate bearing capacity and thus to determine the value of the axial preloading of the brace. The effects of the brace/chord width ratio (β), pre-axial loading (P_{pre}) of the brace, impact velocity (v), and ratio of the drop hammer length to chord width (λ_h) on the performance of tubular structures were preliminarily analyzed, and revealed the failure modes and energy dissipation mechanisms of the SHS T-joints. Finally, the ratio (ψ) of dissipated energy to total system energy is introduced to evaluate the energy dissipation capacity under the aforementioned parameters.

2. Verification of the FE model

2.1. Model information and material properties

According to the test plan, the accuracies of the FE models were verified using static loading [22] and impact tests [23]. The detailed geometries of the specimens are summarized in Table 1, where b, h, t, and L are the width, height, thickness, and length, respectively; R and r denote the outer and inner corner radii, respectively; and the subscripts "0" and "1" indicate the chord and brace components, respectively. The geometric ratios include the ratio (β) of the brace–chord width (b_1/b_0), the ratio (τ) of the brace–chord thickness (t_1/t_0), and the ratio (2Υ) of the chord width to chord thickness (b_0/t_0). The constitutive relationship of the steel is expressed as an elastic–plastic model, as shown in Fig. 1, and the simplified bilinear isotropic hardening model was used for the static specimens. The C–S constitutive model that considers the strain rate was selected for the impact tests and is expressed in Eq. (1).

$$\sigma_{dy} = \sigma_y[1+(\dot{\varepsilon}/D)^{\frac{1}{n}}] \tag{1}$$

where σ_{dy} is the dynamic strength, σ_y is the static strength, $\dot{\varepsilon}$ is the equivalent strain rate, and the rate-dependent constant D and dimensionless parameter n are 6488 s^{-1} and 3.91 [24], respectively. The specific mechanical properties of the steel specimens for the static and impact tests are listed in Table 2.

Table 1
Geometric parameters of the specimens

Specimens	Brace (mm)						Chord (mm)						Geometric Ratios		
	b_1	h_1	t_1	r_1	R_1	L_1	b_0	h_0	t_0	r_0	R_0	L_0	β	τ	2Υ
T-50×100×4-150×150×6 [22]	50.5	100.6	3.96	7.1	10.5	200.3	150.2	151.4	5.950	9.8	13.0	729.9	0.34	0.67	25.25
T-120×120×4-140×140×4 [22]	121.1	121.3	3.91	6.7	9.6	240.5	140.4	141.2	3.994	5.9	8.6	719.0	0.86	0.98	35.16
T8-100c [23]	100	100	5	-	-	500	180	180	8	20	20	1940	0.56	0.625	22.5
T6-60b [23]	60	60	5	-	-	500	180	180	6	12	12	1940	0.33	0.83	30

Table 2
Material properties of the specimens

Specimens	f_y (MPa)		f_u (MPa)		E_s (GPa)	
	Brace	Chord	Brace	Chord	Brace	Chord
T-50×100×4-150×150×6[22]	951.9	1059.1	1098.4	1145.7	200.5	208.5
T-120×120×4-140×140×4[22]	971.4	1008.0	1137.9	1116.4	209.4	208.9
T8-100c [23]	369.8		543.2		208	
T6-60b [23]	369.3		554.5		210	

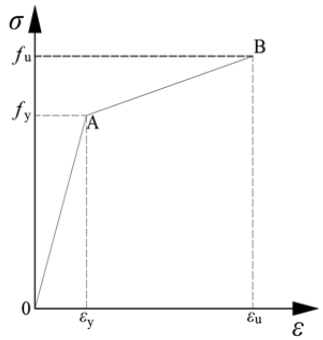

Fig. 1 Bilinear stress–strain curve

2.2. Model simplification

2.2.1. Simplification of static tests

An interface contact between the support and chord was obtained through the Contact pair. The contact properties were determined by defining the normal behavior (hard) and tangential behavior (penalty) with a friction coefficient of 0.3. The reference points (RP-1 and RP-2) were each set at a vertical distance of 20 mm from the bottom of the two supports. The reference points and bottoms of the supports were constrained by coupling, and the degrees of freedom of the two reference points in all directions were limited. The brace and chord were connected by "merge," and the weld simulated welding with a "tie" constraint (the weld design rule was $W_w = t_1$, $W_h = 0.5t_0 + t_1$ [25]). The end of the brace was coupled to the RP-3 point and released the degrees of freedom in the Y direction (i.e., axial direction of the brace). The axial force was loaded by applying the displacement at point RP-3.

2.2.2. Simplification of impact tests

Compared with the static specimens, the impact specimens omitted the end plates on both ends of the chord and coupled the corresponding reference points, where both ends of the chord were completely fixed. The drop hammer was simplified as a rigid body, and the drop hammer and brace end plate contact settings were the same as the support and chord setting properties for the static specimen. With specimens T-120×120×4-140×140×4 and T8-100c used as examples, the simplified models are shown in Fig. 2.

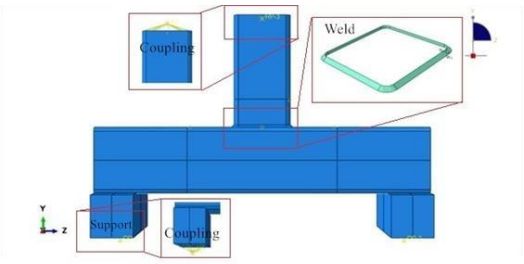

(a) T-120×120×4-140×140×4

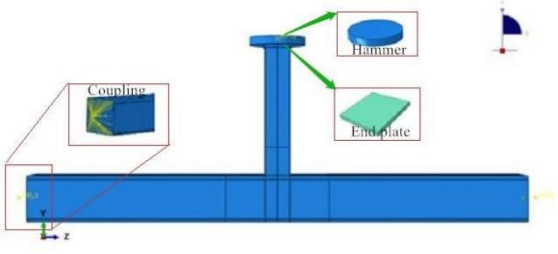

(b) T8-100c

Fig. 2 Simplified specimen models

2.3. Mesh division and sensitivity test

Solid elements are preferred over shell elements for tubular joint members [26–28] because shell elements ignore the stresses along the thickness direction. In this study, all components were modeled using 8-node linear brick solid elements with reduced-integration (C3D8R). The drop hammer and joint meshes were divided using free and structured mesh techniques, respectively. However, because the integrated element (C3D8R) may suffer from hourglass effects in the dynamic analysis, performing local mesh density refinement is necessary. Therefore, based on the sensitivity analysis and accuracy of the FE models, for the joint intersecting area, the study adopted a mesh size of 6 × 6 mm, with the mesh density set to 20 × 20 mm in other areas.

2.4. Verification of FE analytical results

2.4.1. Failure modes

The failure modes of specimens T-50×100×4-150×150×6 and T-120×120×4-140×140×4 are shown in Fig. 3, where the FE results agreed well with the test results. Specimen T-120×120×4-140×140×4 exhibited failure modes of chord face indentation and chord side wall bulging, whereas the difference in β resulted in only chord face failure in specimen T-50×100×4-150×150×6.

Fig. 4 presents a comparison of the experimental and FE models results of specimens T8-100c and T6-60b, where the FE results agreed well with the test results. The failure modes of both specimens were those of chord concavity on upper-face and bulging from web. However, for specimen T6-60b, which had a relatively small width, the indentation depth of the chord upper flange was relatively large, whereas the local buckling deformation of T8-100c was less than that of specimen T6-60b.

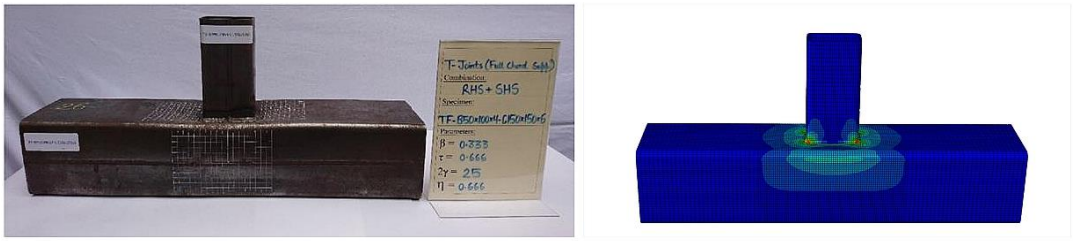

(a) T-50×100×4-150×150×6

(b) T-120×120×4-140×140×4

Fig. 3 Comparison of the FE model and experimental failure modes of static specimens [22]

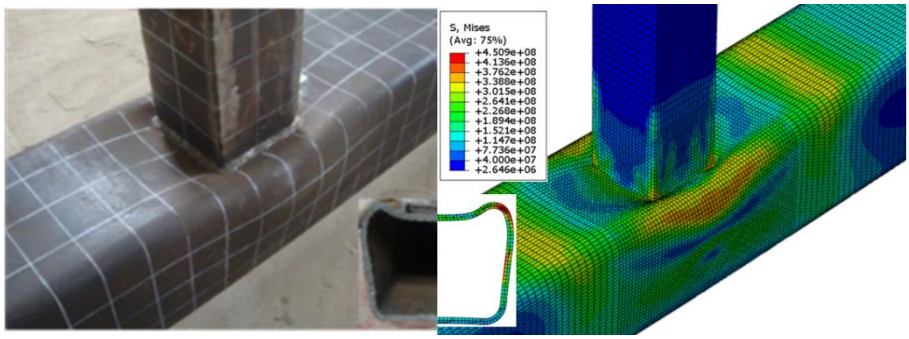

(a) T8-100c

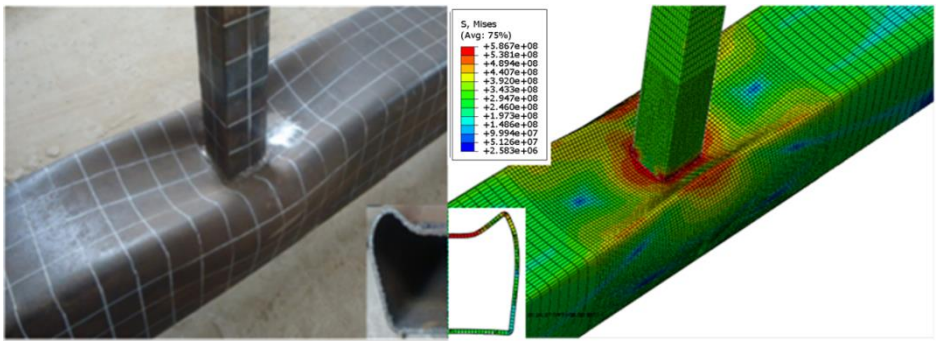

(b) T6-60b

Fig. 4 Comparison of the FE model and experimental failure modes of impact specimens [23]

2.4.2. Verification of the correlation curve

Fig. 5 shows the load versus chord face indentation (relative displacement) curves for the static specimens based on the FE models and test results. The figure shows that specimen T-120×120×4-140×140×4 reached the ultimate bearing capacity, whereas the curve of specimen T-50×100×4-150×150×6 continued to increase. The failure strength of the joint was based on the CIDECT [29] criterion as the first occurrence of P_{ult} (P_u) or $P_{3\%}$. Table 3 presents a comparison of the ultimate bearing capacities derived from the numerical simulation and experimental results. The average error of the values of the FE model was approximately 7% of the experimental values, and the FE results were in reasonable agreement with the experimental results.

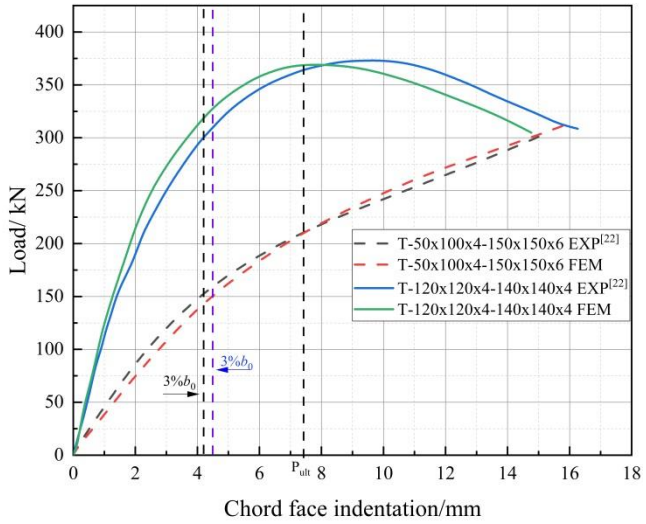

Fig. 5 Comparisons of curves between the FE model and test

Fig. 6 compares the impact force versus time curves for specimens T8-100c and T6-60b. The curve trends show good consistency, and the interval can be divided into four stages, where I–IV correspond to the impact, fluctuation, strengthening, and decline stages, respectively. However, the fluctuation of the FE simulation curves is relatively small in the four stages. Compared with the experimental curves, the impact force values of Stages I and II were higher in the FE simulation. The main reason for this phenomenon is that the FE model ignored the initial stress state of the tube. In particular, specimen T8-100c exhibited greater amplitude fluctuations during the four stages. Still, the shorter impact time was mainly attributed to its increased stiffness and the larger width of the brace/chord as compared with specimen T6-60b.

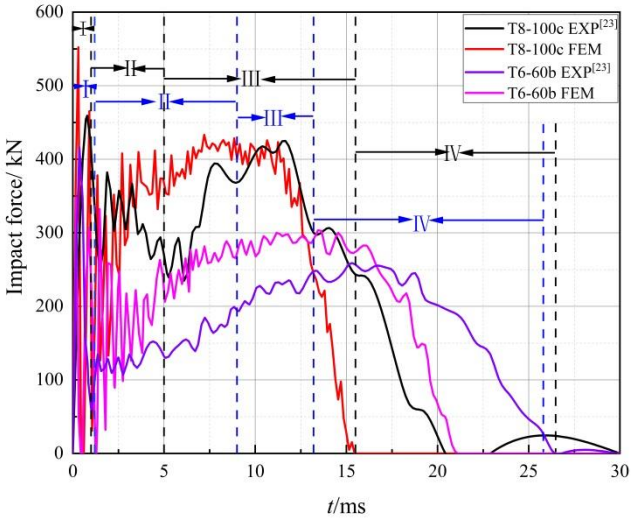

Fig. 6 Time history curves of the impact force under the experimental and numerical models

Table 3
Comparison of the ultimate bearing capacities of the FE models and experimental results

Specimens	P_{max} (kN)	$P_{3\%}$(kN)	$P_{max}/P_{3\%}$	$P_{ult,EXP}$ (kN)	$P_{ult,FEM}$ (kN)	($P_{ult,EXP}$-$P_{ult,FEM}$)/$P_{ult,EXP}$ (%)
T-50×100×4-150×150×6 EXP [22]	-	163.4	-	163.4		-
T-50×100×4-150×150×6 FEM	-	151.2	-	-	151.2	7.4
T-120×120×4-140×140×4 EXP [22]	373.9	346.3	1.08	346.3	-	-
T-120×120×4-140×140×4 FEM	368.38	321.34	1.15	-	321.34	7.2

3. Analysis of FE models of SHS T-joints

3.1. Determination of specimen size

Based on the verified FE model, a T-shaped SHS joint model of a chord subjected to impact was established. The design restrictions complied with specifications outlined in the *Standard for design of steel structures* [25] and *Design of SHS Weld Joints* [30] as well as in practical engineering applications. According to Vander et al. [31], the chord length L_0 should be at least 10 times the chord diameter b_0, as shown in Fig. 7.

A total of 138 FE models were constructed to analyze the effects of the pre-axial pressure (P_{pre}), impact velocity (v), ratio of drop hammer length to chord width ($\lambda_h = l_d/b_0$), and brace–chord width ratio ($\beta = b_1/b_0$) on the impact resistance of SHS T-joints under impact loads. The specific parameters of the specimens are listed in Table 4, including the three static loading specimens and 135 impact specimens. The three static loading specimens (T1-0, T2-0, and T3-0) were used to obtain the static bearing capacities of the specimens and to determine the value of the pre-axial pressure of the brace. The boundary conditions, mesh size, material properties and contact settings between the drop hammer and the joint were kept consistent with the impact specimens [23] in Section 2.

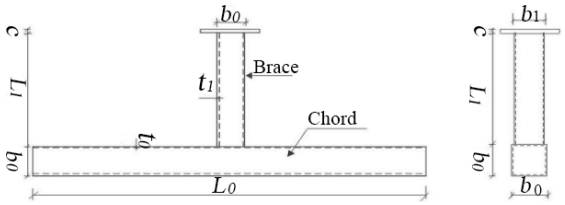

Fig. 7 Geometric properties of the T-joint components

The specimens were named according to the following: T1–T3 denote different β values; 0 P_u, 0.25 P_u, 0.5 P_u, 0.8 P_u, and 1.0 P_u represent the axial pressures of the brace; a, b, and c represent drop hammer impact velocities of 5, 6, and 7 m/s, respectively; and H1, H2, and H3 indicate drop hammer lengths (l_d) of 120, 150, and 240 mm, respectively. For the geometric dimensions of the drop hammer, only the drop hammer length l_d was varied in this study; the other parameters of ω_d, h_d, and r_d were set to 120, 20, and 10 mm, respectively, as shown in Fig. 8.

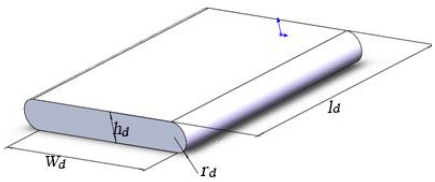

Fig. 8 Geometric properties of the drop hammer

Table 4
Geometric parameters of the FE models

Group	Specimens	Brace (mm)			Chord (mm)			P_{pre} (kN)	v (m/s)	l_d (mm)
		b_1	t_1	L_1	b_0	t_0	L_0			
T1	T1-0	80	5	640	180	6	1940	-	-	-
	T1-0/0.25/0.5/0.8/1.0Pu-a/b/c-H1/H2/H3							0/0.25/0.5/0.8/1.0Pu	5/6/7	120/150/240
T2	T2-0	100	5	640				-	-	-
	T2-0/0.25/0.5/0.8/1.0Pu-a/b/c-H1/H2/H3							0/0.25/0.5/0.8/1.0Pu	5/6/7	120/150/240
T3	T3-0	120	5	640				-	-	-
	T3-0/0.25/0.5/0.8/1.0Pu-a/b/c-H1/H2/H3							0/0.25/0.5/0.8/1.0Pu	5/6/7	120/150/240

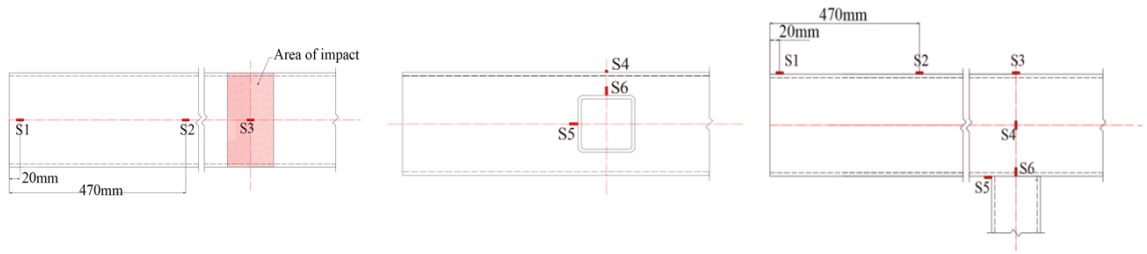

(a) Top view (b) Bottom view (c) Front view

Fig. 9 Arrangement of measuring points

3.2. Load application and position of strain measuring points

The influence of the axial pressure was considered when analyzing the impact resistance of SHS T-joints. Accordingly, two steps are required. In Step One, which employs the static general analysis, the value of the brace preloading axial force is obtained. In Step Two, the dynamic explicit analysis is altered to complete the impact of the drop hammer. The implementation of Step Two depends on the restart technology. The restart function divides the model steps into sets by defining an input file for each set. These sets can be run sequentially, and the information can be transferred from one set to the other, enabling the application of an impact load on the tubular joints after static loading.

Six measurement points were selected to analyze the stress development rule, as shown in Fig. 9. Points S1, S2, and S3 measure the axial stress of the upper flange of the chord, point S4 measures the radial stress at the center of the chord web, and points S5 and S6 measure the axial and radial stresses at the intersecting line of the chord and brace, respectively.

4. Analysis of failure modes

In the studied specimens, failures occurred at the impact area, web, and ends of the chord. A summary of the failure process combined with the research plan enabled two typical working conditions of different preloaded axial forces and ratios of the drop hammer length to chord width to be considered.

4.1. Effects of different pre-axial forces (P_{pre}) on the failure process

The failure histories of the T1-0Pu-a-H1, T1-0.5Pu-a-H1, and T1-1.0Pu-a-H1 specimens are representative to a certain extent and thus can be used for analysis and elaboration. According to the static analysis, when 0.5Pu was applied to the end of the brace, plasticity appeared at the four corners of the intersecting line, and most of the elements at the intersecting area under the action of 1.0Pu exhibited plasticity. Because the specimens did not undergo plastic deformation under 0.25Pu and the plastic state of the 0.8Pu specimens was between that of the 0.5Pu and 1.0Pu specimens, analysis of the aforementioned specimens was omitted. The four moments of the T1-0Pu-a-H1, T1-0.5Pu-a-H1, and T1-1.0Pu-a-H1 equivalent plasticity clouds are shown in Fig. 10 according to the location and order in which plasticity occurred.

When the drop hammer contacted the upper flange of the chord (t = 1.5 ms), T1-0Pu-a-H1 exhibited a more extensive range of plasticity at the impact position, web, and intersection area. The plastic developmental shape of T1-0.5Pu-a-H1 appeared similar, and the plasticity areas were both significantly smaller than those of T1-1.0Pu-a-H1. However, due to chord tension in the T1-0.5Pu-a-H1 specimen, the plasticity scope was somewhat less than that of T1-0Pu-a-H1 and significantly less than that of T1-1.0Pu-a-H1, as shown in Fig. 10(a). Based on the step size calculated by the software, the selected elements began to exhibit plasticity at the chord ends of the three specimens (t = 4.5 ms), as shown in Fig. 10(b). The plasticity area of the T1-1.0Pu-a-H1 specimen almost completely covered the upper flange, bottom flanges and web in the intersecting zone of the joint, whereas the coverage area of the T1-0Pu-a-H1 specimen was slightly smaller, and that of the T1-0.5Pu-a-H1 specimen was smaller still. However, both webs maintained a portion of the elastic scope. As the impact action continued, the bottom flange at both ends of the chord also became plastic (t = 7.5 ms), and the scope of plasticity distribution of the three specimens was similar. Yet the damage to the bottom flange of the T1-1.0Pu-a-H1 specimen was more severe, as shown in Fig. 10(c). Until the drop hammer rebound occurred, as shown in Fig. 10(d) (t = 15 ms), the plastic distribution of the three specimens was nearly identical. However, T1-0.5Pu-a-H1 maintained a slightly elastic scope in the joint area.

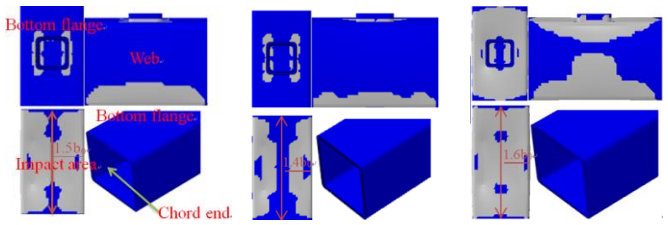

(1) T1-0Pu-a-H1 (2) T1-0.5Pu-a-H1 (3) T1-1.0Pu-a-H1

(a) Moment when the drop hammer contacts the upper flange of the chord (t = 1.5 ms)

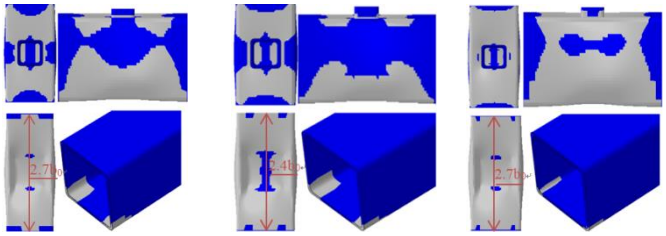

(1) T1-0Pu-a-H1 (2) T1-0.5Pu-a-H1 (3) T1-1.0Pu-a-H1

(b) Moment of buckling of the upper flange at both ends of the chord (t = 4.5 ms)

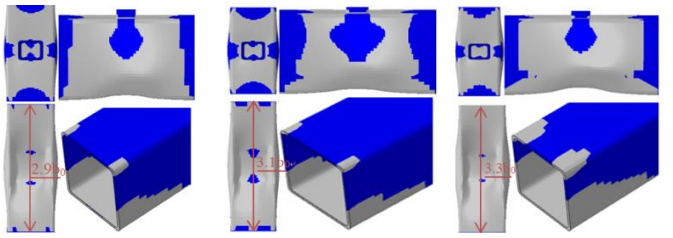

(1) T1-0Pu-a-H1 (2) T1-0.5Pu-a-H1 (3) T1-1.0Pu-a-H1

(c) Moment of buckling of the bottom flange at both ends of the chord (t = 7.5 ms)

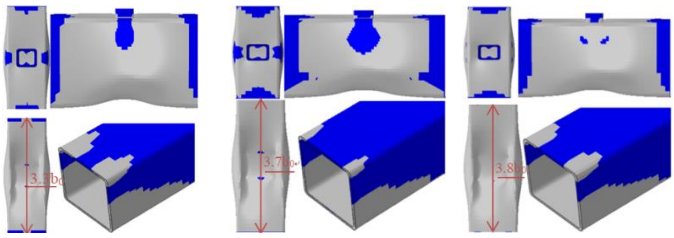

(1) T1-0Pu-a-H1 (2) T1-0.5Pu-a-H1 (3) T1-1.0Pu-a-H1

(d) Moment of drop hammer rebound (t = 15 ms)

Fig. 10 Equivalent plastic development cloud of specimens under different preloads (λ_h = 2/3)

4.2. Influence of the ratio of the drop hammer length to chord width (λ_h) on the failure process

This section examines the cases in which the λ_h values for specimens T1-0Pu-a-H1, T1-0Pu-a-H2, and T1-0Pu-a-H3 were 2/3, 5/6, and 4/3, respectively. Because the failure modes were different from those of the aforementioned specimens, only two states were selected for analysis. When the drop hammer touched the upper flange (t = 1.5 ms), specimens T1-0Pu-a-H2 (λ_h = 5/6) and T1-0Pu-a-H3 (λ_h = 4/3) almost simultaneously exhibited plasticity in the impact area, end of the chord, and web, as shown in Fig. 11(a). By contrast, the plastic scope of T1-0Pu-a-H3 (λ_h = 4/3) at the intersecting area was significantly greater than that of T1-0Pu-a-H2 (λ_h = 5/6) and even more significantly larger than that of specimen T1-0Pu-a-H1 (λ_h = 2/3, as shown in Fig. 10(a)). In particular, the chord end of T1-0Pu-a-H1 (λ_h = 2/3) was entirely in the elastic stage, whereas the other two specimens showed a significant aggravation of damage. Finally, at the moment of hammer rebound, the three specimens exhibited nearly the same degree of failure, as shown in Figs. 10(d) and 11(b). However, a very small area of elasticity was still present in T1-0Pu-a-H1 at the web.

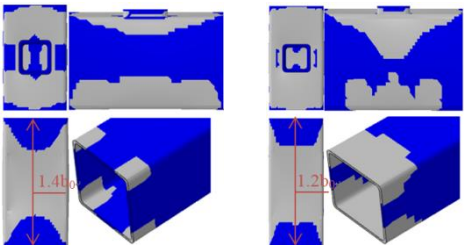

(1) T1-0Pu-a-H2 (λ_h = 5/6) (2) T1-0Pu-a-H3 (λ_h = 4/3)

(a) Moment when the drop hammer contacts the upper flange of the chord (t = 1.5 ms)

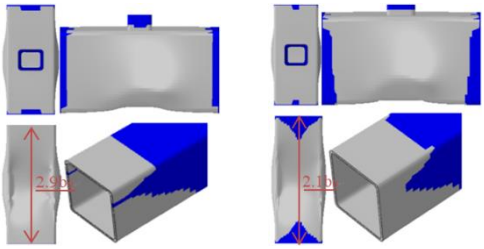

(1) T1-0Pu-a-H2 (λ_h = 5/6) (2) T1-0Pu-a-H3 (λ_h = 4/3)

(b) Moment of drop hammer rebound (t = 15 ms)

Fig. 11 Equivalent plasticity clouds for λ_h of 5/6 and 4/3

5. Time history of the impact force and displacement

5.1. Deformation- time history curves of joints

In this study, the indentation value (Δ) of the upper flange of the chord represents the displacement caused by the impact, which is used to describe the deformation of the joint, as shown in Fig. 12.

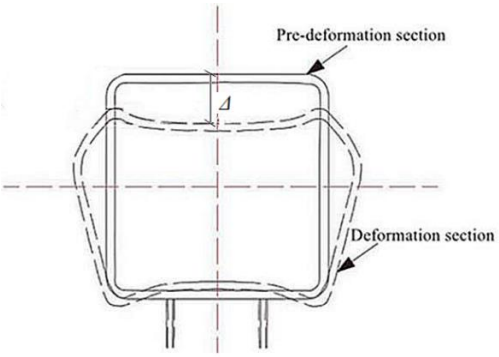

Fig. 12 Calculation of local indentation of the chord upper flange

The displacement-time history curves of the specimens that were subjected to P_{pre} and directly impacted (P_{pre} is 0 Pu) exhibited a similar trend. By contrast, the maximum concave displacement (Δ) of the specimens showed a slight downward trend with increasing P_{pre}, as shown in Fig. 13. Comparing the Δ values in Fig. 13, it can be observed that the effect of P_{pre} on the concave values of the specimens in Fig. 13(b) and Fig. 13(c) is slightly more sensitive than that in Fig. 13(a) but significantly less than the effect of λ_h. The analysis presented in Fig. 11 shows that when λ_h was 5/6 and 4/3, the mechanical characteristics of the joint region were significantly different from those of the specimens with λ_h = 2/3. For instance, the maximum concave displacements of specimens T2-0Pu-a-H1, T2-0Pu-a-H2, and T2-0Pu-a-H3 were 48.2mm, 39.1mm, and 36.1 mm, respectively.

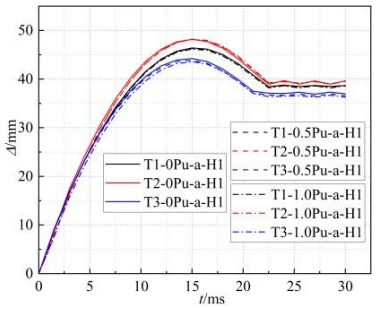

(a) Partial specimen with a drop hammer length of H1

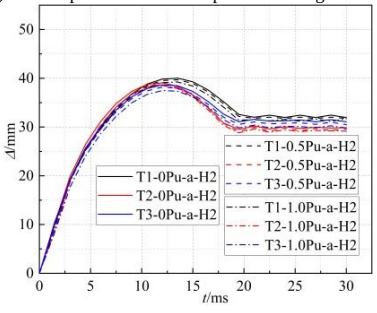

(b) Partial specimen with a drop hammer length of H2

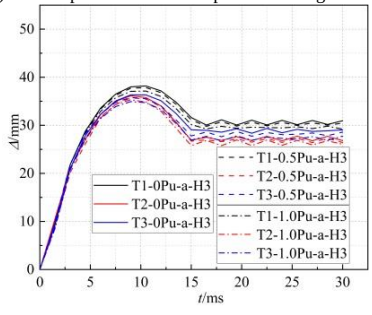

(c) Partial specimen with a drop hammer length of H3

Fig. 13 Displacement-time history curves of specimens

5.2. Impact force-time history curve of joints

As shown in Fig. 10, the equivalent plastic development cloud follows the same basic law. Thus, the impact force-time curves can be divided into four stages:(I) instantaneous impact, (II) impact shock, (III) stable, and (IV) descending, as shown in Fig. 14(a).

As Fig. 14(a) shows, the trends of the curves are significantly different. The overall impact force-time curves of the specimens fluctuate more gently at a drop hammer length of H1, but the total action time is longer. The effect of P_{pre} on the three groups of curves is relatively small, and only in Stage (I) do specimens T1-0.8Pu-a-H2 and T1-0.8Pu-a-H3 exhibit a significant jump. Moreover, the curves are not significantly different in Stages (II)-(IV). Fig. 14(b) shows the effects of variations in λ_h on the impact force-time curves for the same β and P_{pre}. It can be observed that when λ_h = 4/3, the overall value of the impact force-time curve is larger and the impact time is shorter. When v is increased, the overall trend of the curve changes insignificantly, but the action time is significantly increased. Compared with the curves in Fig. 14(c), the curves basically coincide for the specimens at the H1 drop hammer lengths, whereas for the specimens with H2 and H3 drop hammer lengths, the three curves are separated more significantly in Stage (III), and the impact force of the specimens in the T2 group is greater.

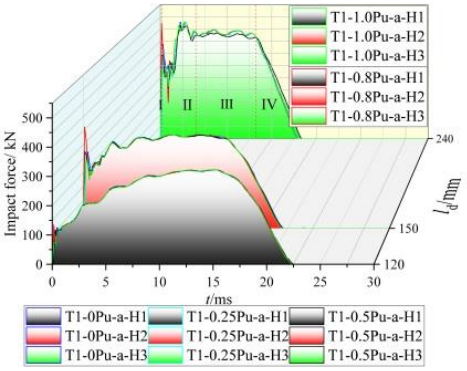

(a) Effect of P_{pre} on the impact force

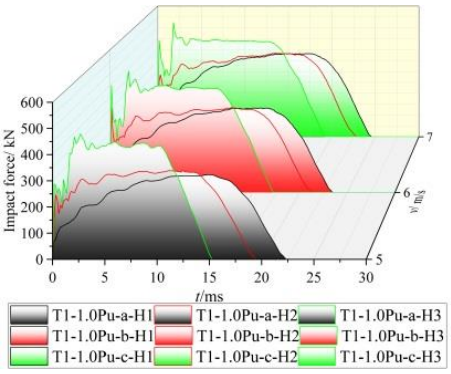

(b) Effect of λ_h on the impact force

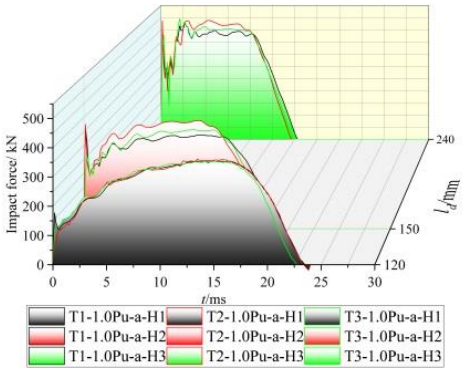

(c) Effect of β on the impact force

Fig. 14 Impact force-time history curves of specimens

6. Evaluation of the impact energy dissipation capacity

6.1. Theoretical analysis of energy dissipation

The impact process actually involves energy transfer and dissipation, and thus analysis of the energy dissipation mechanisms is effective in evaluating the impact resistance performance of tube joints. In the case of an impact on the flange of a T-shaped joint of a square steel tube, the energy conservation equation within the elastic range can be expressed as follows:

$$E_i + E_p = E_c + E_k \tag{2}$$

where E_i represents the kinetic energy of the drop hammer, E_p represents the elastic potential energy of the preloaded brace, E_c represents the elastic potential energy of the deformation of the chord flange, and E_k represents the kinetic energy of the vibrations of the chord and brace.

When the flange of the chord is subjected to an impact load, the chord and brace will undergo elastic deformation, resulting in dissipation of strain energy in the components of the chord and brace. The equation for the strain energy dissipation can be expressed as follows:

$$E_s = \frac{1}{2}\int_V \sigma\dot{\varepsilon}\mathrm{d}V \tag{3}$$

where E_s represents the dissipated strain energy, σ is the stress, $\dot{\varepsilon}$ is the strain rate, and V is the volume of the chord and brace.

The equation for the energy dissipation of the brace preloading under impact loads can be expressed as follows:

$$E_d = 0.5\times(F_p + \Delta F)\Delta\delta \tag{4}$$

where E_d is the energy dissipation, F_p is the preloading force of the brace, ΔF is the increment caused by the impact load on the flange of the chord, and $\Delta\delta$ is the increment of the relative displacement between the brace and chord.

As the failure process proceeds, the plasticity of the chord and brace is developed, as shown in Fig. 10. Energy conservation and dissipation can be expressed as follows:

$$E_i + E_p = E_c + E_k + E_s + E_d \tag{5}$$

After the drop hammer rebounds, the definition can be simplified as follows:

$$E_c + E_k + E_s + E_d = E_l + E_e = E_{diss} \tag{6}$$

where E_l is the energy dissipated by local deformation (concave deformation of the upper and bottom flanges and bulging deformation of the web) and E_e is the energy dissipated by plastic deformation at both ends of the chord.

Significantly, defining the energy dissipation coefficient ψ yields

$$\psi = \frac{E_{diss}}{E_i} \tag{7}$$

Note that because the difference between E_i and E_p is of a large order of magnitude, the effect of E_p is ignored, and the analysis is conducted later.

The coefficient ψ evaluates the storage and loss of energy of an object during the deformation process, which can help us understand the response characteristics of the object under stress, such as its strength, toughness, and durability. This is important for the design and optimization of structures such as square steel tube T-shaped joints.

6.2. Parametric analysis of energy dissipation coefficient ψ

Fig. 15(a) reveals that P_{pre} had no discernible effect on ψ. As P_{pre} increased, the curves of the specimens in groups T1, T2, and T3 remained relatively flat, whereas E_l continued to increase and E_e continued to decrease. However, their changes were comparable, resulting in a nearly horizontal line for ψ. Furthermore, it could be inferred that ψ increased as v increased. Fig. 15(b) illustrates that ψ decreased continuously as λ_h increased with a more pronounced decrease between λ_h = 5/6 and λ_h = 4/3. Simultaneously, E_l

significantly declined, whereas E_e gradually increased. Because the increase in E_e was much smaller than the decrease in E_l ($\Delta E_e < \Delta E_l$), the ψ curve consistently trended downward. Notably, β exerted a more significant effect on ψ than did the other variables, as demonstrated in Fig. 15(c). Specifically, ψ initially decreased and then increased as β increased, with the smallest value appearing at β = 0.56. The energy exhibited a pattern similar to P_{pre} but with greater variability. When β increased from 0.44 to 0.56, the increase in E_l was less than the decrease in E_e ($\Delta E_l < \Delta E_e$), resulting in a downward trend in the curve. However, when β increased from 0.56 to 0.67, the increase in E_l was greater than the decrease in E_e ($\Delta E_l > \Delta E_e$), which produced an upward trend in the curve.

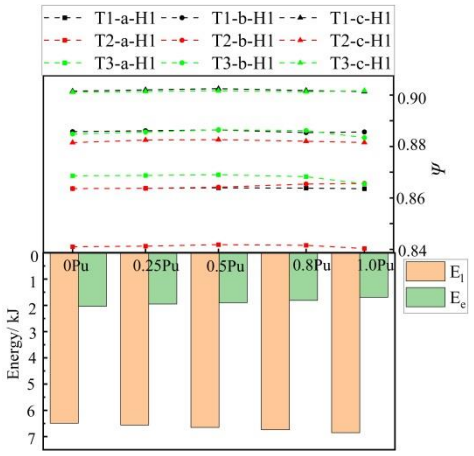

(a) Effect of P_{pre}

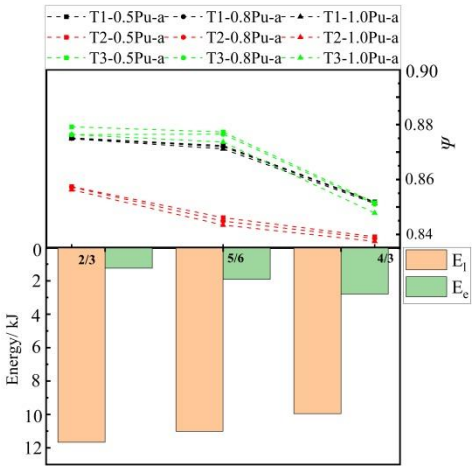

(b) Effect of λ_h

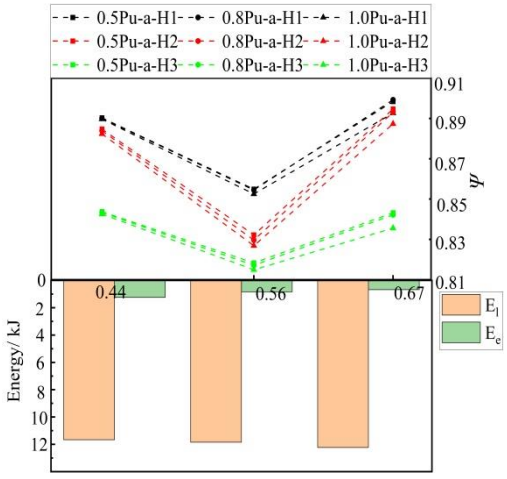

(c) Effect of β

Fig. 15 ψ variation curves of specimens

7. Conclusions

In this study, FE analysis of square tubular T-joints with chord flanges subjected to impact forces was conducted. The failure modes of the tubular joint were studied, and the effects of the pre-axial force, tube diameter ratio, ratio of drop hammer length to chord width, and impact velocity on the mechanical performance of the joint were investigated. The following conclusions were drawn:

1) The damage mode of the joints mainly consisted of local concavity (i.e., local indentation at the impact and intersecting areas) as well as bulging deformation of the web on both sides and plastic deformation at the ends of the chord, in which the effects of λ_h on the displacement values of the local indentation were greatest.

2) The pre-applied axial force of the brace caused tensile stress on the upper flange of the chord. Under the action of the membrane effect, this significantly affected Stage (I) of the impact force–time history curve. When the pre-applied axial pressure did not exceed 0.8 Pu ($P_{pre} \leq 0.8$Pu), the peak value of Stage (I) of the impact force increased with an increase in the pre-applied axial force. However, its effect on the total plastic energy consumption during the impact process was negligible.

3) The impact energy was absorbed through the local concave and plastic deformations at the end of the chord, where E_l played a dominant role. Ψ was used to evaluate the energy dissipation capacity, where ψ continued to decrease with the increase in λ_h. Moreover, the variation of β had a significant influence on ψ; between β = 0.44 and β = 0.56, ψ and β were negatively correlated, while between β = 0.56 and β = 0.67, the curve showed a positive correlation. The values of ψ under different parameters ranged from 0.81 to 0.91, which further confirmed the superior energy absorption capacity of square steel tube joints [32–33].

References

[1] White G.J., Grzebieta R.H. and Murray N.W., “Maximum strength of square thin-walled sections subjected to combined loading of torsion and bending”, International Journal of Impact Engineering, 13(2), 203–214, 1993.
[2] Wardenier J., Packer J.A., Zhao X.L., et al., Hollow Sections in Structural Applications, Bouwen met staal, Rotterdam, The Netherlands, 2002.
[3] Chen Y., Feng R. and Wang J., “Behaviour of bird-beak square hollow section X-joints under in-plane bending”, Thin-Walled Structures, 86, 94–107, 2015.
[4] Shao Y.B., Li T., Seng T.L., et al., “Hysteretic behaviour of square tubular T-joints with chord reinforcement under axial cyclic loading”, Journal of Constructional Steel Research, 67(1), 140–149, 2011.
[5] Zhang R., Zhi X. and Fan F., “Plastic behavior of circular steel tubes subjected to low-velocity transverse impact”, International Journal of Impact Engineering, 114, 1–19, 2018.
[6] Jones N. Structural Impact, Cambridge University Press, 2011.
[7] Cowper G.R. and Symonds P.S., Strain-Hardening and Strain-Rate Effects in the Impact Loading of Cantilever Beams, Brown University, Providence, RI, 1957.
[8] Johnson G.R., “A constitutive model and data for materials subjected to large strains, high strain rates, and high temperatures”, Proceedings of the 7th International Symposium on Ballistics, The Hague, The Netherlands, 541–547, 1983.
[9] Chen K. and Shen W.Q., “Further experimental study on the failure of fully clamped steel pipes”, International Journal of Impact Engineering, 21(3), 177–202, 1998.
[10] Jones N., Birch S.E., Birch R.S., et al., “An experimental study on the lateral impact of fully clamped mild steel pipes”, Proceedings of the Institution of Mechanical Engineers, Part E: Journal of Process Mechanical Engineering, 206(2), 111–127, 1992.
[11] Ng C.S. and Shen W.Q., “Effect of lateral impact loads on failure of pressurized pipelines supported by foundation”, Proceedings of the Institution of Mechanical Engineers, Part E: Journal of Process Mechanical Engineering, 220(4), 193–206, 2006.
[12] Deng P., Chen X., Yang B., et al., “Finite element analysis on the residual bearing capacity of axially preloaded tubular T-joints subjected to impacts”, Structures, 31, 286–304, 2021.
[13] Al-Thairy H. and Wang Y.C., “A numerical study of the behaviour and failure modes of axially compressed steel columns subjected to transverse impact”, International Journal of Impact Engineering, 38(8-9), 732–744, 2011.
[14] Gao F., Xiao Z., Guan X., et al., “Dynamic behavior of CHS-SHS tubular T-joints subjected to low-velocity impact loading”, Engineering Structures, 183, 720–740, 2019.
[15] Bambach M.R., Jama H., Zhao X.L., et al., “Hollow and concrete filled steel hollow sections under transverse impact loads”, Engineering Structures, 30(10), 2859–2870, 2008.
[16] Gupta N.K., Sekhon G.S. and Gupta P.K., “A study of lateral collapse of square and rectangular metallic tubes”, Thin-Walled Structures, 39(9), 745–772, 2001.
[17] Liu B. and Guedes Soares C., “Influence of impact location on the plastic response and failure of rectangular cross section tubes struck transversely by a hemispherical indenter”, Journal of Offshore Mechanics and Arctic Engineering, 139(2), 021603, 2017.
[18] Liu B. and Soares C.G., “Plastic response and failure of rectangular cross-section tubes subjected to transverse quasi-static and low-velocity impact loads”, International Journal of Mechanical Sciences, 90, 213–227, 2015.
[19] Zhao X L and Hancock G J. Square and rectangular hollow sections subject to combined actions[J]. Journal of Structural Engineering, 1992, 118(3): 648–667.
[20] Wang F., “Analysis of punch welding bridge shell fillet based on hyperworks”, Automotive Practical Technology, (07), 31–34, 2012 [In Chinese].
[21] Fu J., Liu Q., Ma Y., et al., “A comparative study on energy absorption of flat sides and corner elements in CFRP square tube under axial compression”, Thin-Walled Structures, 166, 108080, 2021.
[22] Pandey M., Chung K.F. and Young B., “Design of cold-formed high strength steel tubular T-joints under compression loads”, Thin-Walled Structures, 164, 107573, 2021.

[23] Cui P., Liu Y., Chen F., et al., “Dynamic behaviour of square tubular T-joints under impact loadings”, Journal of Constructional Steel Research, 143, 208–222, 2018.
[24] Abramowicz W. and Jones N., “Dynamic axial crushing of square tubes”, International Journal of Impact Engineering, 2(2), 179–208, 1984.
[25] GB50017-2017. Standard for Design of Steel Structures, China Architecture and Buildings Press, Beijing, China, 2017.
[26] Pang H.L.J. and Lee C.W., “Three-dimensional finite element analysis of a tubular T-joint under combined axial and bending loading”, International Journal of Fatigue, 17(5), 313–320, 1995.
[27] Qu H, Huo J, Xu C, et al. Numerical studies on dynamic behavior of tubular T-joint subjected to impact loading[J]. International Journal of Impact Engineering, 2014, 67: 12–26.
[28] Deng P., Zhao S., Zhu Z., et al., “Study on dynamic behavior of tubular T-joints subjected to out-of-plane impact loading”, Journal of Constructional Steel Research, 198, 107556, 2022.
[29] Packer J.A., Wardenier J., Zhao X.L., et al., Design Guide for Rectangular Hollow Section (RHS) Joints under Predominantly Static Loading, Cidect, 2009.
[30] Steel B., Design of SHS Welded Joints, British Steel Welded Tubes, UK, 1991.
[31] Van der Vegte G.J. and Makino Y., “Further research on chord length and boundary conditions of CHS T-and X-joints”, Advanced Steel Construction, 6(3), 879–890, 2010.
[32] Khodaverdlou Z., Basir S.S. and Mohseni P.K., “Numerical and experimental investigation of energy absorption capacity in slotted thin-walled square tube structures”, Journal of the Brazilian Society of Mechanical Sciences and Engineering, 44(8), 368, 2022.
[33] Deng X., Liu F., Cao L., et al., “Energy-absorption characteristics of sandwich corrugated square tubes under axial crushing”, Journal of the Brazilian Society of Mechanical Sciences and Engineering, 44(10), 458, 2022.

Advanced Steel Construction – Vol. 20 No. 1 (2024) 30–38
DOI:10.18057/IJASC.2024.20.1.4

EVALUATION OF LOCAL-PLATE BUCKLING COEFFICIENT FOR THE DESIGN OF COLD-FORMED STEEL-LIPPED CHANNEL CROSS SECTIONS: NUMERICAL SIMULATIONS AND DESIGN RECOMMENDATIONS

Hadeer Mashaly [1], A.H.A Abdelrahman [2,*], Fikry A. Salem [2] and Nabil S. Mahmoud [2]

[1] *Civil Engineering Department, Faculty of Engineering, Horus University, New Damietta, Egypt*
[2] *Structural Engineering Department, Faculty of Engineering, Mansoura University, Mansoura, Egypt*
** (Corresponding author: E-mail: a_hussain@mans.edu.eg)*

ABSTRACT

Recent advancements in design guidelines for cold-formed steel members focus on enhancing the prediction of nominal strengths under various loading conditions. This improvement is achieved through precise accounting for local plate buckling behavior. Nevertheless, the Effective-Width Method (EWM), aligned with current design standards, estimates a lower structural capacity for cold-formed steel members. Assuming buckling precedes the yielding of cross-sections and considering no interactive restraint between adjacent elements, conservative predictions of member strengths are derived. To address this issue, this paper introduces a numerical investigation involving several lipped channel cross-sections with varying web height-to-flange width ratios, intending to assess the local plate buckling coefficient (k-value). Initially, validating a shell finite-element model against test results establishes benchmark strengths for the considered cross-sections. Subsequently, analytical solutions for calculating the k-value are presented and compared with those obtained from numerical solutions. Interactions between cross-sectional adjacent elements are examined, leading to a proposed refined EWM compliant with AISI standards. Finally, a reliability analysis is performed to illustrate the accuracy and reliability of the proposed design method. This research highlights the significance of accurately considering the restraining effect between sectional sub-elements and the importance of boundary conditions influencing the plate buckling coefficient.

ARTICLE HISTORY

Received: 13 October 2023
Revised: 13 October 2023
Accepted: 18 November 2023

KEYWORDS

Local buckling;
Finite element;
Lipped channel;
Buckling coefficient;
Analytical expressions

Copyright © 2024 by The Hong Kong Institute of Steel Construction. All rights reserved.

1. Introduction

Modern structural technology prioritizes environmental practices to mitigate global energy depletion, whether in construction, operation, maintenance, or demolition. Cold-formed steel (CFS) emerges as an eco-friendly and recyclable structural material, minimizing carbon dioxide emissions during its cold-forming process, unlike hot-rolled steel sections that demand higher thermal energy. As a primary load-bearing material, CFS optimizes construction purposes due to its numerous advantages, including a high strength-to-weight ratio, easy installation, and lower energy consumption. It finds wide-ranging applications in construction manufacturing, such as light and short-span structures, light partition walls, and storage rack structures. CFS, derived from the flexion of thin-walled steel sheets, is susceptible to various buckling phenomena, including local buckling (L), distortional buckling (D), and global buckling (G) as. These instability modes exhibit elastic buckling loads before reaching ultimate strength and exhibiting post-buckling behavior. Consequently, the hot-rolled steel design approach is unsuitable for CFS, necessitating advanced guidance in three key areas: i) experimental tests to explore various CFS cross-sections under different load conditions [1]–[10], ii) numerical analyses, such as the finite strip method [11], [12] and shell finite element models [13], offering accurate simulations with realistic geometric imperfections and residual stresses, and iii) the development of simplified design standards [14]–[17] to provide accessible and semi-accurate guidance for the design of CFS sections, reducing reliance on more complex and expensive tools.

Two existing design theories play a pivotal role in assessing the structural capacity of CFS axial columns and flexural beams: the traditional Effective Width Method (EWM) and the recently advanced Direct Strength Method (DSM). The former employs iterative solutions to define the effective width for each element comprising the cross-section. In contrast, the DSM calculates elastic buckling loads in local, distortional, and global buckling modes, addressing cross-section instability and predicting the nominal strength for each buckling mode. Consequently, numerous researchers have dedicated their efforts to examining the buckling behavior of CFS lipped-channel sections under diverse loading and boundary conditions. For example, Bryan [18] derived a solution for critical local buckling stress and the plate buckling coefficient for simply supported plates subjected to compression. Subsequent studies explored different boundary and loading conditions, revealing that the nominal plate strength is independent of critical elastic buckling theory, as noted in [19], due to post-buckling behavior. Kármán [20] delved into nominal buckling strength based on elastic buckling solutions, introducing empirical factors for simply supported plates. Winter [7], in later work, adapted the elastic buckling solution, presenting a formula for nominal plate strength during post-buckling behavior. This formula remains integral to current effective width approaches, including AISI [15] and Eurocode3 (EC3) [16], and is incorporated into various contemporary design methodologies.

More recently, a design theory based on DSM has emerged [14], [21], relying on determining the critical elastic buckling stress for entire cross-sections. Currently, this method is employed in Australia/New Zealand and North America standards.

Taking inspiration from prior investigations, the EWM treated the plate element as simply supported, overlooking any interaction or restraining strength with adjacent elements. Consequently, the predicted nominal post-buckling strength proves conservative when compared to experimental test results. Yu and Yan [22] illustrated the influence of the web height-to-flange width (H/B) ratio on the plate buckling coefficient in the C and Z sections. Mulligan and Pekoz [23] conducted experiments on lipped channel stub columns to quantify local buckling and inspected buckling coefficient values for cross-section sub-elements (web, flange, and stiffener). These values, derived from experimental results, were lower than those for simply supported plate elements due to the consideration of interaction between adjacent elements. Consequently, the impact of the H/B ratio on nominal strength, attributed to the interaction effect, is emphasized. An increase in cross-section width provides support to the web element, thereby increasing nominal buckling strength. This interaction significantly influences the buckling coefficient value (k), primarily dependent on boundary conditions and stress gradient.

This research contributes to advancing the effective width method (EWM) by incorporating elastic local buckling phenomena in assessing the plate buckling coefficient (k), a parameter significantly influenced by the interaction between adjacent sub-elements. Initially, literature-derived test results are employed to validate a newly developed 2D shell finite-element model (SFEM) using ABAQUS [13]. The SFEM incorporates appropriate geometric imperfections and material properties specific to CFS. Subsequently, finite strip analysis in CUFSM [11] is utilized to perform elastic local buckling solutions, which are then compared with various expressions for local plate buckling coefficients in the calculation of critical local buckling stress (F_{cr}). This comparison characterizes the restraining effect between adjacent sub-elements and demonstrates superior performance in representing elastic behavior. The illustration of various elements and analytical methods with different buckling coefficients within the EWM theory is also outlined. These methods are presented to evaluate the impact of restraining interaction between connected sub-elements with varying boundary conditions. Results obtained from the

Direct Strength Method (DSM) are also discussed, revealing that enhancing elastic stability for the gross cross-section may be more accurate than the EWM. Subsequently, after presenting diverse design approaches for CFS, a parametric study is conducted on different CFS-lipped channel cross-sections with various web height-to-flange width ratios. These results are then compared to outcomes from the developed and validated shell finite element models (SFEM) [25-26], which serve as benchmark results for evaluating the reliability of the proposed refined design method (i.e., AISI-Re). This refined method aims to obtain optimum nominal strength for CFS-lipped channel cross-sections. Finally, the findings are summarized, emphasizing the role of the plate buckling coefficient (k) in determining the nominal buckling strength.

2. Finite element modelling

2.1. Shell finite element modeling

Finite Element (FE) analysis is used in ABAQUS [13] to analyze the behavior of thin plates, simulating the experimental tests detailed in [25] and [26]. The linear 4-node shell element with reduced integration (S4R) is selected for modeling the CFS columns. As mentioned in [27], this shell element aligns with the study's goals, which focus on local plate buckling. Based on mesh sensitivity analysis, a maximum mesh size of 5 mm x 5 mm is assumed in element discretization, guaranteeing precise and trustworthy results for a comprehensive parametric investigation. Four elements are used to model the rounded corners of the lipped channel cross-section.

2.2. Modelling parameters

The benchmark experimental settings for the specimens under test were included in the simulations. A 600S137-54 lipped-channel cross-section with an intermediate length of 610 mm was one of the geometrical attributes that were subjected to several loading combinations (axial, uniaxial, and biaxial eccentricities). The reference point was established using a kinematic coupling constraint connecting it to the end cross-sections, and it was situated at the cross-section centroid. With pin-ended boundary conditions, every beam-column was simulated. According to [25], Young's modulus was 203.4 GPa, and the steel yield stress was 364.5 MPa. To construct the real stress-strain curve and account for the inelastic behavior of CFS due to material nonlinearity, the two-stage Ramberg-Osgood model, as presented by Gardner and Yun [31], was used. Initial geometric imperfections were incorporated to thoroughly evaluate the simulations against the experimental tests. This allowed for proper parametric investigations of CFS behavior and demonstrated satisfactory agreement with the results. To ensure the accuracy of the finite element modeling, additional test specimens from various experimental tests were simulated under the same standard conditions to account for pure compression and local buckling failure modes, as detailed in [25].

2.3. Residual stresses and cold-forming effect

The same manufacturing process, including coiling, uncoiling, and shape bending, causes residual stresses and cold-forming effects. Residual stresses show a drop in yield strength, but the cold-forming process raises the yield strength in the corner region, leading to greater strength. The most accurate way to estimate a member's true strength is to model the manufacturing process, including cold-forming effects and residual stresses. While this is frequently a difficult process to carry out, it is essential to avoid modeling them individually. According to several studies, there is no noticeable correlation between residual stress and the final capacity of columns (e.g., Schafer and Peköz; Abdel-Rahman and Sivakumaran; Ellobody and Young) [28-30]. As long as ultimate load capacity is the main consideration, the yield strength in the corner region is enhanced due to the cold-forming process, which reduces the effect of residual stress. The corner effect and residual stress, especially in post-ultimate behavior, significantly affect column behavior but do not affect the final load capacity value, according to Abdel-Rahman and Sivakumaran [29]. This study disregarded the residual stress and corner enhancement in the FE model since it focuses on the ultimate load capacity rather than the post-ultimate load behavior.

2.4. Initial geometrical imperfections

Initial geometric imperfections are introduced by executing the linear perturbation "Buckle" step, enabling the prediction of the buckling mode shape to be scaled within the subsequent nonlinear collapse analysis. Drawing from prior research, various imperfection amplitudes are integrated into the model to ensure thorough validation and accurate verification. The specific amplitude values are outlined in Table 1, along with their corresponding peak loads.

The FE results show that when the imperfection amplitude is adjusted to $6te^{-2t}$, as suggested by Schafer and Peköz [32], the predicted peak loads show good agreement with the experimental test results. Values produced by this configuration are most similar to the experimental findings; mean predicted-to-test ratios for [25] and [26] are 1.0047 and 1.1091, respectively. The coefficients of variation (COV) that correspond to these values are 0.0337 and 0.1287, respectively. For this reason, to make the solutions in the current study seem more realistic, this specific amplitude value was chosen.

Table 1
Peak ultimate loads for experimental and FE results with different imperfection amplitudes

	Specimen	Imperfection magnitude					
		0.24mm	0.005t	t/10	d/400	Schafer and Peköz [32]	Dawson and Walker [33]
Torabian et al, [25]	600S137-54 (1)	0.9964	1.0165	0.9966	0.9945	0.9933	0.9949
	600S137-54 (2)	0.9868	1.0408	0.9883	0.9841	0.9827	1.0405
	600S137-54 (3)	0.9743	1.0855	0.9754	0.9730	0.9700	1.0715
	600S137-54 (4)	1.0264	1.0325	1.0279	1.0250	1.0236	1.0308
	600S137-54 (5)	1.0733	1.1110	1.0897	1.0616	1.0538	1.1126
	Mean	**1.0114**	**1.0573**	**1.0156**	**1.0076**	**1.0047**	**1.0501**
	COV	**0.0391**	**0.0373**	**0.0450**	**0.0356**	**0.0337**	**0.0423**
Roy et al, [26]	C75-L500-1	1.1089	1.1292	1.1202	1.1154	1.0789	1.2345
	C75-L500-2	1.3387	0.0000	1.3732	1.3661	1.2951	1.5421
	C75-L500-3	1.2008	1.2716	1.2090	1.2152	1.2060	1.5023
	C90-L500-1	0.9594	0.9650	0.9676	0.9643	0.9346	1.0416
	C90-L500-2	1.0641	1.1819	1.0910	1.0853	1.0310	1.0074
	Mean	**1.1344**	**0.9095**	**1.1522**	**1.1493**	**1.1091**	**1.2656**
	COV	**0.1265**	**0.5723**	**0.1309**	**0.1311**	**0.1287**	**0.1976**

2.5. Validation and verifications

A noteworthy agreement between FE results and test results in terms of load-displacement response, peak loads (Fig. 1), and failure modes (Fig. 2) is illustrated visually by the results of FE modeling and experimental tests [25]. Furthermore, the ultimate loads from the experiments and FE models are compiled in Table 2. A comparatively low coefficient of variation (COV) of 0.06 accompanies the mean test-to-predicted value of 0.98. Overall, the findings shown in Figs. (1-2) and Table 2 demonstrate that the developed FE models can reliably and efficiently simulate the behavior of lipped-channel sections made of CFS under various loading conditions and buckling modes.

Table 2
Comparisons between test and FE results [25-26]

Specimen	Test		FE		Comparison P_{test}/P_{FE}
	P_{test} (KN)	Buckling Mode	P_{FE} (KN)	Buckling Mode	
600S137-54 (No. 1)	18.09	L	17.9683	L	1.0068
600S137-54 (No. 2)	28.25	L	27.7602	L	1.0176
600S137-54 (No. 3)	43.38	L	42.0804	L	1.0309
600S137-54 (No. 4)	46.86	D	47.9669	D	0.9769
600S137-54 (No. 5)	24.99	D	26.3336	D	0.9490
C75-L500-1	42.20	L	43.004	L	0.9813
C75-L500-2	50.10	L	59.4223	L	0.8431
C75-L500-3	75.90	L	80.187	L	0.9465
C90-L500-1	49.00	L	47.0097	L	1.0423
C90-L500-2	61.10	L	59.5379	L	1.0262
Mean					**0.9821**
COV					**0.0603**

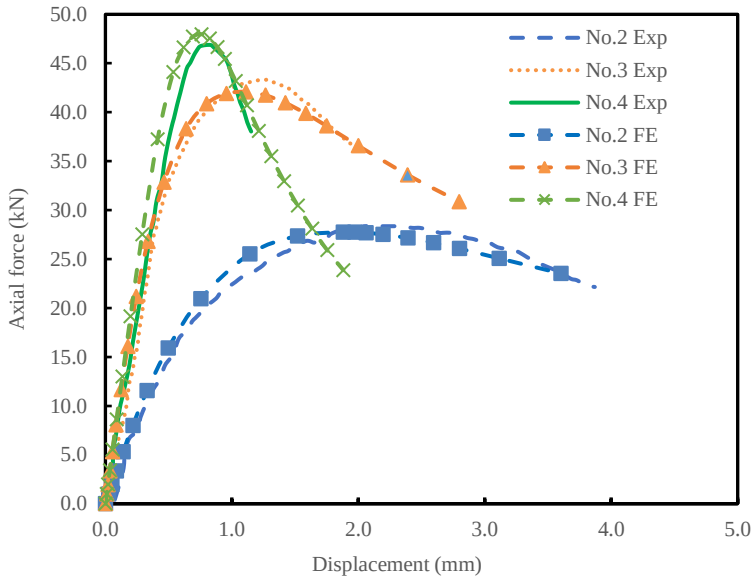

Fig. 1 Load-displacement curves from FEM and experimental tests by Torabian et al, [25]

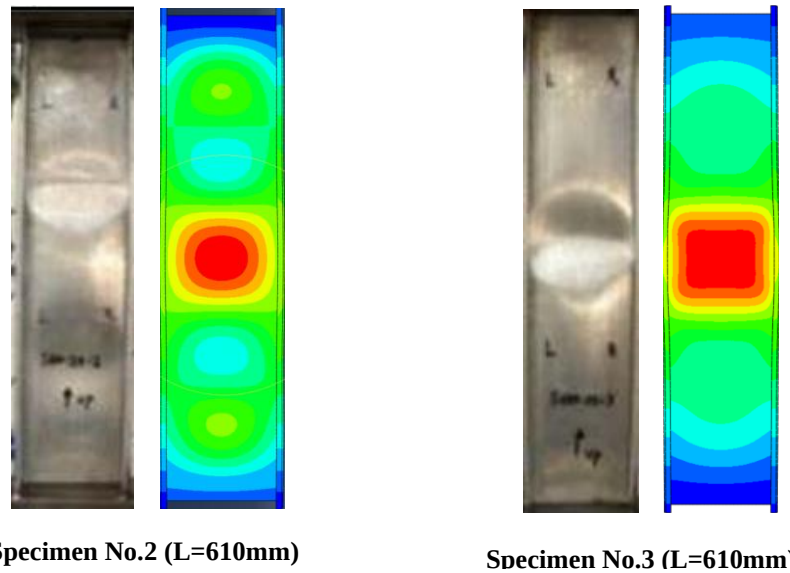

Fig. 2 Failure modes of experimental specimens from Torabian et al, [25] and FEM

3. Analytical solutions of local plate buckling coefficients

The critical local buckling stress (F_{crl}) is considered an essential and effective parameter in cold-formed steel design approaches such as the Direct Strength method (DSM) and Effective Width Method (EWM), whether in AISI [15] or EC3 [16], to compute the cross-sectional nominal strength. The general equation for the plate's critical local buckling stress is as follows:

$$F_{crl} = k_x \frac{\pi^2 E}{12(1-\nu^2)} \left(\frac{t}{x}\right)^2 \quad (1)$$

where k_x is the plate buckling coefficient, E is the modulus of elasticity, t is the plate thickness, ν is the Poisson's ratio of steel, and x is the plate width. Eq. (1) clarifies that the plate buckling coefficient (k_x) affects remarkably the critical local buckling stress (F_{crl}), which in turn affects the nominal strength of the cross-section. As a result, this study clarifies the various design standards and suggested formulas for determining the plate buckling coefficient and how it affects the ultimate strength prediction.

The critical local buckling stress for the lipped channel cross-section is found by taking the minimum local buckling stress of each element that makes up the cross-section. In the present investigation, and as per Eq. (1), four methods are employed to estimate the local buckling stress: 1) the element method, as incorporated in AISI S100 [15], 2) the approximate upper bounds for the element method (an analytical method detailed in [24]), 3) the current AISI [15], and 4) empirical closed-form equations proposed by Ahdab et al. [24].

3.1. The element method

The element method considers no interaction between adjacent elements, following AISI S100 [17]. As seen in Fig. 3, the elements are believed to be free at the unattached edge and simply supported at the attached edge. The plate buckling coefficient under pure compression or stress gradient is generally expressed in Eq. (2).

$$\boldsymbol{k_\psi = 4 + 2(1 - \psi^3) + (1 - \psi)} \quad (2)$$

where k_ψ is the plate buckling coefficient, $\psi = |F_2/F_1|$ is the determinant for the end plate stress ratio, and F_1 is the larger compressive stress at the end plate.

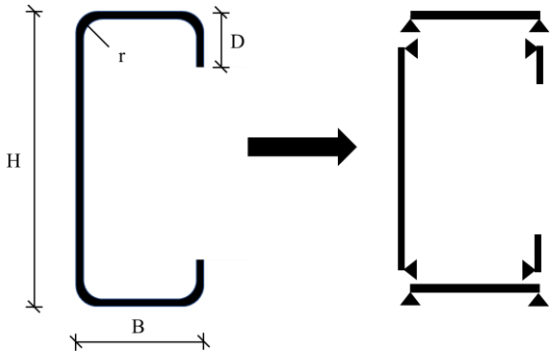

Fig. 3 Simply supported sub-elements in a lipped channel cross section based on the element method

3.2. Approximate upper bounds for element method (analytical method)

This approach assumes that every sub-element in the cross-section has a fixed end condition (Fig. 4), ignoring interactions with other elements. For local buckling solutions, it is acknowledged as a nonconservative method. To compute the plate buckling coefficient in line with the approximate upper bounds for the element method, Eq. (3) expands Eq. (2), which was first presented in [24].

$$\boldsymbol{k_\psi = 6.97 + 3.3(1 - \psi^3) + 3.3(1 - \psi)} \quad (3)$$

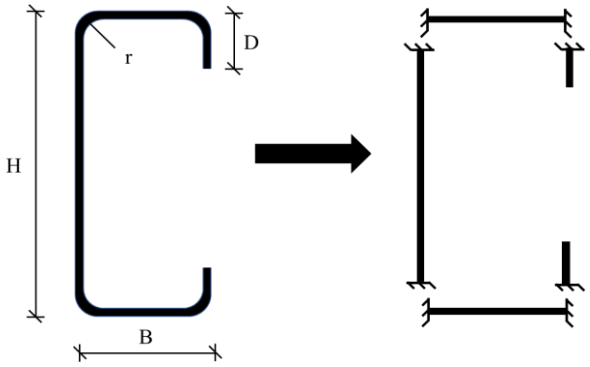

Fig. 4 Fixed supported sub-elements in lipped channel cross section based on the approximate upper bound method

3.3. The empirical closed-formed equation

Ahdab et al. [24] explored a different, semi-accurate method of calculating the plate buckling coefficient by using empirical closed-form equations that accounted for different loading conditions and took sub-element interaction into account. This method considers the geometry of adjacent elements within and beyond a diverse range of lipped channel cross-sections. The closed-form equation for pure compression is presented in Eq. (4), while those for major axis bending are given in Eqs. (5) and (6), as follows:

For $0 \le H/B \le 12$ and $0 \le D/B \le 1$

$$k_H = min\left(4.5\left(\frac{H}{B}\right)^2, 4\left[0.73\left(\frac{D}{B}\right)^{0.36} + 1\right]\right) \quad (4)$$

For $0 \le H/B \le 1$ and $0.15 \le D/B \le 0.4$

$$k_B = \max\left(0.3\left(\frac{B}{H}\right) + 5.2, 0.4\left(\frac{H}{B}\right) + 5.9\right) \ge k_{EWM\ AISI} \quad (5)$$

For $0 \le H/B \le 1$ and $0.15 \le D/B \le 0.4$

$$k_B = min\left(-0.4\left(\frac{H}{B}\right) + 5.9, 22.3\left(\frac{H}{B}\right)^{-1.8}\right) \ge k_{EWM\ AISI} \quad (6)$$

These closed-form equations are first compared with finite strip analysis (CUFSM) results for solutions involving elastic buckling. Subsequently, these are implemented in the AISI [15] methodology (henceforth referred to as AISI-Re) by substituting the current buckling coefficient values, thereby revealing their pivotal role in predicting the nominal buckling strength.

3.4. Results by finite strip method

The elastic buckling stress ($\boldsymbol{F_{cr}}$) for a range of cross-sections with varying web height-to-flange width ratios (H/B) was calculated by finite strip analysis using CUFSM [11]. B = 50.8 mm, D = 5.08 mm, t = 1.4376 mm, and r = 2.8752 mm are the cross-sectional dimensions. There is a 203.5 GPa Young's modulus (E) and a 0.3 Poisson's ratio (ν). Then, utilizing Eq. (1), the critical local buckling stresses were transformed into plate buckling coefficients $\boldsymbol{K_H}$, $\boldsymbol{K_B}$, and $\boldsymbol{K_D}$ so that the results could be compared to those obtained from Ahdab et al.'s closed-form equations [24]. In FSM within CUFSM, to prevent non-unique minima and allow for the automated study of elastic buckling modes in CFS members, the methodology for CUFSM utilization as described in [34] has been implemented. Accordingly, results are shown in Fig. 5 and comprise pure compression and major axis bending. Remarkably, there is a good agreement that validates the accuracy of elastic buckling stress prediction for lipped channel cross-sections. Fig. 5(a) shows that the web plate buckling coefficient under pure compression is slightly affected when the web-to-flange width ratio (H/B) is increased beyond two (≥ 2). On the other hand, as depicted in Fig. 5(b), the flange local buckling coefficient ($\boldsymbol{K_B}$) is significantly impacted by the elastic critical buckling stress ($\boldsymbol{F_{cr}}$) for major axis bending.

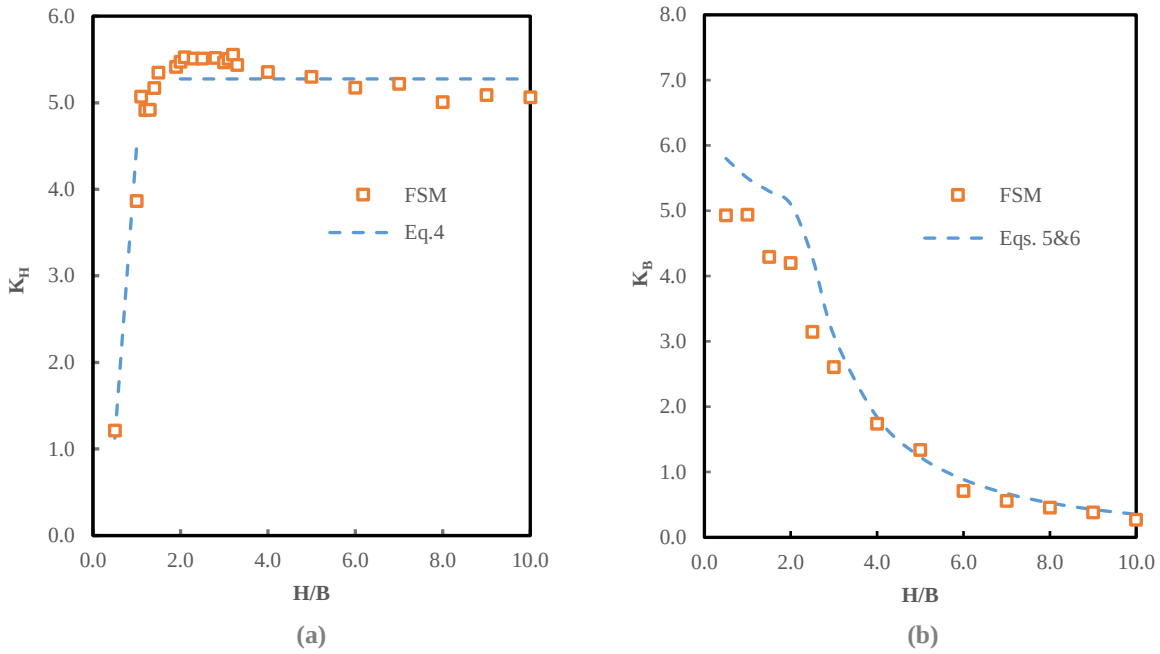

Fig. 5 Plate buckling coefficient versus H/B ratio (a) web buckling coefficients for pure compression, and (b) flange buckling coefficients for major axis bending

4. Design guidelines

4.1. Effective width method

The effective width method (EWM) is used by the current design standards, EC3 [16] and AISI [15], to estimate the nominal strength of columns and beam-columns. The EWM determines the effective width properties for each sub-element in the cross-section under uniform stress, thereby reducing the load-carrying capacity of a simply supported member. The effective width is determined by using Winter's Equation [7], which is given as follows;

$$b_{eff} = \frac{\left(1-\frac{0.22}{\lambda_p}\right)b}{\lambda_p} \leq b \tag{7}$$

$$\lambda_p = \sqrt{\left(\frac{F_y}{F_{crl}}\right)} \tag{8}$$

where b_{eff} is the effective width of the sub-element, λ_p is the slenderness parameter, b is the gross width, F_y is the yield stress, and F_{crl} is the critical local buckling stress of the sub-element, which is calculated from Eq.(1). The modern CFS design specifications make extensive use of the effective width method (EWM). This method relies on figuring out each sub-element's plate buckling coefficient (k), which is important to determine the critical local buckling stress (F_{crl}) and, in turn, the effective width properties. The plate buckling coefficient (k) for stiffened, and unstiffened elements mainly depends on the stress distribution inside the element and the current boundary conditions. For example, AISI considers the effect of the nearby stiffener in lipped channels when calculating the plate buckling coefficient of the compression flange. It is important to note that EWM tends to conservatively estimate the ultimate buckling strength of the considered CFS cross-sections under diverse loading conditions [25]. The adopted values of the local plate buckling coefficients (k), which do not consider the interactions between adjacent sub-elements, are responsible for this conservatism in the effective width properties.

4.2. Direct strength method

The direct strength method (DSM) has recently emerged as an alternative approach, explicitly outlined in Appendix 1 of the AISI specification [21]. This method determines nominal strength through finite strip analysis, finite element analysis, or closed-form solutions, accounting for elastic buckling loads and interactions between sub-elements. Through elastic buckling analysis, the DSM optimizes the use of gross cross-sectional properties. It identifies the three elastic buckling modes (L, D, and G) over the whole cross-section and determines which mode controls the nominal strength. According to previous studies, for lipped channel cross-sections, the DSM's findings are often slightly higher than the EWM's [25]. A summary of the DSM design equations under pure compression is provided as follows:
For global buckling, the nominal strength P_{ne} is calculated from

$$P_{ne} = \left(0.658^{\lambda_c^2}\right) A * F_y \quad For\ \lambda_c \leq 1.5 \tag{9}$$

$$P_{ne} = \left(\frac{0.877}{(\lambda_c^2)}\right) A * F_y \quad For\ \lambda_c > 1.5 \tag{10}$$

$$\lambda_c = \sqrt{\frac{P_y}{P_{cre}}} \tag{11}$$

$$P_{nl} = P_{ne} \quad For\ \lambda_c \leq 0.776 \tag{12}$$

$$P_{nl} = \left[1 - 0.15 * \left(\frac{P_{crl}}{P_{ne}}\right)^{0.4}\right]\left(\frac{P_{crl}}{P_{ne}}\right)^{0.4} P_{ne} \quad For\ \lambda_c > 0.776 \tag{13}$$

$$P_{crl} = A * F_{cr} \tag{14}$$

Nominal Strength for beam column M_{nl} is calculated from equations of the same trend detailed in [21].

5. Refined AISI method (AISI-Re)

In this section, the empirical closed-form equations for the plate buckling coefficient (k) are applied within AISI to predict the nominal ultimate strength, referred to as AISI-Re, intending to achieve two objectives: 1) evaluate the proposed value of the local plate buckling coefficient in light of the current AISI specifications; and 2) conduct a comprehensive parametric study on the nominal strength of various lipped channel columns and beam-columns, quantifying the impact of the buckling coefficient (k) on the predicted strength. Finally, a reliability analysis will more accurately show how the suggested method (AISI-Re) has improved validity compared to the present AISI recommendations.

5.1. Parametric study

A comprehensive parametric study was undertaken on various lipped channel cross-sections under compression and major axis bending. The study focused on local buckling failure modes, employing models of relatively short member lengths (L) by adopting L=H to present an analytical exploration of the

elastic buckling and post-buckling behavior of lipped channel cross-sections. The EWM was utilized, incorporating four k-values for local plate buckling: 1) following AISI specifications, 2) AISI with k-value by element method (AISI-Elem), 3) AISI with k-value by analytical method (AISI-Ana), and 4) AISI-Re with k-value by Ahdab et al., [24], considering interactions between adjacent sub-elements. The only difference between these approaches is the value that is determined for the plate buckling coefficient (i.e., k value), which in turn affects the nominal strength for the typical cross-section. The Young's modulus, the material yield stress, and Poisson's ratio are taken as E = 210 GPa, F_y = 345 MPa, and $\nu = 0.3$, respectively. Results based on EWM with different k values are compared with those obtained from SFEM that represent validated simulations for experimental tests. The dimension parameters include web height (H = 70 mm), thickness (t = 1.5 mm), inner corner radius (R = 2 mm), stiffener length over flange width ratio (D/B = 0.2) to avoid large lip stiffeners and eliminate their effect on the element's theoretical buckling stress [35], and the (H/B) ratio varies with a range from 1 to 2.

5.1.1. Axial compression

As per several design approaches and finite element (FE) models, Fig. 6 shows the web height to flange width ratio (H/B) effect on the nominal strength of different cross-sections under pure compression. All existing design methods and solutions show significant conservatism, with the FE models providing the maximum nominal strength. Since AISI-Ana corresponds to an upper-bound philosophy, it produces the higher results. These curves demonstrate that the direct strength method (DSM) is a less conservative method than AISI for the cross-sections under study. On the other hand, the results from AISI-Re are more compatible with FE models and perform effectively when compared to the present AISI specifications. This can be attributed to implementing more accurate and reliable equations for calculating the plate buckling coefficient (k). Furthermore, it is observed that the nominal strength increases with an increasing H/B ratio up to a specified level when it remains relatively constant. Similar trends are noticed across different design methods. An increase in the H/B ratio up to 1.8 is shown to have a slight effect on the P_n/P_y ratio. With regard to the absence of the flange's local buckling and an increase in the web's local buckling, decreasing the flange width (B) lowers the nominal strength. AISI and AISI-Elem provide almost identical results for (H/B) higher than 1.75, as the flange-lip interaction gradually disappears in AISI when the flange width (B) is decreased. In summary, the sectional dimensions and predicted-to-FE results based on AISI and AISI-Re are presented in Table 3. The mean $P_{predicted}/P_{FE}$ ratio is 0.89 and 0.83, respectively, with corresponding COV values of 0.01 and 0.05. This reconfirms and demonstrates the higher accuracy and reliability of the proposed AISI-Re compared to the current AISI design guidelines.

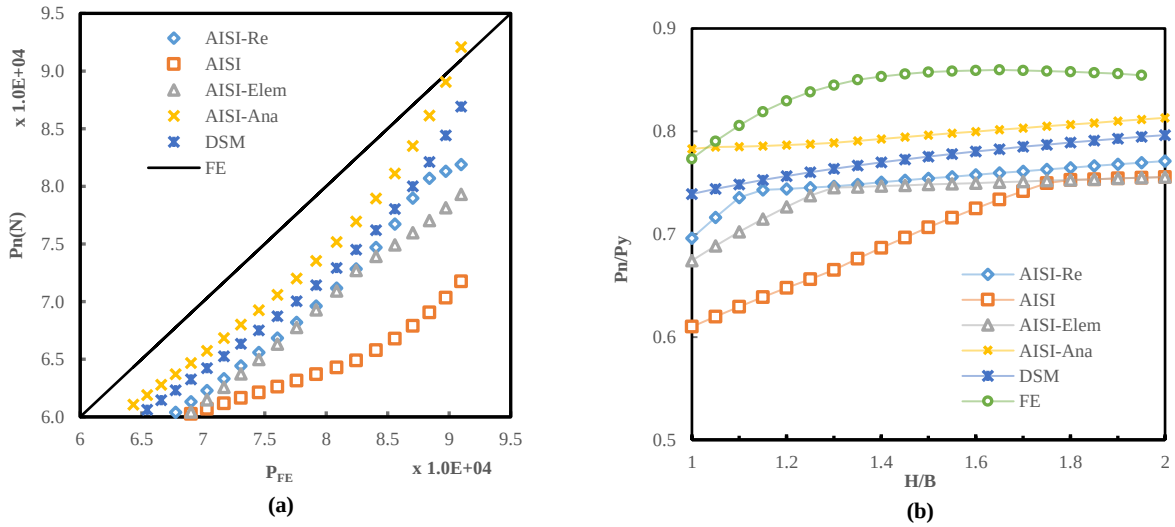

Fig. 6 Comparisons between nominal axial strengths from different design methods and FE results: (a) $\mathbf{P_{FE}}$ versus $\mathbf{P_{predicted}}$, and (b) normalized predicted loads versus H/B ratio

Table 2
Section properties and comparisons between FE results and different design standards for lipped channels under pure compression

No.	H (mm)	H/B	B (mm)	C (mm)	T (mm)	R (mm)	$P_{AISI-Re}/P_{FE}$	P_{AISI}/P_{FE}
1	70	1	70.00	14.00	1.5	2	0.90	0.79
2	70	1.05	66.67	13.33	1.5	2	0.91	0.78
3	70	1.1	63.64	12.73	1.5	2	0.91	0.78
4	70	1.15	60.87	12.17	1.5	2	0.91	0.78
5	70	1.2	58.33	11.67	1.5	2	0.90	0.78
6	70	1.25	56.00	11.20	1.5	2	0.89	0.78
7	70	1.3	53.85	10.77	1.5	2	0.88	0.79
8	70	1.35	51.85	10.37	1.5	2	0.88	0.80
9	70	1.4	50.00	10.00	1.5	2	0.88	0.80
10	70	1.45	48.28	9.66	1.5	2	0.88	0.81
11	70	1.5	46.67	9.33	1.5	2	0.88	0.82
12	70	1.55	45.16	9.03	1.5	2	0.88	0.83
13	70	1.6	43.75	8.75	1.5	2	0.88	0.84
14	70	1.65	42.42	8.48	1.5	2	0.88	0.85
15	70	1.7	41.18	8.24	1.5	2	0.89	0.86
16	70	1.75	40.00	8.00	1.5	2	0.89	0.87
17	70	1.8	38.89	7.78	1.5	2	0.89	0.88
18	70	1.85	37.84	7.57	1.5	2	0.89	0.88
19	70	1.9	36.84	7.37	1.5	2	0.90	0.88
20	70	1.95	35.90	7.18	1.5	2	0.90	0.88
						Mean	**0.89**	**0.83**
						COV	**0.01**	**0.05**

5.1.2. Eccentric compression

A similar parametric study is conducted on cross-sections exposed to major axis bending to improve the prediction of beam-column cross-section strength. The goal is to evaluate the accuracy of different flexural nominal strength prediction methods by comparing their results with benchmark SFEM data. As described in AISI [15], a simple linear interaction equation (Eq. (15)) is used to quantify the effect of varying eccentricities on nominal flexural strength for different cross-sections.

$$\frac{\bar{P}}{P_a} + \frac{\bar{M}_x}{M_{ax}} \leq 1.0 \qquad (15)$$

where

$\bar{P}$ = required compressive axial strength (obtained from FEM models)

P_a = nominal design strength obtained from different design approaches.

$\bar{M}_x$ =required flexural strengths ($= \bar{P} * eccentricity$)

M_{ax} = nominal flexural strengths according to different design approaches.

As shown in Fig. 7, nearly all of the results obtained using the different methods (AISI, AISI-Elem, AISI-Ana, and AISI-Re) are similar for (H/B) greater than 1.65, suggesting that the effective width (i.e., a reduction factor (ρ=1) for each sub-element) is fully used. Because of the reduced interaction between the web and flange and the minor amount of web local buckling seen under major axis bending, it can be concluded that reducing the flange width (B) does not affect the nominal strength of flexural beams. Alternatively, for larger (H/B) ratios, the direct strength method (DSM) produces more conservative results than the effective width method (EWM) because, as reported in [36], decreasing the flange width (B) reduces the elastic buckling stress for the whole gross section, which in turn lowers the nominal strength of the member. In contrast, EWM calculates the critical buckling stress for each element separately. Furthermore, major axis bending supports the web, with its half-height experiencing tension. The nominal strength value is substantially enhanced by AISI-Re under different eccentricities (e.g., e = H/10, H/5, H/2, or H), as shown in Fig. 8, with the fact that it exhibits less conservative M_n/M_y values than prior approaches. It is obvious that the EWM can significantly enhance the prediction of nominal strength by including k of AISI-Re. However, in this case, the EWM continuously underestimates the nominal strength of the analyzed beam columns, independent of the applied k-values. The simpler and more linear interaction equations [1] established for eccentrically loaded lipped channels cause this disparity. Finally, Table 4 presents the summary of predicted-to-FE results. The corresponding mean and COV values confirm the reliability of the suggested AISI-Re method.

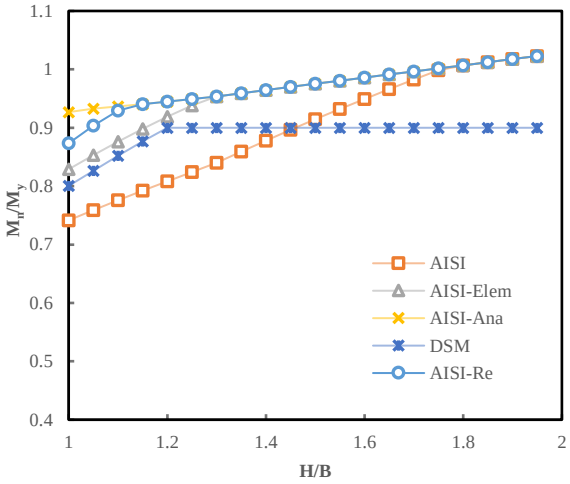

Fig. 7 Comparisons between different design methods and FE results for flexural beams

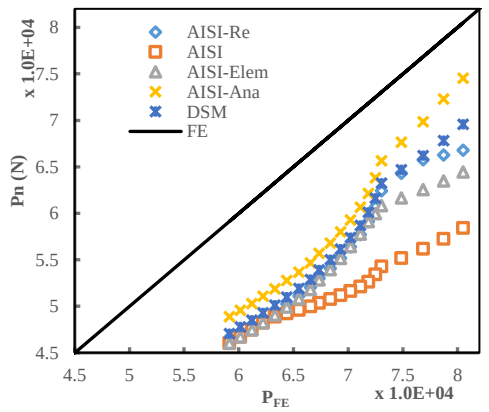

(a) e=H/10

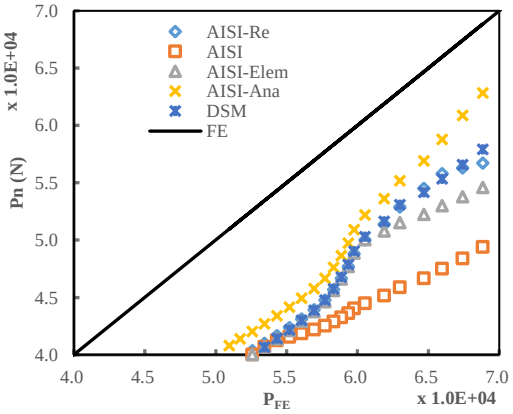

(b) e=H/5

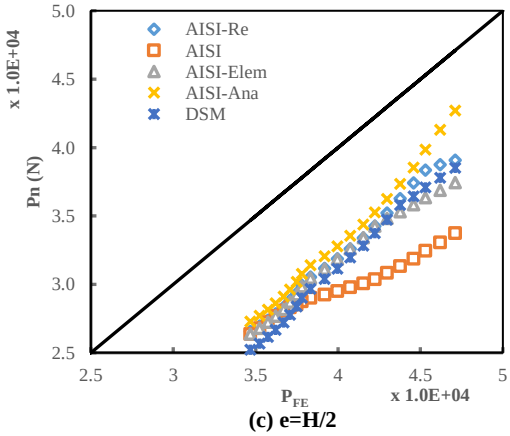

(c) e=H/2

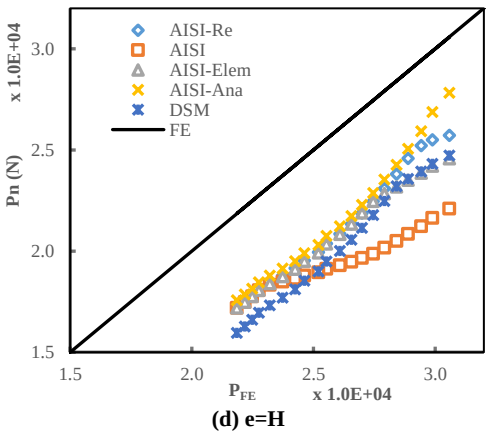

(d) e=H

Fig. 8 Comparisons between different design methods and FE results for eccentrically loaded members; (a) e= H/10, (b) e=H/5, (c) e=H/2, and (d) e=H

Table 4
Comparisons between FE, AISI, and AISI-Re results for eccentrically loaded lipped channels

No.	$e = H/10$		$e = H/5$		$e = H/2$		$e = H$	
	$P_{AISI\text{-}Re}/P_{FE}$	P_{AISI}/P_{FE}	$P_{AISI\text{-}Re}/P_{FE}$	P_{AISI}/P_{FE}	$P_{AISI\text{-}Re}/P_{FE}$	P_{AISI}/P_{FE}	$P_{AISI\text{-}Re}/P_{FE}$	P_{AISI}/P_{FE}
1	0.83	0.73	0.82	0.72	0.83	0.72	0.84	0.72
2	0.84	0.73	0.83	0.72	0.84	0.72	0.85	0.72
3	0.86	0.73	0.85	0.72	0.85	0.72	0.86	0.72
4	0.86	0.74	0.84	0.72	0.84	0.71	0.85	0.72
5	0.85	0.74	0.84	0.73	0.83	0.72	0.84	0.72
6	0.84	0.74	0.83	0.73	0.82	0.72	0.83	0.72
7	0.82	0.73	0.83	0.74	0.81	0.72	0.82	0.72
8	0.81	0.73	0.82	0.74	0.80	0.72	0.81	0.73
9	0.80	0.74	0.80	0.74	0.80	0.73	0.80	0.73
10	0.80	0.74	0.79	0.73	0.80	0.74	0.80	0.74
11	0.79	0.74	0.78	0.74	0.80	0.75	0.80	0.75
12	0.79	0.75	0.78	0.74	0.80	0.76	0.79	0.75
13	0.78	0.75	0.77	0.74	0.79	0.76	0.79	0.76
14	0.78	0.76	0.77	0.75	0.78	0.76	0.79	0.77
15	0.78	0.76	0.77	0.75	0.78	0.76	0.79	0.78
16	0.78	0.77	0.77	0.76	0.77	0.77	0.80	0.79
17	0.78	0.78	0.77	0.76	0.77	0.76	0.80	0.79
18	0.78	0.78	0.77	0.76	0.77	0.76	0.79	0.79
19	0.79	0.78	0.77	0.76	0.77	0.76	0.79	0.79
20	0.79	0.78	0.77	0.76	0.77	0.76	0.79	0.79
Mean	**0.81**	**0.75**	**0.80**	**0.74**	**0.80**	**0.74**	**0.81**	**0.75**
COV	**0.04**	**0.02**	**0.04**	**0.02**	**0.03**	**0.03**	**0.03**	**0.04**

To prove the AISI-Re method's reliability, finite element (FE) results from F. Öztürk et al. [37] are compared with calculated nominal strength according to the aforementioned five design methods. Different major axis eccentric loads are applied to the CFS-lipped-channel beam columns, as described in [37]. Subsequently, the nominal strength (β) parameter is computed as follows:

$$\beta = \sqrt{\left(\frac{M_1}{M_{1y}}\right)^2 + \left(\frac{M_2}{M_{2y}}\right)^2 + \left(\frac{P}{P_y}\right)^2} \tag{16}$$

where $P, M_1,$ and M_2 are the applied axial compression and biaxial bending moments, and $P_y, M_{1y},$ and M_{2y} are the squash load and biaxial yield moments, respectively. The effective performance of AISI-Re is assessed in Fig. 9, with results that agree with the finite element (FE) results in [37]. This further confirms the accuracy and reliability of the AISI-Re method, which prior investigations have supported.

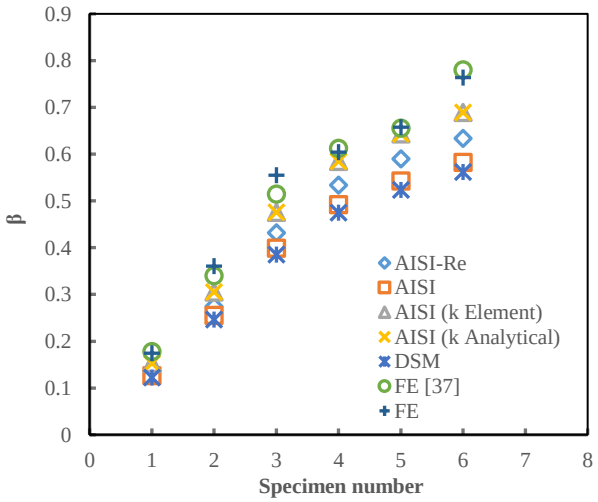

Fig. 9 Comparisons between nominal strength parameters (β) for lipped channel sections obtained from different design methods and FE results

5.2. Reliability analysis

The proposed method is further evaluated against the FE data in a more quantifiable manner by calculating the reliability index (β_o). The reliability is determined concerning the corresponding resistance factor as follows [15]

$$\phi = C_\phi (M_m F_m P_m) e^{-\beta_o \sqrt{v_m^2 + v_F^2 + C_p V_P^2 + V_Q^2}} \tag{17}$$

where ϕ is the resistance factor, C_ϕ is the calibration factor (=1.52) as implemented in [38], M_m and F_m are the mean value of the material factor (=1.05 and 1.0), respectively for combined axial load and bending, P_m is the mean value of FE-to-predicted ratios, β_o is target reliability index which is taken equal to 2.5 for structural members, V_m and V_F are the coefficient of variation of the material and fabrication factor (= 0.1 and 0.05), respectively, C_p is the correction factor that taken to be 1.0 for reliability analysis, V_P is the coefficient of variation of FE-to-predicted ratios as calculated in Table 5 and V_Q is coefficient of variance for the load effect (= 0.21 for LRFD); see[15].

Results of the reliability analysis are summarized in Table 5, wherein the mean values of FE-to-predicted ratios and the corresponding COV values determine the reliability index for two sets of resistance factors $\phi(= 0.85)$ and $(= 0.9)$. Furthermore, a target reliability index of 2.5 is used to compute the resistance factors. The table reveals that the proposed AISI-Re gives more accurate results than the AISI design method, which is significantly conservative for the studied cross sections. The derived reliability indices of the linear interaction equation in AISI [15] are 3.24 ($\phi = 0.85$) and 3.00 ($\phi = 0.9$) for the AISI-Re design method, which are significantly higher than the desired reliability indices of 2.5. The results indicate that the current specification for predicting the nominal strength [15] needs to be improved by evaluating the plate buckling coefficient (k), as demonstrated in the AISI-Re, to achieve closer results to the validated FE results.

Table 5
Reliability analysis for AISI-Re and current AISI design method

Eccentricity	No.	AISI-Re($\beta_{FE}/\beta n$)					EWM AISI($\beta_{FE}/\beta n$)				
		P_m	V_p	$\beta_o(\varphi=0.85)$	$\beta_o(\varphi=0.9)$	$\varphi(\beta o=2.5)$	P_m	V_p	$\beta_o(\varphi=0.85)$	$\beta_o(\varphi=0.9)$	$\varphi(\beta o=2.5)$
$e=0$	20	1.12	0.010	3.12	2.88	0.986	1.21	0.05	3.38	3.14	1.05
$e=H/10$	20	1.17	0.020	3.30	3.06	1.028	1.26	0.04	3.57	3.33	1.10
$e=H/5$	20	1.17	0.020	3.30	3.06	1.028	1.26	0.04	3.57	3.33	1.10
$e=H/2$	20	1.15	0.010	3.23	2.99	1.012	1.24	0.04	3.50	3.27	1.08
$e=H$	20	1.13	0.010	3.16	2.92	0.994	1.22	0.05	3.41	3.17	1.06
All	100	1.15	0.017	3.24	3.00	1.01	1.24	0.04	3.50	3.27	1.08

6. Conclusions and summary

This paper aims to establish a practical design for cold-formed steel-lipped-channel cross-sections, offering a framework to enhance the existing codified effective width method (EWM). An AISI-Re design approach is proposed, incorporating an assessed and validated k-value for local plate buckling. A parametric study is undertaken to evaluate the impact of the local plate buckling coefficient on the design of cold-formed steel (CFS) lipped channel cross-sections with varying (H/B) ratios, whether utilizing the codified EWM or the recent direct strength method (DSM). Additionally, results obtained from a validated finite element (FE) model are presented as benchmark solutions for the nominal strength of the analyzed members. Based on the generated results, the proposed AISI-Re design, which takes into account the interaction between adjacent sub-elements through the local plate buckling coefficient (i.e., k-value), demonstrates enhanced accuracy and reliability. Conclusions drawn from the results presented in this paper are as follows:

- The local buckling coefficient (k) significantly influences elastic and inelastic buckling strength calculation for cold-formed steel (CFS) lipped-channel cross-sections.
- Considering the restraining effect between sectional sub-elements is essential for adjacent sub-elements, as it expresses boundary conditions that substantially impact the plate buckling coefficient.
- The direct strength method (DSM) is regarded as a more reliable approach than the effective width method (EWM) in pure compression loading conditions, and its effectiveness can be further enhanced by incorporating a more realistic and accurate k-factor.
- AISI-Re can be seen as an improved method aligning with existing AISI standards. It provides realistic buckling strengths and closely aligns with experimental test results.
- The refined k-factors demonstrate a notable effect within the range of $1 \leq (H/B) \leq 2$ compared to the existing AISI values.

Acknowledgments

The second author is grateful for financial support from the competitive research projects - research unit - Mansoura University for the project ‘‘Solar Energy Storage System Using a Medium of Sustainable Geopolymer Concrete’’ (MU-Eng-22-15).

References

[1] A. D. Martins, D. Camotim, and P. B. Dinis, “Local-distortional interaction in cold-formed steel beams: Behaviour, strength and DSM design,” *Thin-Walled Struct.*, vol. 119, no. August, pp. 879–901, 2017, doi: 10.1016/j.tws.2017.06.011.

[2] M. T. Chen, B. Young, A. D. Martins, D. Camotim, and P. B. Dinis, “Experimental investigation on cold-formed steel stiffened lipped channel columns undergoing local-distortional interaction,” *Thin-Walled Struct.*, vol. 150, no. February, 2020, doi: 10.1016/j.tws.2020.106682.

[3] D. Cava, D. Camotim, P. B. Dinis, and A. Madeo, “Numerical investigation and direct strength design of cold-formed steel lipped channel columns experiencing local-distortional-global interaction,” *Thin-Walled Struct.*, vol. 105, pp. 231–247, 2016, doi: 10.1016/j.tws.2016.03.025.

[4] J. Becque and K. J. R. Rasmussen, “Experimental investigation of local-overall interaction buckling of stainless steel lipped channel columns,” *J. Constr. Steel Res.*, vol. 65, no. 8–9, pp. 1677–1684, 2009, doi: 10.1016/j.jcsr.2009.04.025.

[5] P. B. Dinis, D. Camotim, B. Young, and E. M. Batista, “CFS lipped channel columns affected by L-D-G interaction. Part II: Numerical simulations and design considerations,” *Comput. Struct.*, vol. 207, pp. 200–218, 2018, doi: 10.1016/j.compstruc.2017.03.017.

[6] B. Young, P. B. Dinis, and D. Camotim, “CFS lipped channel columns affected by L-D-G interaction. Part I: Experimental investigation,” *Comput. Struct.*, vol. 207, pp. 219–232, 2018, doi: 10.1016/j.compstruc.2017.03.016.

[7] G. Winter, “Strength of thin steel compression flanges,” *Trans. Am. Soc. Civ. Eng.*, vol. 112, no. 1, pp. 527–554, 1947.

[8] A. Moldovan, “Compression tests on cold-formed steel columns with monosymmetrical section,” *Thin-Walled Struct.*, vol. 20, no. 1–4, pp. 241–252, 1994, doi: 10.1016/0263-8231(94)90068-X.

[9] B. Young, N. Silvestre, and D. Camotim, “Cold-Formed Steel Lipped Channel Columns Influenced by Local-Distortional Interaction: Strength and DSM Design,” *J. Struct. Eng.*, vol. 139, no. 6, pp. 1059–1074, 2013, doi: 10.1061/(asce)st.1943-541x.0000694.

[10] M. Dundu, “Buckling of short cold-formed lipped channels in compression,” *J. South African Inst. Civ. Eng.*, vol. 56, no. 2, pp. 46–53, 2014.

[11] B. W. Schafer, “CUFSM 3.12, elastic buckling analysis of thin-walled members by finite strip analysis.” 2006.

[12] T. L. G. CHEUNG YK, “Finite Strip Method [M].” Boca Raton: CRC Press, 1998.

[13] “Abaqus/CAE User’s Manual, version 6.14-2, USA, 2014.” “Dassault Syst{\`e}mes Simulia Corp.”

[14] *Standards Australia/Standards New Zealand. Cold-formed steel structures, AS/NZS 4600;1996.*

[15] American Iron and Steel Institute, “North American Specification Steel Structural Members,” *North Am. Specif. Steel Struct. Members*, p. 78, 2016.

[16] D. Dubina, R. Landolfo, and V. Ungureanu, “Design of cold-formed steel structures.: Eurocode 3: design of steel structures. Part 1-3, Design of cold-formed steel structures,” 2012.

[17] ECP-205 (LRFD), “Egyptian Code of Practice for Steel Construction.” 2008.

[18] G. H. Bryan, “On the Stability of a Plane Plate under Thrusts in its own Plane, with Applications to the ‘Buckling’ of the Sides of a Ship,” *Proc. London Math. Soc.*, vol. 1, no. 1, pp. 54–67, 1890.

[19] L. Schuman and G. Back, *Strength of rectangular flat plates under edge compression*, no. 356. NACA, 1930.

[20] T. Von Kármán, “Strength of thin plates in compression,” *Trans. ASME*, vol. 54, p. 53, 1932.

[21] B. W. Schafer, “The direct strength method of cold-formed steel member design,” *J. Constr. steel Res.*, vol. 64, no. 7–8, pp. 766–778, 2008.

[22] C. Yu and W. Yan, “Effective Width Method for determining distortional buckling strength of cold-formed steel flexural C and Z sections,” *Thin-Walled Struct.*, vol. 49, no. 2, pp. 233–238, 2011, doi: 10.1016/j.tws.2010.11.006.

[23] G. P. Mulligan and T. Pekoz, “Local buckling interaction in cold-formed columns,” *J. Struct. Eng.*, vol. 113, no. 3, pp. 604–620, 1987.

[24] M. D. Ahdab, A. W. Fischer, C. Ding, B. Glauz, and B. W. Schafer, “Local buckling expressions for lipped channels,” *Struct. Stab. Res. Counc. Conf. 2022, Held conjunction with NASCC Steel Conf.*, pp. 1–17, 2022.

[25] S. Torabian, B. Zheng, and B. W. Schafer, “Experimental response of cold-formed steel lipped channel beam-columns,” *Thin-Walled Struct.*, vol. 89, pp. 152–168, 2015, doi: 10.1016/j.tws.2014.12.003.

[26] K. Roy *et al.*, “Cold-Formed Steel Lipped Channel Section Columns Undergoing Local-Overall Buckling Interaction,” *Int. J. Steel Struct.*, vol. 21, no. 2, pp. 408–429, 2021, doi: 10.1007/s13296-020-00447-w.

[27] A. H. A. Abdelrahman, S. Liu, Y. P. Liu, and S. L. Chan, “Simulation of Thin-Walled Members with Arbitrary-Shaped Cross-Sections for Static and Dynamic Analyses,” *Int. J. Struct. Stab. Dyn.*, vol. 20, no. 12, pp. 1–22, 2020, doi: 10.1142/S021945542050128X.

[28] B. W. Schafer, Z. Li, and C. D. Moen, “Computational modeling of cold-formed steel,” *Thin-Walled Struct.*, vol. 48, no. 10–11, pp. 752–762, 2010, doi: 10.1016/j.tws.2010.04.008.

[29] N. Abdel-Rahman and K. S. Sivakumaran, “Material properties models for analysis of cold-formed steel members,” *J. Struct. Eng.*, vol. 123, no. 9, pp. 1135–1143, 1997.

[30] E. Ellobody and B. Young, “Structural performance of cold-formed high strength stainless steel columns,” vol. 61, pp. 1631–1649, 2005, doi: 10.1016/j.jcsr.2005.05.001.

[31] L. Gardner and X. Yun, “Description of stress-strain curves for cold-formed steels,” *Constr. Build. Mater.*, vol. 189, pp. 527–538, 2018, doi: 10.1016/j.conbuildmat.2018.08.195.

[32] B. Schafer and T. Peköz, “Geometric imperfections and residual stresses for use in the analytical modeling of cold-formed steel members,” *Int. Spec. Conf. Cold-Formed Steel Struct. Recent Res. Dev. Cold-Formed Steel Des. Constr.*, pp. 649–664, 1996.

[33] R. G. Dawson and A. C. Walker, “Post-buckling of geometrically imperfect plates,” *J. Struct. Div.*, vol. 98, no. 1, pp. 75–94, 1972.

[34] Z. Li and B. W. Schafer, “Application of the finite strip method in cold-formed steel member design,” *J. Constr. Steel Res.*, vol. 66, no. 8–9, pp. 971–980, 2010.

[35] M. R. Bambach, “Design of uniformly compressed edge-stiffened flanges and sections that contain them,” *Thin-Walled Struct.*, vol. 47, no. 3, pp. 277–294, 2009, doi: 10.1016/j.tws.2008.07.011.

[36] B. W. Schafer and T. Pekoz, “Direct strength prediction of cold-formed steel members using numerical elastic buckling solutions,” 1998.

[37] F. Öztürk, S. M. Mojtabaei, M. Şentürk, S. Pul, and I. Hajirasouliha, “Buckling behaviour of cold-formed steel sigma and lipped channel beam–column members,” *Thin-Walled Struct.*, vol. 173, no. August 2021, p. 108963, 2022, doi: 10.1016/j.tws.2022.108963.

[38] V. Z. Meimand and B. W. Schafer, “Impact of load combinations on structural reliability determined from testing cold-formed steel components,” *Struct. Saf.*, vol. 48, pp. 25–32, 2014, doi: 10.1016/j.strusafe.2013.10.006.

Advanced Steel Construction – Vol. 20 No. 1 (2024) 39–52
DOI:10.18057/IJASC.2024.20.1.5

COMPRESSION BEHAVIOUR OF BI-ANGLED BUILT-UP CRUCIFORMS LOADED THROUGH ONE ANGLE

Gorripotu Kishore Kumar * and Raghavan Ramalingam

Department of Civil Engineering, National Institute of Technology, Tiruchirappalli, India
** (Corresponding author: E-mail: gorripotukishorekumar@gmail.com)*

ABSTRACT

Angles are popularly used in built-up steel sections. The behaviour of common sections built-up by angles such as boxes and tees are established, and design provisions are available in design codes. The cruciform arrangement, consisting of vertex-to-vertex connected angles, has been studied recently as a strengthening arrangement for lattice tower primary members, where the load is not applied through the centroid on the built-up section, like in common built-up sections. The behaviour of such cruciforms need to be studied further for establishing their efficiency as compression members. This study consists of experimental tests followed by numerical parametric study of such cruciforms. Experimental tests on cruciform of slenderness 80, 100 and 120 were performed followed by numerical finite element analysis for validation. A parametric study was conducted on 36 bi-angled cruciforms with slenderness, connector spacing, number of bolts and angle width-thickness ratio as the chosen parameters. Predictions by national design codes were compared with the numerical results. The influence of these parameters on the load sharing rate between the angle sections were observed and it is seen that slenderness has the highest influence while the number of bolts per connector has least influence. Equal load sharing was achieved for cruciforms of lesser slenderness, showing that the arrangement can be an efficient strengthening arrangement.

ARTICLE HISTORY

Received: 21 June 2023
Revised: 9 October 2023
Accepted: 18 November 2023

KEYWORDS

Built-up section;
Cruciform;
Strengthening;
Compression

Copyright © 2024 by The Hong Kong Institute of Steel Construction. All rights reserved.

1. Introduction

Steel angles are the primarily used sections to construct lattice towers such as telecommunication and electrical transmission towers [1]–[3]. These towers are built by bolted connections of single or double angles for primary leg members and single angles for secondary members at higher elevation. Angles are also versatile due to which they are used in various built-up arrangements such as Tee (back to bank), Channel (toe to toe), box sections and design procedures for such built-up sections are available in international design standards. The behavior of angles is unique due to their unsymmetric geometry because of which Indian and other standards contain dedicated clauses to determine their compression capacity. Built-up sections in steel structures are adopted when the required cross-section to withstand the design load is not available and are recently also being adopted for retrofit of distressed members in service.

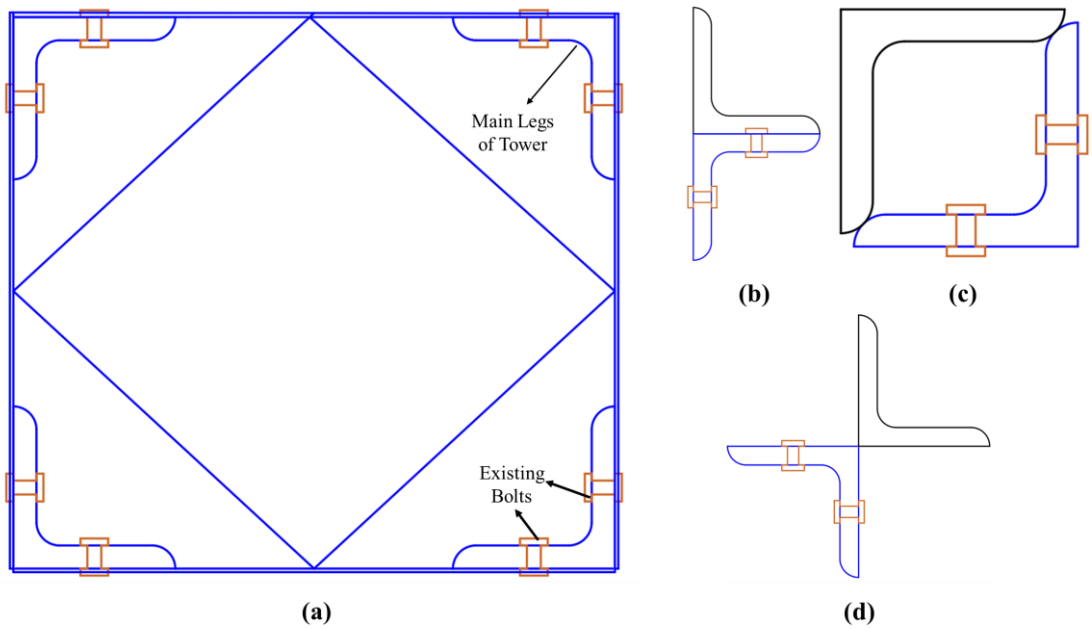

Fig. 1 Different Built-up options with angle sections for a tower; (a) Existence tower plan; (b) bi-angled T section; (c) bi-angled box section; (d) bi-angled cruciform section

Among various built-up options for existing tower legs for retrofit, Tee (Fig. 1 (b)) is not possible practically due to presence of bolts (Fig. 1 (a)) at both sides of the angle section and box section (Fig. 1(c)) is not possible due to presence of root radius at edges where the angles will have to be joined. Hence for an existing tower the cruciform arrangement offers the most practical solution since it minimally interferes with the two sides of the angle section which is to be retrofitted (Fig. 1(d)). A number of arrangements are cruciform by geometry (e.g., aligned, alternate etc.). But only the arrangement using uniformly spaced cleat angles for connecting the existing and reinforcing angles, have been called “cruciform” (Fig. 2) by researchers.

Extensive literature is available on the behaviour of built-up sections composed of angle sections. Tetra-angled cruciforms [4]–[6] have been studied as a built-up section comprising of angles as well as the effect of inter-connectors on the behaviour of these members. Flexural-Torsional buckling occurs depending on connector spacing [7] and overall slenderness [8]. Force sharing between the two members of a built-up section up to 30% have been seen in some studies [9], though this is influenced by the connection pattern viz. single cross plate, double cross plate, cleat angle etc.

Bolt-slip is a common occurrence in sections used in towers, with the most widely adopted slip model for the angle sections proposed by Ungkurapinan et. al [10] experimental programme. Recent studies demonstrate the resemblance

of joint models including slip [11] with experimental observation, and the initial torque has a prominent influence on ultimate load and stiffness [12]. The application of additional angles to strengthen towers is seen earlier in the form of diaphragm retrofit by Albermani [13], [14]. Among available tower primary leg retrofit patterns in literature, the studies by University of South Australia have determined that the cruciform is superior in terms of capacity improvement [15], and the improvement in tower ultimate capacity was also shown through testing of small-scale tower with leg-retrofit by cruciform arrangement [16]. Literature on efficiency of cruciform retrofit in improving the whole tower capacity are also present [17], [18]. Other retrofit options such as provision of casings [19], box [20] and others [21], [22] have also been attempted. Xie and Zhang [23] conducted an experimental test on a bottom panel of tower assembly by retrofitting the diagonal members and found that vulnerable members of the assembly changed from diagonal to main member after retrofitting. The component method of Eurocode 8 can be used to evaluate the connection in these members [24].

From the practical implementation view it is seen that the cruciform of Vertex-to-Vertex connection is more suitable [15], [22] for field application of retrofitting tower legs. But it is found that experimental work for determining in detail the behaviour of cruciform arrangement is lacking in the literature. Hence from the literature it is seen that further investigations on behaviour of cruciform of bi-angled section are needed to ascertain their effectiveness as a built-up section. Further, the existence-to-retrofit angle connections are to be specifically suitable for in-situ retrofitting. Such an option is presented in [15], [22]. The present study investigates the mechanical behavior of such cruciform retrofit section under compression loading experimentally and numerically using ABAQUS. Parameters chosen for study are (a) Slenderness Ratio, (b) Connector Spacing, (c) Number of bolts per connector and (d) Width to thickness ratio. The present study will help in understanding the ultimate behaviour of bi-angled cruciform section along with load sharing rate between Existing Member (EM) and newly added Reinforcing Member (RM).

2. Experimental setup

As shown in the Fig. 2 Vertex-to-vertex cleat angles were used to connect both Existing Member (EM) and Reinforcing Member (RM) to form the bi-angled Cruciform section with 5.6 grade of 10 mm sized bolt. Fig. 2 (a) and Fig. 2 (b) shows the cross-sectional views with connectors and without connectors, respectively. Fig. 2 (b) shows the loading point P and "e" is the eccentricity of the loading point, whereby load will be initially taken by EM then transferred to RM through Vertex-to-vertex cleat angles.

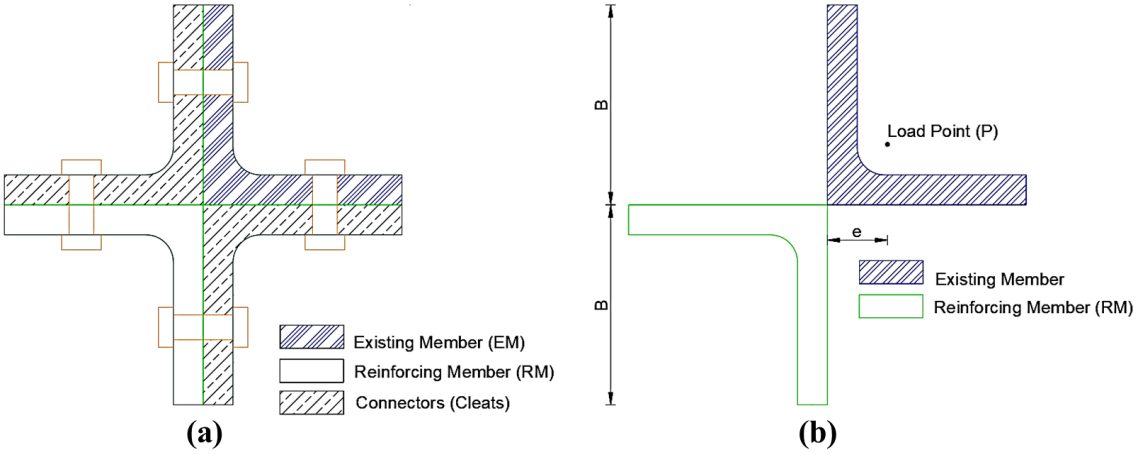

Fig. 2 Cross-sectional view of Bi-Angled Cruciform Section; (a) with connectors; (b) without connectors

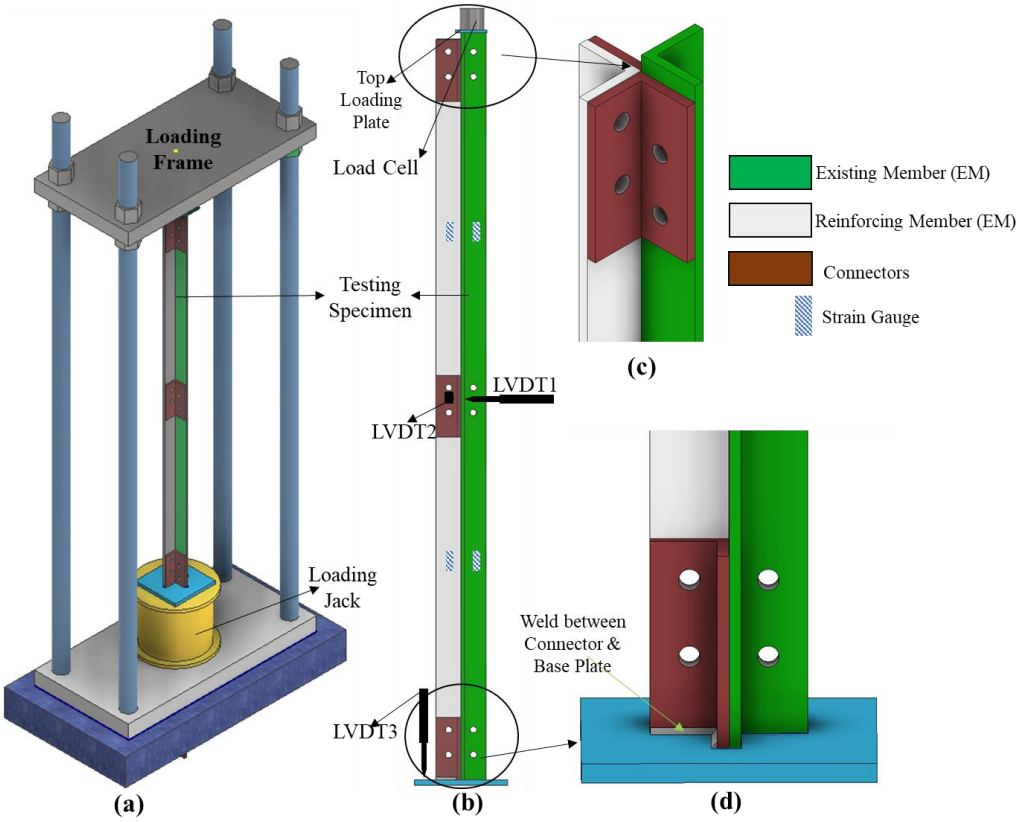

Fig. 3 Testing setup for Bi-Angled Cruciform Section with position of Strain gauge and LVDT

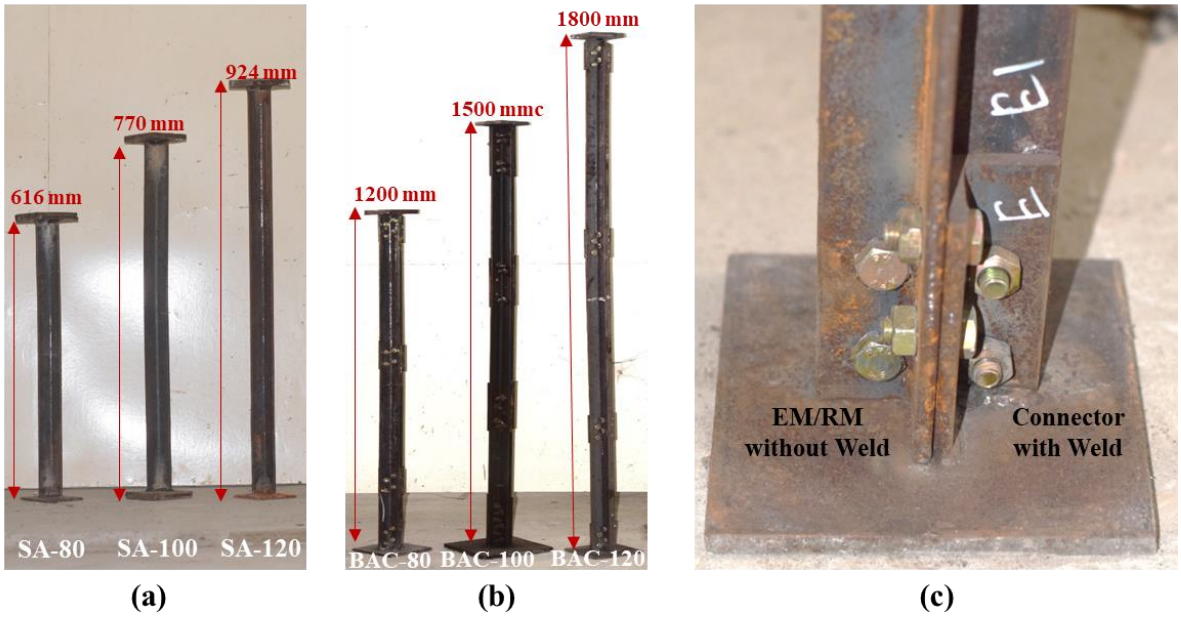

Fig. 4 Details of Experimental Specimens; (a) Single Angle specimens; (b) Bi-Angled Cruciform specimens; (c) Bottom Connector Details

The slenderness of the specimens of both single-angle and cruciform was chosen as the common parameter so that a comparative picture of change in failure (buckling) mode can be observed. The steel angle section of ISA 40X40X6 of E350 grade as per IS:2062-2011 was chosen for both single-angle and bi-angled cruciform experiments.

Fig. 3 mentions the detailed test setup and specimen details along with the location of strain gauges and LVDTs. A total of six strain gauges were used during the experiment for each Bi-Angled Cruciform (BAC) specimen, three for EM and three for RM. All these strain gauges were placed at the mid height of each segment (portion of specimen between two connectors). Three LVDTs (LVDT 1 and LVDT 2 to measure the lateral and transverse displacements at mid height and LVDT 3 to measure the axial displacement) were used. The loading point is the centroid of the EM (Fig. 2), and the top loading plate is welded only with EM (top of Fig. 3 (b)) . The level difference (Fig. 3 (c)) in the top surfaces of EM and RM, ensures that the load is initially taken by EM and then transferred to the RM through the bolted cleat angles over some distance.

The bottom plate was welded to the bottom connectors alone and not to the EM and RM (Fig. 3 (d) and Fig. 4 (c)). This was done in order to replicate the real field conditions where the main member of the tower is connected to the foundation via coping. During the experiment, some fabrication errors were found in the bi-angled cruciform section SR100 whereby the elevational difference between EM and RM was insufficient and SR120 specimen had an overall inclination of 2^0 with vertical. The same errors which occurred during fabrication were included in the numerical model later for model validation purpose.

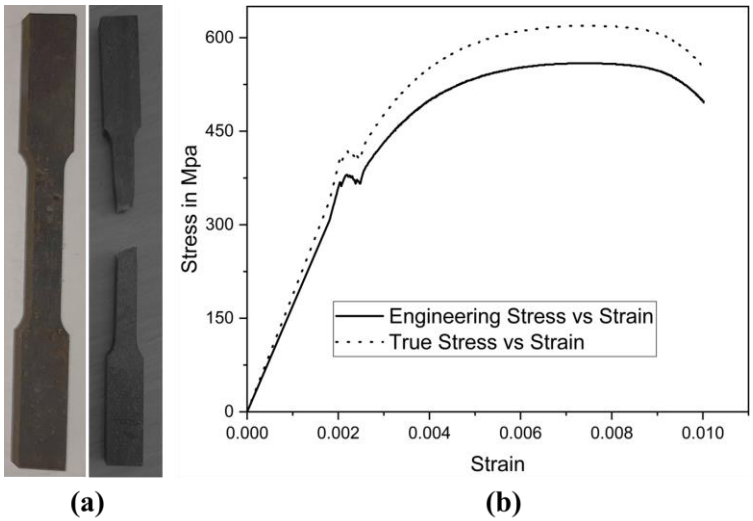

Fig. 5 Coupon Testing; (a) Coupon specimen before and after testing (b) Stress-Strain Plot

Eqn (1) to (5) were used to determine the various cross-sectional properties of BAC (Fig. 2 (b)), the chosen cruciform has cross-sectional area (A) 888 mm^2, centroidal moments of inertia (I_x) of both angles and product of inertia (I_{xy}) 260596 mm^4 and 56952 mm^4, respectively. The cleat angle are neglected for moment of inertia calculation of cruciform.

$$A = 2T\,(2B - T) \tag{1}$$

$$I_x = \frac{4B^4 - \{(B-T)^4 + 3(B^2 - T^2)\}}{6} \tag{2}$$

$$I_{xy} = \frac{T^2(2B^2 - T^2)}{2} \tag{3}$$

$$I_{min} = I_x - I_{xy} \tag{4}$$

$$r_{min} = \sqrt{\frac{I_{min}}{A}} \tag{5}$$

Bolt hole clearance, pitch, edge distance, and end distance are considered based on the regulations of IS:802-1995 (Code of Practice for structural steel Overhead Transmission Line Towers) [25] , while the centre-to-centre spacing of the connectors is based on the AISC 360-16 [26] specification, which states that individual components of compression members composed of two or more

shapes shall be connected to one another at intervals, *a*, such that the slenderness ratio, a/r_i, of each of the component shapes between the fasteners does not exceed three-fourths times the governing slenderness ratio of the built-up member. The least radius of gyration, r_i, shall be used in computing the slenderness ratio of each component part.

AISC 360-16 [26] suggests that for a built-up member to function as an effective structural member pretension is required. From the torque equation T=KFD, the required torque to obtain a pretension force of magnitude 10kN for bolts was evaluated as 20 N-m by considering K value as 0.2 [27] and this value of torque was applied to tighten the bolts. Sequence of tightening of bolts was performed from middle to outer as suggested in reference [10].

Three number of coupon specimens were extracted in accordance with the ASTM E8/E8M−13a [28] provisions and tension test was performed to find the grade of the steel and stress-strain properties. Fig. 5 (a) and Fig. 5 (b) shows the coupon specimen used for the tension test and average stress-strain (both engineering and true values) graph.

Detailed test setup for the single angles and cruciform specimens including location of LVDT, strain gauges, load cell shown in Fig. 3 The loading was stopped during each experiment after load started to drop, post the ultimate load based on safety considerations due to the deflection of specimen. Plots of load-deflection, strains and related results are plotted in section 4.

3. Numerical modelling

In order to obtain greater understanding on the physical behavior of these sections, a parametric study was performed. A numerical model was developed using ABAQUS. All parts named Existing Member (EM), Reinforcing Member (RM), and Connectors were created in the part module using the 3D solid extrude option. Bolt and nut were developed as a single unit called a fastener. The material density was taken as 7850 kg/m^3, with 0.3 as the friction coefficient. Boundary conditions of pinned at the base of bottom plate and twist and vertical deflection allowed at loading point were applied based on deformation observed in experiment.

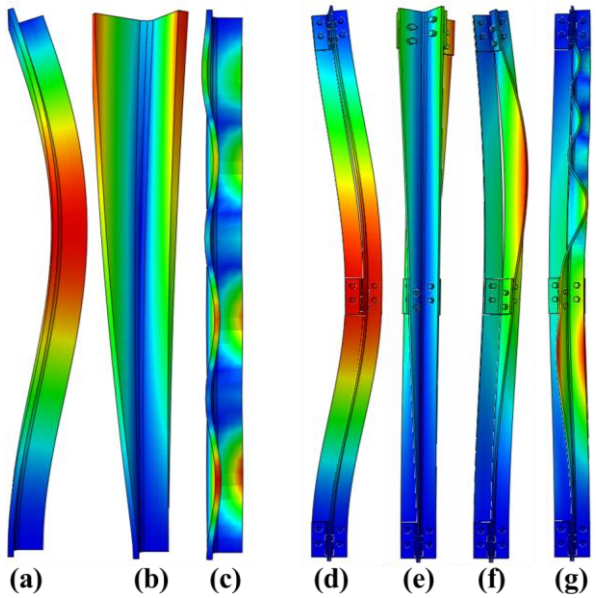

Fig. 6 Buckling Modes; (a) SA-F; (b) SA-T; (c) SA-LB; (d) BAC-F; (e) BAC-T; (f) BAC-FT; (g) BAC-LB

Table 1
List of models generated for Experimental results Validation and their global buckling modes

S. No	Name of Model	Size of Section	λ	L	First 4 Buckling Modes
1	SR80-SA-Num	ISA 40X40X6	80	616	F, T, LB, LB
2	SR100-SA-Num		100	770	F, T, LB, LB
3	SR120-SA-Num		120	924	F, T, LB, LB
4	SR80-BAC-Num		80	1200	F, T, TF, TF
5	SR100-BAC-Num		100	1500	F, T, TF, TF
6	SR100-BAC-Im-Num		100	1500	F, T, TF, TF
7	SR120-BAC-Num		120	1800	T, TF, F, TF
8	SR120-BAC-Im-Num		120	1800	T, TF, F, TF

SR, λ - Slenderness Ratio; L – Length of specimen; Num – Numerical model; Im – Imperfection modified; F - Flexural Buckling about Minor Axis; T - Torsional Buckling; TF - Torsional-

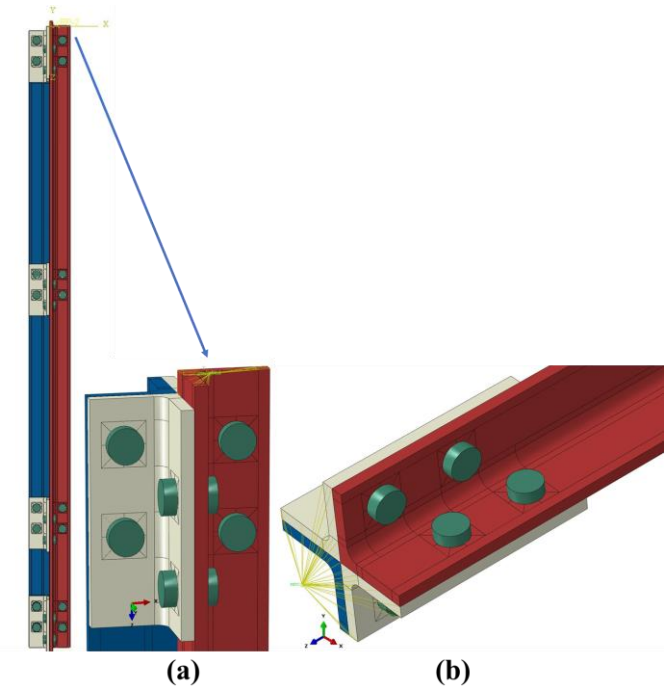

Fig. 7 Cruciform model with MPC connected to EM; (a) Top, (b) Bottom

Multipoint constraints (MPC) beam elements are used for application of boundary conditions and load (Fig. 7). The bolt load of 10kN is applied as the bolt pretension. The total analysis is conducted in two stages [3] – stage 1 includes the prediction of buckling modes from linear perturbation analysis to incorporate the imperfections. Stage 2 was non-linear analysis performed by Static-RIKS by incorporating the imperfections from stage 1 analysis. Imperfections factors of 0.5, 0.1, 0.1 and 0.1 (decided based on the trial and error to match with the experimental behaviour) for the first four buckling modes were incorporated through the keyword edit (Fig. 6, Table 1). Different global seed size of 5, 10 and 15 were tried for the analysis and it was found that ultimate behaviour was same for all mesh sizes and hence mesh size of 15 was adopted to minimize the computational time. Eight noded brick elements (C3D8R) with reduced integration were assigned [15], [29]. Two interactions were considered - penalty friction formulation with a friction coefficient of 0.25 in tangential behaviour and hard contacted pressure-overclosure with a penalty (Standard) for constraint enforcement method by specifying contact stiffness of 2000 N-mm with a linear behaviour [22].

4. Results and discussions

Experiments were performed on single angles and Bi-Angled cruciforms of same slenderness to evaluate their mechanical behaviour and capacities. Numerical validation of all models were done using the experimental results. Comparison of experiment and numerical results are presented in Table 2.

4.1. Experimental results

Table 2 shows the ultimate capacities obtained from testing. During the experiments, flexural buckling was observed for the all-single angles and cruciform sections of SR 80 and SR 100, whereas for SR 120 cruciform section, flexural-torsional buckling was observed. Due to insufficient elevational difference between EM and RM (SR 100 specimen) due to fabrication error, top plate attained contact with RM and therefore load was taken by both EM and RM from early stages of loading leading to higher failure load.

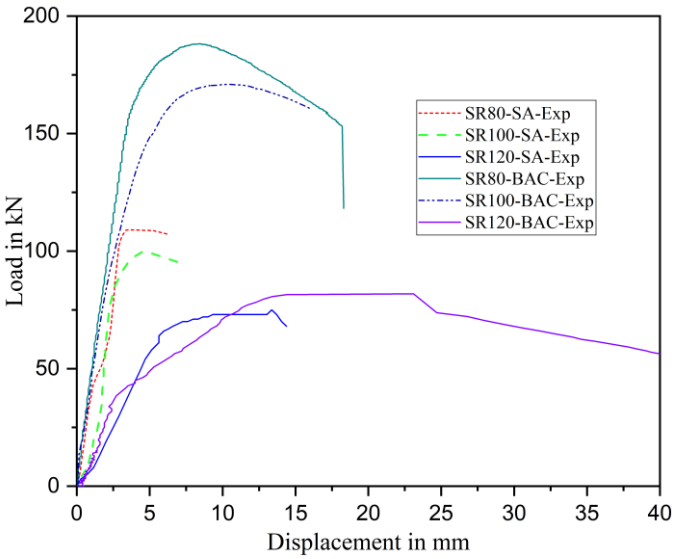

Fig. 8 Load vs Lateral Displacement for Single Angle (SA) and Bi-Angled Cruciform (BAC) Experiments

Fig. 8 show the load vs lateral displacement curves for all single angles and cruciform specimens, from the figure it is found that there is no much difference observed in the stiffness of both 80 and 100 slenderness specimens, whereas the stiffness of 120 slenderness specimen is significantly lower. This is because the Flexural-Torsional buckling drives the deflection of the specimen and also the effect of 2^0 inclination.

4.2. Numerical results and validation

For the specimen of slenderness 100 which had insufficient elevation difference between EM & RM, the ultimate capacity was 171.1kN since load was taken by both members from the start. Numerical capacity of SR100-BAC-Num was 169.26 kN. Therefore, a numerical model (SR100-BAC-Im-Num) of slenderness 100 was developed including the desired elevational difference between EM and RM and its capacity was 133.22 kN. Since SR120 model had an overall inclination of 2^0 the same was included in the numerical model for validation. The models 'SR120-BAC-Num' and 'SR120-BAC-Im-Num' are numerical models validated with inclination of 2^0 and without inclination, respectively.

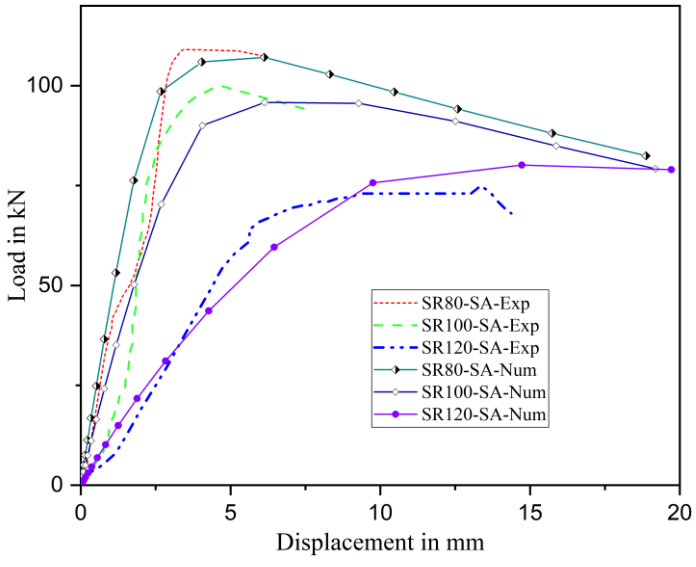

Fig. 9 Load vs Lateral Displacement for Single Angle Specimens

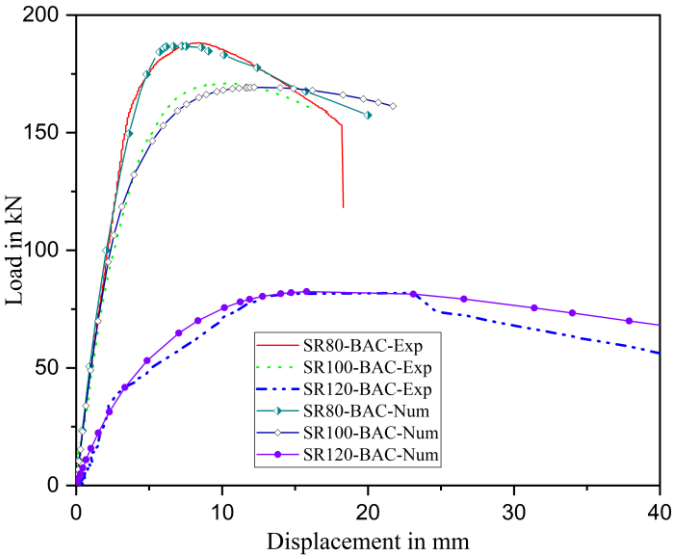

Fig. 10 Comparison of Exp-Num for Load vs Lateral Displacement for Bi -Angles Cruciform

For single angles and bi-angled Cruciform sections of all slenderness ratios, numerical capacity matched with experimental capacity and load vs lateral displacement curves (Fig. 9 and Fig. 10) were in good agreement with numerical results. The initial stiffness of SR80 and SR100 coincided and their load carrying capacities obtained from experiment (and numerical) were 188.2 kN (and 186.9 kN) and 171.1 kN (and 169.2 kN) respectively. The stiffness of 120 slenderness specimen is very low when compared with other slenderness specimens. Secondary moments in a column is prominent at higher slenderness ratios and also the eccentric loading amplifies the reduction in lateral stiffness in this specimen.

Comparison of load vs axial displacement for cruciform specimens are presented in Fig. 13. From that curves it is observed that, unlike lateral stiffness there is not much difference in axial stiffness between various slenderness specimens. As the curvature and the lateral deflection of a member increases, the compressive stresses on the concave side of the member also increases until the member fails due to excessive yielding. In the numerical analysis this corresponds to the increment where specimen reaches ultimate load. For Single angles (Fig. 11) and bi-angled Cruciform specimens (Fig. 12) the bending was observed about minor axis (v-v axis) in both experimental and numerical analysis.

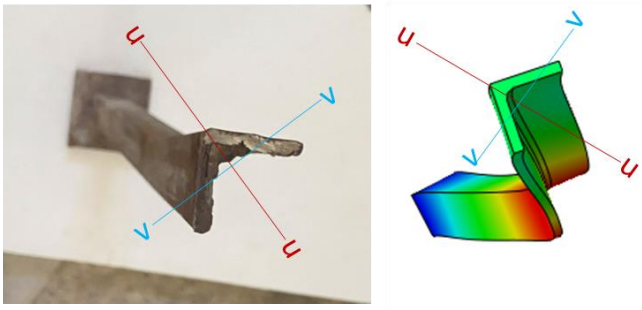

Fig. 11 Buckling axis for Single Angle Specimen

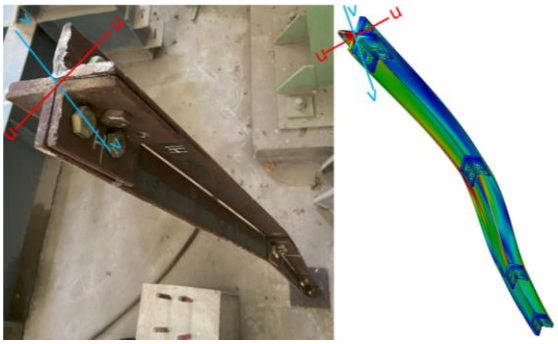

Fig. 12 Buckling axis for Bi-Angled Cruciform Specimen

Comparison of load vs lateral displacement for SR 100 and SR 120 with and without fabrication errors Fig. 14. Stiffness of SR100-BAC-Im-Num (Model with elevational difference) was similar to experimental specimen, but there is considerable difference in their load carrying capacities, showing that providing elevational difference between the EM and RM affects the ultimate capacity. For SR120 model stiffness and capacity are greater for the specimen without inclination - 97.27kN compared to 82.47kN with inclination. Fig. 15, Fig. 16 and Fig. 17 show the deformed shapes of experimental cruciform specimens along with numerical model deformed shapes obtained from numerical analysis.

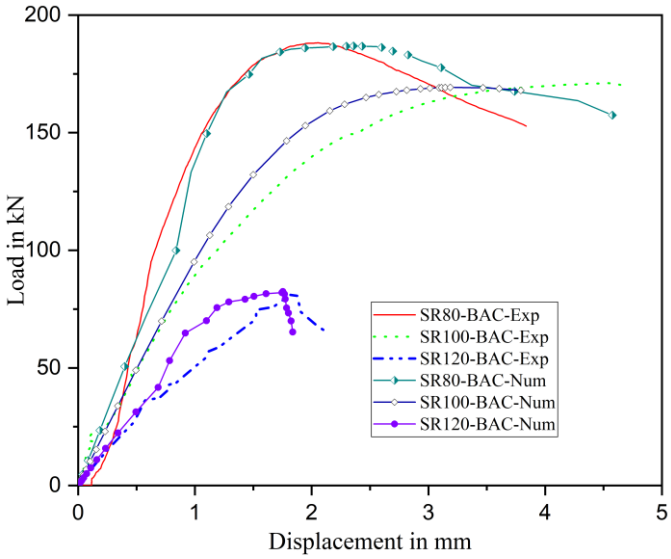

Fig. 13 Load vs Axial Displacement of Cruciform Specimens (Exp-Numerical Comparison)

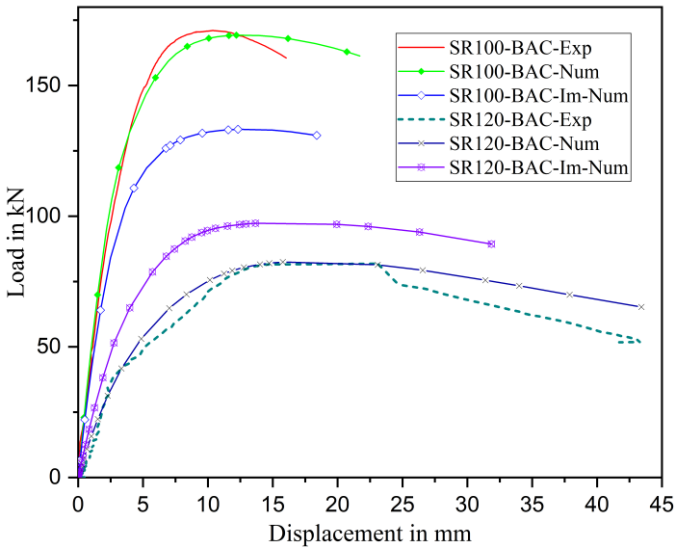

Fig. 14 Load vs Lateral Displacement for SR100 and SR120 Bi-Angles Cruciform (Comparison of models inclusive of fabrication errors)

Fig. 18 (a) to Fig. 18 (f) show the Load vs Micro Stain curves from the experiments in EM & RM for the cruciform sections and same are compared with numerical values. During the experiments, for all specimens, the highest strain at any load was recorded in the top segment of EM and least strain recorded in the top segment of RM and the same is seen in the validated numerical models. In the bottom segments of SR 80 and SR 100 specimens, the difference between the strains in EM and RM was low, indicating that the loads carried by EM and RM in the bottom segment are almost equal. In case of SR120 greater difference in strains between EM and RM compared to SR80 and SR100 were observed in the bottom segment, which may be due to higher slenderness ratio within each segment and initial inclination. In each figure, the top segment of EM which records the highest strain is the left most curve, while top segment of RM which carries least strain is the right most curve. The bottom segments of both EM and RM which carry intermediate, but similar strains, are seen in the middle of each figure. Strain in EM decreases from top segment to bottom segment, where as in RM its increases from top to bottom, which clearly depicts the load transfer through the connected angle cleats.

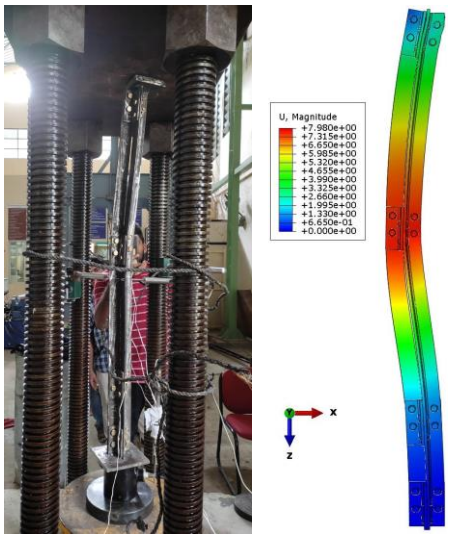

Fig. 15 SR80 Deformed Shape (Exp-Numerical)

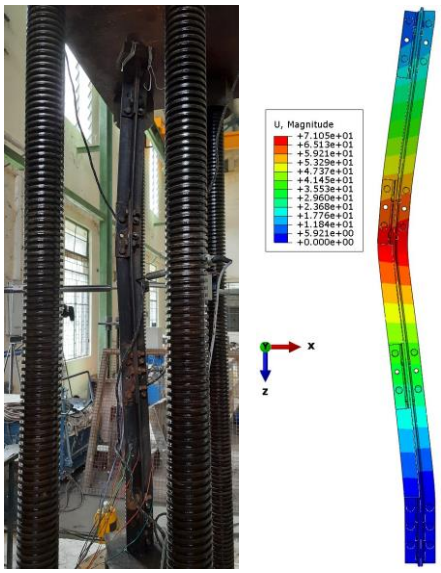

Fig. 16 SR100 Deformed Shape (Exp-Numerical)

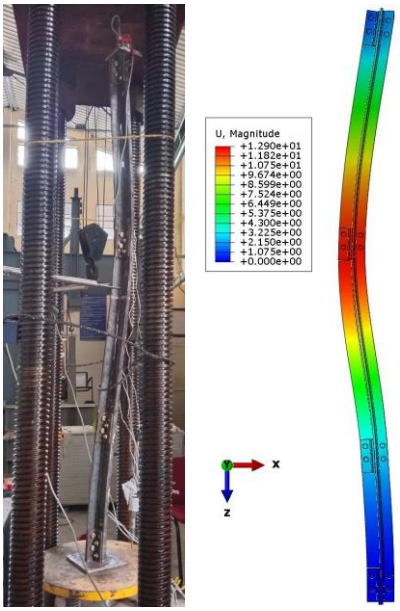

Fig. 17 SR120 Deformed Shape (Exp-Numerical)

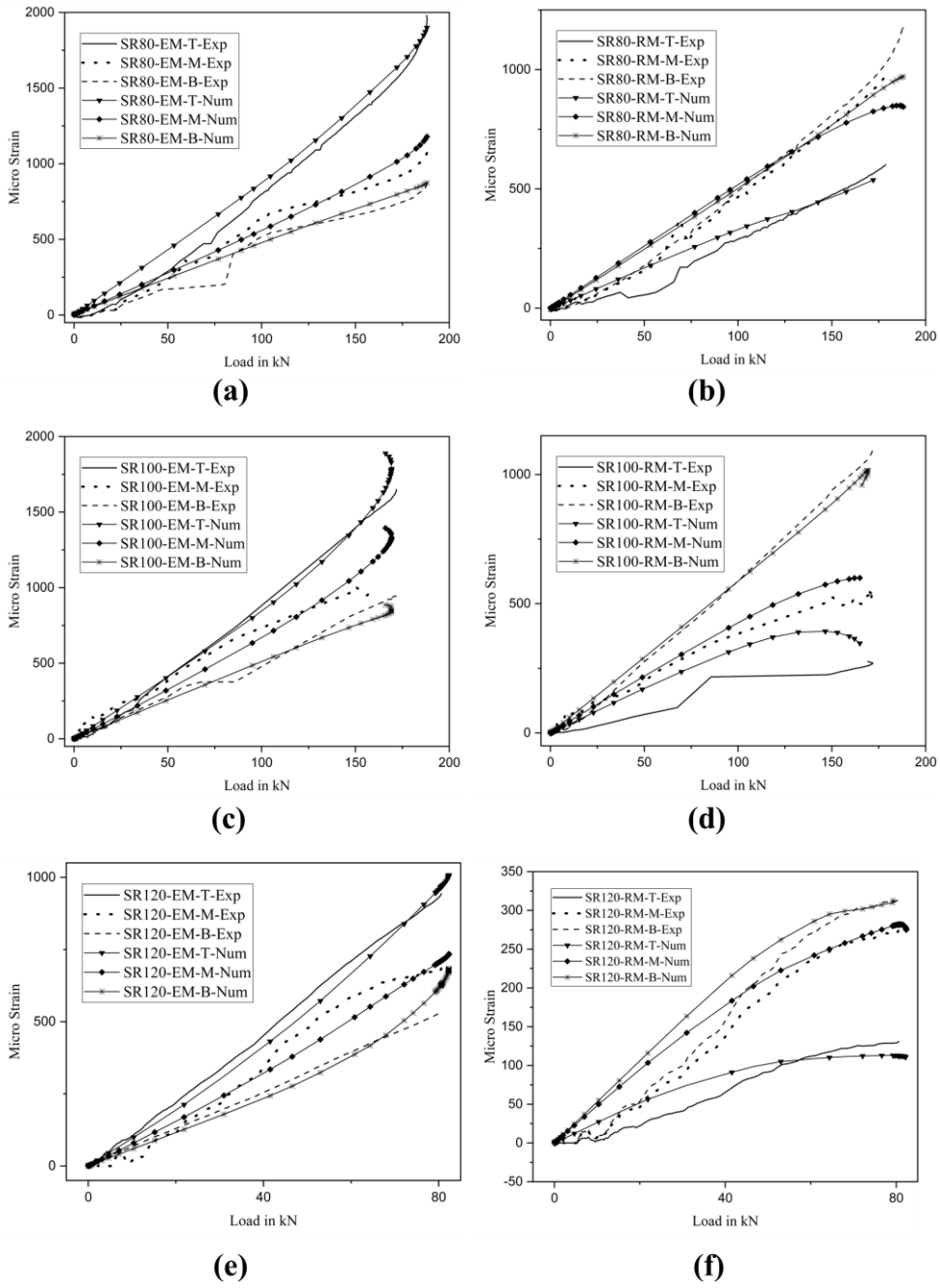

Fig. 18 Comparison of Load vs Micro Strain (T-Top; M-Middle; B-Bottom)

4.3. Codal predictions

The experimental and numerical capacities were also compared with the codal predictions. Capacity of single and bi-angled cruciform sections were calculated with the help of Indian Standard [30], European Standard[31] and AISC[26] codal provisions and compared with experimental results. From the specifications of design of compression member, the following set of equations (6-9) were used to determine the capacity by using IS:800-2007 [30] and BS EN 1993-1-1:2005 / EN 1993-1-1:2005 (E) [31]. Partial safety factors were avoided in calculations.

$$N_{b,Rd} = \chi A f_y \tag{6}$$

$$\chi = \frac{1}{\phi+[\phi^2-\lambda^2]^{0.5}} \quad but\ \chi \leq 1.0 \tag{7}$$

$$\bar{\lambda} = \sqrt{\frac{Af_y}{N_{cr}}} \tag{8}$$

$$N_{cr} = \frac{\pi^2 EI}{L_c^2} \tag{9}$$

Sections E3 & E4 of AISC: 360-16 [26] were used for determining the flexural buckling & Torsional and Flexural-Torsional buckling capacities of section respectively. The procedure available in E6 was followed to determine the modified slenderness ratio for built-up cruciforms.

$$P_n = F_{cr} A_g \tag{10}$$

Flexural Buckling Strength

$$F_{cr} = \left(0.658^{\frac{F_y}{Fe}}\right) F_y \tag{11}$$

$$F_e = \frac{\pi^2 E}{\left(\frac{L_c}{r}\right)^2} \tag{12}$$

Modified slenderness ratio for built-up section, K_i considered as 0.86.

$$\left(\frac{L_c}{r}\right)_m = \sqrt{\left(\frac{K_i a}{r_i}\right)^2 + \left(\frac{L_c}{r}\right)_o^2} \tag{13}$$

Torsional and Flexural-Torsional buckling strength

$$F_e = \left(\frac{\pi^2 EC_w}{L_{cz}^2} + GJ\right)\frac{1}{I_x + I_y} \quad (14)$$

The effective length factor (K) for the codal predictions was taken as 0.85, due to absence of degree of restraint properties for coping kind of support condition, the K value was decided based on the deformed shape of bi-angled cruciform experimental specimens. For the determination of effective slenderness ratio, radius of gyration about the minor principle axis (r_{vv}) was used since the buckling (Fig. 10 and Fig. 12) for both single and bi-angled cruciform was observed about minor principle axis.

Table 2 shows that experimental and numerical results of single angles are close to the Codal predictions of IS [30] and Euro [31] code. The capacity predicted by AISC code [26] is higher than that of the other two codes. Codal capacity (using the flexural buckling specifications with respect to IS & Euro codes) for 100 & 120 slenderness cruciform were unconservative in comparison to experimental and numerical capacity. Codal capacity (with Flexural-Torsional Buckling) in accordance with AISC specifications were in better agreement with numerical capacity for 100 & 120 slenderness specimens. Codal flexural buckling capacities obtained through IS and Euro codes are similar, since the codal expressions in both codes are identical.

Table 2
Comparison of Experimental -Numerical-Analytical Results for Experimental Specimens

S. No	Name of Model	Capacity of Section (kN)				
		Experimental	Numerical	Analytical		
				IS Code [30]	Euro [31]	AISC [26]
1	SR80-SA-Num	109.04	107	108.55 (F)	108.55 (F)	121.3 (F)
2	SR100-SA-Num	100.1	95.8	95.4 (F)	95.4 (F)	108.82 (F)
3	SR120-SA-Num	75.072	81.7	77.7 (F)	77.7 (F)	95.21 (F)
4	SR80-BAC-Num	188.237	186.87	180.1 (F)	180.15 (F)	177.55 (TF)
5	SR100-BAC-Num	171.1	169.26	-	-	-
6	SR100-BAC-Im-Num	-	133.22	145 (F)	145.03 (F)	136.46 (TF)
7	SR120-BAC-Num	81.81	82.47	-	-	-
8	SR120-BAC-Im-Num	-	97.271	111.8 (F)	111.8 (F)	97.04 (TF)

4.4. Parametric study

The parameters varied are: (a) Slenderness ratio – 80, 100 & 120; (b) Spacing of connectors – according to AISC specifications, spacing equal to (¾)L times the ratio of r_{min} of single angle to Bi-Angled cruciform section and L times the ratio of r_{min} of single angle to Bi-Angled cruciform section, where L is length of full section; (c) Number of bolts per connector – 4 & 6; (d) Width to thickness ratio (represented as Wt.R) of angle section – 6.7, 10 & 15. Fig. 19 shows, specimens with different spacing of connectors and number of bolts per connector used in the parametric study. A total of thirty-six models were thus developed and analyzed to figure out the influence of the considered parameters on capacity and load sharing rate. The list of various models along with their capacities obtained from codal predictions and numerical are mentioned in the Table 3.

Table 3
Consolidated Results for all Parametric models

S.No	Model	L (mm)	Theoretical Capacity in kN				Avg Stress in MPa	Num-Cap (kN)	Axial Stiffness (kN/mm)
			IS Code	Euro Code	AISC 360-16				
			FB	FB	FB	TFB			
1	SR80-TFS-4B-Wt.R.6.7	1200	180.1	180.2	212.9	177.6	200	186.8 (F)	122.77
2	SR80-TFS-4B-Wt.R.10	1552	191.1	191.1	226.4	190.9	215	191.2 (F)	104.93
3	SR80-TFS-4B-Wt.R.15	2368	291.7	291.6	354.5	288.6	325	274.4 (F)	96.25
4	SR80-TFS-6B-Wt.R.6.7	1200	180.1	180.2	212.9	177.6	200	190.8 (F)	124.75
5	SR80-TFS-6B-Wt.R.10	1552	191.1	191.1	226.4	190.9	215	195.6 (F)	105.68
6	SR80-TFS-6B-Wt.R.15	2368	291.7	291.6	354.5	288.6	325	290.8 (F)	105.84
7	SR80-S-4B-Wt.R.6.7	1200	180.1	180.2	212.9	154.2	173.6	172.9 (F)	119.58
8	SR80-S-4B-Wt.R.10	1552	191.1	191.1	226.4	164.8	185.6	171.5 (F)	96.8
9	SR80-S-4B-Wt.R.15	2368	291.7	291.6	354.5	248.5	279.8	264.2 (F)	93.85
10	SR80-S-6B-Wt.R.6.7	1200	180.1	180.2	212.9	154.2	173.6	176.8 (F)	121.76
11	SR80-S-6B-Wt.R.10	1552	191.1	191.1	226.4	164.8	185.6	187.7 (F)	102.91
12	SR80-S-6B-Wt.R.15	2368	291.7	291.6	354.5	248.5	279.8	271.9 (F)	101.57
13	SR100-TFS-4B-Wt.R.6.7	1500	145	145	181.3	136.5	143.7	133.2 (F)	95.61
14	SR100-TFS-4B-Wt.R.10	1940	150.2	150.7	192.1	143.7	151.3	154.1 (F)	78.41
15	SR100-TFS-4B-Wt.R.15	2960	229.9	229.7	293.1	211.2	222.3	228.9 (F)	78.01
16	SR100-TFS-6B-Wt.R.6.7	1500	145	145	181.3	136.5	143.7	144.7 (F)	98.79
17	SR100-TFS-6B-Wt.R.10	1940	150.2	150.7	192.1	143.7	151.3	166.6 (F)	81.611
18	SR100-TFS-6B-Wt.R.15	2960	229.9	229.7	293.1	211.2	222.3	240.8 (F)	82.17
19	SR100-S-4B-Wt.R.6.7	1500	145	145	181.3	106.9	112.5	123.4 (F)	92.89
20	SR100-S-4B-Wt.R.10	1940	150.2	150.7	192.1	112.6	118.5	139.8 (F)	77.19

21	SR100-S-4B-Wt.R.15	2960	229.9	229.7	293.1	169.2	178.1	211.1 (F)	76.12
22	SR100-S-6B-Wt.R.6.7	1500	145	145	181.3	106.9	112.5	137.4 (F)	96.002
23	SR100-S-6B-Wt.R.10	1940	150.2	150.7	192.1	112.6	118.5	142.4 (F)	81.02
24	SR100-S-6B-Wt.R.15	2960	229.9	229.7	293.1	169.2	178.1	217.1 (F)	81.32
25	SR120-TFS-4B-Wt.R.6.7	1800	111.8	111.9	141.7	97.04	66.9	97.2 (TF)	77.29
26	SR120-TFS-4B-Wt.R.10	2328	118.1	118.1	149.6	99.49	68.6	104.1 (TF)	62.42
27	SR120-TFS-4B-Wt.R.15	3552	180.2	180.1	228.2	144.9	99.9	161.0 (TF)	61.25
28	SR120-TFS-6B-Wt.R.6.7	1800	111.8	111.9	141.7	97.04	66.9	106.2 (TF)	81.45
29	SR120-TFS-6B-Wt.R.10	2328	118.1	118.1	149.6	99.49	68.6	109.9 (TF)	65.02
30	SR120-TFS-6B-Wt.R.15	3552	180.2	180.1	228.2	144.9	99.9	167.4 (TF)	65.74
31	SR120-S-4B-Wt.R.6.7	1800	111.8	111.9	141.7	68.57	47.3	96.0 (TF)	76.73
32	SR120-S-4B-Wt.R.10	2328	118.1	118.1	149.6	70.9	48.9	96.7 (TF)	61.33
33	SR120-S-4B-Wt.R.15	3552	180.2	180.1	228.2	106.4	73.4	152.1 (TF)	59.93
34	SR120-S-6B-Wt.R.6.7	1800	111.8	111.9	141.7	68.57	47.3	100.6 (TF)	79.221
35	SR120-S-6B-Wt.R.10	2328	118.1	118.1	149.6	70.9	48.9	100.9 (TF)	64.25
36	SR120-S-6B-Wt.R.15	3552	180.2	180.1	228.2	106.4	73.4	156.2 (TF)	64.89

Wt.R - Width/Thickness Ratio; for Wt.R 6.7 ISA40X40X6, Wt.R 10 ISA 50X50X5, Wt.R 15 ISA 75X75X5 were used; TFS - (3/4)*Spacing & S - Spacing (S); 4B - 4 Bolts per each cleat angle, 6B - 6 Bolts per each cleat angle; L – Length of the model; C/C-C – Centre to Centre of connectors.

From Fig. 20 (a) to Fig. 20 (c) it is seen that the load vs lateral displacement behavior varies with spacing of connectors as well as the number of bolts per connector. For any slenderness ratio and width to thickness ratio of 6.7, sections with TFS (3/4 spacing) and six bolts per connector takes highest load due to low slenderness ratio of each segment and longer load transfer path. The effect of width to thickness ratio is depicted in Fig. 20 (d) which shows the stress vs lateral displacement for the SR80 specimen with TFS (3/4 spacing) and four bolts per connector at various width to thickness ratios. It clearly seen that the stiffness of model decreases with the increase in the width to thickness ratio since stiffness of individual angle leg tends to reduce with increasing width to thickness ratio, leading to reduction in the overall stiffness of the section.

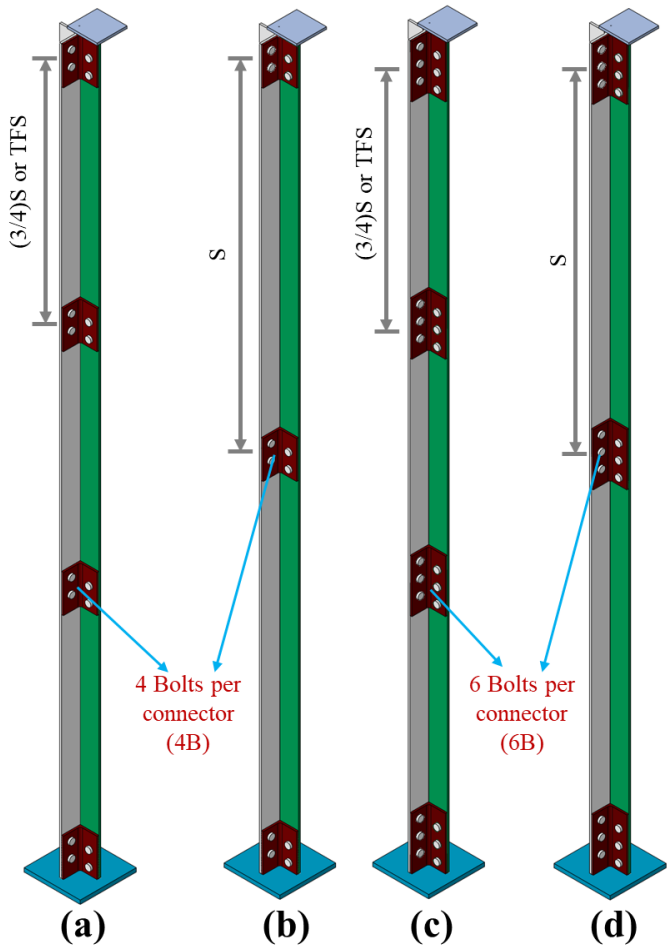

Fig. 19 (a) Various Cruciform sections in parametric study; (a) (¾)S with 4 bolts per connector, (b) "S" with 4 bolts per connector, (c) (¾)S with 6 bolts per connector, (d) "S" with 6 bolts per connector

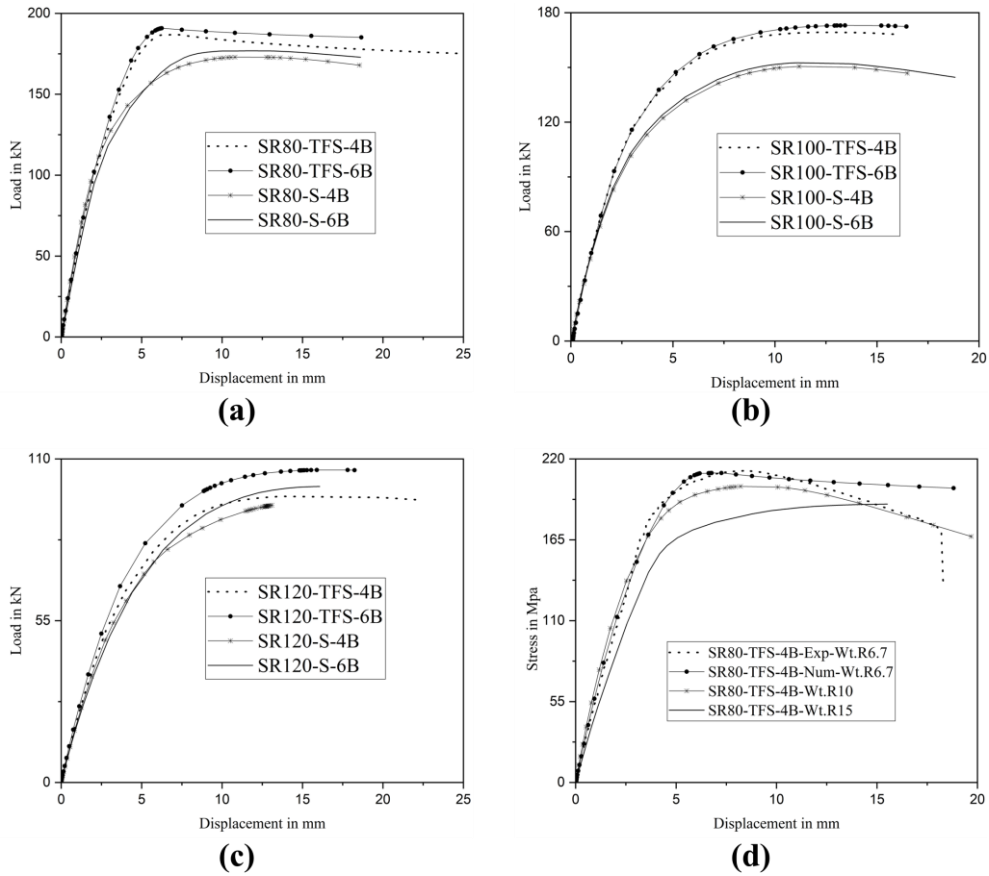

Fig. 20 (a) Load vs Lateral Displacement for 80 Slender and width to thickness ratio of 6.7; (b) Load vs Lateral Displacement for 100 Slender and width to thickness ratio of 6.7; (c) Load vs Lateral Displacement for 120 Slender and Wt.R6.7; (d) Stress vs Lateral Displacement for SR80 with various width to thickness ratios

Table 3 also shows the axial stiffness (kN/mm) for all parametric study models. For specimens of same slenderness, compared to other parameters, it was noticed from the results that the axial stiffness is highly influenced by variation in width to thickness ratio. As an example, for SR80-TFS-4B model and width to thickness ratio of 6.7, stiffness is 122.77 kN/mm whereas it reduces to 104.93 kN/mm and 96.25 kN/mm for width to thickness ratio of 10 and width to thickness ratio of 15 respectively. There is slight reduction in the stiffness observed for any model when spacing of connectors increased from TFS (¾ S) to S, and slight increase in stiffness when number bolted increased from 4 to 6. Axial stiffness of models with TFS-4B-Wt.R6.7 reduces from 122.77 kN/mm for SR80 to 95.61 kN/mm for SR100 and its further reduces to 77.29 for SR120, showing that slenderness ratio influences the axial stiffness considerably.

4.5. Load sharing rate

One of the major objectives of study was to investigate the load transferring mechanism from the Existing Member (EM) to Reinforcing Member (RM) through the cleat angles. The stress transmission from EM to RM is clearly observed from Fig. 21 in the axial direction for all cruciform specimens. All figures show EM on the right hand side and RM on the left hand side. It is clearly visible that stress in EM reduces from top to bottom, whereas for RM it increases. It is observed that the high stress which is present in the top segment of EM (Fig. 21) reduces with increase in the slenderness ratio, which is due to reduction in the capacity of the specimen with increase in slenderness ratio. The three rows in Fig. 22 show the cross-sectional stress variation among the EM and RM at mid-height of each segment for SR 80, SR 100 and SR 120 for width to thickness ratio of 6.7.

Field output values by probing S33 (in axial direction) was extracted for every element at the mid height cross section of each segment and then multiplied by the element cross-sectional area which provides the total load at the cross-section in a particular member (EM or RM). As an example, for 80SR-TFS-4B-Wt6.7, the load sharing details are mentioned in Table 4. The load sharing at the bottom segment is of utmost interest for practical purpose, hence Table 5, Table 6 and Table 7 show the consolidated load sharing only at the bottom segment of all specimens of 80SR, 100SR and 120SR respectively.

4.5.1. Effect of connector spacing on load sharing

From Fig. 23 it is clear that, for models with same slenderness ratio and number of bolts per connector, there is a reduction in percentage of load transferring from EM to RM in models with connector spacing of S when compared with TFS (3/4 Spacing). Percentage reduction of load sharing for models with spacing S varies from an average of 19.9% to a maximum of 29.9%. The individual segments slenderness ratio is high in the models with spacing S, when compared with the models with TFS, which is the plausible reason for less load transferring in models with spacing S.

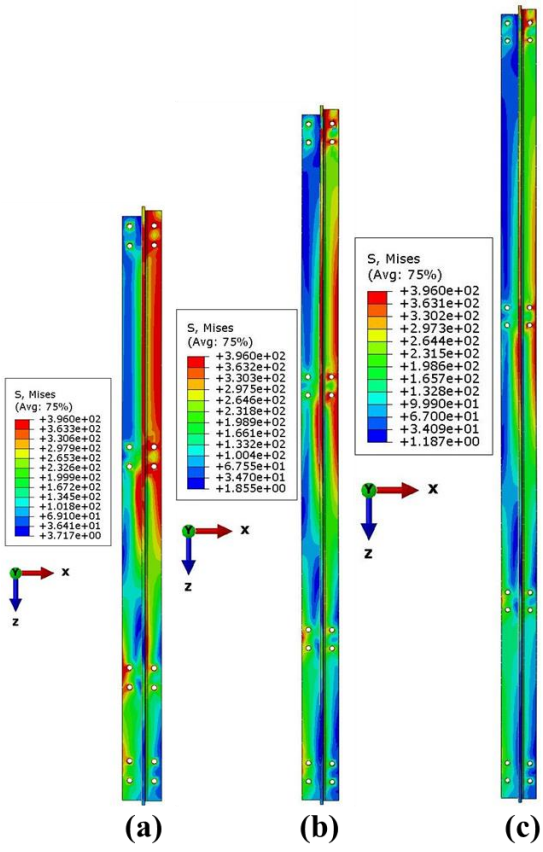

Fig. 21 Variation of Stresses in the EM & RM in longitudinal direction (a) SR80; (b) SR100; (c) SR120

4.5.2. Effect of bolts per connector on load sharing

There is a considerable influence of the number of bolts per connector in the load sharing between the EM and RM. This can be observed in Fig. 23 by comparing any two bar columns with different bolts per connector and all other parameters same. There is an average increase of 19.29% to maximum of 35.7% of load sharing happens in models with 6B (six bolts per connector) than compared to models with 4B (four bolts per connector). The cumulative intensity of bolt pre-tension force is more in models with 6B, which establishes a greater bearing resistance between the EM and RM than models with 4B, which may lead to higher load sharing for 6B models.

4.5.3. Effect of slenderness ratio on load sharing

It is clear from Fig. 23 that for any combination of parameters with increase in slenderness ratio load sharing reduces. Average of 6.52% to a maximum of 12.8% reduction in load sharing for 100 slenderness specimens observed compared to 80 slender specimens. It is about 28.2% average to 35.06% maximum for 120 slenderness compared to 100 slenderness specimens. SR120 specimen's flexural torsional type of failure which differs from failure mode of SR80 and SR100 (Flexural mode) causes the lower load sharing rate. In addition, segmental slenderness ratio for SR120 specimen is higher than in other two specimens.

Table 4
Load Sharing of 80SR-TFS-4B-Wt6.7 (80SR Exp)

Location @mm	Load		Percentage of Load in RM
	Existing Member (EM)	Reinforcing Member (RM)	
Top of EM	185.33		
Top Segment @ 305	142.86	43.52	23.35%
Middle Segment @755	122.06	65.08	34.78%
Bottom Segment @1055	83.43	102.03	55.02%

Table 5
Load Sharing between the EM & RM at Mid height of last segment for 80SR specimens

S. No	Model	Total Capacity in kN	Load Sharing in kN		Percentage of Load in RM
			Existing Member (EM)	Reinforcing Member (RM)	
1	80SR-TFS-4B- Wt.R.6.7	186.87	83.43	102.03	54.60%
2	80SR-TFS-6B-Wt.R.6.7	190.89	76.56	114.14	59.90%
3	80SR-S-4B-Wt.R.6.7	172.93	99.13	73.61	42.57%
4	80SR-S-6B-Wt.R.6.7	176.869	92.75	83.40	47.15%
5	80SR-TFS-4B-Wt.R.10	191.23	99.67	91.19	47.68%
6	80SR-TFS-6B-Wt.R.10	195.648	94.79	98.70	50.45%
7	80SR-S-4B-Wt.R.10	171.55	113.38	60.52	35.28%
8	80SR-S-6B-Wt.R.10	187.74	108.90	80.92	43.10%
9	80SR-TFS-4B-Wt.R.15	274.478	167.00	107.72	39.25%
10	80SR-TFS-6B-Wt.R.15	290.852	153.07	136.91	47.07%
11	80SR-S-4B-Wt.R.15	264.242	188.32	73.33	28.97%
12	80SR-S-6B-Wt.R.15	271.954	168.59	102.43	37.66%

Table 6
Load Sharing between the EM & RM at Mid height of last segment for 100SR specimens

S. No	Model	Total Capacity in kN	Load Sharing in kN		Percentage of Load in RM
			Existing Member (EM)	Reinforcing Member (RM)	
1	SR100-TFS-4B-Wt.R.6.7	133.22	67.46	67.70	50.82%
2	SR100-TFS-6B-Wt.R.6.7	144.78	61.53	82.90	57.40%
3	SR100-S-4B-Wt.R.6.7	123.45	74.46	47.35	38.36%
4	SR100-S-6B-Wt.R.6.7	137.415	74.57	64.01	46.58%
5	100SR-TFS-4B-Wt.R.10	154.197	84.07	68.76	44.59%
6	100SR-TFS-6B-Wt.R.10	166.695	87.55	77.96	46.77%
7	100SR-S-4B-Wt.R.10	139.83	91.73	47.23	33.78%
8	100SR-S-6B-Wt.R.10	142.483	84.78	56.41	39.59%
9	100SR-TFS-4B-Wt.R.15	228.616	142.61	83.67	36.60%
10	100SR-TFS-6B-Wt.R.15	240.884	133.70	106.54	44.23%
11	100SR-S-4B-Wt.R.15	211.164	149.24	61.18	27.75%
12	100SR-S-6B-Wt.R.15	217.104	145.38	71.30	32.84%

4.5.4. Effect of width to thickness ratio on load sharing:

From the results, it is found that for any slenderness ratio there is considerable reduction in the load sharing rate with increase in the width to thickness ratio of the angle legs. For example in case of SR80 with TFS spacing and 4B connectors for Wt.R 6.7 the load sharing rate is 55.02% where for the Wt.R 15 load sharing is 39.12%. From Fig. 23 for any set of other constant parameters

with increase in width to thickness ratio from 6.7 to 10, it was observed that average of 14.45% to maximum of 22.31% reduction in load sharing happened. Similarly, for width to thickness ratio of 10 to 15 there is 14.06% average to 21.34% reduction in load sharing can be seen.

Table 7
Load Sharing between the EM & RM at Mid height of last segment for 120SR specimens

S. No	Model	Total Capacity in kN	Load Sharing in kN		Percentage of Load in RM
			Existing Member (EM)	Reinforcing Member (RM)	
1	120SR-TFS-4B-Wt.R 6.7	97.271	63.20	33.84	34.79%
2	120SR-TFS-6B-Wt.R.6.7	106.247	63.20	44.25	41.65%
3	120SR-S-4B-Wt.R.6.7	96.053	70.25	26.74	27.84%
4	120SR-S-6B-Wt.R.6.7	100.644	64.37	33.89	33.67%
5	120SR-TFS-4B-Wt.R.10	104.124	73.23	30.15	28.96%
6	120SR-TFS-6B-Wt.R.10	109.995	69.84	39.24	35.67%
7	120SR-S-4B-Wt.R.10	96.724	75.75	22.09	22.84%
8	120SR-S-6B-Wt.R.10	100.922	68.87	30.98	30.69%
9	120SR-TFS-4B-Wt.R.15	161.034	121.43	38.64	23.99%
10	120SR-TFS-6B-Wt.R.15	167.419	118.56	48.43	28.93%
11	120SR-S-4B-Wt.R.15	152.144	119.93	32.04	21.06%
12	120SR-S-6B-Wt.R.15	156.259	107.00	42.27	27.05%

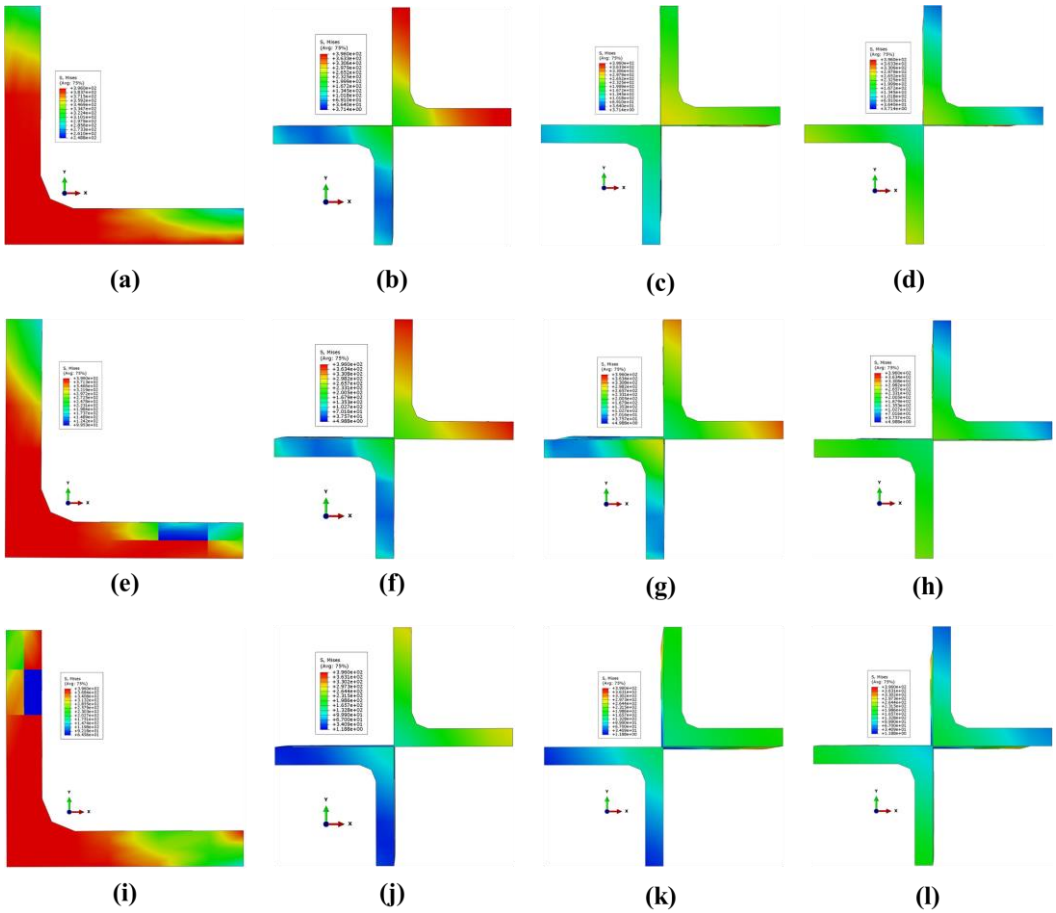

Fig. 22 Stress distribution in between EM & RM at various cross – sections top to bottom (left to right) for Wt.R.6.7; (a) to (d) – SR80-TFS-4B; (e) to (h) – SR100-TFS-4B; (i) to (l) – SR120-TFS-4B

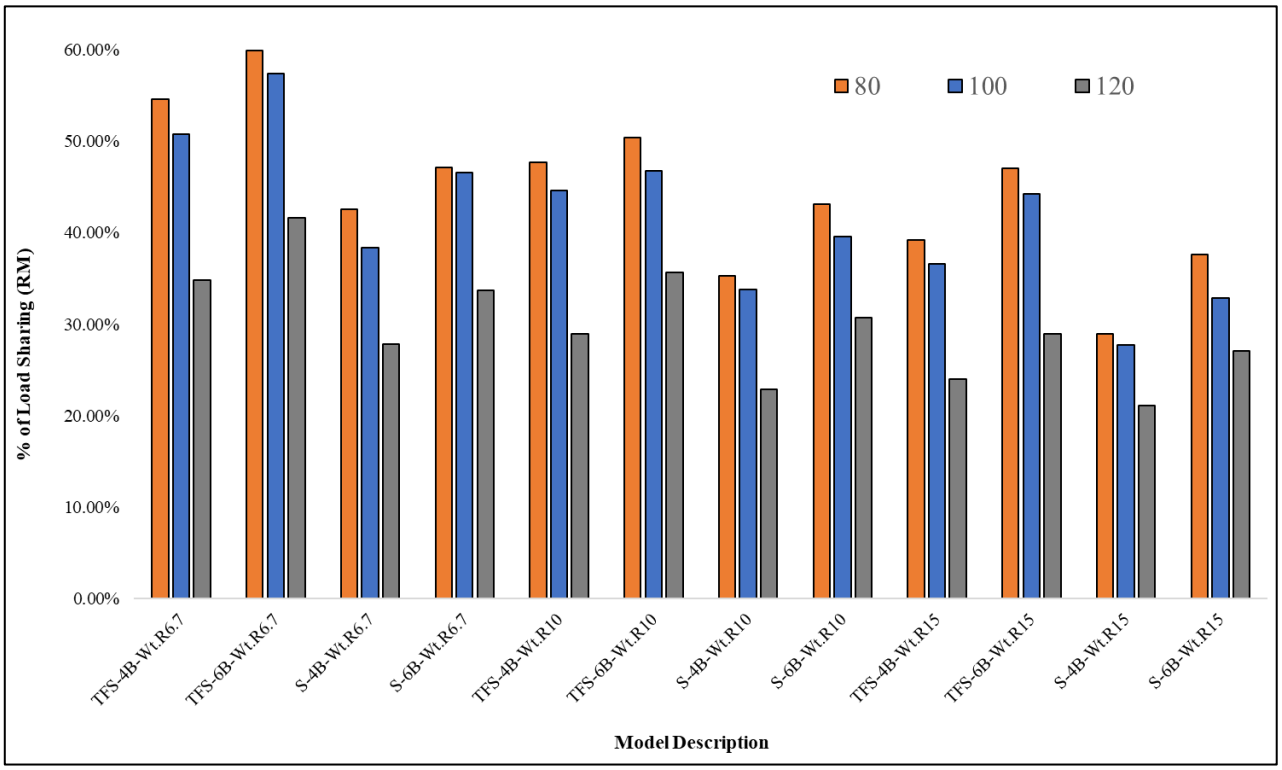

Fig. 23 Variation of Percentage of Load Carrying by RM with Various Slenderness Ratio

5. Conclusions

In the present study, the behavior of Bi-Angled Cruciform (BAC) sections made by connecting two angle sections vertex to vertex were tested for three different slenderness ratio (80, 100 and 120) under compression through one angle. Numerical models developed in ABAQUS were validated with the experimental results followed by a parametric study with 36 models to investigate the effect of various parameters, namely, slenderness ratio, spacing of connectors, number of bolts per connector and width to thickness ratio. The experimental and numerical capacities were also compared with codal predictions using Indian Standard, Euro Code and AISC specifications. The load sharing between the EM and RM is the key result to show the application of the retrofit arrangement. The following conclusions can be drawn:

i. These bi-angled cruciform provide 20% to 83% increase in capacity as single angles of same slenderness as against 100% increase expected theoretically. The increase percentage decreases with overall specimen slenderness. However, this increase in capacity shows that the cruciform arrangement is capable as a quick in-situ solution for intervention.

ii. The experiment (SR100-BAC) where the top loading plate attained contact with RM shows that there is a significant difference in capacity (21%) in comparison with cruciform loaded through the centroid of EM which transfer loads via the connectors to RM. This difference is not significant at lower slenderness (SR80).

iii. All models of SR80 and SR100 failed by flexural buckling while SR120 models fail in flexural-torsional mode. Consequently, IS and Euro code prediction were close to the numerically obtained values when using flexural buckling equation. The AISC code which contains a slenderness factor (K_i) for built-up sections over predicts the flexural buckling capacity.

iv. From the diagrams, the transfer of load from EM to RM is shown to be more efficient in cruciform arrangement for lower slenderness. For higher slenderness, improvements can be obtained with more fasteners per connection and/or lower inter-connection spacing. The load-sharing rate ranges from 20% in the top segments to up to 50% at the bottom most segments highlighting the importance of the connection arrangements in achieving the required load sharing.

v. From the conducted parametric study results, the influence of parameters can be ranked in descending order as follows: overall slenderness, angle leg width to thickness ratio, spacing of connectors and lastly, bolts per connector. On overall load sharing in SR120 specimens is only 35%, and width to thickness ratio 15 leads to sharing rate as low as 22%. Therefore, these parameters can be chosen carefully to achieve efficient load transfer in the built-up cruciform for the retrofit.

vi. The ideal load sharing rate in any retrofitting technique is 50% each in Existing Member (EM) and Reinforcing Member (RM). From the results it is seen that this is achieved only at lower slenderness ratio (80) and low width to thickness ratio (6.7) and when employing TFS-spacing for connectors. The load share in the RM falls below 50% at the same slenderness ratio when the connector spacing is S. For the two higher slenderness ratios (100 and 120) the load share in RM does not reach 50% for any case, even though in all cases the TFS-spacing resulted in the higher load share in RM. Therefore AISC 360-16 [26] recommendation pertaining to maximum connector spacing shall be followed in order to achieve the maximum possible load share in RM, though this will not always result in 50% load share.

Consideration of the preload in Existing Member (EM) before addition of the Reinforcing Member (RM) and influence of the preload on the overall built-up section can be taken as future scope of research.

Nomenclature

SA	Single Angle	f_y	Characteristic yield stress (IS 800)
BAC	Bi-Angled Cruciform section	λ	non-dimensional effective slenderness ratio (IS 800)
SR 80	Slenderness Ratio of 80, Similarly for SR100 and SR 120	α	Imperfection factor (IS 800 & EN 1993-1-1:2005)
TFS	Center to center connector spacing equal to "(¾)*L times the ratio of r_{min} of single angle to Bi-Angled cruciform section"	N_b, R_d	Design buckling resistance of compression member (EN 1993-1-1:2005)
S	Center to center connector spacing equal to "L times the ratio of r_{min} of single angle to Bi-Angled cruciform section"	χ	Reduction factor (EN 1993-1-1:2005)

4B	4 Bolts per one angle cleat	$\bar{\lambda}$	Non-dimensional slenderness (EN 1993-1-1:2005)
6B	6 Bolts per one angle cleat	N_{cr}	Elastic critical force (EN 1993-1-1:2005)
Wt.R 6.7	Width to thickness ratio of 6.7 for angle, similarly Wt.R 10 and Wt.R 16	L_c	Effective Length (EN 1993-1-1:2005)
A	Cross-sectional area of SA or BAC	I	Moment of Inertia (EN 1993-1-1:2005)
I_x/I_y	Moment of Inertia about x-x axis/y-y axis	P_n	Nominal axial strength (AISC 360-16)
I_{xy}	Product of Inertia	F_{cr}	Critical stress (AISC 360-16)
I_{min}	Minimum moment of Inertia	A_g	Gross area of member (AISC 360-16)
r_{min}	Minimum radius of gyration	F_y	Specified minimum yield stress (AISC 360-16)
SR	Slenderness Ratio	F_e	Elastic buckling stress (AISC 360-16)
L	Length of SA/BAC specimens	$(Lc/r)_m$	Modified slenderness ratio for built-up section (AISC 360-16)
P_d	Design compressive strength (IS 800)	C_w	Warping Constant (AISC 360-16)
A_e	effective sectional area (IS 800)	L_{cz}	Effective length of member for buckling about longitudinal axis (AISC 360-16)
f_{cd}	Design compressive stress (IS 800)		

References

[1] A. H. A. Abdelrahman, Z.-L. Du, Y.-P. Liu, and S.-L. Chan, "Stability design of single angle member using effective stress-strain method," Structures, vol. 20, pp. 298–308, Aug. 2019, doi: 10.1016/j.istruc.2019.04.013.

[2] W.-Q. Jiang, Y.-P. Liu, S.-L. Chan, and Z.-Q. Wang, "Direct Analysis of an Ultrahigh-Voltage Lattice Transmission Tower Considering Joint Effects," Journal of Structural Engineering, vol. 143, no. 5, May 2017, doi: 10.1061/(ASCE)ST.1943-541X.0001736.

[3] A. Hussain, Y.-P. Liu, and S.-L. Chan, "Finite Element Modeling and Design of Single Angle Member Under Bi-axial Bending," Structures, vol. 16, pp. 373–389, Nov. 2018, doi: 10.1016/j.istruc.2018.11.001.

[4] E. Murtha-Smith and H. R. Adibjahromi, "Restrained Warping in Cruciform Compression Members," Journal of Structural Engineering, vol. 114, no. 1, pp. 198–210, Jan. 1988, doi: 10.1061/(ASCE)0733-9445(1988)114:1(198).

[5] M. C. Temple, S. S. S. Sakla, D. Stchyrba, and D. Ellis, "Arrangement of interconnectors for starred angle compression members," Canadian journal of civil engineering, vol. 21, no. 1, 1994, doi: 10.1139/l94-007.

[6] I. S. Botelho et al., "Starred rolled stainless steel angle sections under compression: An experimental and numerical investigation," Thin-Walled Structures, vol. 158, Jan. 2021, doi: 10.1016/j.tws.2020.107177.

[7] J. ke Han, C. lei Zhang, Z. bao Li, and X. ming Wang, "Stability analysis of closely star-battened member of transmission tower," International Journal of Steel Structures, vol. 17, no. 3, pp. 949–956, Sep. 2017, doi: 10.1007/s13296-017-9007-8.

[8] B. Li, P. Cao, D. Zhang, and Y. Guo, "Experimental research on behavior of Q420 dual-angle steel with cruciform section under dynamic compression," Journal of Vibroengineering, vol. 19, no. 3, pp. 2031–2042, 2017, doi: 10.21595/jve.2016.17794.

[9] R. Balagopal, N. Prasad Rao, R. P. Rokade, and P. K. Umesha, "Studies on strengthening techniques for existing transmission line and communication towers," in Lecture Notes in Civil Engineering, vol. 12, Springer, 2019, pp. 639–648. doi: 10.1007/978-981-13-0365-4_54.

[10] N. Ungkurapinan, S. R. D. S. Chandrakeerthy, R. K. N. D. Rajapakse, and S. B. Yue, "Joint slip in steel electric transmission towers," Eng Struct, vol. 25, no. 6, pp. 779–788, 2003, doi: 10.1016/S0141-0296(03)00003-8.

[11] E. Baran, T. Akis, G. Sen, and A. Draisawi, "Experimental and numerical analysis of a bolted connection in steel transmission towers," J Constr Steel Res, vol. 121, pp. 253–260, Jun. 2016, doi: 10.1016/j.jcsr.2016.02.009.

[12] C. Lu, X. Ma, and J. E. Mills, "The structural effect of bolted splices on retrofitted transmission tower angle members," J Constr Steel Res, vol. 95, pp. 263–278, Apr. 2014, doi: 10.1016/j.jcsr.2013.12.011.

[13] F. Albermani, M. Mahendran, and S. Kitipornchai, "Upgrading of transmission towers using a diaphragm bracing system," Eng Struct, vol. 26, no. 6, pp. 735–744, May 2004, doi: 10.1016/j.engstruct.2004.01.004.

[14] Q. Xie and L. Sun, "Failure mechanism and retrofitting strategy of transmission tower structures under ice load," J Constr Steel Res, vol. 74, 2012, doi: 10.1016/j.jcsr.2012.02.003.

[15] Y. Zhuge, J. E. Mills, and X. Ma, "Modelling of steel lattice tower angle legs reinforced for increased load capacity," Eng Struct, vol. 43, pp. 160–168, Oct. 2012, doi: 10.1016/j.engstruct.2012.05.017.

[16] J. E. Mills, X. Ma, and Y. Zhuge, "Experimental study on multi-panel retrofitted steel transmission towers," J Constr Steel Res, vol. 78, pp. 58–67, Nov. 2012, doi: 10.1016/j.jcsr.2012.06.004.

[17] V. K. Shukla, M. Selvaraj, and K. V. Kumar, "Failure Analysis of a Cruciform-Leg Transmission Line Tower," International Journal of Steel Structures, vol. 21, no. 2, pp. 539–548, Apr. 2021, doi: 10.1007/s13296-021-00454-5.

[18] C. Lu, X. Ma, and J. E. Mills, "Modeling of retrofitted steel transmission towers," J Constr Steel Res, vol. 112, pp. 138–154, Sep. 2015, doi: 10.1016/j.jcsr.2015.04.005.

[19] L. Sun, M. Trovato, and B. Stojadinović, "In-situ retrofit strategy for transmission tower structure members using light-weight steel casings," Eng Struct, vol. 206, 2020, doi: 10.1016/j.engstruct.2020.110171.

[20] X. Guo, S. Zong, Z. Shen, S. Zhu, and S. Yuan, "Mechanical behavior of in-service axial compression angle steel members strengthened by welding," Journal of Building Engineering, vol. 32, Nov. 2020, doi: 10.1016/j.jobe.2020.101736.

[21] B. Mou, Y. Zhou, Q. Qiao, and J. Liu, "Compressive behavior of bolted built-up steel columns fabricated using angle section columns," Journal of Building Engineering, vol. 44, Dec. 2021, doi: 10.1016/j.jobe.2021.103260.

[22] G. Liang, L. Wang, Y. Liu, and N. Geng, "Mechanical behavior of steel transmission tower legs reinforced with innovative clamp under eccentric compression," Eng Struct, vol. 258, May 2022, doi: 10.1016/j.engstruct.2022.114101.

[23] Q. Xie and J. Zhang, "Experimental study on failure modes and retrofitting method of latticed transmission tower," Eng Struct, vol. 226, 2021, doi: 10.1016/j.engstruct.2020.111365.

[24] A. M. Taha, M. A. Dabaon, M. H. El-Boghdadi, and M. F. Hassanein, "Experimental testing and evaluation of real-scale lap-splice bolted connections used in typical lattice steel transmission towers," Thin-Walled Structures, vol. 171, Feb. 2022, doi: 10.1016/j.tws.2021.108790.

[25] "Indian Standard USE OF STRUCTURAL STEEL IN OVERHEAD TRANSMISSION LINE TOWERS-CODE OF PRACTICE IPJSRT 1 MATERIALS, LOADS AND PERMISSIBLE STRESSES Section 1 Materials and Loads," 1995.

[26] "Specification for Structural Steel Buildings," 2016.

[27] John H. Bickford, Introduction to the Design and Behavior of Bolted Joints, 4th ed. CRC Press, Taylor & Francis group, 2008.

[28] "Designation: E8/E8M − 13a Standard Test Methods for Tension Testing of Metallic Materials 1," 2019, doi: 10.1520/E0008_E0008M-13A.

[29] A. H. A. Abdelrahman, Y.-P. Liu, and S.-L. Chan, "Advanced joint slip model for single-angle bolted connections considering various effects," Advances in Structural Engineering, vol. 23, no. 10, pp. 2121–2135, Jul. 2020, doi: 10.1177/1369433220906226.

[30] B. of Indian Standards, "IS 800 (2007): General Construction In Steel - Code of Practice."

[31] "EN 1993-1-1: Eurocode 3: Design of steel structures - Part 1-1: General rules and rules for buildings."

Advanced Steel Construction – Vol. 20 No. 1 (2024) 53–59
DOI:10.18057/IJASC.2024.20.1.6

STUDY ON FLEXURAL CAPACITY OF PROFILED STEEL SHEET - POLYURETHANE SANDWICH SLABS

Wen-Tao Qiao [1, 2, *], Zhi-Yuan Huang [1], Teng Wang [3], Kai-Li Cui [1] and Li-Jun Meng [1]

[1] *School of Civil Engineering, Shijiazhuang Tiedao University, Shijiazhuang, China*
[2] *Key Laboratory of Roads and Railway Engineering Safety Control (Shijiazhuang Tiedao University), Ministry of Education, Shijiazhuang, China*
[3] *State-owned Enterprise Comprehensive Service Center of Ningjin County Finance Bureau, Xingtai, China*
** (Corresponding author: E-mail: qwt@stdu.edu.cn)*

ABSTRACT

Widely employed in enveloped structures, the metal-faced sandwich panel boasts thermal insulation, noise abatement, lightweight, and remarkable assembly efficiency. In this paper, a new type of profiled steel sheet and polyurethane sandwich slab (PSSPSS) was proposed. Through static load tests and numerical simulations, the flexural properties of the PSSPSS were studied, and the influence of individual geometric parameters on the flexural capacity of the structure was evaluated. The results of this analysis led to the derivation of the calculation formulas for the deflection and flexural bearing capacity of the PSSPSS. These results demonstrate that the bearing capacity and failure mode of the structure, as determined by test and simulation, are in perfect agreement. The sandwich slab's failure is mainly demonstrated by an overabundance of deflection, with the peak being 1/42 of the span, and the channel steel at the middle span being distorted and snapped. The slab deflection calculation formula's results, when compared to the test results, demonstrate a mere 2.1% error, thus confirming its accuracy. The slab thickness, profiled steel sheet thickness, polyurethane foam density, and slab span all contribute to higher bearing capacity and improved stiffness in the structure, yet the effect of the slab span is more evident. The slab span, however, has a more profound effect on stiffness. The flexural bearing capacity formula's applicability is indicated by the maximum error being within 10%, as demonstrated by the comparison of the formula's results with the FEA results for the sandwich slab with varying parameters.

ARTICLE HISTORY

Received: 18 May 2023
Revised: 11 October 2023
Accepted: 18 November 2023

KEYWORDS

Sandwich slab;
Channel steel;
Profiled steel sheet;
Polyurethane foam;
Flexural capacity

Copyright © 2024 by The Hong Kong Institute of Steel Construction. All rights reserved.

1. Introduction

Under the dual influence of policy guidance and market demand, various new prefabricated building systems have been proposed[1]. Now, sandwich slabs with metal materials as panels are widely used in the construction field due to their unique structure and excellent combination performance. Among them, the metal surface layer has a protective effect on the core layer, preventing it from weathering, avoiding mechanical damage, and isolating water and water vapor. The core layer can connect the two surface layers as a whole and bear the load together. When the surface layer is buckling under load, the core layer can support the surface layer and increase the buckling resistance of the surface layer, and it also has the functions of heat insulation and sound insulation[2].

Metal panels and a variety of lightweight core materials have become the ideal materials for wall panels and roof panels due to their remarkable combination advantages. Some scholars have researched the metal-faced sandwich panels and put forward relevant design theories. Noor. A.K. et al.[3] proposed three analytical models that are commonly used in the study of mechanical properties of sandwich panels. The first one is a simplified model, which is often used to solve the problems of panel wrinkles. The second one is a two-dimensional model based on Reissner theory, Hough theory, and Polushakov-Duqing Hua theory, and the two-dimensional model is more accurate and widely used. The third is a three-dimensional and quasi-three-dimensional continuum model, which uses an equivalent homogeneous segmented anisotropic body to replace panels and cores, and the analysis is the most sophisticated but also the most complex. Y.H. Mugahed. et al.[4,5] carried out a theoretical analysis on the extremes of fully composite and non-composite action of sandwich slabs and proposed a typical analysis method to determine the degree of composite action. Jongchol Choe. et al.[6-8] proposed a new one-dimensional layered model that uses Euler Bernoulli beam theory in the skin and higher-order kinematics in the core, this model can efficiently and accurately characterize the critical load and post-buckling behavior of sandwich structures. Aktham. et al.[9] proposed the FEA method for sandwich slabs under eccentric loading. Hartsock. J. A. and Chong. K. P. et al.[10-12] took the single-span simply-supported sandwich panel under uniform load and mid-span concentrated load as the research object, analyzed the bending deformation and internal force calculation, and compared with the test results, which were in good agreement. On this basis, Allen[13,14] proposed the calculation method of the mechanical properties of sandwich plates under uniform load and concentrated load. Sohel[15,16] proposed a theoretical model to predict the flexural and punching resistance and a good correlation with test results is obtained. A large deflection analysis considering plate membrane action is also proposed to predict the force-deflection relation of Steel-Concrete-Steel sandwich slabs. In addition, based on the theoretical analysis model proposed by the above scholars, some scholars have carried out a lot of analysis and research on the mechanical properties of sandwich structures and proposed different calculation models. Davies. J. M.[17-19] conducted a large number of finite element analyses on the pressed metal panel sandwich slab, and successively proposed the finite element analysis method of the bending performance of the sandwich slab and the combined action of bending and compression. The sandwich panel was divided into two parts, the flange and the core layer. The core part considered the bending deformation and shear deformation of the core, while the flange part ignored the shear deformation of the flange and only considered its bending deformation. The formula of mid-span deflection of single-span sandwich panels under uniform load and concentrated load is obtained by this approximate calculation method. Chong and Hartsoek[20] proposed and summarized the structural behavior of sandwich slabs, including flexural stresses, deflections, vibration, and thermal stresses. Russo and Zuccarello[21] carried out experimental and numerical evaluation of the mechanical behavior of sandwich structures, constituted by fiber-glass laminate skins over PVC foam or polyester mat cores. Ramtekka et al.[22,23] studied the application of a three-dimensional mixed finite element model to the flexure of a sandwich plate. Kachalla.[24,25] proposed a new method to analyze the longitudinal bearing capacity of composite slabs based on the partial shear method and the European code. Besides, Davies and Hakmi studied on local buckling behavior of foam-filled thin-walled steel sandwich beams using the effective width concept. There have been some other studies on the axial load-bearing behavior of sandwich composite panels[26-29]. In summary, a large number of studies have been conducted on the bearing capacity and deformation of sandwich roof panels and wall panels mainly through experimental research, numerical simulation, and theoretical analysis. However, due to the low bearing capacity and poor stiffness, metal-faced sandwich panels are rarely used on floors.

In view of the advantages, a new type of assembled sandwich slab structure is proposed in this paper, that is, based on the structure of metal-faced sandwich panels, the double-layer deep profiled steel sheet and channel steel are combined, and the rigid polyurethane foam material is filled as the core of the sandwich panel. In this paper, the flexural bearing capacity and parameter influence of PSSPSS were studied using experiment and finite element simulation analysis. On this basis, the calculation formulas of deflection and flexural bearing capacity of the sandwich slab were derived.

2. Structure of the slab

PSSPSS is mainly composed of profiled steel sheets, channel steel, and rigid polyurethane foam. Based on the structure of metal faced sandwich slab, the channel steel is used as the frame, the double-layer deep profiled steel plate

is used as the metal panel, and the rigid polyurethane foam material is used as the core layer of the sandwich slab. The structure of the sandwich slab is shown in Fig. 1**.**

As one of the materials with the best thermal insulation performance, rigid polyurethane foam can effectively improve the thermal insulation performance of the floor. At the same time, in the process of polyurethane foaming, the core material will automatically bond and firmly adhere to the surface layer, eliminating the procedure of spraying adhesives. In addition, the utilization of channel steel as the foundation of the floor slab not only enhances the bearing capacity and bending rigidity of the floor slab; but also facilitates the connection between the floor and the wall in assembly.

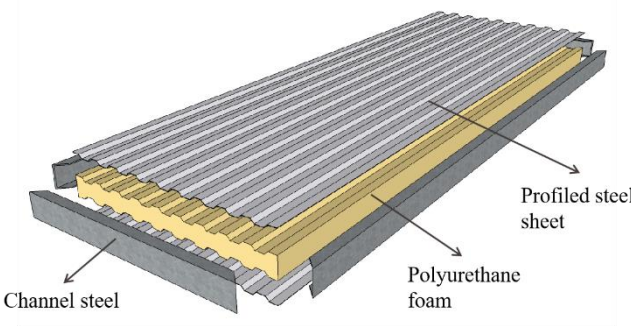

Fig. 1 Sandwich slab structure diagram

3. Experimental studies

3.1. Test specimen

In the test, a full-scale PSSPSS test piece with dimensions of 4100mm×1200mm×140mm is designed and produced. Q235 steel is the source of the profiled sheet, which is 2mm in thickness, and [14a is the channel steel. The section characteristics of the specimen are shown in Fig.2.

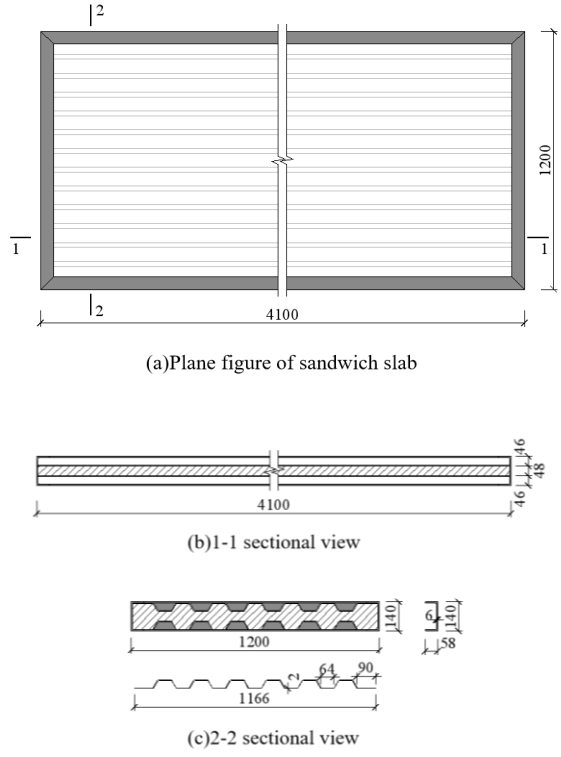

Fig. 2 Section characteristics and size of the sandwich slab

3.2. Material properties

The samples of the steel material are taken from the same batch of steel as the specimen. The steel is divided into hot-rolled steel and cold-formed steel, and each steel is divided into three groups. According to the Chinese specification GB/T228.1 - 2010[30], the tensile tests are carried out on the steel samples of steel sheet and channel steel. The test results are shown in Table 1 and Fig. 3.

Table 1
Summary of material properties

Specimen	Yield strength/MPa	Tensile strength/MPa
SS-1	270	360
SS-2	273.8	365
SS-3	277.5	370
Average	273.75	365
CS-1	282	376
CS-2	273.75	365
CS-3	287.25	383
Average	281	375

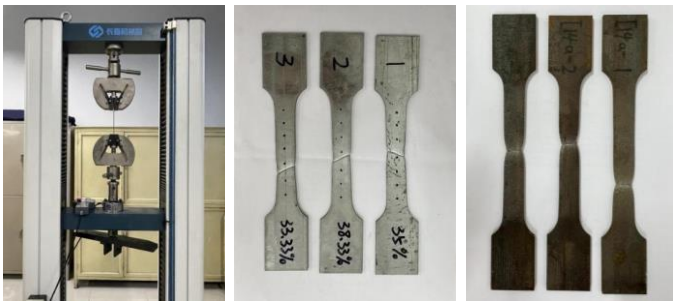

(a)Test device (b)Steel sheet after tensile test (c) Channel steel after tensile test

Fig. 3 Steel tensile test

The material properties of rigid polyurethane foam refer to the relevant provisions in Chinese standards GB / T 21558 - 2008[31] and GB / T 8813 - 2020[32], and are calculated according to the formula in Reference [33], the formulas are as follows:

Elastic modulus:

$$E = 4.6 \times (\rho / 38)^2 \tag{1}$$

Shear modulus:

$$G = 1.725 \times (\rho / 38)^2 \tag{2}$$

Compressive strength:

$$f_y = 0.15 \times (\rho / 38)^{3/2} \tag{3}$$

Shear strength:

$$f_y = 0.078 \times (\rho / 38)^{3/2} \tag{4}$$

After calculation, the properties of polyurethane foam can be obtained, as shown in Table 2.

Table 2
Mechanical properties of rigid polyurethane foam

Compressive strength/MPa	Compression modulus/MPa	Shear strength/MPa	Shear modulus/MPa	Poisson's ratio
0.38	15.61	0.20	5.85	0.3

3.3. Loading device and procedure

In the test, the self-balancing gantry reaction frame and the hydraulic actuator are used to apply a load, and the monotonic static force is evenly

distributed at the third point positions of the sandwich slab through the secondary distribution beam. To avoid the load-acting direction not perpendicular to the test piece plane due to the downward deflection of the specimen, the single-span hinge supports are placed at both ends of the distribution beam. Both ends of the specimen are equipped with sliding and fixed hinge supports to ensure that the sandwich floor can move horizontally. Among them, a round steel with a diameter of 50mm is in direct contact with the steel sheet as the sliding hinge support and another round steel is welded to the steel sheet as the fixed hinge support. At the same time, 20mm steel plates are placed at the supports of the sandwich slab to avoid local damage to the specimen caused by stress concentration. The test loading device is shown in Fig. 4 and Fig. 5

Before the test was officially loaded, 10 kN was applied for preloading to check whether the supports and all the instruments were working properly, and then the test was officially loaded after unloading. The load control method was used for staged loading, and before the maximum deflection of the sandwich slab reached 1/200 of the slab span (elastic limit stage), the load for each level was 10kN. After that, the load was applied at each level of 5 kN, and the loading was stopped until the specimen was destroyed and could not continue to bear the load. Real-time monitoring is carried out through force sensors during the test process, and test data is collected using the DHDAS dynamic signal acquisition system. When the specimen exhibits obvious failure or the beam end load drops to 85% of the peak load, it is considered specimen failure and the test is terminated.

Fig. 4 Loading device

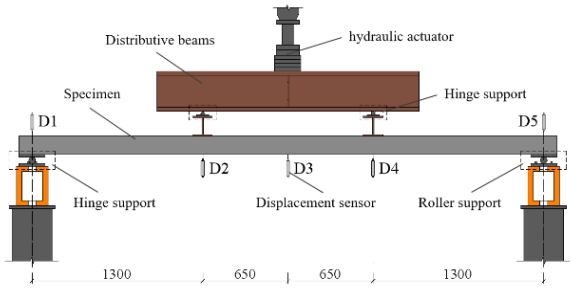

Fig. 5 Sketch of loading device

3.4. Experiment results and analysis

3.4.1. Failure process

The deflection deformation of the specimen was small at the initial stage of loading. When the load increased to 0.4*Pu*, the mid-span deflection was 19.5mm, and the deflection was 1/200 of the span, reaching the limit value of the normal service limit state of the sandwich slab. At this time, there was, a slight sound inside the sandwich slab, but the specimen had no obvious deformation, as shown in Fig. 6(a). When the load increased to about 0.7*Pu*, a continuous "creak" sound began to emit inside the specimen, the deflection of the sandwich slab grew rapidly and a significant bending deformation occurred, as shown in Fig. 6(b). Subsequently, with a small increase in the load value, the deflection of the specimen increased rapidly. When the load increased to *Pu*, the midspan deflection reached 93.4mm and the deflection was about 1/42 of the span. The midspan position of the channel steel was more affected by the bending moment, and the flange bulged outward due to local buckling, the specimen reached the ultimate bearing capacity state, as shown in Fig. 6(c).

（a）Initial state of the specimen

（b）Intermediate state of the specimen

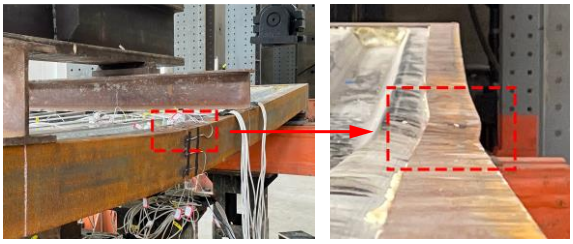

（c）Final failure state of the specimen

Fig. 6 Loading and failure process of the specimen

3.4.2. Deflection

The load-deflection curve of the sandwich slab at the midspan is shown in Fig. 7, where the load value does not include the self-weight of the specimen, and the deflection value is corrected by the displacement of the supports (the corrected deflection value = the deflection values at the midspan and the loading points minus the support displacement value).

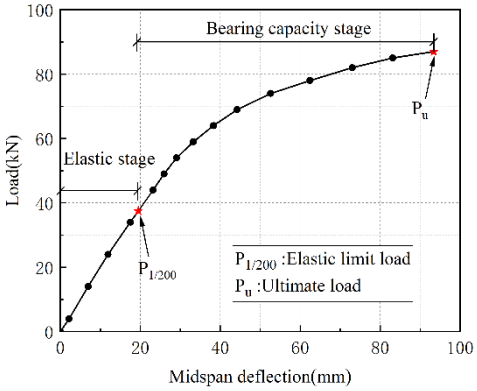

Fig. 7 Midspan load-deflection curve of sandwich slab

From the load-deflection curve at midspan, it can be seen that the load and deflection of the sandwich slab change linearly at the initial stage of loading, the stiffness of the specimen remains unchanged, about 1.9kN/mm. When the sandwich slab is loaded to the elastic limit load, the curve still maintains a linear relationship, indicating that the sandwich slab is in an elastic state during the elastic limit state. As the load increases, the channel steel at the midspan yields, the curve turns, and the stiffness of the specimen decreases slightly, the stiffness is about 1.2kN/mm, while the load value continues to rise, indicating that the profiled steel plate and the polyurethane core layer continues to function. When the specimen is damaged, the lower tensile steel sheet and the channel steel both reach the yield state.

4. Numerical simulation

4.1. Finite element model

In the model of PSSPSS, there are five main components: profiled steel .accurately simulate the actual components in the model, appropriate unit types should be selected based on their cross-sectional and material characteristics.

Based on the test, the geometric dimensions, material properties, loading scheme, and boundary conditions of the finite element model are consistent with the test specimen. In the model, the profiled steel sheet is equipped with a four-node reduced-integration shell element (S4R), while the channel steel and polyurethane sandwich has an eight-node hexahedral reduced-integration solid element (C3D8R). The core layer is made of polyurethane foam, which is closely bonded with steel sheet and channel steel to ensure cooperative work in the test, so the tie is used between the profiled steel sheet, channel steel, and core layer. In order to avoid local damage to the model caused by stress concentration, the steel backing plates are set at the loading point, and the supports, and bound with the contact of the sandwich slab. The loading point is coupled with the steel backing plate, and the two points are loaded symmetrically with displacement control. The boundary conditions at both ends of the sandwich slab are hinged, one end constrains U1, U2, U3, UR2, UR3, and the other end constrains U1, U2, UR2, UR3. Using the structured grid control method, the model is divided into regular grid cells, and the size is selected as 0.02m. The finite element model is shown in Fig. 8. Based on the test, the geometric dimensions, material properties, loading scheme, and boundary conditions of the finite element model are consistent with the test specimen. In the model, the profiled steel sheet is equipped with a four-node reduced-integration shell element (S4R), while the channel steel and polyurethane sandwich has an eight-node hexahedral reduced-integration solid element (C3D8R). The core layer is made of polyurethane foam, which is closely bonded with steel sheet and channel steel to ensure cooperative work in the test, so the tie is used between the profiled steel sheet, channel steel, and core layer. In order to avoid local damage to the model caused by stress concentration, the steel backing plates are set at the loading point, and the supports, and bound with the contact of the sandwich slab. The loading point is coupled with the steel backing plate, and the two points are loaded symmetrically with displacement control. The boundary conditions at both ends of the sandwich slab are hinged, one end constrains U1, U2, U3, UR2, UR3, and the other end constrains U1, U2, UR2, UR3. Using the structured grid control method, the model is divided into regular grid cells, and the size is selected as 0.02m. The finite element model is shown in Fig. 8.

The finite element model employs rigid polyurethane foam as an isotropic material, the ideal elastoplastic model as the constitutive model, and the double broken line model as the constitutive model of steel. Refer to Table 1 and Table 2 for each parameter.

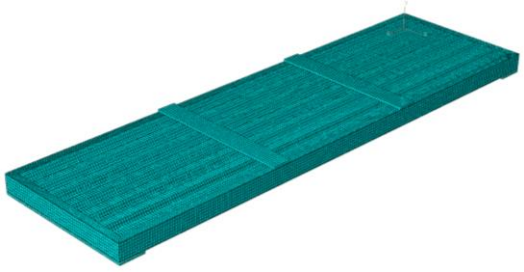

Fig. 8 Finite element model

4.2. Numerical simulation results and analysis

Table 3 displays a comparison between the test data and finite element calculations of the bearing capacity under elastic and bearing capacity limit states. Fig. 9 shows the comparison of midspan load-deflection curves of the sandwich slab obtained from FEA and test. It can be seen that the overall changing trends of the two load-deflection curves are basically the same, and the differences between the normal service load and the failure load of the two curves are all small, the differences are 5.7% and 3.3%, respectively. Due to the possible nonuniformity of the polyurethane foaming density, the uncertainty of the properties of the polyurethane material is caused, which makes the properties of the polyurethane material in the finite element model deviate from the test piece. Secondly, the boundary conditions in the finite element model cannot be guaranteed to be completely consistent with the support conditions in the test, and the manual data collection will also cause a deviation in the results. Finally, there are errors between the finite element simulation results and the experimental results.

Table 3
Comparison of experimental and numerical simulation results

Bearing capacity	Test value/kN	numerical simulation value/kN	Ratio/%
$P_{1/200}$	37.50	35.49	5.70
P_u	87.00	84.34	3.20

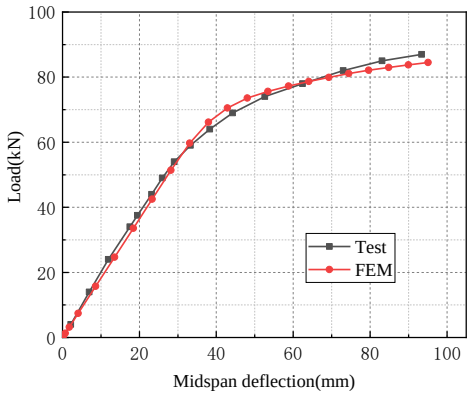

Fig. 9 Comparison of load-deflection curves

In addition, When the specimen reaches its maximum bearing capacity, the mid-section of the channel steel buckles and bulges outward. The sandwich slab's failure characteristics, as seen in Fig.10, were found to agree with those from the test, in comparison to the finite element simulation. Therefore, the finite element model proposed in this paper can better simulate the flexural performance of the sandwich slab.

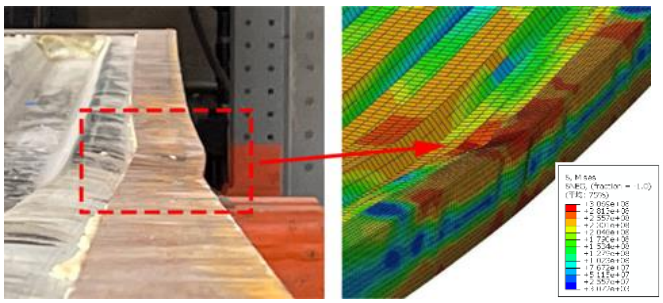

Fig. 10 Comparison of test and FEM failure characteristics

4.3. Parametric analysis

To further study the flexural mechanical properties of the profiled steel sheet-polyurethane sandwich slab, based on the test results and FEA results of the sandwich slab in Section 3.1 and Section 4.1, the parametric analysis of the sandwich slab is carried out to obtain the influence of various factors on the flexural performance of the sandwich slab. The parameters are shown in Table 4.

Table 4
Variation of parameters of sandwich slabs

Geometry			Material
Slab thickness/mm	Slab span/mm	Steel sheet thickness/mm	PU density/(kg·m^{-3})
120	2700	1	45
140	3300	1.5	65
160	3900	2	75
180	4500	2.5	90
200	5100	3	—

4.3.1. Slab thickness

Fig.11 reveals that, with a rise in slab thickness, the bearing capacity and stiffness of the sandwich slab are significantly enhanced, with an even greater increase. This is evidenced by the comparison of load-deflection curves and

finite element calculation results. Compared with the slab thickness of 120mm, when the slab thickness is 200mm, the flexural capacity of the sandwich slab is increased by 267% under the limit state of elastic, and 172% under the ultimate state of bearing capacity.

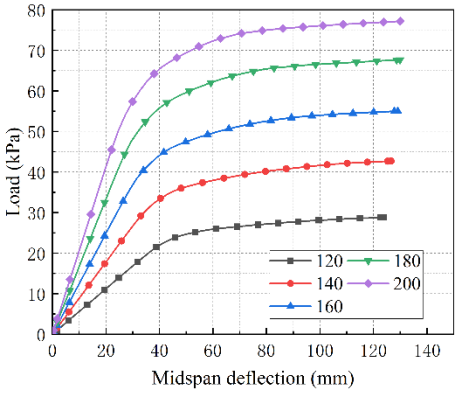

Fig. 11 Load-deflection curves of slab thickness variations

4.3.2. Slab span

As shown in Fig. 12, by comparing the load-deflection curves and the finite element calculation results of the sandwich slab with different slab spans, it can be found that compared with the slab span of 5100mm, when the slab span is 2 700mm, the flexural capacity of the sandwich slab is increased by 283% under the limit state of elastic, 167% under the limit state of bearing capacity. The sandwich slab's bearing capacity and stiffness are significantly enhanced, and the alteration of the slab span has a more noticeable impact on the slab's flexural bearing capacity when it is in the under-the-limit state of elasticity. As the slab span is reduced, the bearing capacity and stiffness of the sandwich slab are progressively increased, and the stiffness turning point is gradually advanced, thus increasing the stiffness of the sandwich slab.

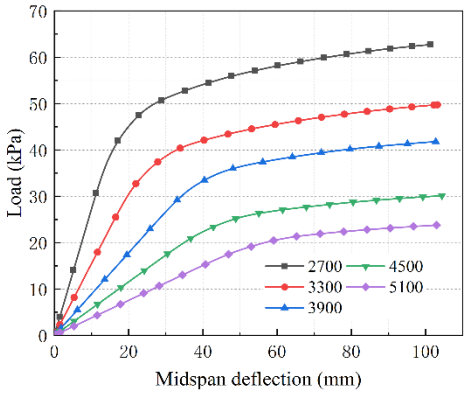

Fig. 12 Load-deflection curves of slab span variation

4.3.3. Profiled steel sheet thickness

Fig. 13 shows the influence of the profiled steel sheet thickness on the load-deflection curve of the sandwich slab. It can be seen from Fig. 13 that the bearing capacity and stiffness of the sandwich slab improved significantly with the increase of the profiled steel sheet thickness. When it is increased from 1mm to 3mm, the bearing capacity of the sandwich slab increases by 127 % in the elastic limit state and 187 % in the bearing capacity limit state. It can be seen that when the profiled steel sheet is thin, the corresponding load-deflection curve changes abruptly when the deflection is large. Compared with the corresponding finite element program, it is found that the compressed steel sheet buckles at the midspan, which can indicate that the thinner profiled steel sheet will change the failure mode of the sandwich slab.

4.3.4. Polyurethane foam density

The influence of rigid polyurethane foam density on the load-deflection curve of the sandwich slab is shown in Fig. 14. It can be seen that with the increase of polyurethane density, the bearing capacity and stiffness of sandwich slab have been improved to a certain extent, but the improvement is not obvious. The elastic limit state of the sandwich slab bearing capacity rises 26% when the density shifts from 45kg/m³ to 90kg/m³, and 15% when it reaches its ultimate state.

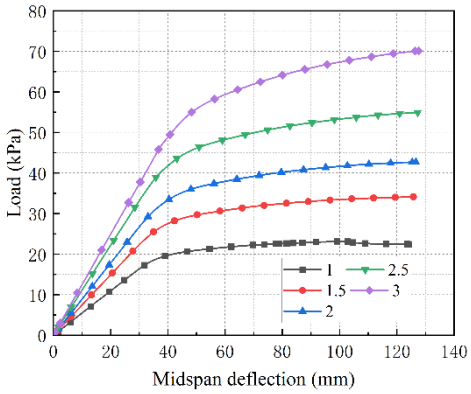

Fig. 13 Load-deflection curves of profiled steel sheet thickness variation

5. Calculation of slab deflection and flexural capacity

The shear modulus of the core material, with its special structural form, is minuscule, and when compressed, it will cause considerable shear deformation; thus, the shear deformation of the core material cannot be overlooked. The flexural stiffness of the core material is minimal, and its contribution to the bending deformation resistance can be disregarded[17]. Therefore, the bending deformation of the sandwich slab is mainly controlled by steel sheet and channel steel, and the shear deformation is shared by steel sheet, channel steel, and core material.

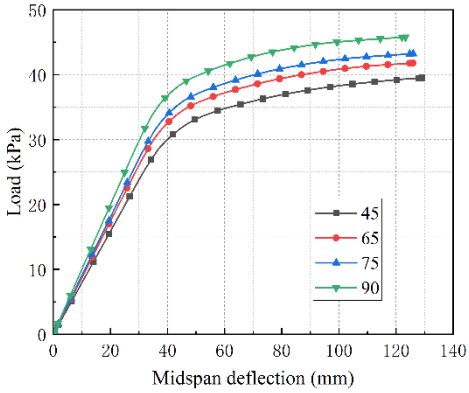

Fig. 14 Load-deflection curves of polyurethane foam density variation

5.1. Approximate calculation of slab stiffness

For a deep-profiled steel sheet, its flexural rigidity needs to be considered, while for polyurethane, the influence of the stiffness of the core layer on the sandwich slab cannot be considered. Therefore, the flexural rigidity of PSSPSS to the neutral axis is mainly determined by the stiffness of the profiled steel sheet itself, the stiffnesses of the profiled steel sheet, and the channel steel to the neutral axis of the sandwich slab.

Flexural rigidity of sandwich slab：

$$K = EI_1 + EI_2 + EI_3 \tag{5}$$

Where K is the total stiffness of the sandwich slab; EI_1 is the stiffness of the profiled steel sheet itself; EI_2 is the stiffness of the profiled steel sheet to the neutral axis of the sandwich slab; EI_3 is the stiffness of channel steel to the neutral axis of the sandwich slab.

5.2. Equivalent thickness and equivalent shear modulus of the core layer

Fig. 15 is the cross-sectional diagram of PSSPSS. According to the cross-sectional characteristics of the deep-profiled sandwich slab, the following relationship can be obtained:

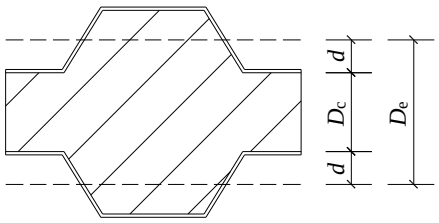

Fig. 15 Diagram of a cross-section of sandwich slab

Effective core thickness:

$$D_e = D_c + 2d \tag{6}$$

Effective cross-sectional area:

$$A_e = A_c D_e / D_c = A_c \left(D_c + 2d\right) / D_c \tag{7}$$

Effective shear modulus:

$$G_e = G_c D_e / D_c = G_c \left(D_c + 2d\right) / D_c \tag{8}$$

Where D_c is the core thickness (mm); A_e is the cross-sectional area of the core layer (mm^2); G_e is the shear modulus of core material (MPa); d is the distance from the centroid axis of profiled steel sheet to the flange edge of steel sheet (mm).

5.3. Calculation of deflection under uniform load

Based on the experimental study, finite element comparative verification, and finite element variable parameter analysis of PSSPSS, according to the calculation formula of the sandwich slab in Chinese standard GB/T 23932 - 2009[34] and the theory of sandwich beam, the deflection calculation formula of the sandwich slab is theoretically deduced, and the formula is as follows:

$$\omega = \frac{5qL^4}{384K} + \frac{k\beta qL^2}{8A_e G_e} \tag{9}$$

Where L is the span of the sandwich slab (mm); K is the flexural rigidity of the sandwich slab; k is the non-uniformity coefficient of shear stress (1.2 for rectangular section); β is the shear distribution coefficient; A_e is the cross-sectional area of the core layer (mm^2); G_e is the shear modulus of core material (MPa).

The deflection of the sandwich slab calculated by the above formula is 19.9mm, and the finite element simulation value is 19.5mm. The theoretical calculation value is higher than the finite element result, and the error is only 2.1%, which shows that the theoretically derived formula can be used to calculate the deflection of PSSPSS in the elastic limit state.

5.4. Calculation of flexural capacity under uniform load

The flexural capacity of the sandwich slab is mainly controlled by the deformation during the elastic limit state. When the plate deflection reaches l/200, the flexural bearing capacity of PSSPSS under uniform load can be determined by the following formula, which generally dictates that the maximum deflection of the sandwich slab should not exceed 1/200 of the slab span.

$$q = \frac{\omega}{\dfrac{5L^4}{384K} + \dfrac{k\beta L^2}{8A_e G_e}} \tag{10}$$

The flexural bearing capacity of the sandwich slab with different parameters in the elastic limit state is calculated and compared with the FEA results, which are based on the calculation formula of flexural capacity of the sandwich slab under uniform load. The calculated flexural capacities are compared with the FEA results, as shown in Fig. 16. The results of the proposed equations are in agreement with the FEA results, with errors of only 10% being observed. The errors are only about 10%. This means that the formula has good applicability.

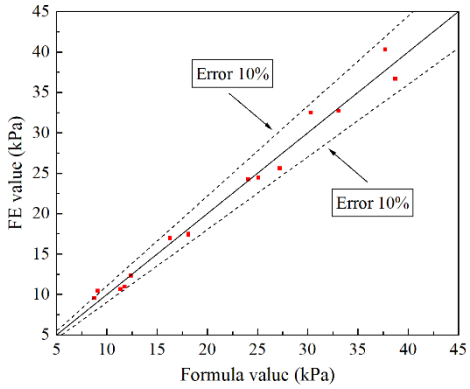

Fig. 16 Error distribution of flexural bearing capacity formula and simulation results

6. Conclusion

Using ABAQUS software for finite element analysis and variable parameter analysis, this article designs and manufactures a set of experimental components for static test research, utilizing the PSSPSS as the research object. Subsequently, the results of the experiment and finite element analysis are used to derive the deflection calculation formula and flexural bearing capacity calculation formula of the sandwich panel, leading to the following conclusions:

(1) The mid-span deflection of the sandwich slab is too large when damaged, reaching a maximum of 93.4mm - approximately 1/42 of the span. The tensile profiled steel panel and channel steel have both reached the yield state, and the mid-span position of the channel steel is deformed and buckled. However, due to the supporting effect of the deep corrugations of the profiled steel plate and the core layer, the buckling resistance of the metal surface layer is increased, so that the buckling of the profiled steel sheet does not occur.

(2) The experimental data and numerical simulation results, when compared, demonstrate that bearing capacity errors are minimal under normal service load and failure load, at 5.7% and 3.3%, respectively. Simulation of the sandwich slab failure characteristics and stress by the finite element method yielded results that were in perfect harmony with the experimental ones, demonstrating the finite element model's capability of accurately replicating the sandwich slab's mechanical performance and confirming the accuracy of the experimental results.

(3) The sandwich slab bearing capacity is significantly affected by the slab thickness, profiled steel sheets thickness, and span, whereas the density of polyurethane foam and stiffeners has no major effect. With the increase of plate thickness and profiled steel plate thickness, the flexural bearing capacity of sandwich panels is significantly improved. The reduction of plate span has a more significant effect on the flexural bearing capacity of panels under normal use. The increase of polyurethane foam density slightly improves the bearing capacity of sandwich panels.

(4) Additionally, for the calculation of the deflection of sandwich slabs, a calculation formula is derived based on existing theories and compared with experimental results, with an error of only 2.1%, verifying the correctness of the formula; Based on the formula for calculating the deflection of sandwich slabs, a formula for calculating the flexural bearing capacity of sandwich slabs is derived. The results of the calculation of the bearing capacity of sandwich slabs with different parameters are compared with the results of finite element analysis. The maximum error is 9.97%, indicating that the proposed formula for flexural bearing capacity has certain applicability.

Acknowledgments

This research was funded by the Local Science and Technology Development Fund Project Guided by the Central Government (206Z7601G) and the Natural Science Foundation of Hebei Province (E2020210074 & E2022210084).

References

[1] Lawson RM, Ogden RG, et al. Application of modular construction in high-rise buildings [J]. 2012, 18(2): 148-54.
[2] Faidzi MK, Abdullah S, Abdullah M F, et al. Review of current trends for the metal-based sandwich panel: Failure mechanisms and their contribution factors [J]. Engineering Failure Analysis, 2021, 123: 105302.
[3] Noor AK, Burton WS, Bert CW. Computational models for sandwich panels and shells[J]. Appl Mech Rev, 49(3), 1996.

[4] Mugahed Amran YH, Raizal SM. Rashid and Farzad Hejazi. Response of precast foamed concrete sandwich panels to flexural loading[J]. Journal of Building Engineering 2016, 7: 143–158.
[5] Mugahed Amran YH, Abang Ali AA, Rashid R SM, et al. Structural behavior of axially loaded precast foamed concrete sandwich panels [J]. Construction and Building Materials, 2016, 107: 307-20.
[6] Choe J, Huang Q, Yang J, et al. An efficient approach to investigate the post-buckling behaviors of sandwich structures [J]. Composite Structures, 2018, 201: 377-88.
[7] Huang Q, Choe J, Yang J, et al. An efficient approach for post-buckling analysis of sandwich structures with elastic-plastic material behavior [J]. 2019, 142: 20-35.
[8] Huang Q, Choe J, Yang J, et al. The effects of kinematics on post-buckling analysis of sandwich structures [J]. 2019, 143: 106204.
[9] Aktham Alchaar and Farid Abed. Finite element analysis of a thin-shell concrete sandwich panel under eccentric loading[J]. Journal of Building Engineering 2020.
[10] Hartsock JA. Design of Foam-Filled Structures[D]. Technomic, Stamford, Connection, 1969.
[11] Hartsock JA, Chong KP. Analysis of sandwich panels with formed faces, Proc[J]. ASCE. J. Strcuc. Div., 102(ST4), 1976.
[12] Chong KP, Wang KA, Griffith GR. Analysis of continuous sandwich panels in building systems[J]. Building and Environment, 1979, 14(2): 125-130.
[13] Allen HG. Sandwich panels with thick or flexurally stiff faces, Sheet Steel in Building, Proc[J]. Mtg Iron and Steel Institute, RIBA, March 1972.
[14] Allen HG. Sandwich construction[D]. University of Southampton, Department of Civil Engineering, Report CE/1/72, January 1972.
[15] K.M.A. Sohel and J.Y. Richard Liew. Steel-concrete-steel sandwich slabs with lightweight core - Static performance[J]. Engineering Structures 2011; 33: 981–992.
[16] K.M.A. Sohel and J.Y. Richard Liew. Behavior of steel-concrete-steel sandwich slabs subject to impact load[J]. Journal of Constructional Steel Research 2014; 100: 163–175.
[17] Davies JM. Sandwich panels[J]. Thin-walled structures, 1993, 16(1-4): 179-198.
[18] Davies JM. Design Criteria for Structural Sandwich Panels[J]. The Structural Engineer，1987.65A(12): 435~441.
[19] Davies JM. Lightweight Sandwich Construction[J]. CIB Working Commission PP.195~215.82~140.
[20] Chong KP and Hartsoek JA. Structural analysis and design of sandwich panels with cold-formed steel facing[J]. J Thin-Walled Struct 1993; 16: 79–96.
[21] Russo A and Zuccarello B. Experimental and numerical evaluation of the mechanical behavior of GFRP sandwich panels[J]. Compos Struct 2007; 81: 575–586.
[22] Ramtekka GS, Desai YM and Shah AH. Application of a three-dimensional mixed finite element model to the flexure of sandwich plate[J]. Comput Struct 2003; 81: 2183–2196.
[23] Ramtekkar G, Desai Y, et al. Mixed finite-element model for thick composite laminated plates [J]. 2002, 9(2): 133-56.
[24] Kachalla Mohammeda, Izian Abd Karima, and Rasheed Abed Hammood. Composite slab strength determination approach through reliability analysis[J]. Journal of Building Engineering 2017; 9: 1–9.
[25] Mohammed K, Karim IA, Aziz F. Composite Slab Numerical Strength Test Method Under Partial Connection Approach; proceedings of the GCEC 2017: Proceedings of the 1st Global Civil Engineering Conference 1, F, 2019 [C]. Springer.
[26] Davies JM and Hakmi MR. Postbuckling behavior of foam-filled thin-walled steel beams[J]. J Construct Steel Res 1991; 20: 75–83.
[27] Davies JM. Axially loaded sandwich panels[J]. J Struct Eng 1987; 113: 2212–2230.
[28] Mousa MA and Uddin N. Global buckling of composite structural insulated wall panels[J]. Mater Des 2011; 32: 766–772.
[29] Mousa MA and Uddin N. Structural behavior and modeling of full-scale composite structural insulated wall panels[J]. Eng Struct 2012; 41: 320–334.
[30] GB/T 228.1-2010. Metallic materials - Tensile testing - Part 1:Method of test at room temperature[S]. Beijing: China Standards Press, 2010.
[31] GB/T 21558-2008. Rigid polyurethane cellular plastics are used in the thermal insulation of buildings [S]. Beijing: China Standards Press, 2008.
[32] GB/T 8813-2020. Rigid cellular plastics - Determination of compression properties[S]. Beijing: China Standards Press, 2020.
[33] Xiaoxiong Cha. insulation panels for building - metal face and non-metal face[M]. Beijing: Science Press, 2011.
[34] GB/T 23932-2009. Double skin metal faced insulating panels for building[S]. Beijing: China Standards Press, 2009.

Advanced Steel Construction – Vol. 20 No. 1 (2024) 60–68
DOI:10.18057/IJASC.2024.20.1.7

STUDY ON MECHANICAL PROPERTIES OF HONEYCOMB REGULAR HEXAGON DAMPER

Xiao-Dong Li * and Shao-Feng Li

College of Civil Engineering, Lanzhou University of Technology, Lanzhou Gansu 730050
** (Corresponding author: E-mail: xdli@lut.edu.cn)*

ABSTRACT

Traditional metal dampers have the advantages of easy processing, convenient production, and good mechanical properties. However, most of the traditional metal dampers are single design, and their application is limited by the size of the dampers. Based on the honeycomb metal damper, a honeycomb regular hexagon metal damper with a free connection is proposed in this paper. Firstly, the failure mechanism, hysteretic curve, skeleton curve, stiffness degradation curve, and energy dissipation curve of the single energy-dissipating supporting member and the triple two-row supporting member were obtained through the low-cycle reciprocating loading test. Then the R-O mechanical model was fitted to the skeleton curve obtained from the test. Then, three kinds of honeycomb regular hexagon dampers were modeled by ABAQUS finite element simulation software, and the finite element simulation results were compared with the test results. The results show that the energy dissipation support in this paper has a good bearing capacity and energy dissipation capacity, and the development trend of simulation results align with the experimental results. The energy dissipation capacity of the energy dissipation support can be improved, and the multi-section yield can be achieved by connecting multiple energy dissipation units.

Copyright © 2024 by The Hong Kong Institute of Steel Construction. All rights reserved.

ARTICLE HISTORY

Received: 25 May 2023
Revised: 18 October 2023
Accepted: 18 November 2023

KEYWORDS

Honeycomb metal damper;
Energy dissipation support;
Seismic performance;
Hysteretic curve;
Finite element simulation;
Skeleton curve

1. Introduction

Previous earthquakes have shown that adjacent buildings are often damaged or collapsed due to collision under the action of earthquakes [1]. This phenomenon can be seen in many earthquake disasters at home and abroad [2-4]. The application of metal dampers in building structures can improve the energy dissipation capacity and seismic performance of buildings [5-6]. Li et al. [7] proposed a "dual function" metal damper set in the actual steel structure building, which proved that the damper could improve the seismic performance of the structure. Wang et al. [8] proposed a corrugated mild steel damper. The pseudo-static test confirmed that the new damper has the best mechanical performance when the steel plate wave angle is 60°, and the thickness of the steel plate is 6 mm. Based on elastoplastic mechanics, Wu et al. [9] proposed a metal damper restoring force model applied to simulate energy dissipation and a damping system. The results show that the new restoring force model can accurately predict the performance of metal dampers under different conditions and has good universality. Guo et al. [10] designed a steel bar damper, carried out a theoretical analysis of the new damper, and studied its mechanical properties through numerical analysis and a low-cycle reciprocating test. Finally, the optimal shape of a single steel bar is obtained, which proves that the damper can achieve full section yield and prevent stress concentration. Mehmet Alpaslan Köroğlu, et al. [11] has shown from experiment of energy dissipation and seismic performance of structures that damper at beam-column joints can be improved. Zhang et al. [12] proposed a new type of U-shaped steel damper self-centering beam-column connection, and the proposed self-centering connection can provide reliable energy dissipation and self-centering ability. Chen et al. [13] used the general finite element software ABAQUS to discuss the hysteretic characteristics of shear plate dampers under axial pressure. In the past few years, scholars have proposed several new steel dampers with high energy consumption capacity, including mild steel plate dampers [14], shape memory alloy dampers [15-16], U-shaped steel damper [17-19], friction damper [20-22].

Most of the dampers in building structures are single dampers and research on interconnecting dampers is rare. In this paper, a kind of metal energy dissipation brace which can be freely connected is proposed so that the application of dampers in building structures is not limited by size. To understand the hysteretic performance and energy dissipation performance of the support, hysteretic performance, stiffness degradation, and energy dissipation analysis of the energy dissipation support were firstly analyzed through the low-cycle reciprocating test, which proved that the energy dissipation support has good working performance. Secondly, the finite element simulation of the damper is carried out by ABAQUS, and the simulation results are compared with the test results to verify the accuracy of the test.

2. Structure and test design of the energy dissipation support device

2.1. Construction of single support unit

The connectable energy dissipation devices developed in this study are referred to as hexagonal honeycomb dampers, which are categorized into three types: foundation, one-way, and two-way. Their advantages include low steel consumption and good energy dissipation performance. The foundation-type support monomer is divided into the main body unit and ear plate. The main body unit is a regular hexagon, primarily used to dissipate seismic energy. The ear plate connects the left and right monomers, increases the contact area between the left and right support main bodies, and improves the energy dissipation capacity. The ear plate was welded to the support body. The upper and lower parts of the support body were provided with a diamond-shaped notch to connect the upper and lower parts of each monomer. The energy dissipation device was improved by changing the upper and lower corners of the primary element to a circular arc and the diamond notch to a welded ear plate to reduce the influence of stress concentration. Considering the in-plane instability of the energy dissipation units and possible multidirectional earthquake action, the bidirectional/unidirectional brace was further improved by changing the primary body of the energy dissipation device to a bidirectional layout. The new damper was integrally cut and welded from a Q235 steel plate, forming the primary energy dissipation section. Bending deformation was expected to occur at each corner of the regular hexagon under load. However, multisection yielding can be formed to enhance the deformation and bearing capacities of the damper. Fig. 1 shows the single energy dissipation unit.

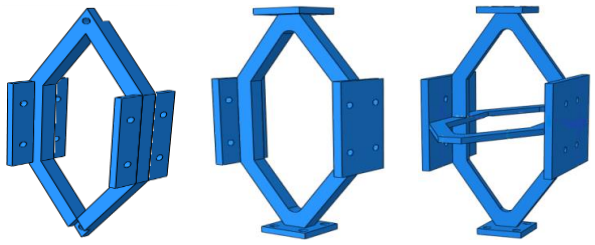

(a) (b) (c)

Fig. 1 3D schematic of each energy dissipation unit type: (a) foundation, (b) one-way, and (c) two-way

2.2. Calculation of individual supporting capacity

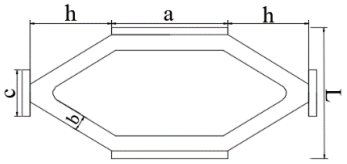

Fig. 2 Single energy dissipation unit dimensions: a-padeye width, b-web width, c-side padeye width, h-energy dissipation section length, and L-energy dissipation unit width

Fig. 2 shows a single energy dissipation unit. According to the elastoplastic mechanics, when a single energy dissipation unit is loaded, the yield and plastic moments at any cross-section of the energy dissipation section can be calculated as follows:

$$M_y = \frac{1}{6}sb^2\sigma_y - \frac{b}{6}F_y, \tag{1}$$

$$M_p = \frac{1}{4}sb^2\sigma_y - \frac{F_{max}^2}{4sb\sigma_y}, \tag{2}$$

where s is the thickness of the energy dissipation section, M_y is the yield bending moment, M_p is the plastic bending moment, σ_y is the yield strength of the material, F_y is the yield bearing capacity of a single energy dissipation unit, and F_{max} is its maximum bearing capacity. F_y and F_{max} can be calculated using Eqs. (3) and (4).

$$F_y = M_y/h \tag{3}$$

$$F_{max} = M_p/h \tag{4}$$

Accordingly, the yield bearing capacity F_y and maximum bearing capacity F_{max} of a single energy dissipation unit can be obtained as follows:

$$F_y = \frac{sb^2\sigma_y}{6h+b}, \tag{5}$$

$$F_{max} = s\sigma_y(\sqrt{4h^2+b^2} - 2h) \tag{6}$$

2.3. Specimen design

Six specimens were designed for the tests. The specimens are denoted by GJ-1, GJ-2, GJ-3, GJ-4, GJ-5, and GJ-6. GJ-1, GJ-3, and GJ-5 are single energy dissipation units. GJ-2, GJ-4, and GJ-6 are energy dissipation supports forming a 3×2 unit using the single energy dissipation units GJ-1, GJ-3, and GJ-5, respectively, which was connected through bolts. The dimensions of the supporting monomers in each component were the same. The bolts used between each support unit were 4.8 grade M4 ordinary hexagonal socket bolts. Fig. 3 shows the primary dimensional parameters and locations of each component (unit/mm).

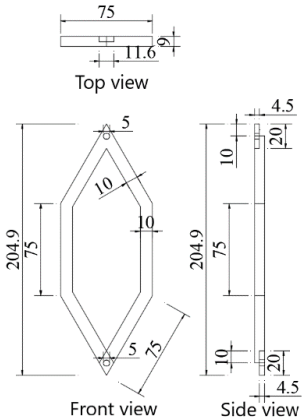

(a) GJ-1

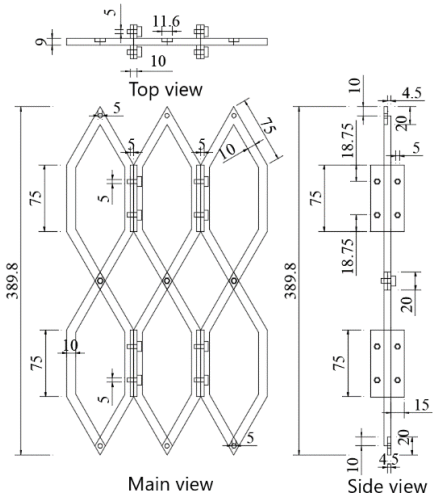

(b) GJ-2

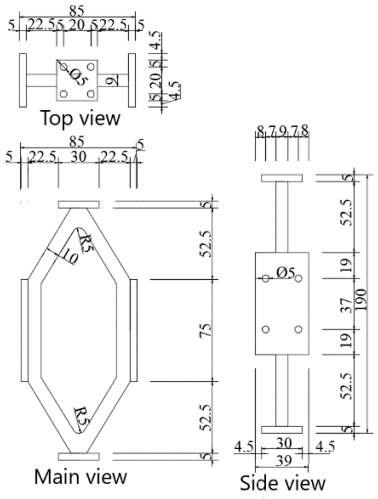

(c) GJ-3

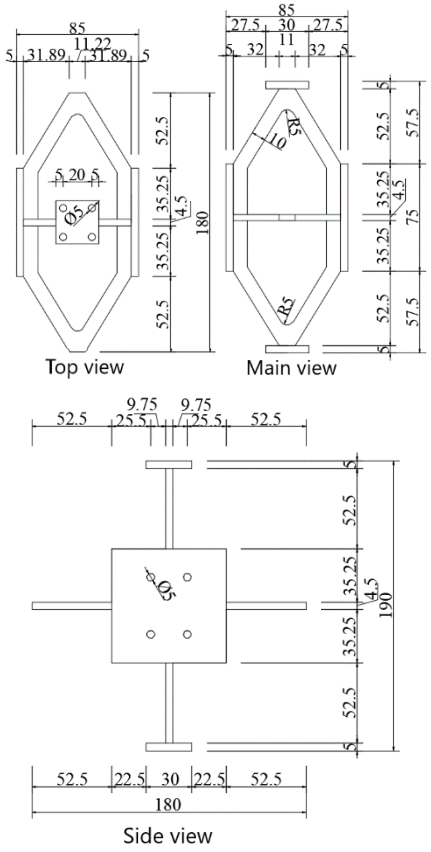

(d) GJ-5

Fig. 3 Geometric dimensions and construction of each test member

2.4. Material property test

The dampers used in this study were made of a 9 mm thick Q235 steel plate. The mechanical properties of the steel plate under uniaxial tension were tested in accordance with the GB/T228.1-2010 Metallic Materials Tensile Testing Part 1: Room Temperature Test Method [23] and completed in the laboratory of the School of Science, Lanzhou University of Technology. Table 1 lists the test results.

Table 1
Mechanical properties of Q235

Sample mark	b (mm)	Fy (Mpa)	Fu (Mpa)	Fy/Fu	δ (%)
1	9	421	576	0.731	20.3
2	9	439	583	0.753	21.2
3	9	434	584	0.743	20.4

Note: b is the width of the sample, Fy is the yield strength of the material, Fu is the tensile strength of the material, Fy/Fu is the material yield ratio, and δ is the elongation after fracture.

2.5. Test equipment and loading system

The test was performed at the Key Laboratory for Disaster Prevention and Reduction of Civil Engineering in Western China and the Civil Engineering Laboratory of Lanzhou University of Technology. A low-cycle reciprocating loading test was performed on the test piece using a microcomputer-controlled electrohydraulic servo single-channel loading device produced by Hangzhou Bangwei Company. The maximum force and displacement of the device were 1000 kN and 200 mm, respectively. The loading methods of test pieces GJ-1, GJ-3, and GJ-5 are as follows: First, two steel plates were used to connect the actuator and base; subsequently, the bolt holes were set at the corresponding positions of the steel plates, and two clips with grooves were used to buckle the test pieces on the upper and lower steel plates. Finally, the steel plates were connected to the grooves of the upper and lower cover plates with bolts. For members GJ-2, GJ-4, and GJ-6, to distribute the force more evenly and simulate the actual working condition of the energy dissipation support device, a 255 mm long steel bar was welded on both sides of the member, and a clip with a groove was added between the two upper and lower support units. Fig. 4 shows the installation diagram of the two components and the loading device diagram. In the test, six members were subjected to displacement loading. The specimen compression was positive, whereas the tension was negative.

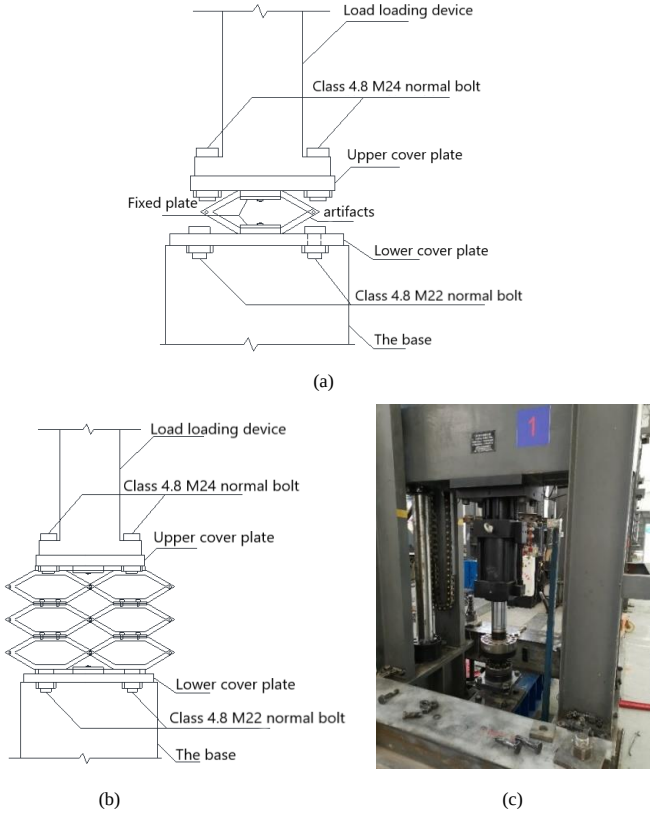

Fig. 4 Mounting diagram of components (a) GJ-1, GJ-3, and GJ-5 and (b) GJ-2, GJ-4, and GJ-6. (c) Schematic of the loading device

The loading displacement at the beginning of the test was 0.5 mm, which increases by 0.5 mm at each stage before reaching 5 mm. After the displacement reached 5 mm, the loading displacement at each level was increased to 1 mm until the component load dropped to 85% of the ultimate load, which was a sign of failure, and the loading was stopped. Fig. 5 shows the loading system and cycle times for each component.

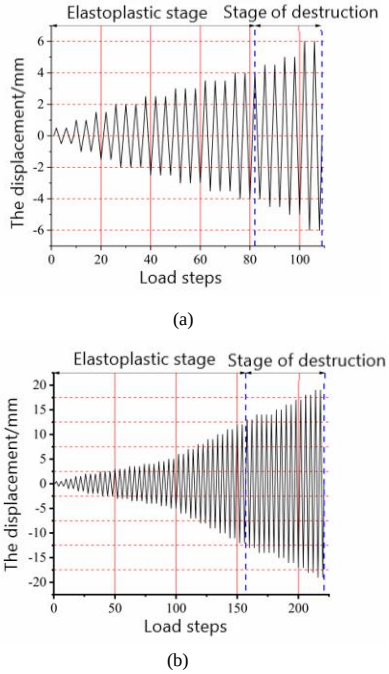

Fig. 5 Loading system of components (a) GJ-1, GJ-3, and GJ-5 and (b) GJ-2, GJ-4, and GJ-6

3. Test results and analysis

3.1. Loading test

In the actual test, owing to the bolt processing problems and improper installation process, some bolts could not achieve the expected connection effect; therefore, some padeye connections were welded to strengthen the connection between the pads without affecting the main body of the energy dissipation support unit. Deformation occurred on the bolt holes at the upper and lower ends of component GJ-1 when the loading displacement amplitude was 3 mm. When the displacement amplitude was 3.5 mm, tiny cracks appeared on the diamond grooves at the upper and lower ends of the component. The cracks on the grooves of the component gradually expanded along the grooves with a continuous increase in displacement. When the displacement was 6 mm, the bearing capacity of the component decreased below 85%, and the loading was stopped. GJ-3 and GJ-5 improved the problem of stress concentration in GJ-1; therefore, the limit displacement was also improved. When GJ-3 was loaded to 8 mm, the short side of the energy dissipation unit arc and the corner of the connection between the energy dissipation unit and padeye almost simultaneously exhibited slight cracks. The cracks gradually expanded with continued loading until they were completely destroyed. The failure mode of GJ-5 was the same as that of GJ-3. Tiny cracks appeared, and the bearing capacity decreased below 85% when GJ-5 was loaded to 9 mm and 14 mm. For member GJ-2, the bolt connection between the energy dissipation elements exhibited relative dislocation when the displacement amplitude was 13 mm. Small cracks appeared at the joints at both ends of the energy dissipation brace, and an expansion trend was observed when the displacement amplitude was 14 mm. When the displacement amplitude was 14–19 mm, cracks appeared at the joints on both sides of the bolted connection between the energy dissipation elements and gradually expanded to the bolt with increased load amplitude. When the load reached 16 mm, the cracks at this location formed a through-crack from the end of the diamond groove to the bolt hole, and the bearing capacity of the component decreased significantly. When the component was loaded to 19 mm, its bearing capacity decreased to less than 85% of the ultimate load, and the test was completed. The failure modes of components GJ-4 and GJ-6 were similar, and a problem of uneven contact surfaces owing to machining errors was encountered. The left and right connecting bolts were staggered when GJ-4 was loaded to 14 mm. After reaching 17 mm, tiny cracks appeared at the ear plate connection of each energy dissipation unit and continued to expand until the component was damaged. The left and right

connecting bolts were staggered when GJ-6 was loaded to 15 mm. Tiny cracks appeared after loading to 18 mm. The component was damaged when GJ-6 was loaded to 21 mm. Fig. 6 shows the cracks and final failure mode of each component.

According to the comprehensive test phenomenon, GJ-1 and GJ-2 weakened this position of the component because the joints were set at both ends of the energy dissipation unit. The joint position of each component had an increasing stress concentration with increasing bearing capacity of the two components. Finally, this position failed before the other positions. GJ-3 and GJ-5 changed the connection mode between the energy dissipation units; there was no stress concentration at the joint, thereby significantly improving the bearing and energy dissipation capacities. Furthermore, GJ-1 and GJ-3 had a tilt degree during crack formation to final failure, whereas GJ-5 had no apparent tilt compared with GJ-1 and GJ-3. Many cracks or failures occurred when GJ-2, GJ-4, and GJ-6 were damaged. Therefore, connecting multiple energy dissipation elements enables multisection failure of members and improves the bearing and energy dissipation capacities.

3.2. Hysteretic behavior

The hysteresis curve of each component had a degree of pinching under tension because the displacement between the component and actuator base was small, and there were errors and defects in the component. This phenomenon was more apparent in the GJ-1 and GJ-2 tests owing to the component processing problem and because the initial error of the actuator was not well adjusted. This phenomenon was significantly improved after subsequent tests. The primary supporting body of each component was inclined, and the bolted connection was unstable during the loading process, resulting in different bearing capacities of the component under tension and compression. This also resulted in an asymmetric hysteretic curve. Figs. 7 and 8 show the corresponding hysteretic properties and skeleton curves for each specimen, respectively. The hysteretic curves of each specimen were approximately shuttle-shaped until the bearing capacity of the damaged member degraded slightly, indicating that the specimen had good energy dissipation and deformation capacities. Table 2 lists the test results for the six test pieces.

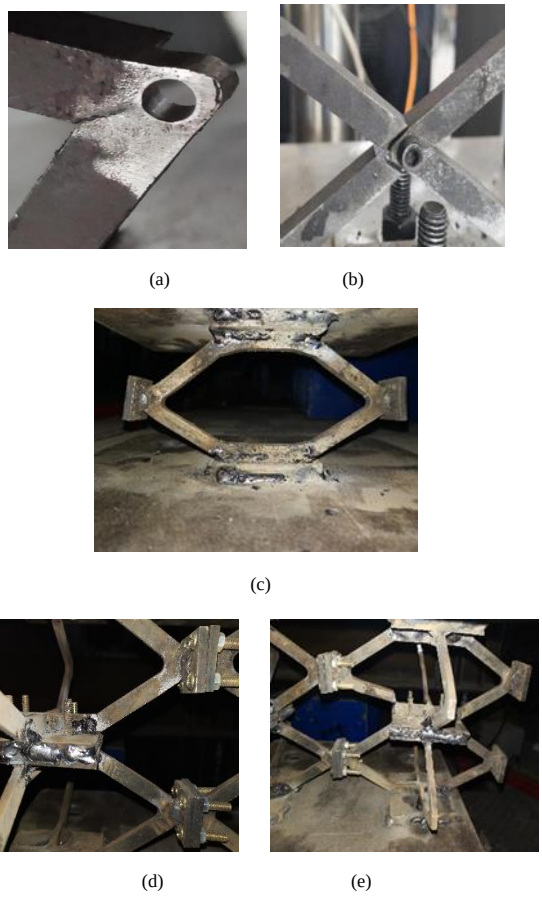

(a) (b) (c) (d) (e)

Fig. 6 Illustrations of different component failures. (a) Cracks appear. (b) Connection starts to break. (c) Crack expands gradually during loading. (d) Cracks appear on multiple sections. (e) Ultimate destruction

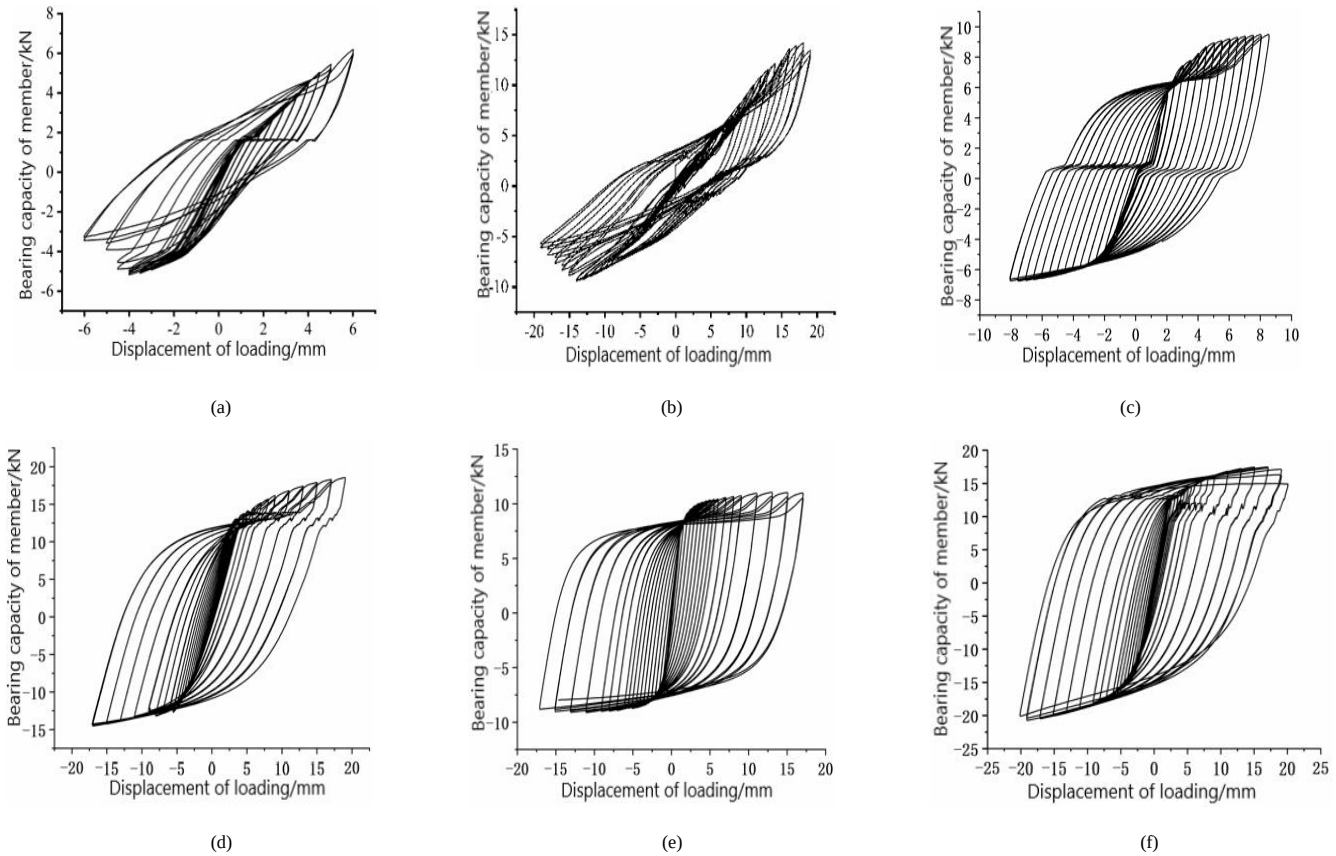

(a) (b) (c) (d) (e) (f)

Fig. 7 Hysteresis curve of components (a) GJ-1, (b) GJ-2, (c) GJ-3, (d) GJ-4, (e) GJ-5, and (f) GJ-6

Table 2
Experiment results of energy dissipation support device

Component No	Loading direction	K_0 (kN/mm)$^{-1}$	Fy/kN	Uy/mm	Fp/kN	Up/mm	Fu/kN	Uu/mm	μ
GJ-1	Negative direction	2.10	2.88	0.88	5.18	4.00	4.40	4.76	5.41
	Forward	1.03	3.02	0.93	6.19	6.00	5.86	7.06	7.59
GJ-2	Negative direction	1.32	3.67	1.54	9.40	14.00	7.99	15.73	10.24
	Forward	1.22	4.53	1.83	14.15	18	13.01	19	10.41
GJ-3	Negative direction	3.54	3.09	0.87	6.52	8.07	5.64	9.33	10.73
	Forward	1.75	3.38	1.12	9.31	8.56	8.82	9.67	8.63
GJ-4	Negative direction	3.39	5.63	1.80	14.32	18.24	12.56	19.56	10.87
	Forward	3.93	6.24	1.77	18.57	18.99	17.23	20.13	11.36
GJ-5	Negative direction	6.71	4.26	1.12	8.82	17.00	7.23	17.63	15.73
	Forward	6.78	5.41	1.14	10.99	17.01	9.16	18.63	16.36
GJ-6	Negative direction	5.71	6.24	1.87	20.08	20.04	19.32	21.42	11.47
	Forward	5.93	5.63	1.76	17.43	20.01	16.46	20.75	11.78

Note: K_0 is the initial stiffness, Fy is the yield load, Uy is the equivalent yield displacement (obtained by geometric method), Fp is the peak load (highest point of the skeleton curve), Up is the peak displacement, Fu is the ultimate load (load when the specimen fails or when the load drops to 85%), Uu is the limit displacement, and μ is the ductility coefficient.

The tensile bearing capacity was less than its corresponding compression bearing capacity when the number of energy dissipation support units increased. The initial stiffness of the members had a downward trend as the number of single members increased. However, the bearing capacity of the members also exhibited a significant increase, primarily because members GJ-2, GJ-4, and GJ-6 were connected by multiple energy dissipation units through bolts compared with members GJ-1, GJ-3, and GJ-5. This decreased the integrity of the component. Thus, the initial stiffness of the components GJ-2, GJ-4, and GJ-6 was relatively smaller than that of a single energy dissipation support element.

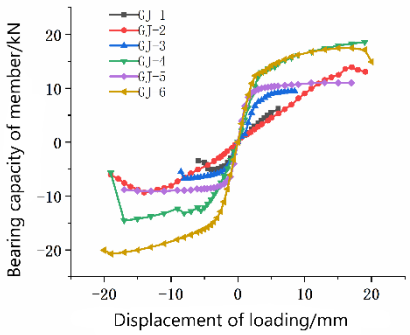

Fig. 8 Skeleton curve of each component

Table 2, Figs. 7(a, c, and e), and Fig. 8 illustrate that the initial stiffness, yield load, and ductility coefficient of GJ-3 and GJ-5 improved compared with those of GJ-1 after changing the connection mode and corners between energy dissipation devices; thus, their energy dissipation and bearing capacities also improved significantly. GJ-5 was plumper and more symmetrical than GJ-1 and GJ-3, indicating that the capacity of the energy dissipation unit can be improved by solving the tilting phenomenon of the supporting body in the loading process.

Table 2, Figs. 7(b, d, and f), and Fig. 8 show that GJ-6 had a fuller hysteretic curve and higher energy dissipation and bearing capacities than GJ-2 and GJ-4. This indicates that the two-way design of GJ-5 can effectively prevent the in-plane displacement of the primary support body and instability of the font caused by connection or loading errors and ensure its energy dissipation and bearing capacities when multiple energy dissipation units are connected.

3.3. Hysteretic behavior

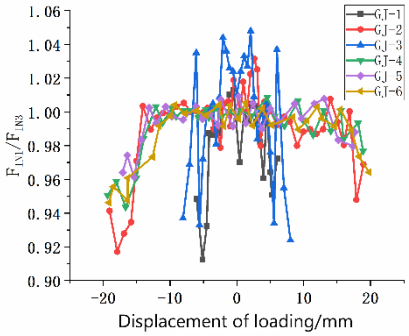

Fig. 9 Bearing capacity degradation curve

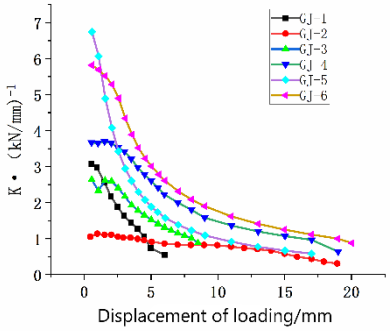

Fig. 10 Stiffness degradation curve

The ratio of the maximum load FIn1 of each stage to the maximum load FIn3 of the second cycle was recorded as the bearing capacity degradation rate to investigate the load-bearing performance of each energy dissipation support device. Under cyclic loading, the equivalent secant stiffness was used to characterize the stiffness of each specimen with a gradual increase in displacement. Figs. 9 and 10 illustrate the bearing capacity and stiffness degradation curves of each member, respectively.

Fig. 9 shows that the degradation of the bearing capacities of different members presents similar change rules: the degradation rate of each member was 0.91–1.04, and the degradation degree of the bearing capacity of each member was small. This indicates that the three single energy dissipation units and the 2×3 units have a good load-bearing capacity.

As shown in Fig. 10, members GJ-1, GJ-3, and GJ-5 are single energy dissipation units with large initial stiffness. The stiffness degradation of a single energy dissipation unit was high, whereas those of the 2×3 units were gradual. Therefore, for members GJ-2, GJ-4, and GJ-6, although their initial stiffness showed a downward trend compared with that of a single energy dissipation unit, their stiffness degradation curves were relatively smooth. This indicates that the stiffness degradation resistance of the energy dissipation support device was better than that of a single energy dissipation element.

3.4. Evaluation of energy dissipation performance of components

The equivalent viscous damping coefficient ξ_e is an important index for evaluating the energy dissipation capacity of structures [24]. Eq. (7) and Fig. 11 show the calculation method for the equivalent viscous damping coefficient. The shaded area in the Fig represents the area of a single hysteresis loop.

$$\xi_e = \frac{1}{2\pi} \cdot \frac{S_{ABC}+S_{CDA}}{S_{OBE}+S_{ODF}} \tag{7}$$

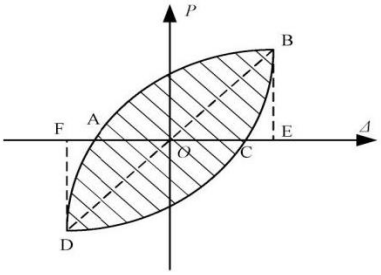

Fig. 11 Schematic of equivalent viscous damping coefficient calculation

This study used the equivalent viscous damping coefficient curve to evaluate the energy dissipation capacity of the energy dissipation braces. As illustrated in Fig. 12, the overall trend of the equivalent viscous damping coefficient of each member increased with an increase in displacement. The equivalent viscous damping coefficient of member GJ-1 did not decrease before failure and reached 0.32, indicating that a single energy dissipation element has a good energy dissipation capacity. The equivalent viscous damping coefficient corresponding to each loading displacement of component GJ-2 fluctuated to varying degrees. A significant fluctuation was observed, particularly when U=1.5–2.5 mm. However, the equivalent viscous damping coefficient of GJ-2 remained above 0.19, reaching a maximum of 0.27. Moreover, the energy dissipation curve of this component exhibited an upward trend. The viscous damping coefficients of members GJ-3, GJ-4, GJ-5, and GJ-6 initially increased rapidly and stabilized between 0.4 and 0.5. The equivalent viscous damping coefficients of each member did not decrease before failure, indicating that the damper has good energy dissipation capacity.

GJ-5 had the largest equivalent viscous damping coefficient, followed by GJ-3, and GJ-1 was the lowest. This indicates that solving the problem of stress concentration and in-plane instability of the energy dissipation element can improve the energy dissipation capacity of the component. The equivalent viscous damping coefficients of members GJ-2, GJ-4, and GJ-6, composed of multiple energy dissipation units, were lower than those of members GJ-1, GJ-3, and GJ-5, composed of their corresponding single energy dissipation units. This indicates that the energy dissipation capacity of the energy dissipation device reduces slightly with an increase in the energy dissipation units.

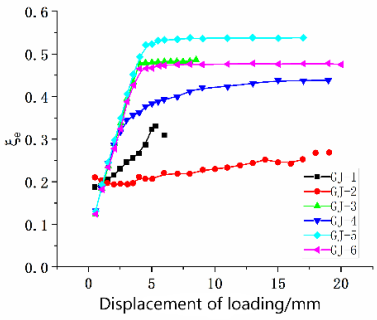

Fig. 12 Comparison of equivalent viscous damping coefficient curves of various components

3.5. Resilience model

This study selected the Ramberg–Osgood (RO) model, which is a continuous curve model, as the restoring force model of the energy dissipation brace to fit the skeleton curve obtained from the test. It has the problem of discontinuous derivatives at individual turning points that the general broken-line model does not have and is more consistent with engineering practice. Moreover, this model requires fewer parameters; therefore, it is a widely used mechanical model. Fig. 13 shows the skeleton curve of the RO model. The skeleton curve is expressed as

$$\frac{U}{U_y} = \frac{F}{F_y}\left(1 + \alpha \left|\frac{F}{F_y}\right|^{\gamma-1}\right), \tag{8}$$

where α and γ are curve shape coefficients; α controls the elastic proportional limit of the curve, and the least square method is used to obtain $\alpha = 0.5$. The control curve represents the stiffness after yielding. $\gamma = 7.1 \cdot ln(t/S) + 29.5$ [25], where t and S are the width and side length of each side of the energy dissipation unit, respectively. When $\gamma = 1$, the curve is completely elastic and plastic. When $\gamma = \infty$, the curve is ideal elastic and plastic. F_y and U_y are the yield load and yield displacement, respectively.

After substituting each loading displacement, the skeleton curve under the RO model can be obtained through calculation, where F_y and U_y denote the yield load and yield displacement in each loading direction, as listed in Table 2. This study fitted only the "rising" segment of the skeleton curve because the RO model does not fit the descending segment. Fig. 14 compares the skeleton curves obtained from the test and calculation of each component.

According to the skeleton curve results calculated using the RO model and those obtained using the test hysteresis curve, the test result of each component in the early stage of loading was more consistent with the RO recovery model. The fitting degree of the two curves decreased with increased loading displacement. However, the RO mechanical model can better fit the energy dissipation brace.

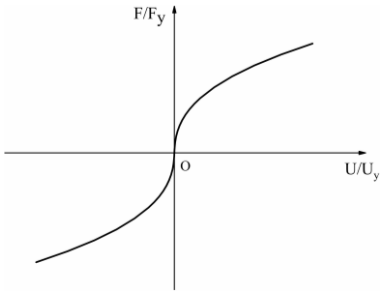

Fig. 13 Ramberg–Osgood (RO) restoration model skeleton curve

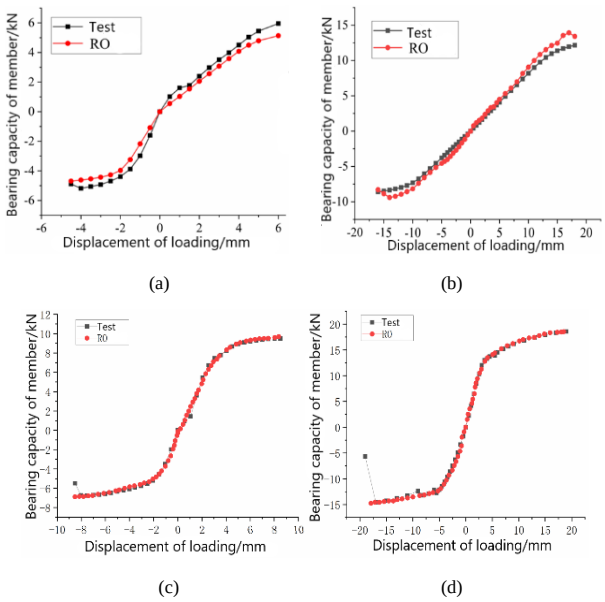

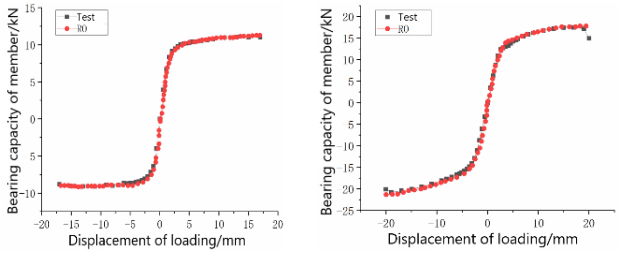

(e) (f)

Fig. 14 Skeleton curve comparison of the RO model and each component test: (a) GJ-1, (b) GJ-2, (c) GJ-3, (d) GJ-4, (e) GJ-5, and (f) GJ-6

4. Finite element simulation analysis of dissipative components

4.1. Basic information of finite element model

By using ABAQUS finite element analysis software, a three-dimensional model was established for three different forms of honeycomb regular hexagon dampers. In the finite element model, honeycomb regular hexagon dampers included energy dissipators and ear plates, whose main function was to make the bearing capacity evenly distributed on the energy dissipators. In addition, eight nodes of linear hexahedron elements were used for the grid division of the finite element model. Furthermore, local mesh refinement was carried out on key research sites, such as around bolt holes and the arc of the honeycomb energy dissipation ring, to observe the failure characteristics of the main body of energy dissipation, which greatly reduced the error of simulation results caused by the grid division of the model. Compared with the test, the factors such as residual stress, initial eccentricity, insufficient welding, and welding heat influence are ignored in the finite element analysis. The finite element analysis ignores the influence of sliding distance and assembly void under low cyclic load. Q235 steel was used in the finite element model of the damper, which was completely consistent with the field test, and Tie binding was used to connect the contact surface. The finite element model and mesh division of the damper is shown in Fig 15.

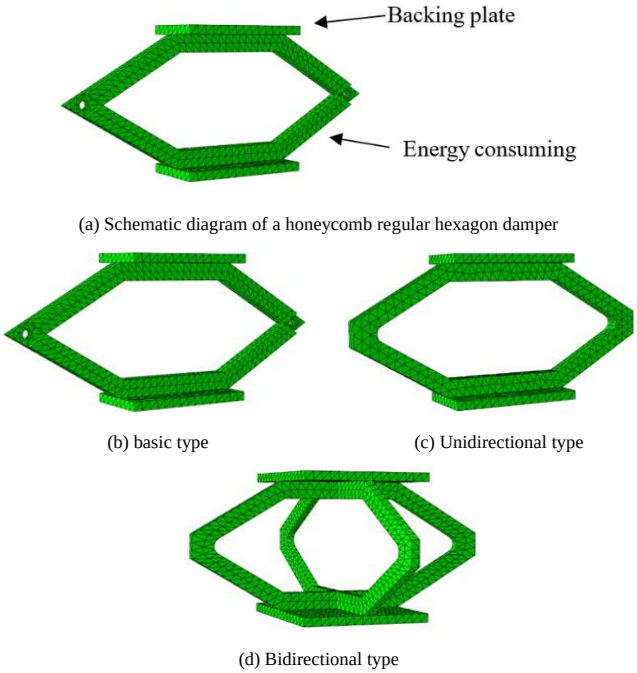

(a) Schematic diagram of a honeycomb regular hexagon damper

(b) basic type (c) Unidirectional type

(d) Bidirectional type

Fig. 15 Finite element model and meshing diagram of a damper

4.2. Finite element model loading conditions and other parameter information

Other parameters of the finite element model are completely consistent with those described in field tests. The basic type of honeycomb regular hexagon damper corresponds to GJ-1, the unidirectional type of honeycomb regular hexagon damper corresponds to GJ-3, and the bidirectional type of honeycomb regular hexagon damper corresponds to GJ-5. In the finite element model, the boundary condition is to simulate the fixed constraint with the six degrees of freedom constraints in the bottom lug plate. To prevent excessive local deformation caused by adverse factors such as stress concentration in the loading process from affecting the simulation results, coupling points were set at the loading position, and displacement loading was carried out on the upper lug plate by coupling constraint mode. The loading mode was cyclic hysteretic loading. The loading process is in complete agreement with the field test. The boundary conditions of the finite element model are shown in Fig 16.

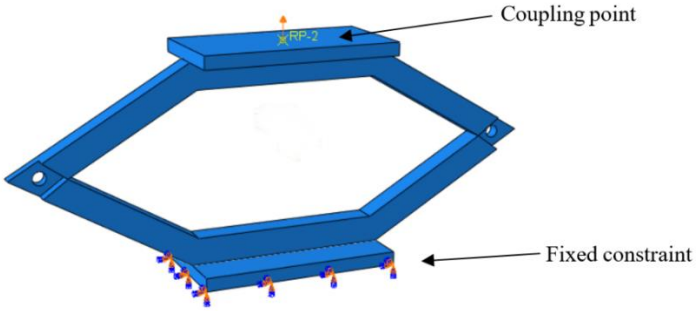

Fig. 16 Boundary conditions of finite element model

4.3. Comparison of failure phenomena

Compared with the honeycomb regular hexagon damper finite element simulation, the failure position of the honeycomb regular hexagon damper test is almost the same as the position of large stress distribution in the finite element model of the damper. However, the phenomenon that the edge of the energy-dissipating body part is separated from the connecting part of the lug plate cannot be simulated in the finite element analysis. Therefore the ductility performance of the two is not completely consistent. But there are other factors of experimental error. In the field test process, there are also some problems, such as uneven connection surface between member and actuator and uneven weld machining, so the field test results are slightly different from the finite element simulation. The comparison between the site failure site of each component and the finite element simulation failure site is shown in Fig 17.

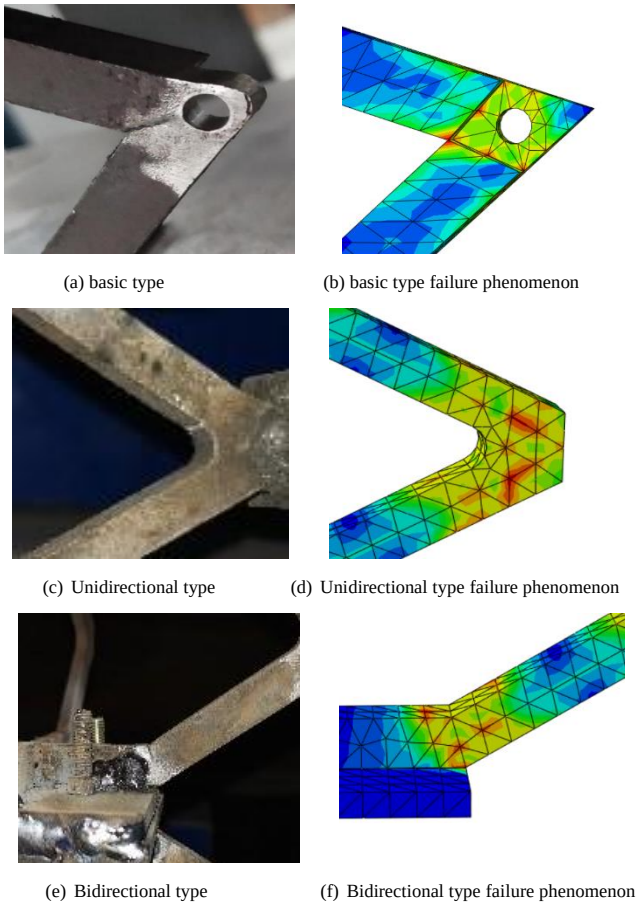

(a) basic type (b) basic type failure phenomenon

(c) Unidirectional type (d) Unidirectional type failure phenomenon

(e) Bidirectional type (f) Bidirectional type failure phenomenon

Fig. 17 Comparison between the site failure phenomenon of each component and the finite element simulation failure phenomenon

As can be seen from FIG. 17, the honeycomb regular hexagon damper foundation first appears to crack at the end of the diamond groove and gradually breaks down. The failure mode of unidirectional and bidirectional honeycomb regular hexagonal dampers is similar, and the stress distribution is large at the arc of the energy-dissipating body, and the angle between the ear plate and the energy-dissipating body, but the stress concentration phenomenon does not appear. The stress distribution in the stress program of the finite element model of the damper is consistent with the failure characteristics of the damper specimen in the field test.

4.4. Comparison of hysteresis curves

As shown in Fig 18 (a), in the comparison between the honeycomb regular hexagon damper basic type field test and finite element test, many unfavorable factors appeared in the field test, such as certain initial displacement errors of the actuator, gap between the damper and the actuator, and uneven welding between the energy dissipation body and the ear plate. The above adverse factors led to the field test did not reach the ideal bearing capacity and a certain degree of pinching phenomenon. In the unidirectional field test of the honeycomb regular hexagon damper, the initial displacement error of the actuator is improved to ensure full contact between the damper and the actuator at the beginning of displacement loading. However, due to the machining problem of the ear plate, the connection between the component and the actuator is uneven, resulting in certain slippage in the displacement loading process, and the bearing capacity is not up to the ideal state. The comparison of the field test and finite element results is shown in Fig 18 (b). In the bidirectional field test of the honeycomb regular hexagon damper, the initial displacement error of the actuator is solved, the contact surface between the damper and the actuator is smooth, and the no-slip phenomenon occurs in the displacement loading process. The hysteresis curve of the field test is fuller and has a higher bearing capacity than that of the foundation type and unidirectional type, but there are some processing problems in the weld between the energy dissipation body and the ear plate. The weld strength is not enough, and there is a certain gap, which makes the field test hysteresis curve under tension and compression asymmetry, and also makes the bearing capacity under tension not reach the ideal bearing capacity. However, the maximum bearing capacity under compression is not much different from the finite element simulation results, and the field test and finite element simulation hysteresis curve trend are the same. The consistency of finite element simulation and field test results is indirectly explained. The comparison of the field test and finite element results of the bidirectional honeycomb regular hexagon damper is shown in Fig 18 (c).

5. Conclusions

The application of dampers in building structures is often limited by their size. Based on the research on the interconnect dampers proposed in this paper. According to the hysteresis curve obtained from the low-cycle reciprocating motion and finite element software model analysis, the following conclusions were drawn:

(1) The damper described in this paper has good hysteretic energy dissipation capacity, especially in the case of large deformation; there is still a full hysteretic loop, and because the damper can be connected, the length is adjustable, so it has good applicability.

(2) According to the bearing capacity degradation curve, stiffness degradation curve, and equivalent viscous damping coefficient curve of components obtained from the low-cycle reciprocating test, it can be seen that the dampers mentioned in the paper all have good load-holding capacity; Among the single dampers GJ-1, GJ-3, and GJ-5, GJ-3, and GJ-5 have the higher bearing capacity and energy dissipation capacity than GJ-1 after solving the problem of stress concentration. Among the three dampers, the hysteretic curves of GJ-5 are fuller and more symmetrical, indicating that the bidirectional design of the support body is conducive to solving the problem of in-plane instability of the energy dissipation member. The three-connection and two-row energy dissipation support test of each energy dissipation unit proves that the connection of multiple energy dissipation units can improve the bearing capacity and energy dissipation performance and can achieve multi-section yield.

(3) The R-O restoring force model based on the damper is also proposed, and the skeleton curve of the damper is simulated. The skeleton curve of the damper can be roughly estimated by the mechanical properties of the material selected by the damper and the size of the energy dissipation support. The comparison with the experimental results shows that the inferred results of this method are reliable.

(4) The yield characteristics of each honeycomb regular hexagon damper are almost identical to those of the large stress part of the stress program in the finite element model of the damper, which fully demonstrates the unity of the finite element simulation results and field test results. According to the hysteretic curve results, the finite element simulation ignored the welding residual deformation and initial defects of the component, as well as the initial error of the actuator and other adverse factors, so there was no slip phenomenon in the finite element simulation results. The energy dissipation laws of the three kinds of dampers in field tests and finite element simulation are the same. The energy dissipation capacity of unidirectional and bidirectional honeycomb regular hexagonal dampers is higher than that of the basic type, while the energy dissipation capacity of the bidirectional type is slightly higher than that of the unidirectional type.

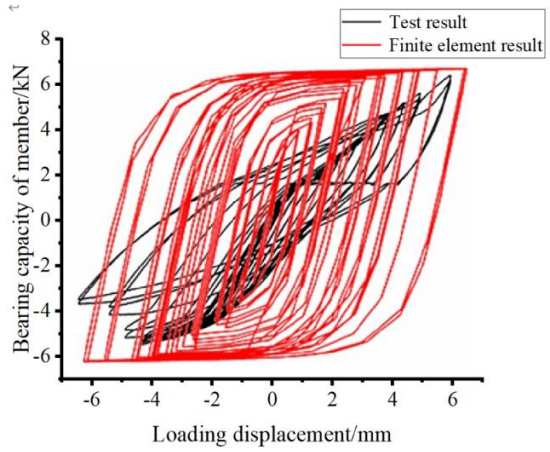

(a) Honeycomb regular hexagonal base type

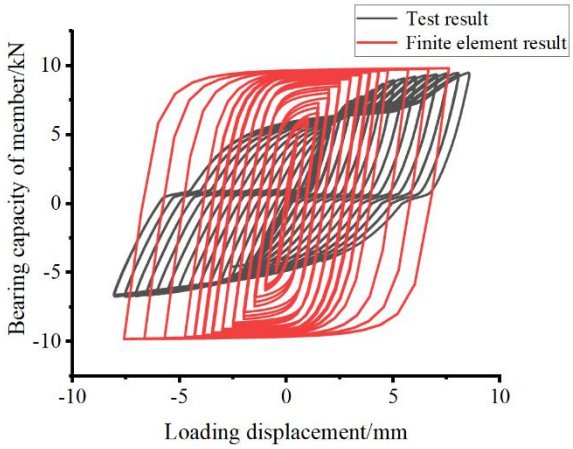

(b) Honeycomb regular hexagonal unidirectional type

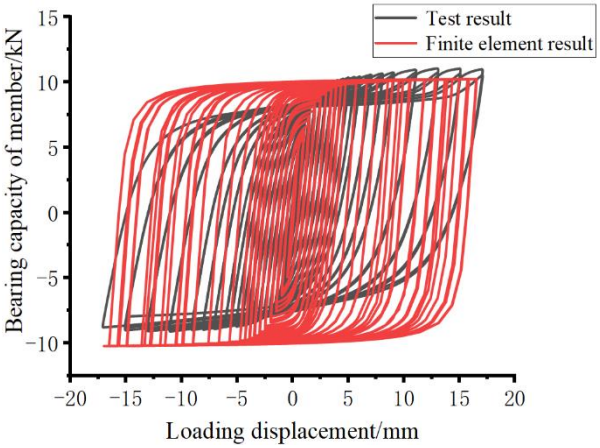

(c) Honeycomb regular hexagonal bidirectional type

Fig. 18 Hysteresis curve comparison

Acknowledgements

We thank the Key Laboratory for Disaster Prevention and Reduction of Civil Engineering in Western China, the Civil Engineering Laboratory of

Lanzhou University of Technology, and the joint efforts of all teachers and students. We would like to thank Editage (www.editage.cn) for English language editing.

Funding: This work was supported by the National Natural Science Foundation of China [grant number 51968043].

References

[1] Y. Zhou, Q. Liang, X. Fang, A review on the earthquake-induced structural pounding, China Civ. Eng. J. 52, 12–22, 2019. (in Chinese).
[2] G. Tselentis, The Athens earthquake of 7 September 1999, Bull. Seismol. Soc. Am. 90, 1143–1160, 2000. https://doi.org/10.1785/0119990168.
[3] G.L. Cole, R.P. Dhakal, F.M. Turner, Building pounding damage observed in the 2011 Christchurch earthquake, Earthquake Engng Struct. Dyn. 41, 893–913, 2012. https://doi.org/10.1002/eqe.1164.
[4] Y. Liu, M. Nishiyama, M. Tani, M. Kurata, K. Iwata, Steel beam with web opening reinforced by induction heating, J. Constr. Steel Res. 176, 106399, 2021. https://doi.org/10.1016/j.jcsr.2020.106399.
[5] V. Gattulli, F. Potenza, U. Di Sabatino, Dissipative coupling for the seismic enhancement of adjacent structures, Eng. Struct. 199, 109520, 2019. https://doi.org/10.1016/j.engstruct.2019.109520.
[6] H. Gokdemir, Failure of horizontal support system to adjacent buildings during reconstruction in Eskisehir, Eng. Fail. Anal. 103 (2019) 82–94. https://doi.org/10.1016/j.engfailanal.2019.04.041.
[7] Li G, Li H N. Experimental study and application in steel structure of ‘dual functions’ metallic damper[J]. Advanced Steel Construction, 9(3), 247-258, 2013.
[8] W. Wang, J. Wang, S.Q. Su, H. Zhang, Y. Liang, Z.-X. Xiang, Experimental research on mechanical behavior of corrugated antisymmetric mild steel damper, J. Build. Struct. 41, 92–100, 2020. (in Chinese).
[9] Wu Zhenhao, Zhuang Liangdong, Huang Yuan. Development and application of a new restoring force model for metallic dampers[J/OL]. China Civil Engineering Journal: 1-12. (In Chinese)
[10] W. Guo, C.-Z. Ma, C. Zeng, Experimental study of a novel steel strip damper, Build. Struct. 48(2), 413–417, 2018. (in Chinese).
[11] Köroğlu M A, Köken A, Dere Y. Use of different shaped steel slit dampers in beam to column connections of steel frames under cycling loading[J]. Advanced Steel Construction, 14(2), 251-273, 2018.
[12] Zhang Y, Li Z, Zhao W, et al. A performance study of beam column connections of self-centering steel frame with U-shaped steel dampers[J]. Advanced Steel Construction, 12(4): 446-465, 2016.
[13] Chen Z, Fan H, Bian G. Parametric analysis of shear panel dampers under high axial compression[J]. Advanced Steel Construction, 11(1): 1-14, 2015.
[14] Teruna D R, Majid T A, Budiono B. Experimental study of hysteretic steel damper for energy dissipation capacity[J]. Advances in Civil Engineering, 2015, 2015: 1-12.
[15] Dutta S C, Majumder R. Shape memory alloy (SMA) as a potential damper in structural vibration control[C]//Advances in Manufacturing Engineering and Materials: Proceedings of the International Conference on Manufacturing Engineering and Materials (ICMEM 2018), 18–22 June, 2018, Nový Smokovec, Slovakia. Springer International Publishing, 2019: 485-492.
[16] Qiu C, Wang H, Liu J, et al. Experimental tests and finite element simulations of a new SMA-steel damper[J]. Smart Materials and Structures, 2020, 29(3): 035016.
[17] Suzuki K, Watanabe A, Saeki E. Development of U-shaped steel damper for seismic isolation system[J]. Nippon Steel Technical Report, 2005, 92: 56-61.
[18] Bagheri S, Barghian M, Saieri F, et al. U-shaped metallic-yielding damper in building structures: Seismic behavior and comparison with a friction dmper[C]//Structures. Elsevier, 2015, 3: 163-171.
[19] Khatibinia M, Jalaipour M, Gharehbaghi S. Shape optimization of U-shaped steel dampers subjected to cyclic loading using an efficient hybrid approach[J]. Engineering Structures, 2019, 197: 108874.
[20] Gagnon L, Morandini M, Ghiringhelli G L. A review of friction damping modeling and testing[J]. Archive of Applied Mechanics, 2020, 90: 107-126.
[21] Monir H S, Zeynali K. A modified friction damper for diagonal bracing of structures[J]. Journal of Constructional Steel Research, 2013, 87: 17-30.
[22] Lee C H, Kim J, Kim D H, et al. Numerical and experimental analysis of combined behavior of shear-type friction damper and non-uniform strip damper for multi-level seismic protection[J]. Engineering Structures, 2016, 114: 75-92.
[23] National Standard of the People’s Republic of China. GB/T 228. 1-2010 Metallic materials-Tensile testing-Part 1: Method of test at room temperature. Beijing: Standards Press of China. 9–19, 2010. (in Chinese).
[24] Y. Chen, T. Liu, H.-J. Jiang, Z.-W. Wan, Experimental study on mechanical properties of annular Q235 steel dampers, J. Build. Struct. 39, 139–147, 2018. (in Chinese).
[25] A. Baird, T. Smith, A. Palermo, et al., Experimental and numerical study of U-shape flexural plate (UFP) dissipaters, in: Technical Conference and AGM, Auckland, NZ, 21–23 March 2014, New Zealand Society for Earthquake Engineering, 2014 paper Number P2.

Advanced Steel Construction – Vol. 20 No. 1 (2024) 69–80
DOI:10.18057/IJASC.2024.20.1.8

SEISMIC PERFORMANCE AND REPLACEABILITY OF STEEL FRAME STRUCTURES WITH REPLACEABLE BEAM SEGMENTS

Ling-Yun Zhao [1], Dang Guo [2], Yuan-Qiang Yang [1], Yan-Song Diao [1, *] and Xiu-Li Liu [1]

[1] *School of Civil Engineering, Qingdao University of Technology, Shandong Qingdao 266033, China*
[2] *The First Company of China Eighth Engineering Division Ltd, Shandong Jinan 250000, China*
** (Corresponding author: E-mail: diaoys@163.com)*

ABSTRACT

This study assessed the seismic performance and replaceability of steel frame structures incorporating replaceable beam segments. A reduced-beam-section beam-column joint featuring a replaceable energy dissipation beam segment was specifically designed for this purpose. The joint underwent quasi-static analysis subjected to low-cycle reciprocating loading. The study extended to a single-story, single-span plane steel frame, where reduced-beam-section beam-column joints with replaceable energy dissipation beam segments were analyzed for hysteretic and deformation behavior. Moreover, the exploration of parameters such as end-plate opening clearance and rotation deformation was undertaken to inform the simplification of the overall plane frame model. Meanwhile, multi-scale models were developed for an eight-story, four-span, reduced-beam-section steel frame (RBSSF) with a replaceable energy dissipation beam segment and a rigid steel frame (RSF). These models were employed to analyze the elastoplastic time-history characteristics and the replaceability of the beam segment. The results demonstrated that the reduced-beam-section beam-column joint with a replaceable energy dissipation beam segment exhibited a relatively full hysteresis curve, affirming high ductility, energy dissipation, and plastic deformation capacities. Notably, damage and plastic development in the steel beam primarily concentrated in the low-yield-point replaceable energy dissipation beam segment. The small end-plate opening clearance ensured cooperative deformation between the end plates facilitated by the bolts. Comparatively, the RBSSF structure displayed superior seismic performance to the RSF structure during earthquakes, with the replaceable energy dissipation beam segment satisfying replaceability requirements under moderate seismic conditions.

ARTICLE HISTORY

Received: 30 June 2023
Revised: 11 January 2024
Accepted: 29 January 2024

KEYWORDS

Multi-scale model;
Replaceability;
Replaceable energy dissipation beam segment;
Seismic performance;
Steel frame

Copyright © 2024 by The Hong Kong Institute of Steel Construction. All rights reserved.

1. Introduction

Traditional seismic structural designs typically focus on augmenting the strength, stiffness, or ductility through effective seismic measures to avoid brittle failure or collapse. However, this approach often results in plastic damage and residual deformation, presenting challenges in terms of repair [1]. Structures incorporate energy dissipation components or isolation layers to mitigate seismic responses and damage [2]. Recently, the concept of resilient structures has been introduced in seismic engineering. These structures meet the basic performance requirements and can recover and maintain functionality after an earthquake, which ensures safety, facilitates efficient post-disaster relief operations, and enables rapid reconstruction. Scholars have extensively evaluated and discussed resilient structural systems, considering various aspects such as structure, community, city, and society [3]. Resilient structures have emerged as a central focus and development direction in seismic engineering. A resilient structure [4,5] integrates rocking [6-12], self-centering [13-21], replaceable components [22-24], and additional energy dissipation devices [25-27] to diminish the structural response, damage, and residual deformation during earthquakes. The strategic placement of replaceable energy dissipation members in parallel with rocking or self-centering mechanisms contributes to diverse and resilient structural systems, maximizing their effectiveness.

Luo [28] innovatively designed a beam-column joint based on damage control principles. The joint incorporated an L-shaped plate with a stable connection to the main structure, possessing robust plastic deformation capability. This plate was the primary damage element, and its replaceability after damage was a notable feature. Shen et al. [29] conducted a quasi-static test on beam-column joints employing reduced-beam end-plate-bolted and web-channel-bolted connections. The results revealed the independent control of joint strength and stiffness, superior energy dissipation capacity for the end-plate-bolted segment, larger plastic angle for the web-channel-bolted connection, and efficient beam segment inspection and replacement after damage. Wang et al. [30] conducted experiments and numerical analysis on a reduced replaceable beam joint, demonstrating its efficacy in damage control, along with commendable hysteretic energy dissipation and replaceability. Zhang et al. [31] performed a pseudo-dynamic test on a scale sub-structure model of a web friction-type prestressed steel frame structure. Their findings showed reduced cable force loss, minimized residual deformation, and the realization of post-earthquake self-centering and structural function recovery through effective mechanisms, such as gap opening and closing and friction energy dissipation. Castiglioni et al. [32] conducted an experimental study on a beam-column joint featuring replaceable rectangular steel plate webs, confirming stable hysteretic energy dissipation characteristics and high ductility. Oh et al. [33] proposed a seismic performance-enhancing metal damper at the end of a steel beam, demonstrating effective energy dissipation and concentrated plastic deformation on a replaceable steel plate damper with a slit, leading to a favorable hysteretic performance. Shao and Chen [34] engineered a beam-column joint incorporating angle steel as the energy dissipation component, showcasing excellent hysteretic energy dissipation. Angle steel functioned as a "damage fuse" and could be readily replaced post-damage. Hu [35] introduced a high-strength steel beam-column joint with a fused connection plate, demonstrating its ability to meet load-bearing capacity demands and concentrate damage through a quasi-static test, and emphasized the pivotal role of connection plate strength in seismic performance. He et al. [36] conducted a quasi-static analysis of a beam-column joint filled with low-yield-point steel at weakened positions of the steel beam flanges and webs. The analysis indicated high ductility and energy dissipation capacity but highlighted significant buckling deformation of the steel beam. Wang et al. [37] designed a beam-column joint with a low-yield-point steel connection component, demonstrating through quasi-static analysis its effectiveness as a fuse with commendable hysteretic energy dissipation capacity. The load-bearing capacity coefficient emerged as a crucial factor influencing the joint's seismic performance. Chi and Liu [38] proposed a post-tensioned self-centering column base incorporating a buckling restrained steel plate, with a quasi-static test confirming no structural damage at a 4% rad displacement angle. The buckling restrained steel plate emerged as the primary source of energy dissipation, resulting in stable hysteretic behavior.

Current investigations into the replaceable form of steel frame structures have primarily focused on integrating various replaceable energy dissipation components at the beam end and column base. Scarce attention has been paid to researching the seismic performance and replaceability of the beam segment itself within a steel frame structure featuring a replaceable energy dissipation beam segment. Consequently, this study focused on the design of a reduced-beam-section beam-column joint incorporating a replaceable energy dissipation beam segment. The seismic performance and beam replaceability of the resulting reduced-beam-section steel frame (RBSSF) were examined, and the findings were compared with those of a conventional rigid steel frame (RSF).

2. Seismic performance of a beam-column joint with a replaceable energy dissipation beam segment

2.1. Design of the joint

The design of the reduced-beam-section beam-column joint, featuring a

replaceable energy dissipation beam segment, adhered to established standards, including the Chinese standard for the design of steel structures (GB50017-2014) [39], Chinese code for seismic design of buildings (GB50011-2010) [40], AISC 358-16 [41], and pertinent provisions and studies [29]. The specific parameters of the joint are detailed in Table 1.

Table 1
Parameters of the designed joint model

Segment	Steel beam	Column	Replaceable beam segment
Section size	H400×250×12×20	□400×400×30	H400×220×12×20
Steel grade	Q235B	Q345B	LYP160

2.2. Establishment of finite element model

In this study, we established a numerical model of the joint using the finite element software ABAQUS. The C3D8R element was employed for all members, with the normal contact direction set as "hard" and the tangent direction as the "penalty function", incorporating a friction coefficient of 0.45 [39]. The high-strength bolts followed a bilinear constitutive model, while the other steels adopted a trilinear constitutive model, as illustrated in Fig. 1. Pertinent parameters are detailed in Table 2. Von Mises yield criterion and mixed-hardening criterion [42] were selected, and the loading system adhered to the American AISC seismic code provisions [43]. The finite element model subjected to low-cycle cyclic loading translated the story drift angle into beam-end displacement. The loading amplitude curve is depicted in Fig. 2, and the node model is presented in Fig. 3.

Table 2
Material properties of the steel frame joint

Material	Stress (N/mm^2)			Strain (%)			Elastic modulus (N/mm^2)	Poisson ratio
	σ_y	σ_u	σ_t	ε_y	ε_u	ε_t	E	M
Q235	235	420	330	0.114	15	22	206000	0.3
Q345	345	554	480	0.167	25	36	206000	0.3
LYP160	160	273	230	0.077	28.6	54	206000	0.3
High strength bolt	945	1254	-	0.456	9	-	206000	0.3

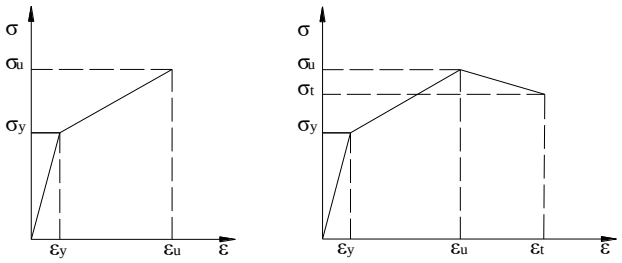

(a) (b)

Fig. 1 Constitutive model of the steel frame joint: (a) Bilinear constitutive model, (b) Trilinear constitutive model

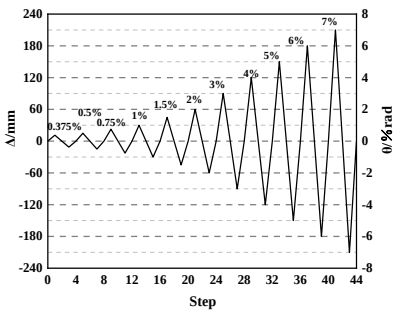

Fig. 2 Loading amplitude curve

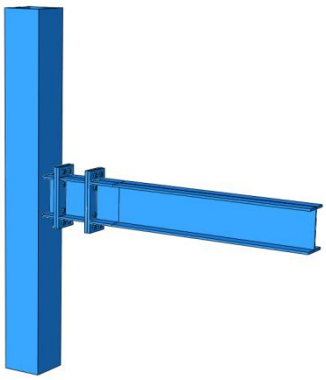

Fig. 3 Model of reduced beam section joint

2.3. Verification of the finite element modeling method

To validate the finite element model described earlier, an experimental model featuring a fabricated steel frame joint splicing a Z-shaped cantilever beam segment [44] was simulated using the finite element method. The finite element model utilized C3D8R solid elements for each segment, and other parameters and boundary conditions were derived from the reference [44]. The resulting model is depicted in Fig. 4. A comparison between the experimental and finite element simulation results is presented in Fig. 5.

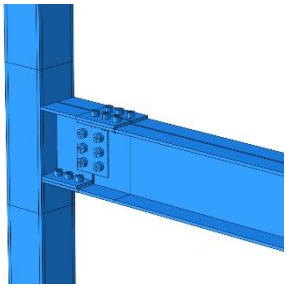

Fig. 4 Finite element model of the experimental model [44]

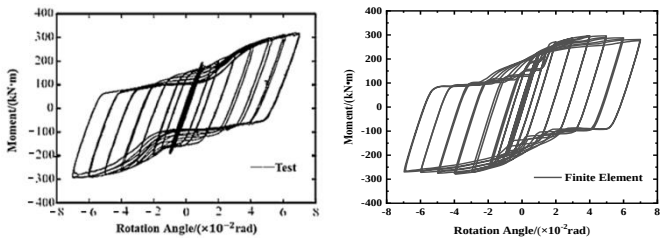

(a)

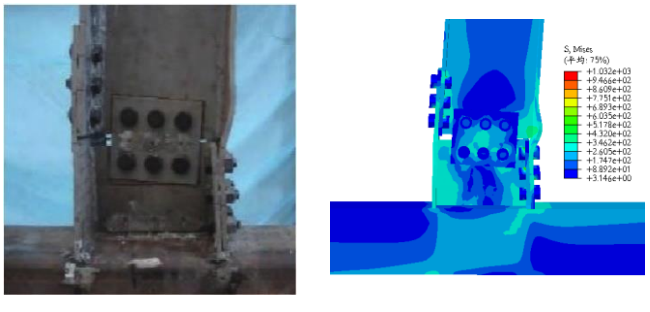

(b)

Fig. 5 Comparison between the experimental and finite element simulation results: (a) Comparison of hysteresis curves, (b) Comparison of failure modes

Fig. 5 illustrates that the hysteresis curve and failure mode of the finite element model aligned with the test results, and the simulation accurately captured the plate slip. This confirms the viability of the finite element modeling method employed in this study and establishes the reliability of the analysis results.

2.4. Results of finite element analysis

2.4.1. Hysteresis curves

The hysteresis curve depicted in Fig. 6 represents the load-displacement (P–Δ) characteristics of the designed joint under cyclic loading. The curve directly elucidates the seismic performance of the designed joint.

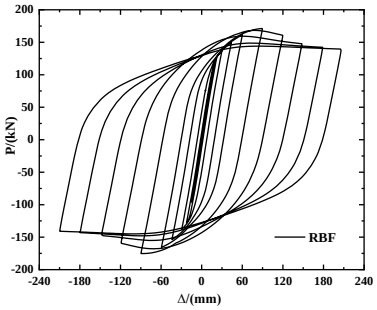

Fig. 6 Hysteresis curve of the designed joint

The joint exhibited elasticity during the initial loading stages, resulting in a small area in the hysteresis curve. As the displacement load at the beam end increased, the joint transitioned to the elastic-plastic stage, as evidenced by the decreased slope of the curve, indicating stiffness degradation. Concurrently, the load-bearing capacity and deformation increased, leading to a fuller hysteresis curve. Upon reaching the ultimate load, a further increase in the displacement load at the beam end led to a gradual decline in the joint's load-bearing capacity. Consideration of joint destruction occurred when the load-bearing capacity reached 85% of the ultimate load.

2.4.2. Backbone curve

The backbone curve represents the envelope of the load extreme points on the hysteresis curve at each loading level. It serves as a crucial reference for identifying the characteristic points of the joints. The depicted backbone curve of the designed joint is presented in Fig. 7.

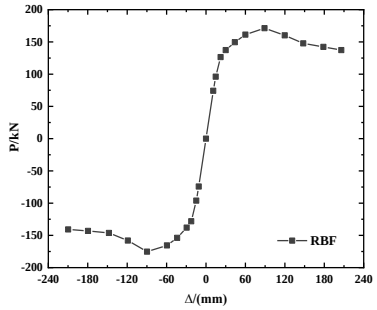

Fig. 7 Backbone curve of the designed joint

Table 3
Comparison of the load and displacement at different characteristic points

Joint type		Yield		Ultimate		Destroy	
		P_y (kN)	Δ_y (mm)	P_{max} (kN)	Δ_{max} (mm)	P_u (kN)	Δ_u (mm)
Reduced beam section	Positive	140.37	33.79	171.20	89.12	145.52	162.13
	Negative	154.13	45.33	-175.25	89.75	148.96	143.09

In Fig. 7, it is evident that the positive and negative backbone curves of the designed joint lack complete symmetry, possibly attributed to the Bauschinger effect. Initially, the backbone curve approximated a straight line during the initial loading stage. As the displacement load at the beam end increased, the slope of the backbone curve gradually decreased, deviating from a straight line. Nevertheless, the joint load-bearing capacity continued to increase, peaking at the ultimate load-bearing capacity before progressively declining until the joint failed.

In this study, the geometrography method determined the equivalent yield point of the joint. The ultimate load corresponded to the peak point on the backbone curve, with the corresponding displacement identified as the ultimate displacement. Joint failure was recognized at 85% of the ultimate load, and the associated displacement was termed failure displacement [45]. Table 3 presents a comparison of the load and displacement of the designed joint at the three characteristic points.

2.4.3. Stiffness degradation curve

Stiffness degradation denotes a gradual reduction in the specimen stiffness as the applied load increases, serving as an indicator of material damage. This phenomenon is quantified by the secant stiffness K_i [45].

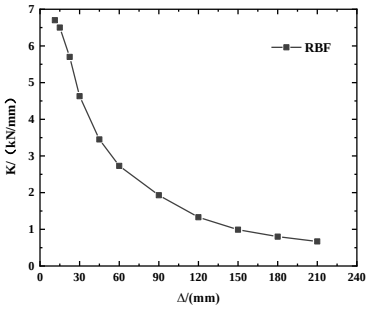

Fig. 8 Stiffness degradation curve of the designed joint

As shown in Fig. 8, the stiffness degradation curve of the reduced-beam-section beam-column joint, featuring a replaceable energy dissipation beam segment, exhibited an initial rapid decline in stiffness, followed by a comparatively slower decrease in the later stage.

2.4.4. Ductility and energy dissipation capacity

The seismic performance of joints is commonly evaluated using parameters such as ductility coefficient, total energy consumption (W_t), equivalent viscous damping coefficient (ζ_{eq}), and energy dissipation coefficient (E). These parameters are detailed in Table 4.

Table 4
Ductility coefficient and energy consumption index of the designed joint

Displacement ductility coefficient μ			W_t (kN·m)	ζ_{eq}	E
Positive	Negative	Mean			
4.79	3.16	3.98	334.45	0.48	3.01

The analysis in Table 4 revealed that the mean value of the displacement ductility coefficient (μ) for both the positive and negative directions was 3.98, indicating a high level of ductility in the designed joint. The joint exhibited an equivalent viscous damping coefficient (ζ_{eq}) of 0.48, coupled with a large hysteresis area and high total energy consumption, indicating a commendable seismic energy dissipation capacity.

2.4.5. End-plate opening analysis

This section investigated the opening and closing clearance of the joint end plate, laying the groundwork for the subsequent simplification of the overall model. Measuring points 1–9 on the joint end plate were strategically chosen for studying the opening clearance, with points 2, 4, 6, and 8 aligned with the bolt axis positions, as illustrated in Fig. 9.

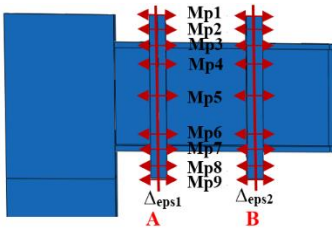

Fig. 9 Layout of measuring points (Mp)

The relationship curve, Δ_{eps}-θ_b, between the opening and closing clearances of the end plate and the beam-end rotation angle under low-cycle cyclic loading is depicted in Fig. 10. Here, the clockwise direction was considered positive for beam-end rotation, whereas counterclockwise was negative.

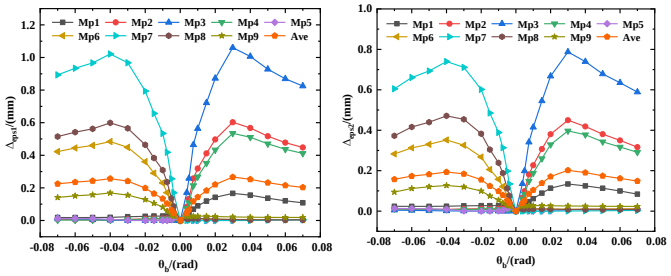

(a) (b)

Fig. 10 Relationship between end-plate opening and closing clearance and beam-end rotation angle: (a) Position A, (b) Position B

Throughout the loading process, as damage and plastic development predominantly occurred in the replaceable energy dissipation beam section, the opening clearance of the end plate remained minimal. Consequently, the bolts ensured close contact, fostered coordinated deformation between the end plates, and facilitated a stable force transfer mechanism for this connection mode.

2.5. Establishment and performance verification of the simplified joint model

2.5.1. Establishment of the simplified joint model

This section established and analyzed a simplified model of a reduced-beam-section beam-column joint featuring a replaceable energy dissipation beam segment. The coordinated deformation between the end plates, as revealed in the analysis of the joint end plate opening (Section 2.3.5) and the single-story single-span end plate (Section 3.2.2), prompted the removal of high-strength bolts in the simplified joint model based on the refined joint model. Instead, a tie constraint was implemented for the end plate contact, resulting in the simplified joint model depicted in Fig. 11.

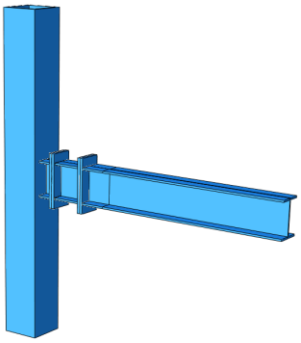

Fig. 11 Simplified joint model

2.5.2. Verification of mechanical properties of the simplified joint model

A quasi-static analysis was conducted to validate the accuracy of the simplified joint model for simulating the mechanical performance of the joint. The hysteresis and backbone curves of the simplified joint model were obtained and compared with those of the refined joint model, as illustrated in Figs. 12 and 13. Table 5 presents a comparison of the element number and calculation time between the refined and simplified joint models.

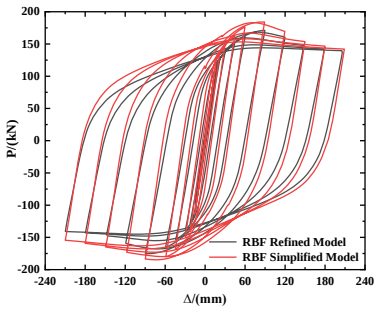

Fig. 12 Comparison of hysteresis curve of the refined and the simplified joint models

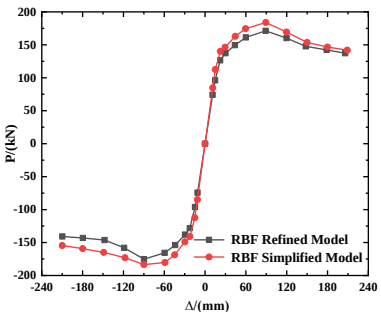

Fig. 13 Comparison of the backbone curve of the refined and the simplified joint models

Figs. 12 and 13 show a slightly higher load-bearing capacity in the simplified joint model than in the refined joint model. This discrepancy is attributed to the enhanced stiffness of the end plates resulting from the binding constraints. However, the hysteresis and backbone curves of both models were aligned, confirming the accurate simulation of the mechanical properties using the simplified joint model.

Table 5
Comparison of element number and calculation time between the refined and simplified joint models

Models	Number of elements	Calculation time (min)	Efficiency (%)
Refined model	66550	694	-
Simplified model	27430	159	336

Note: The computer for these simulations was equipped with an Intel Core i9-7980XE CPU operating at 2.6 GHz, 16 GB RAM, and an NVIDIA GeForce RTX 2080 GPU with 16 GB memory.

3. Seismic performance and end-plate deformation analysis of single-story, single-span plane frame

3.1. Establishment of finite element model

The modeling method, contact setting, and material constitutive relationship for the single-story, single-span plane frame model were consistent with those detailed in Section 2.2. To expedite convergence and reduce the computation time, connectors were utilized to streamline the representation of the bolts. Despite the advantage of eliminating the need to define the contact and mesh, connectors do not capture the response of bolts. A fixed constraint was implemented at the bottom of the column to restrict the out-of-plane displacement. Additionally, a reciprocating horizontal displacement load was applied to the column coupling point (RP-1) on the left side of the frame, as illustrated in Fig. 14. The loading system is further illustrated in Fig. 15.

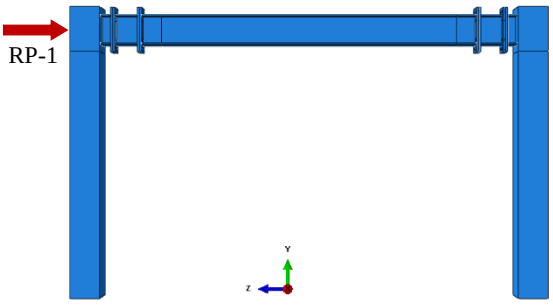

Fig. 14 Single-story single-span plane frame

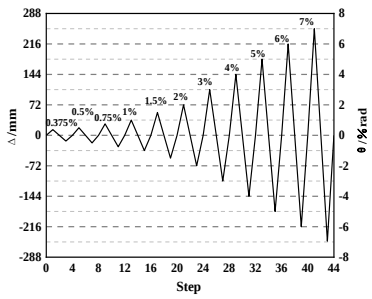

Fig. 15 Loading amplitude curve of column end

3.2. Analysis of finite element calculation results

3.2.1. Hysteresis curve

The load-displacement (P-Δ) curve of the single-story single-span plane frame is depicted in Fig. 16.

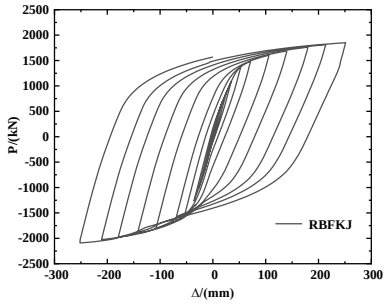

Fig. 16 Hysteresis curve of the RBF plane frame

During the initial loading stage, the plane frame structure exhibited an elastic state, resulting in a limited hysteresis curve area. As the horizontal displacement of the column end gradually increased, the structure transitioned into an elastoplastic state, accompanied by a decreasing curve slope, indicative of stiffness degradation. Simultaneously, the load-bearing capacity and deformation increased, leading to an expanded hysteresis curve. Notably, the hysteresis curve displayed a continuous shuttle-shaped loop throughout the loading process, suggesting excellent plastic deformation and energy dissipation capacity in the single-story, single-span plane steel frame with reduced-beam-section beam-column joints featuring a replaceable energy dissipation beam segment.

3.2.2. End plate opening analysis

In this section, an examination of the opening and closing clearance of the end plate was conducted, laying the groundwork for overall model simplification. Measuring points 1–9 on the end plate of the single-story, single-span plane steel frame were selected to study the opening clearance, and their layout is depicted in Fig. 17. Among these, measuring points 2, 4, 6, and 8 corresponded to the positions of the bolt axis.

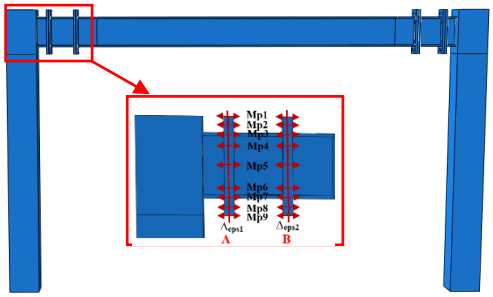

Fig. 17 Layout of opening clearance measuring points (Mp)

The Δ_{eps}-θ_c curve, depicting the relationship between the opening and closing clearances of the end plate and the beam end rotation angle under horizontal low-cycle cyclic loading, is presented in Fig. 18. Notably, the beam end rotation direction was considered positive in the clockwise direction and negative in the counterclockwise direction.

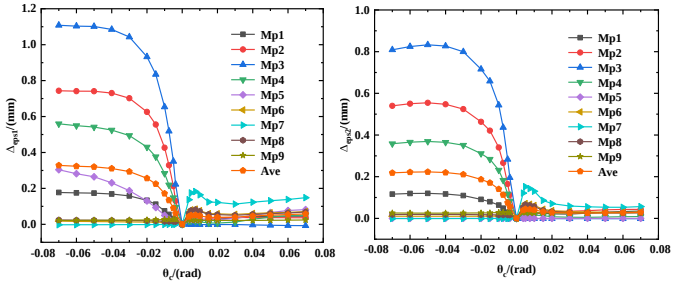

(a) (b)

Fig. 18 Relationship between the opening and closing clearance of the end plate and the beam end rotation angle: (a) Position A, (b) Position B

Fig. 18 illustrates that throughout the loading process, the opening clearance of the end plate remained minimal due to the concentration of damage and plastic development in the replaceable energy dissipation beam section of the steel beam. Consequently, the bolts ensured close contact and coordinated deformation between the end plates, facilitating a stable force transfer mechanism in this connection mode. The discrepancies in the end-plate opening and closing clearance curves between the joint and the single-story single-span plane steel frame can be attributed to the different loading positions: the joint loaded at the beam end and the frame loaded at the column end. A subsequent study of the frame structure with this joint ignored the effect of the end-plate opening.

3.2.3. Analysis of the end-plate rotation angle

In this section, the horizontal displacements of measuring points 1–9 at positions A and B of the single-story, single-span plane frame end plate are extracted and presented in Fig. 19. This study investigated the rotation angle, flatness of the end plate under different loading displacements, and replaceability of the replaceable energy dissipation beam section after an earthquake. The relationship between the end-plate height and the horizontal displacement of measuring points 1–9 (D_{ep}-Δ_{eps} curve) under varying rotation angles of the column end is depicted in Fig. 20. Furthermore, the analysis results of the rotation angle at positions A and B of the end plate are summarized in Table 6.

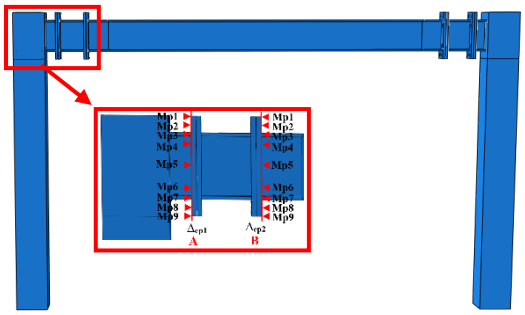

Fig. 19 Measuring points (Mp) of the end-plate displacement

Table 6
Analysis results of the rotation angle at positions A and B of the end plate

Rotation angle at column end (rad)	Rotation angle at position A (rad)	Relative rotation angle (rad)	Rotation angle at position B (rad)	Relative rotation angle (rad)
0.00375	0.0025	-0.00125	0.0013	-0.00245
0.005	0.0044	-0.0006	0.0015	-0.0035
0.0075	0.0076	0.0001	0.0008	-0.0067
0.01	0.0113	0.0003	0.0001	-0.0099
0.015	0.0181	0.0031	-0.0014	-0.0164
0.02	0.0241	0.0041	-0.0026	-0.0226
0.03	0.0353	0.0053	-0.0048	-0.0348
0.04	0.0464	0.0064	-0.0072	-0.0472
0.05	0.0593	0.0093	-0.0099	-0.0599
0.06	0.0702	0.102	-0.0125	-0.0725
0.07	0.0823	0.0123	-0.0155	-0.0855

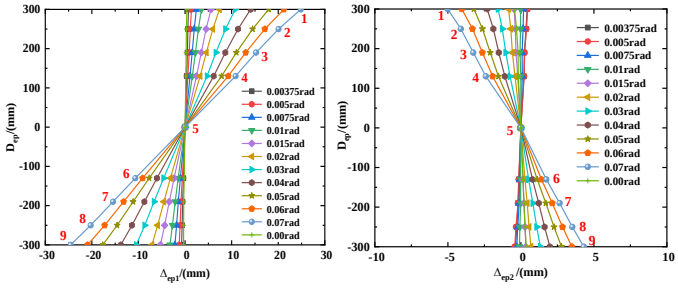

(a) (b)

Fig. 20 Displacement curve of the end plate: (a) Position A, (b) Position B

The displacements of measuring points 1–9 at positions A and B formed approximately straight lines during the loading process. This suggests the absence of significant buckling on the end plate, ensuring its flatness. Consequently, the connection between the end plates remained relatively stable, and the end plate deformation was minimal. These conditions meet the anticipated construction and replacement requirements, facilitating the post-earthquake replacement of the replaceable energy dissipation beam section.

4. Dynamic elastoplastic time-history analysis of steel frames

To assess the seismic performance of the plane steel structure featuring the designed joint, this section conducted an elastoplastic time-history analysis on an eight-story, four-span RBSSF with a replaceable energy dissipation beam segment and an RSF.

4.1. Project profile

The structure's specifications included a 4.2 m height for the bottom floor, a 3.6 m for the remaining floors, and a 6.0 m span. The seismic fortification intensity was Richter magnitude 8 (0.2 g), with a class II site classification. The designed earthquake fell under group I, with an aseismic grade of III and a designated service life of 50 years. The standard dead (live) load values were 5.0 (2.0) kN/m^2. The section sizes and steel properties of the steel beam, column, and replaceable beam segment are detailed in Table 7.

Table 7
Parameters of the steel frame

Segment	1st–3rd floor	4th–6th floor	7th and 8th floors
Frame beam	H400×250×12×20	H400×250×12×20	H400×250×12×20
Frame column	□400×400×30	□400×400×25	□400×400×20
Replaceable beam segment	H400×220×12×20	H400×220×12×20	H400×220×12×20

4.2. Establishment and validation of the multi-scale model

In this study, multi-scale modeling technology was employed to construct a nonlinear finite element model to enhance the accuracy and efficiency of the seismic performance analysis of steel frames. Multi-scale modeling integrates fine and macro models through the collaboration of different-scale elements. Previous research [46-48] has validated the feasibility of this modeling approach and the associated interface connection method.

The ABAQUS software was utilized to establish the multi-scale plane steel frame model. As shown in Fig. 21, the behavior of the replaceable beam segment and end plate was simulated using solid elements. In contrast, the shell elements modeled the behavior of the node domain and the short beam segment. Additionally, the behavior of the other frame columns and beams was represented using beam elements. The coupling command [42] ensured the connection and collaboration between the shell and beam elements.

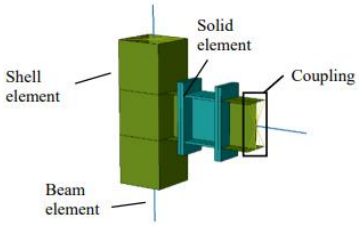

Fig. 21 Multi-scale plane steel frame models of the RBSSF and RSF established in this study for elastoplastic time-history analysis

Fig. 22 depicts the multi-scale plane steel frame models of the RBSSF and RSF established in this study for elastoplastic time-history analysis.

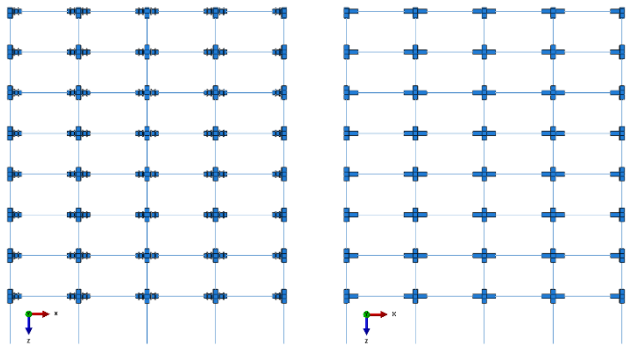

Fig. 22 Schematic diagram of multi-scale plane steel frame structures: (a) RBSSF, (b) RSF

4.3. Modal analysis

Modal analysis of the RBSSF and RSF structures was conducted using ABAQUS software. The first three-order vibration modes of the structures are illustrated in Fig. 23, and the corresponding natural vibration periods and circular frequencies for these modes are provided in Table 8.

Table 8
Natural vibration period and circular frequency of the frame structures

Frame	T_1	ω_1	T_2	ω_2	T_3	ω_3
RBSSF	1.98	3.16	0.64	9.88	0.35	18.11
RSF	1.95	3.21	0.63	10.03	0.34	18.34

Note: T_i and ω_i represent the ith natural vibration period and circular frequency of the structure, respectively.

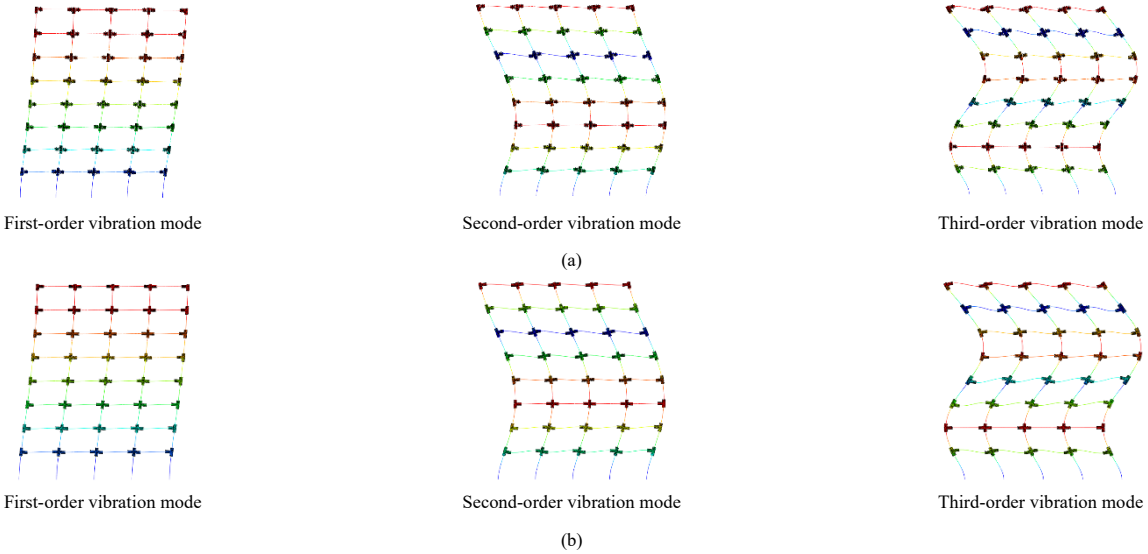

Fig. 23 First three order vibration modes of plane steel frame: (a) RBSSF, (b) RSF

In the elastoplastic time-history analysis of the structure, the impact of damping could not be disregarded. Rayleigh damping was chosen as the structural damping model in this study. The mass damping coefficient (α) and stiffness damping coefficient (β) were determined based on the natural frequency and period of the structure, as outlined in Table 9.

Table 9
Structural damping coefficients α and β

Frame	Mass damping coefficient α	Stiffness damping coefficient β
RBSSF	0.2395	0.00766
RSF	0.2434	0.00755

4.4. Selection of seismic wave

In this study, seismic wave records were meticulously chosen based on parameters such as seismic fortification intensity, seismic intensity grade, and site soil type, following the guidelines from ATC-63 [49] and the Chinese code for seismic design of buildings (GB50010-2010) [40]. Ultimately, the El Centro wave (natural wave), Westmoreland wave (natural wave), and RH4TG035 (artificial wave) were selected for elastoplastic time-history analysis. To ensure consistency in the peak acceleration with the target peak acceleration, the seismic acceleration time-history curves of the three groups of seismic waves were amplitude-modulated to 0.4 g, as illustrated in Fig. 24.

4.5. Determination of performance objectives

This study chose the maximum and residual inter-story displacement angles as the structural demand indices when subjected to earthquake motion, considering the deformation and failure criteria. The prescribed limits for the inter-story and residual inter-story displacement angles under various seismic levels were determined based on prior research [50-53] (Table 10). The scope of the residual inter-story displacement angle primarily governs the replaceability of the energy dissipation beam.

4.6. Time-history analysis results of the steel frame structure under earthquake action

4.6.1. Displacement response analysis of the top floor

The time-history curves depicting the displacement of the RBSSF and RSF structures during frequent, moderate, and rare earthquakes are presented in Figs. 25–27.

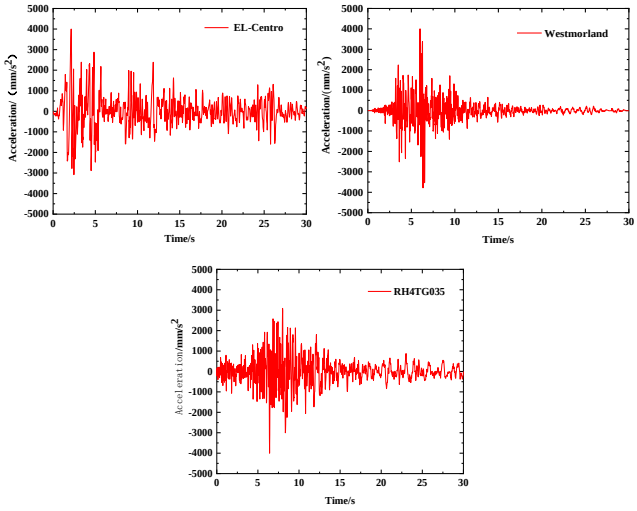

Fig. 24 Seismic acceleration time-history curves after amplitude modulation to 0.4 g

Table 10
Performance level of the steel frame structure with replaceable energy dissipation beam

Seismic level	Performance level	Structural function description	Inter-story displacement angle	Residual inter-story displacement angle
Frequent earthquake	Basically intact Slight damage	The replaceable beam section may experience slight plastic deformation, while the main portion remains elastic, preserving the overall structural integrity.	< 0.4% < 0.8%	< 0.15%
Moderate earthquake	Medium damage	The replaceable beam section incurs additional damage, with slight damage to the main portion, enabling normal functioning after replacing the damaged beam section.	< 1.2%	< 0.5%
Rare earthquake	Severe damage	The replaceable beam section sustains severe damage, leading to varying degrees of damage in the beam and column-bearing members. Partial removal of damaged members allows for the appropriate use of the structure.	< 1.8%	< 1.0%

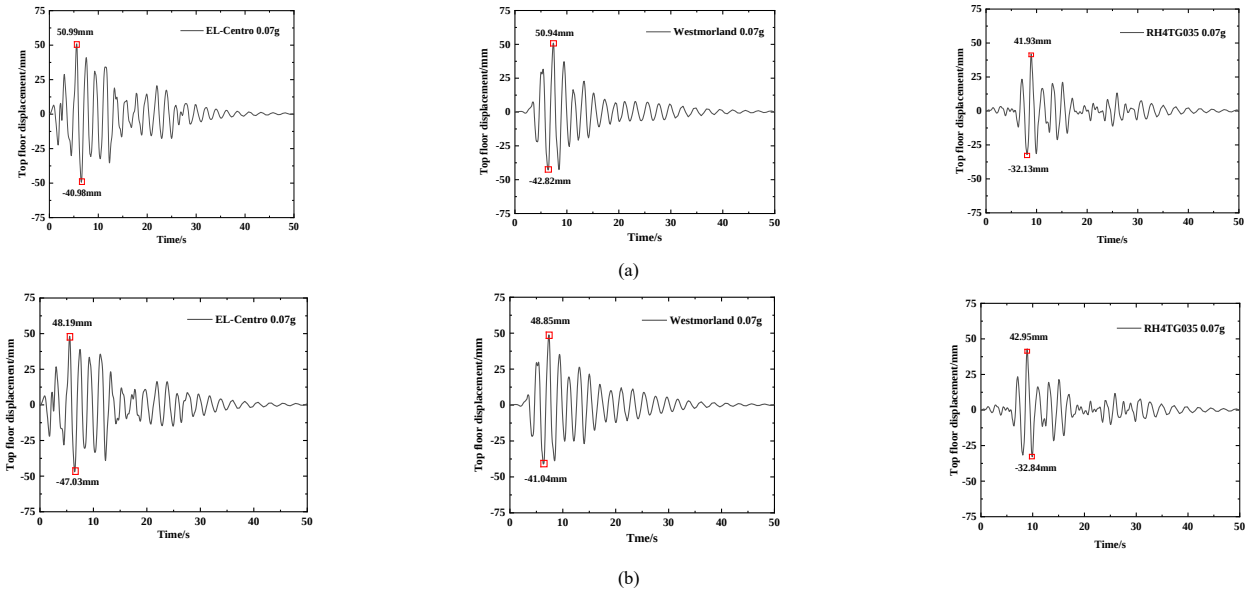

Fig. 25 Time-history curves of the top floor displacement of the steel frame under frequent earthquakes: (a) RBSSF, (b) RSF

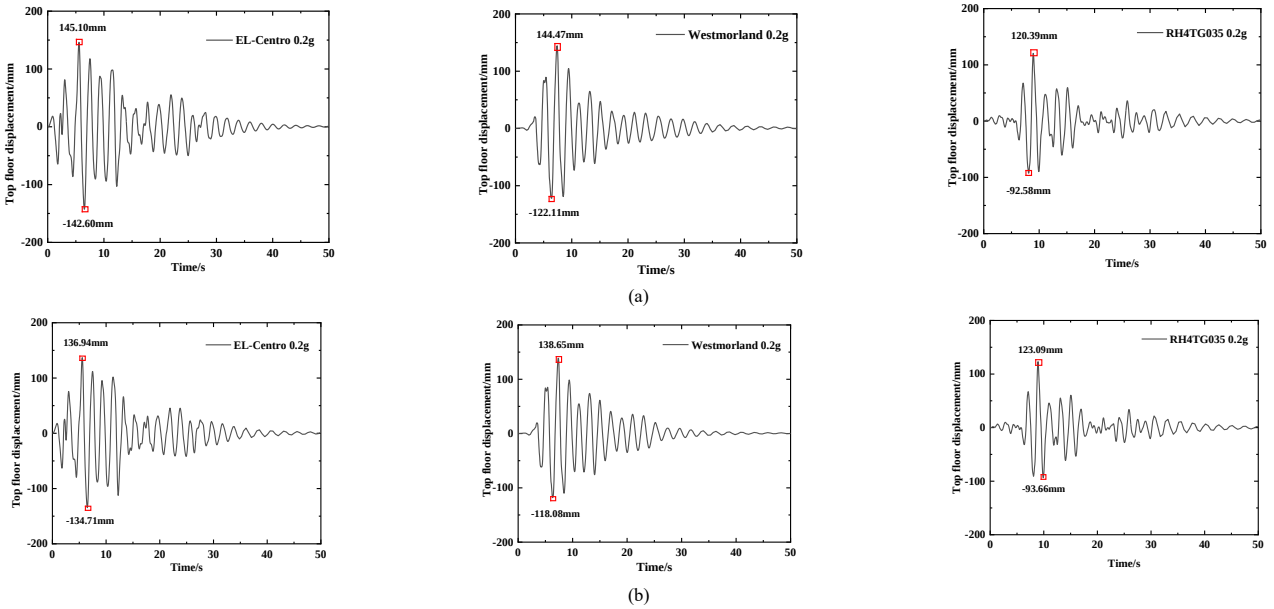

Fig. 26 Time-history curves of the top floor displacement of the steel frame under a moderate earthquake: (a) RBSSF, (b) RSF

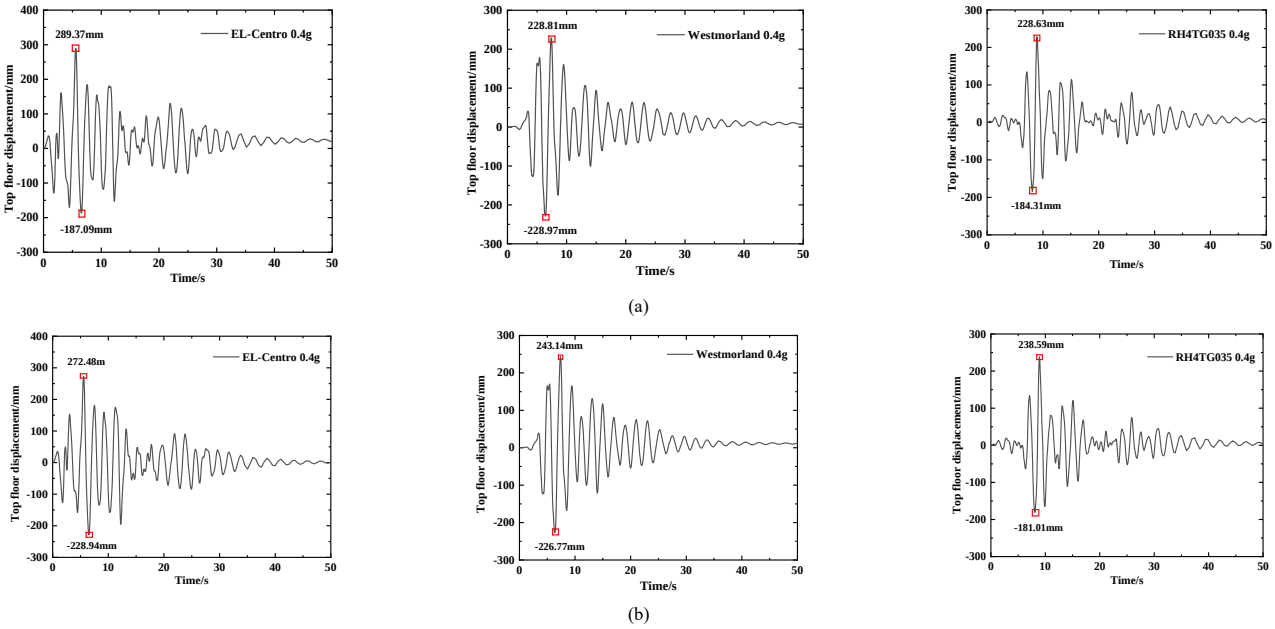

Fig. 27 Time-history curves of the top floor displacement of the steel frame under a rare earthquake: (a) RBSSF, (b) RSF

Figs. 25–27 revealed that the occurrence of the maximum displacement in the RBSSF structure lagged behind that of the RSF structure. However, the time-history curves for the top floor displacement exhibited similar trends for both the structures. Under frequent and moderate earthquakes, the maximum displacement of the RBSSF structure's top floor was slightly larger than that of the RSF structure. This discrepancy may be attributed to the RBSSF structure's reduced beam sections, resulting in an overall smaller stiffness than that of the RSF structure. Conversely, during a rare earthquake, the maximum displacement of the RSF structure's top floor slightly exceeded that of the RBSSF structure. This can be attributed to the full plastic energy dissipation of the replaceable energy dissipation beam section, with damage concentrated mainly in this section. In contrast, the primary structure of the steel frame experienced relatively minor damage.

4.6.2. Shear force response analysis of the base

The time-history curves illustrating the base shear force responses of the RBSSF and RSF structures under frequent, moderate, and rare earthquakes are depicted in Figs. 28–30.

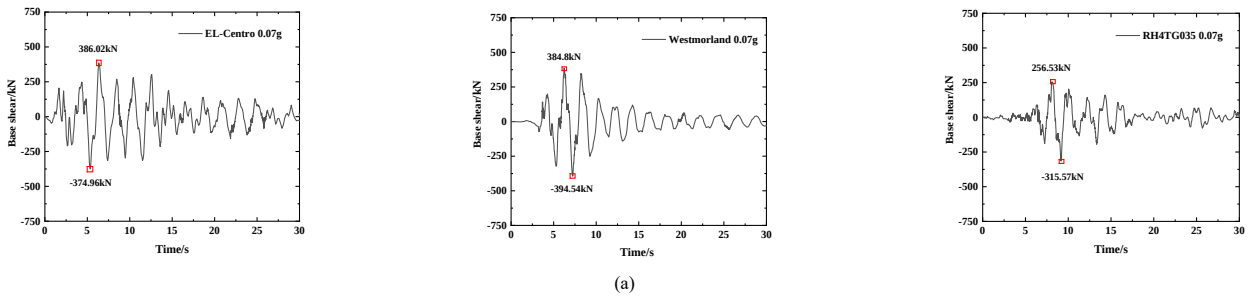

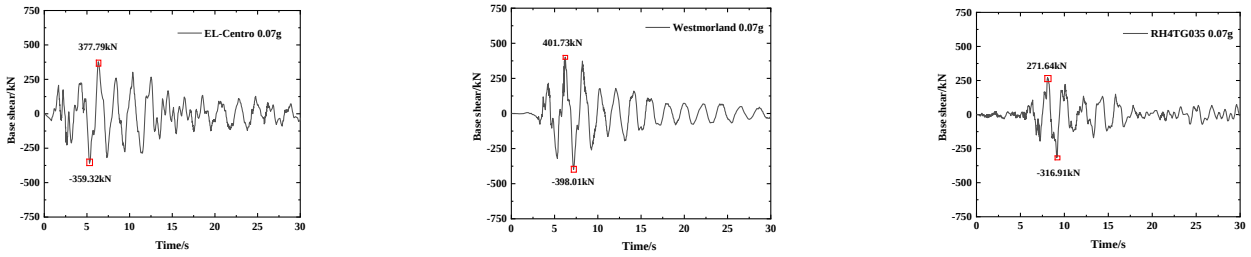

(b)

Fig. 28 Time-history curves of the base shear force of the steel frame under frequent earthquakes: (a) RBSSF, (b) RSF

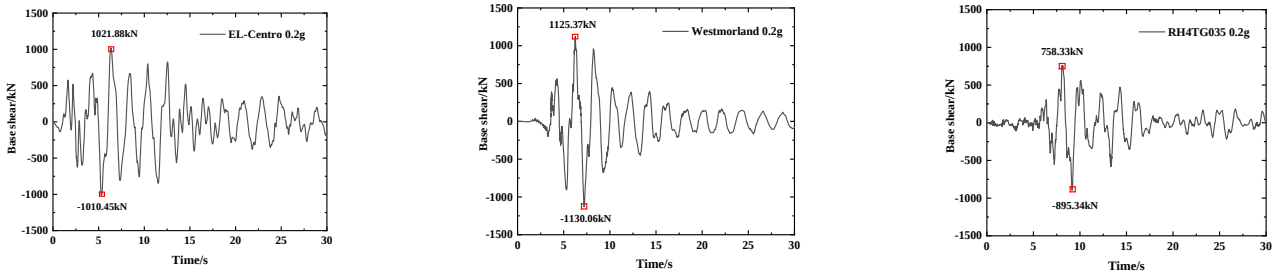

(a)

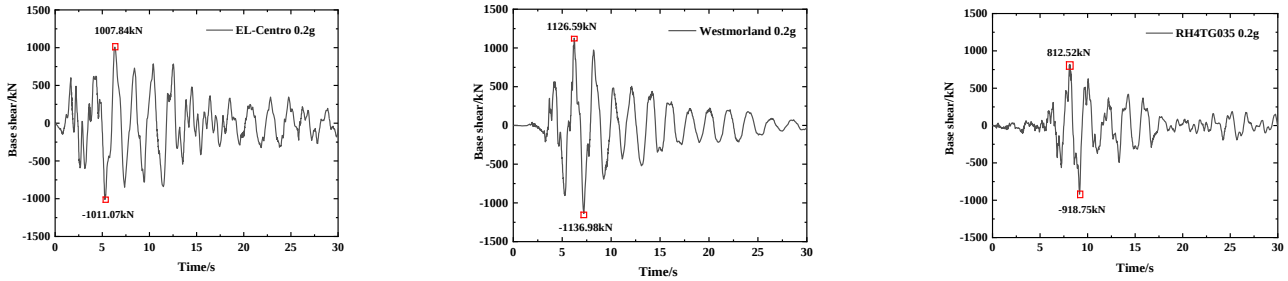

(b)

Fig. 29 Time-history curves of the base shear force of the steel frame under a moderate earthquake: (a) RBSSF, (b) RSF

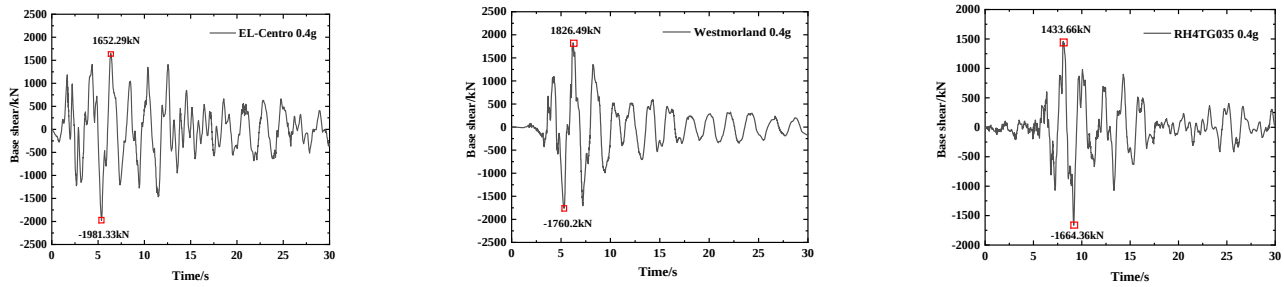

(a)

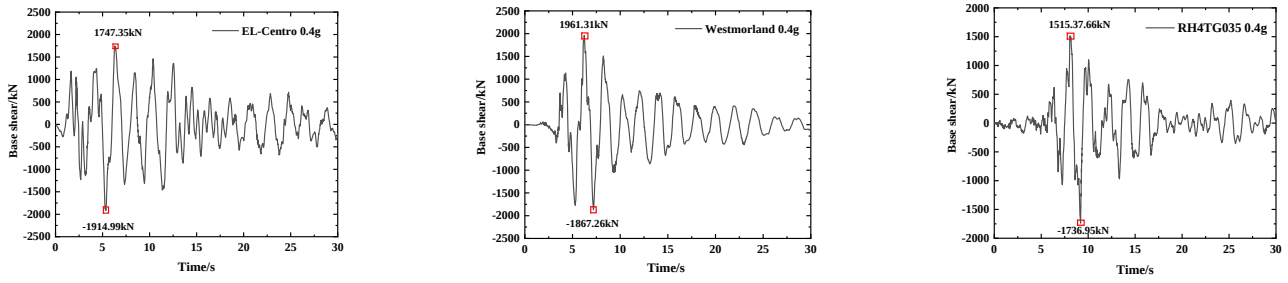

(b)

Fig. 30 Time-history curves of the base shear force of the steel frame under a rare earthquake: (a) RBSSF, (b) RSF

Figs. 28–30 show that the maximum base shear force in the RBSSF structure occurred later than that in the RSF structure under frequent, moderate, and rare earthquakes. The patterns observed in the time-history curves for the base shear forces of both structures were similar. Notably, the maximum base shear force of the RBSSF structure was marginally smaller than that of the RSF structure, contributing to a certain degree of damage reduction in the frame columns.

4.6.3. Analysis of inter-story displacement angle

The inter-story displacement angle (θ_{MIDR}) curves depicting the behavior of the RBSSF and RSF structures under frequent, moderate, and rare earthquakes are presented in Figs. 31–33.

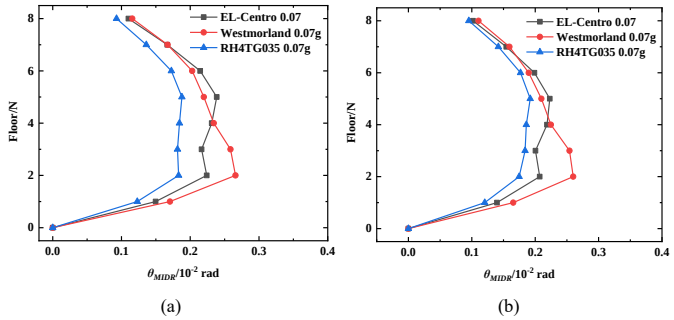

Fig. 31 Inter-story displacement angle curves of the steel frame under frequent earthquakes: (a) RBSSF, (b) RSF

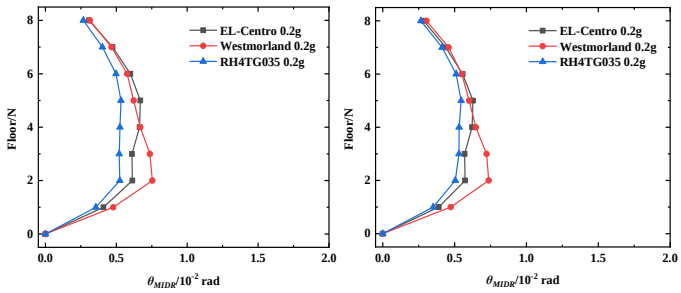

Fig. 32 Inter-story displacement angle curves of the steel frame under a moderate earthquake: (a) RBSSF, (b) RSF

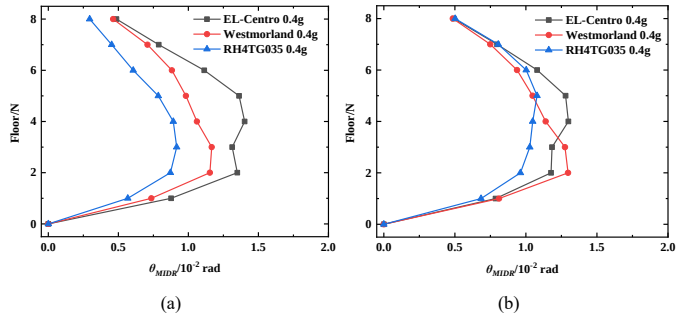

Fig. 33 Inter-story displacement angle curves of the steel frame under a rare earthquake: (a) RBSSF, (b) RSF

Figs. 31–33 revealed consistent weak floor positions and a consistent pattern in the inter-story displacement angle curves for both RBSSF and RSF structures subjected to the same seismic waves. The maximum inter-story displacement angles of both structures remained within the prescribed limits under various seismic conditions, satisfying the structural requirements. During frequent and moderate earthquakes, the RBSSF structure exhibited a slightly larger maximum inter-story displacement angle than the RSF structure. This divergence may be attributed to the full plastic energy dissipation in the replaceable energy dissipation beam section, where damage is primarily concentrated, leading to relatively minor damage and residual deformation in the main structure of the steel frame. Conversely, under rare earthquakes, the inter-story displacement angle of the RBSSF structure was relatively smaller than that of the RSF structure.

5. Feasibility analysis of energy dissipation beam replacement

Residual displacement is crucial for evaluating the seismic and toughness performance of structures and for gauging the structural recoverability and replaceability [54]. However, residual inter-story displacement provides a holistic view of the structure's overall residual deformation, lacking specificity about local residual deformation. This section analyzed the feasibility of beam segment replacement by considering the residual inter-story displacement angle and residual rotation angle of the end plate of the replaceable beam segment.

5.1. Residual inter-story displacement angle

This section extracted and analyzed the residual inter-story displacement angle (θ_{RIDR}) of the RBSSF structure. The corresponding curves under various seismic conditions are presented in Fig. 34, and detailed analysis results are provided in Table 11.

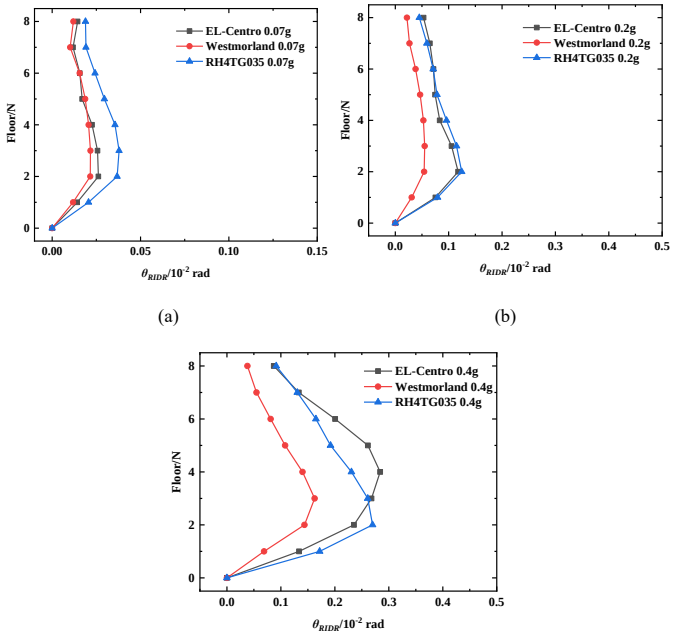

Fig. 34 Residual inter-story displacement angle curves of the RBSSF structure under earthquake action: (a) Frequent earthquake, (b) Moderate earthquake, (c) Rare earthquake

Table 11
Residual inter-story displacement angle of the RBSSF structure under earthquake action

Seismic level	Seismic wave	Floor (N)	Residual inter-story displacement angle (% rad)
Frequent earthquake	EL-Centro	2	0.026
	Westmorland	2	0.022
	RH4TG035	3	0.037
	Average	-	0.028
Moderate earthquake	EL-Centro	2	0.117
	Westmorland	2	0.054
	RH4TG035	2	0.124
	Average	-	0.098
Rare earthquake	EL-Centro	4	0.284
	Westmorland	3	0.163
	RH4TG035	2	0.270
	Average	-	0.239

From Fig. 34 and Table 11, it can be concluded that the residual inter-story displacement angle of the RBSSF structure under frequent, moderate, and rare earthquakes remained within the prescribed limits. Hence, it meets the requirements for the residual inter-story displacement angle of the structure.

5.2. Residual rotation angle of the end plate

In this section, we examined the residual rotation angle of the end plate of the replaceable beam section at the side span of the floor, where the residual inter-story displacement angle was the largest (Fig. 35). Due to the binding constraint between the end plates, the end plate exhibited relatively high stiffness, ensuring its flatness. Consequently, the analysis focused on the horizontal displacement of measuring points 1–3 at positions A and B of the end plate. The residual displacement curves (D_{ep}-Δ_{ep}) for measuring points 1–3 along the height direction of the end plates at positions A and B under different seismic conditions are illustrated in Fig. 36, with the corresponding analysis results of the residual rotation angle of the end plate presented in Table 12.

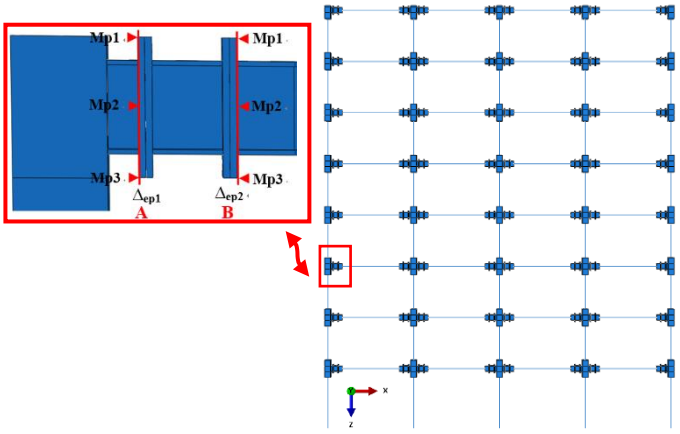

Fig. 35 Schematic diagram of measuring point selection for the end-plate residual displacement

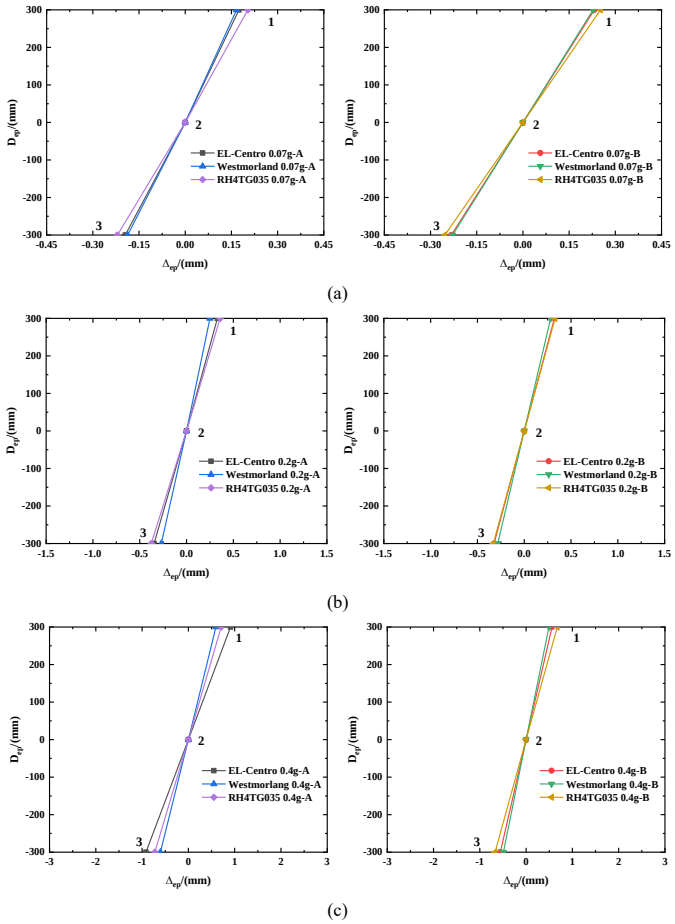

Fig. 36 Residual displacement curves of the replaceable beam segment under seismic action: (a) Frequent earthquake, (b) Moderate earthquake, (c) Rare earthquake

Fig. 36 and Table 12 revealed that during seismic activity, both the residual rotation angle and the relative residual rotation angle of the end plate remained significantly below the installation tolerance limit for steel structure members, set at 0.15% rad. Consequently, the replacement of the energy dissipation beam section was feasible. However, under rare earthquake conditions, the maximum residual rotation angle of the end plate at positions A and B exceeded the installation tolerance limit of the steel structure members (0.15% rad). In contrast, the relative residual rotation angle remained below this limit. This suggests the limited replaceability of the energy dissipation beam segment.

In conclusion, if only the residual inter-story displacement angle of the structure was considered as the criterion for the replaceability of the energy dissipation beam segment, the structure clearly met the replaceability requirement under rare earthquake conditions. Nevertheless, when the rotation angle of the end plate between the replaceable beam segment and the steel beam surpassed the component installation tolerance limit, the replacement of the energy dissipation beam segment became challenging or unattainable. Therefore, it is crucial to consider both the overall and local residual deformations when assessing the structural replaceability.

Table 12
Residual rotation angle of the replaceable beam segment under seismic action

Seismic level	Seismic wave	Residual rotation angle at position A (% rad)	Residual rotation angle at position A (% rad)	Relative residual rotation angle between positions A and B (% rad)
Frequent earthquake	EL-Centro	0.0615	0.0774	0.0159
	Westmorland	0.0589	0.0760	0.0171
	RH4TG035	0.0706	0.0842	0.0136
	Average	0.0637	0.0792	0.0155
Moderate earthquake	EL-Centro	0.1127	0.1076	0.0049
	Westmorland	0.0867	0.0942	0.0075
	RH4TG035	0.1225	0.1099	0.0126
	Average	0.1073	0.1039	0.0083
Rare earth-quake	EL-Centro	0.3046	0.1862	0.1184
	Westmorland	0.1999	0.1637	0.0362
	RH4TG035	0.2389	0.2242	0.0147
	Average	0.2478	0.1914	0.0564

6. Conclusions

In this study, a beam-column joint featuring a reduced-beam section and a replaceable energy dissipation beam segment was meticulously designed. After the design phase, a comprehensive quasi-static analysis was conducted on the joint and the single-story, single-span steel frame incorporating this novel joint. The analysis included exploring the seismic performance, failure modes, opening clearance, and end plate rotation angles. These findings laid the groundwork for streamlining an overall plane frame. Moreover, multi-scale models for both the RBSSF and RSF structures were crafted. Elastoplastic time-history analyses were then employed to scrutinize the replaceability of the beam segment and ascertain the practical requirements for replacement. The primary conclusions derived from this study are summarized as follows:

1. The hysteresis curve of the joint featuring a replaceable low-yield-point energy dissipation segment exhibited notable completeness, signifying high ductility and effective energy dissipation with a robust plastic deformation capacity.

2. Throughout the entire loading process, damage and plastic development predominantly occurred in the replaceable low-yield-point energy dissipation beam. The minimal opening clearance of the end plate ensured close bolt contact, fostering coordinated deformation between the end plates. Consequently, a stable force transfer mechanism was established in this connection mode. Additionally, the simplified joint model adeptly replicated the mechanical and deformation characteristics of the refined joint model.

3. In response to frequent, moderate, and rare earthquakes with a Richter magnitude of 8, the time-history curves depicting the development trends of the top floor displacement and base shear force in both the RBSSF and RSF structures exhibited similarities. The maximum inter-story displacement angles in both structures adhered to the code requirements. Notably, under frequent and moderate earthquakes, the RBSSF structure, characterized by reduced beam sections, demonstrated larger maximum top floor displacement and inter-story displacement angles than the RSF structure. This difference can be attributed to the RBSSF's overall lower stiffness. Conversely, the RBSSF structure exhibited smaller maximum top floor displacement and inter-story displacement angles during rare earthquakes than the RSF structure. Furthermore, the maximum base shear force in the RBSSF structure was consistently lower than that in the RSF structure under all earthquake scenarios, highlighting the superior seismic performance of the RBSSF structure.

4. The residual inter-story displacement angle of the RBSSF structure during frequent, moderate, and rare earthquakes with a Richter magnitude of 8 met the prescribed limits for the residual inter-story displacement angle in the performance target. Additionally, the residual rotation angle of the end plate in the replaceable energy dissipation beam segment satisfied the replaceable deformation limit under frequent and moderate earthquakes. However, under rare earthquakes, the residual angle of the end plate in the replaceable energy dissipation beam section slightly exceeded the limit, posing challenges for replacing the energy dissipation beam segment. Both overall residual and local

residual deformations should be considered when assessing replaceability.

5. This study investigated the seismic performance and replaceability of a reduced-beam-section beam-column joint with a replaceable energy dissipation beam segment through numerical simulations. Future research should further validate these results by using model tests.

Acknowledgments

This study was supported by the Shandong Natural Science Foundation Project (ZR2021ME239).

References

[1] David, B., "The dilemma of existing buildings: Private property, public risk", SPUR (San Francisco Bay Area Planning and Urban Research Association), 2009.
[2] Zhou, Y., Wu, H. and Gu, A.Q., "Earthquake engineering: from earthquake resistance, energy dissipation, and isolation, to resilience", Engineering Mechanics, 36(6), 1-12, 2019. (In Chinese)
[3] Lü, X.L., Quan, L.M. and Jiang, H.J., "Research trend of earthquake resilient structures seen from 16WCEE", Earthquake Engineering and Engineering Dynamics, 37(03), 1-9, 2017. (In Chinese)
[4] Zhou, Y. and Lü, X.L., "State-of-the-art on rocking and self-centering structures", Journal of Building Structures, 32(9), 1-10, 2011. (In Chinese)
[5] Lü, X.L. and Chen, C., "Research progress in structural systems with replaceable members", Earthquake Engineering and Engineering Dynamics, 34(01), 27-36, 2014. (In Chinese)
[6] Housner, G.W., "The behavior of inverted pendulum structures during earthquakes", Bulletin of the Seismological Society of America, 53(2), 403-417, 1963.
[7] Wada, A., Qu, Z., Ito, H., Motoyui, S., Sakata, H. and Kasai, K., "Seismic Retrofit Using Rocking Walls and Steel Dampers", ATC and SEI Conference on Improving the Seismic Performance of Existing Buildings and Other Structures, 2009.
[8] Zhang, F.W., Li, X.M., Xu, Q.F., Gong, C.C., Chen, X. and Liu, Q., "Experimental study on seismic behavior of frame-rocking wall structure", Journal of Building Structures, 36(8), 73-81, 2015. (In Chinese)
[9] Li, Y.W., Li, G.Q., Jiang, J. and Wang, Y.B., "Seismic performance improvement of tension-only-braced frames with energy-dissipative rocking columns", Engineering Structures, 196, 109286, 2019.
[10] Jia, M.M., Zhou, Z., Lü, D.G. and Yang, N., "Demand stiffness ratio and earthquake response analysis of rocking truss-steel frame system", Engineering Mechanics, 35(10), 66-74, 2018. (In Chinese)
[11] Zhang, W.J., Li, G.Q. and Ssun, F.F., "Seismic behavior of rocking-truss-frame with dampers", Journal of Tongji University (Natural Science), 47(9), 1235-1243, 2019. (In Chinese)
[12] Dong, J.Z., Zhang, F.W. and Li, X.M., "Experimental study on the seismic performance of frame-prestressed rocking wall structures", Engineering Mechanics, 36(4), 167-176, 2019. (In Chinese)
[13] Du, Y.F. and Wu, D.Y., "Performance analysis of light energy dissipative rocking frame designed on the basis of stiffness demand", China Civil Engineering Journal, 47(1), 24-35, 2014. (In Chinese)
[14] Chen, S.C., Liu, B.T., Cheng, S.N. and Yan, W.M., "Residual drift response analysis and calculated method of self-centering rocking wall structural systems", Journal of Guangzhou University (Natural Science Edition), 15(1), 45-50, 2016. (In Chinese)
[15] Lin, Y.C., Sause, R. and Ricles, J., "Seismic Performance of a Large-Scale Steel Self-Centering Moment-Resisting Frame: MCE Hybrid Simulations and Quasi-Static Pushover Tests", Journal of Structural Engineering, 139(7), 1227-1236, 2013.
[16] Lin, Y.C., Sause, R. and Ricles, J.M., "Seismic Performance of Steel Self-Centering, Moment-Resisting Frame: Hybrid Simulations under Design Basis Earthquake", Journal of Structural Engineering, 139(11), 1823-1832, 2013.
[17] Holden, T., Restrepo, J. and Mander, J.B., "Seismic Performance of Precast Reinforced and Prestressed Concrete Walls", Journal of Structural Engineering, 129(3), 286-296, 2003.
[18] Smith, B.J., Kurama, Y.C. and Mcginnis, M.J., "Behavior of Precast Concrete Shear Walls for Seismic Regions: Comparison of Hybrid and Emulative Specimens", Journal of Structural Engineering, 139(11), 1917-1927, 2013.
[19] Wu, H., Lü, X.L., Jiang, H.J., Shi, W.X. and Li, J.B., "Experimental study on seismic performance of prestressed precast concrete shear walls", Journal of Building Structures, 37(5), 208-217, 2016. (In Chinese)
[20] Gu, A.Q., Zhou, Y., Xiao, Y., Li, Q.W. and Qu, G., "Experimental study and parameter analysis on the seismic performance of self-centering hybrid reinforced concrete shear walls", Soil Dynamics & Earthquake Engineering, 116, 409-420, 2019.
[21] Xu, L.H., Zhang, G. and Yan, X.T., "Seismic performance study of reinforced concrete frame with self-centering braces", Engineering Mechanics, 37(2), 90-97, 2020. (In Chinese)
[22] He, H.X., Liao, L.C. and Shi, T., "Damping performance experiment and damage analysis of replacement connection with low-yield-point steel", Advanced Steel Construction, 17(2), 169-180, 2021.
[23] Chen, Y.Y. and He, X.Z., "Tests on moment resistant frame connection with replaceable angles", Steel Construction (Chinese & English), 35(8), 1-16, 2020.
[24] Wang, M., Zhang, C.Y., Sun, Y. and Dong, K.P., "Seismic performance of steel frame with replaceable low yield point steel connection components and the effect of structural fuses", Journal of Building Engineering, 47, 103862, 2022.
[25] Xu, L.H., Xie, X.S. and Li, Z.X., "Mechanics and performance study of self-centering variable damping energy dissipation brace", Engineering Mechanics, 35(1), 201-208, 2018. (In Chinese)
[26] Jiang, Z.Q., Yang, X.F., Zhang, A.L., Niu, Z.Y. and Wang, Q., "Experimental study on energy consuming devices for earthquake-resilient prefabricated cross joints", Journal of Building Structures, 41(1), 15-23, 2020. (In Chinese)
[27] Zhang, Y.X., Liu, A.R., Zhang, A.L. and Liu, X.C., "Seismic performance analysis of a resilient prestressed steel frame with intermediate column containing friction dampers", Advanced Steel Construction, 13(3), 241-257, 2017.
[28] Luo, J.L., "Study on seismic performance of buckling restrained steel beam-column connections based on damage control", Shandong University, 2018. (In Chinese)
[29] Shen, Y.L., Christopoulos, C., Mansour, N. and Tremblay, R., "Seismic design and performance of steel moment-resisting frames with nonlinear replaceable links," Journal of Structural Engineering, 137(10), 1107-1117, 2011.
[30] Wang, J., "Experimental study on seismic behavior of replaceable steel beams in assembled RCS hybrid structures", Huaqiao University, 2017. (In Chinese)
[31] Zhang, A.L., Zhang, Y.X., Zhao, W. and Fei, C.C., "Pseudo dynamic tests for a resilient prefabricated prestressed steel frame", Journal of Vibration and Shock, 35(5), 207-215, 2016. (In Chinese)
[32] Castiglioni, C.A., Kanyilmaz, A. and Calado, L., "Experimental analysis of seismic resistant composite steel frames with dissipative devices", Journal of Constructional Steel Research, 76, 1-12, 2012.
[33] Oh, S.H., Kim, Y.J. and Ryu, H.S., "Seismic performance of steel structures with slit dampers", Engineering Structures, 31(9), 1997-2008, 2009.
[34] Shao, T.F. and Chen, Y.Y., "Experimental study on steel H-beams with replaceable energy dissipation angle", Journal of Building Structures, 37(7), 38-45, 2016. (In Chinese)
[35] Hu, Y.Y., "Research on seismic damage-control fuses used in high-strength steel beam-to-column joint", Institute of Engineering Mechanics, China Earthquake Administration, 2017. (In Chinese)
[36] He, H.X., Chen, K. and Li, R.F., "Seismic analysis of replaceable steel connection with low yield point metal", Journal of Vibration, Measurement and Diagnosis, 36(6), 1050-1056, 2016. (In Chinese)
[37] Wang, M., Bi, P., Yang, W.G. and Wu, Z.Z., "Study on mechanical behavior of ductile steel frame connection with low yield point steel 'structural fuse'", Journal of Building Structures, 40(11), 90-101, 2019. (In Chinese)
[38] Chi, H. and Liu, J., "Seismic behavior of post-tensioned column base for steel self-centering moment resisting frame", Journal of Constructional Steel Research, 78, 117-130, 2012.
[39] GB50017-2014. "Standard for design of steel structures", China Planning Publishing House, 2014. (In Chinese)
[40] GB50011-2010. "Code for seismic design of buildings", China Building Industry Press, 2010. (In Chinese)
[41] AISC358-16. "Prequalified Connections for Special and Intermediate Steel Moment Frames for Seismic Applications", American Institute of Steel Construction, 2016.
[42] Liu, W.T., "The GTN damage model with combined hardening rule", Beijing Jiaotong University, 2014. (In Chinese)
[43] ANSI/AISC 341-05. "Seismic Provisions for Structural Steel Buildings", American Institute of Steel Construction, 2005.
[44] Zhang, A.L., Guo, Z.P., Liu, X.C. and Jiang, Z.Q., "Experimental study on aseismic behavior of prefabricated steel-frame-joints with Z-shaped cantilever-beam splicing", Engineering Mechanics, 34(8), 31-41, 2017. (In Chinese)
[45] JGJ/T101-2015. "Specification for seismic test of buildings", China Building Industry Press, 2015. (In Chinese)
[46] Shi, Y.J., Wang, M., Wang, Y.Q., "Analysis on seismic behavior of overall steel frame with different welded connection constructions", Engineering Mechanics, 29(11), 71-79, 2012. (In Chinese)
[47] Wang, M., "Damage and degradation behaviors of steel frames under severe earthquake", Tsinghua University, 2013. (In Chinese)
[48] Hong, W., "Analysis of lateral collapse-resistance of steel frame based on beam-to-column connections and buckling restrained brace", Southeast University, 2019. (In Chinese)
[49] ATC-63. "Quantification of Building Seismic Performance Factors", ATC-63 Project Report, 2008.
[50] SEAOC. "Vision 2000: Performance based seismic engineering of building", Structural Engineers Association of California, 1995.
[51] FEMA P 58-1, "Seismic Performance Assessment of Buildings", Applied Technology Council and Federal Emergency Management Agency, 2012.
[52] Uma, S.R., Pampanin, S. and Christopoulos, C., "Development of Probabilistic Framework for Performance-Based Seismic Assessment of Structures Considering Residual Deformations", Journal of Earthquake Engineering, 14(7), 1092-1111, 2010.
[53] Wu, D.Y. and Lü, X.L., "Probabilistic performance assessment of self-centering dual systems", Journal of Building Structures, 38(8), 14-24, 2017. (In Chinese)
[54] Chen, Y.Y., He, X.Z., Ke, K. and Chen, Y.S., "Characteristics and technical issues on structural systems with replaceable damage-concentrated elements", Journal of Building Structures, 37(2), 1-10, 2016. (In Chinese)

Advanced Steel Construction – Vol. 20 No. 1 (2024) 81–92
DOI:10.18057/IJASC.2024.20.1.9

STRUCTURAL MORPHOLOGY AND DYNAMIC CHARACTERISTICS ANALYSIS OF DRUM-SHAPED HONEYCOMB-TYPE III CABLE DOME WITH QUAD-STRUT LAYOUT

Hui Lv [1, 2, *], Hao Zhang [1], Zhong-Yi Zhu [3], Shi-Lin Dong [2] and Xin Xie [1]

[1] *College of Civil Engineering and Architecture, Nanchang Hangkong University, Nanchang 330063, China*
[2] *Space Structures Research Center, Zhejiang University, Hangzhou 310058, China*
[3] *Beijing Institute of Architectural Design,Beijing 100045,China;*
** (Corresponding author: E-mail: lvhui@nchu.edu.cn)*

ABSTRACT

The drum-shaped honeycomb-type III cable dome with a quad-strut layout abandons the traditional concept, incorporating a multi-support pole concept, making it one of the most structurally diverse types of cable dome structures. Its upper chord cable mesh is evenly divided, resulting in a simple and efficient structural design. This design approach reduces the usage of cables and struts, making pre-stressing and tensioning construction more convenient. Furthermore, the structure exhibits good cost-effectiveness. Based on the node force equilibrium equations, a general formula is derived for calculating the internal forces of prestressed cables and struts in the prestressed state of the structure. Additionally, the variation of prestress distribution with geometric parameters of the cable dome structure is analyzed. A numerical model with a span of 120 meters was established in the general finite element software Ansys to investigate the influence of structural parameters on the structural natural frequency characteristics. Moreover, using the nonlinear dynamic analysis method, the dynamic response of the structure under multidimensional seismic loads was compared and analyzed. The research results indicate that the prestress distribution of the structure is reasonable, with a greater amount of prestress in the outer ring compared to the inner ring. This observation suggests that the stiffness of the structure is primarily supported by the outer ring structure. The structural natural modes of vibration predominantly exhibit vertical deformation, indicating that the vertical stiffness of the structure is weaker than the circumferential direction. Furthermore, when subjected to seismic loading, the internal forces in cables and struts, as well as the dynamic displacements of key nodes, are relatively small, demonstrating excellent seismic performance.

ARTICLE HISTORY

Received: 4 November 2023
Revised: 5 February 2024
Accepted: 7 February 2024

KEYWORDS

Drum-shaped honeycomb-type;
Structural morphology analysis;
Parametric analysis;
Natural vibration mode;
Seismic analysis

Copyright © 2024 by The Hong Kong Institute of Steel Construction. All rights reserved.

1. Introduction

The concept of prestressing the entire structure was initially proposed by the American engineer Fuller, who envisioned a structural system that remains continuously under tension as a whole while experiencing discrete areas of compression. The fundamental idea behind this concept is that "compressed islands exist in the ocean of tension" [1]. In the 1980s, the American engineer Geiger further evolved and developed Fuller's ideas, introducing the Geiger-type cable dome structure, which was successfully applied in the construction of the sports arena and fencing hall for the 1988 Seoul Olympics [2,3]. To address the issues of weak out-of-plane stiffness and limited capacity to withstand asymmetric loads in the Geiger-type cable dome structure, the American engineer Levy proposed the Levy-type cable dome structure. This design incorporates triangular spatial trusses internally, significantly enhancing the overall stability of the structure. The Levy-type cable dome structure found successful application in the main stadium, Georgia Dome, during the 1996 Atlanta Olympics [4]. However, this structural arrangement increases the number of struts, due to the dense grid division in the inner ring, making the construction of inner ring nodes and membrane installation more challenging [5].

In order to address the issues encountered in the two classic cable dome structural forms, in 2005, Shilin Dong et al. proposed the Kewitte-type cable dome and two hybrid cable domes, incorporating the arrangement patterns of various grid shell structures into the cable dome structures [6]. All of these structures feature advantages such as uniform grid division and even stiffness distribution. In 2010, Shilin Dong et al. introduced an innovative spatial structural system that combines a single-layer grid shell with a cable dome [7]. Subsequently, Shilin Dong et al. introduced a new type of honeycomb-type cable dome with a multi-strut layout structural system [8,9]. In this cable dome design, the upper chord consists of ridge cables arranged in a honeycomb pattern, while multiple support struts connect to the lower chord nodes. After the introduction of the innovative research on the honeycomb-type cable dome structural system, Shilin Dong and Hui Lv et al. have recently proposed the drum-shaped honeycomb-type cable dome with a quad-strut layout [10]. This concept deviates from the traditional cable dome concept that typically involves tension cables and compressed strut islands. Instead, it incorporates the idea of multiple support struts, resulting in three cable dome structural forms: the drum-shaped honeycomb-type I, II, and III cable domes with a quad-strut layout. The analysis methods for determining the prestressed state of these three cable dome structures have also been explored.

The cable dome structure is a typical flexible structure where its structural stiffness is primarily provided by prestressing. Therefore, the analysis of prestressed modes and structural morphology is the foundation and key to the theoretical analysis of cable dome structures. Pellegrino et al. proposed the theory of equilibrium matrices [11,12]. For structures with known geometric dimensions and topological relationships, the relationship between the structural member topology and internal forces can be expressed in matrix form using node equilibrium equations. Furthermore, Xingfei Yuan et al. introduced the concept of globally feasible prestress modes for cable domes, taking advantage of the structure's symmetry. They employed the method of quadratic singular value decomposition to determine prestress modes that would ensure geometric stability in cable dome structures [13].

Regarding cable dome structures, which are characterized by flexibility, lightness, large spans and significant nonlinearity, researchers in the field have conducted extensive studies on their dynamic characteristics. Pengcheng Li et al. explored the natural vibration characteristics of the cable-stiffened single-layer latticed shell through modal analysis. They also analyzed the structure's nonlinear behavior when subjected to the El Centro earthquake waves [14]. In a separate study, Zhenwei Li et al. investigated the internal connections between multiple square loop-string cables and grid beams, providing valuable insights for seismic-resistant structures [15]. Hao Zhang et al. analyzed the dynamic response of the cable dome structure, specifically focusing on the consequences of local cable or strut failures, distinguishing the importance of structural cables and struts [16]. Chi Zhu et al. have introduced a method aimed at enhancing the efficiency of structural dynamic testing and propose a dynamic response reconstruction method that accounts for step excitation, alongside a corresponding high-precision non-measurement point selection strategy [17]. However, regarding the drum-shaped honeycomb-type cable dome, current research has only focused on the static performance of the structure.

Accordingly, this paper aims to further investigate the mechanical characteristics of the novel drum-shaped honeycomb-type III cable dome with a quad-strut layout. Based on the node equilibrium equations and under the conditions of symmetry and periodicity, analytical formulas for the prestressed cable forces in the structure were derived. Additionally, the paper analyzed the influence of various design parameters on the distribution of prestressing forces within the structure. By considering a 120 m cable dome as an example, the paper analyzed the natural frequency characteristics of the structure and

investigated the impact of various structural parameters on these characteristics. Building upon the results of the natural frequency analysis, a time history analysis method was employed to calculate the dynamic responses of cable forces in different struts and the displacements of key nodes under multidimensional seismic loads. This analysis provided valuable insights into the structure's ability to withstand seismic forces. The research finding provides a reference for the practical engineering design of this specific cable dome configuration.

2. Structural configuration and pre-stress state analysis

2.1. Structural configuration

As shown in Fig. 1, the main structure of the drum-shaped honeycomb-type III cable dome with a quad-strut layout is composed of ridge cables, ring cables, diagonal cables, struts and rigid ring beams. In Figs. 1a and 1b, the labels *N*, *T*, *B*, *H*, and *V* represent the upper chord circumferential ridge cables, radial ridge cables, diagonal cables, ring cables and struts respectively. The subscripted numbers indicate the concentric circles from the inside out, while the letters indicate the types of components. Within the main hexagonal grid of the upper chord, two diagonal cables and four struts are arranged in a skip pattern. The lower chord nodes are positioned along the radial axis of the main hexagonal grid, and ring cables connect each lower chord node. Additionally, the inner upper chord ridge cable connects two adjacent main hexagonal grids, forming secondary hexagonal grids.

For the drum-shaped honeycomb-type cable dome with a multi-strut layout, it can be represented usingthe symbol ${}_n\overline{H}_{ms}$ with three subscripts, where *n* represents the number of circumferential divisions, *m* represents the number of ring cables, and *s* represents the number of struts converging at the lower chord nodes. The structure shown in Fig. 1 can be denoted by the symbol ${}_{24}\overline{H}_{24\mathrm{III}}$, where III indicates the upper chord ridge cable arrangement scheme.

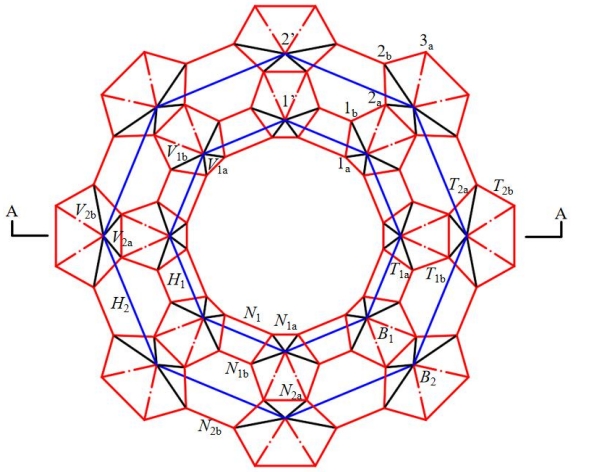

(a) Schematic plan

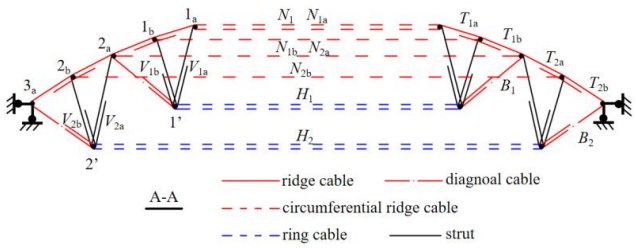

(b) Sectional view (A-A)

Fig. 1 Schematic diagram of the ${}_{24}\overline{H}_{24\mathrm{III}}$ cable dome

The advantages of the ${}_{24}\overline{H}_{24\mathrm{III}}$ cable dome are as follows:

(1) The upper chord ridge cable grid of the ${}_{24}\overline{H}_{24\mathrm{III}}$ cable dome is evenly divided, inheriting the advantages of simplicity and efficiency from the drum-shaped honeycomb-type cable dome with a multi-strut layout. This design feature allows the cable dome to adapt to a variety of circumferential broken-line cable dome shapes, meeting the architectural design requirements.

(2) There are a total of 8 pairs of outer ring diagonal cables in the structure. Simultaneously tensioning all outer ring diagonal cables can effectively reduce the risk of ring cable slippage.

(3) There are 4 compression struts converging at the lower chord node of the ${}_{24}\overline{H}_{24\mathrm{III}}$ cable dome, forming a continuous double-V spatial structure in the circumferential direction. This spatial configuration enhances the lateral stiffness at the upper and lower nodes. Additionally, the number of components converging at the inner and outer upper chord nodes is 4 and 5 respectively, creating a spatial load-bearing system. This design significantly improves the stability and load-bearing performance of the entire cable dome structure, making it suitable for the use of a rigid roof system.

(4) The strut-to-cable quantity ratio of the ${}_{24}\overline{H}_{24\mathrm{III}}$ cable dome is only 1:1.9, which is significantly lower compared to ratios of 1:3 for Gerger-type cable domes and 1:5 for Levy-type cable domes [18]. This suggests that the ${}_{24}\overline{H}_{24\mathrm{III}}$ cable dome is more economical, considering that the cost of cable materials is typically higher than that of rod materials.

2.2. Analysis method of prestressed state

The ${}_{24}\overline{H}_{24\mathrm{III}}$ cable dome structure simplifies the analysis and computation process by considering a single substructure when the spatial arrangement meets axial symmetry conditions and is divided into n equal parts in the circumferential direction. The analysis and computation of the substructure should refer to the plan and section diagrams shown in Fig. 2. The internal forces of each component should be labeled with the respective component names. The angles between the upper chord cables, struts, diagonal cables and the horizontal plane are denoted as α_{ia}, α_{ib}, ϕ_{ia}, ϕ_{ib}, β_i respectively. Under the action of axially symmetric prestress, by establishing the equilibrium equations for the nodal forces, it is possible to calculate the relationships between the internal forces of cables and struts in the cable dome structure. For nodes located on two symmetric axes simultaneously, a vertical force equilibrium equation can be established. For nodes along the radial symmetric axis, two equilibrium equations can be established. For general nodes that do not align with a symmetric axis, three node equilibrium equations can be established.

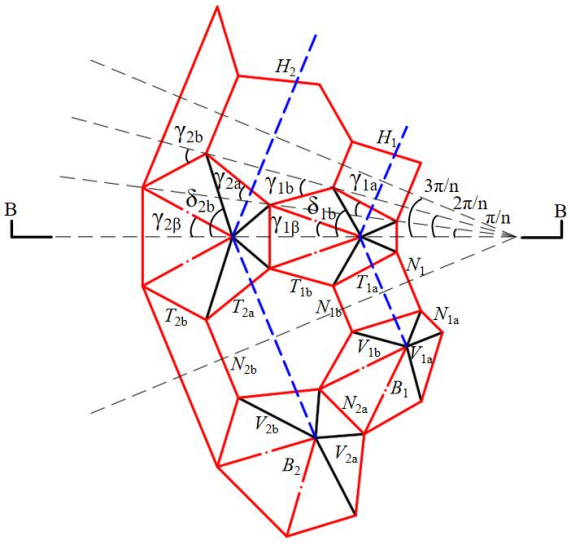

(a) Analysis model (plan view)

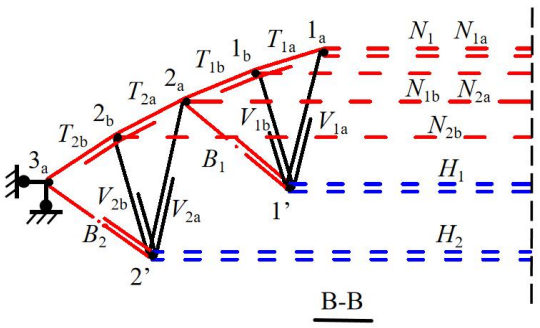

(b) Sectional view (B-B)

Fig. 2 Analysis model of the ${}_{24}\overline{H}_{24\mathrm{III}}$ cable dome

For the ${}_{24}\bar{H}_{24\mathrm{III}}$ cable dome, there are a total of 17 types of components. Equations (1) - (6) collectively form a set of 16 node equilibrium equations. The number of these equations is one less than the number of unknown internal forces in the cables and struts. Therefore, this structure is classified as a statically determinate structure of the first degree. The nodal equilibrium equation group is as follows:

For node 1_a:

$$\left.\begin{aligned}
&\bullet\ T_{1a}\cos\alpha_{1a}\cos\gamma_{1a}+V_{1a}\cos\varphi_{1a}\cos(\delta_{1\mathbf{a}}+\frac{\pi}{\mathrm{n}})\ =N_1\sin\frac{2\pi}{\mathrm{n}}+N_{1a}\sin\frac{\pi}{\mathrm{n}}\\
&\bullet\ T_{1a}\cos\alpha_{1a}\sin\gamma_{1a}-V_{1a}\cos\varphi_{1a}\sin(\delta_{1\mathbf{a}}+\frac{\pi}{\mathrm{n}})=N_{1a}\cos\frac{2\pi}{\mathrm{n}}-N_1\cos\frac{\pi}{\mathrm{n}}\\
&\bullet\ T_{1\mathbf{a}}\sin\beta_{1a}+2V_{1a}\sin\varphi_{1a}=0
\end{aligned}\right\}\quad(1)$$

For node 1':

$$\left.\begin{aligned}
&\bullet\ 2B_1\cos\beta_1\cos\gamma_{1\beta}+2V_{1b}\cos\phi_{1b}\cos\delta_{1b}\ =2H_1\sin\frac{3\pi}{n}\\
&\quad+2V_{1a}\cos\phi_{1a}\cos\delta_{1a}\\
&\bullet\ 2B_1\cos\beta_1+2V_{1b}\sin\phi_{1b}+2V_{1a}\sin\phi_{1a}=0
\end{aligned}\right\}\quad(2)$$

For node 1_b:

$$\left.\begin{aligned}
&\bullet\ T_{1b}\cos\alpha_{1\mathbf{b}}\cos\gamma_{1b}=T_{1a}\cos\alpha_{1a}\cos(\gamma_{1\mathbf{a}}-\frac{\pi}{n})\\
&\quad+V_{1b}\cos\phi_{1b}\cos(\delta_{1b}-\frac{2\pi}{n})\ N_{1b}\sin\frac{\pi}{n}\\
&\bullet\ T_{1b}\cos\alpha_{1\mathbf{b}}\sin\gamma_{1b}+T_{1a}\cos\alpha_{1a}\sin(\gamma_{1\mathbf{a}}-\frac{\pi}{n})\\
&\quad+V_{1b}\cos\phi_{1b}\sin(\delta_{1b}-\frac{2\pi}{n})\ -N_{1b}\cos\frac{\pi}{n}\\
&\bullet\ T_{1b}\sin\alpha_{1\mathbf{b}}-T_{1a}\sin\alpha_{1\mathbf{a}}+V_{1b}\sin\phi_{1b}=0
\end{aligned}\right\}\quad(3)$$

For node 2_a:

$$\left.\begin{aligned}
&\bullet\ T_{2a}\cos\alpha_{1a}\cos\gamma_{2\mathbf{a}}+V_{2a}\cos\phi_{2a}\cos(\delta_{2a}+\frac{\pi}{n})\\
&\quad=T_{1b}\cos\alpha_{1b}\cos(\gamma_{1b}-\frac{\pi}{n})\ +B_1\cos\beta_1\cos(\gamma_{1\beta}-\frac{\pi}{n})\\
&\quad+N_{2a}\sin\frac{\pi}{n}\\
&\bullet\ T_{2a}\cos\alpha_{2a}\sin\gamma_{2a}-V_{2a}\cos\phi_{2a}\sin(\delta_{2a}+\frac{\pi}{n})\\
&\quad+T_{1b}\cos\alpha_{1b}\sin(\gamma_{1b}-\frac{\pi}{n})-B_1\cos\beta_1\sin(\gamma_{1\beta}-\frac{\pi}{n})\\
&\quad-N_{2a}\cos\frac{\pi}{n}=0\\
&\bullet\ T_{2a}\sin\alpha_{2a}+V_{2a}\sin\phi_{2a}-T_{1b}\sin\alpha_{1b}\\
&\quad+B_1\cos\beta_1=0
\end{aligned}\right\}\quad(4)$$

For node 2':

$$\left.\begin{aligned}
&\bullet\ 2B_2\cos\beta_2\cos\gamma_{2\beta}+2V_{2b}\cos\phi_{2b}\cos\delta_{2b}\\
&\quad=2H_2\sin\frac{3\pi}{n}\ +2V_{2a}\cos\phi_{2a}\cos\delta_{2a}\\
&\bullet\ 2B_2\sin\beta_2+2V_{2b}\sin\phi_{2b}+2V_{2a}\sin\phi_{2a}\\
&\quad=0
\end{aligned}\right\}\quad(5)$$

For node 2_b:

$$\left.\begin{aligned}
&\bullet\ T_{2b}\cos\alpha_{2b}\cos\gamma_{\mathbf{2b}}=T_{2a}\cos\alpha_{2a}\cos(\gamma_{2\mathbf{a}}-\frac{2\pi}{n})\\
&\quad+V_{2b}\cos\phi_{2b}\cos(\delta_{2a}-\frac{\pi}{n})+N_{2b}\sin\frac{\pi}{n}\\
&\bullet\ T_{2b}\cos\alpha_{2b}\sin\gamma_{2b}+T_{2a}\cos\alpha_{2a}\sin(\gamma_{2\mathbf{a}}-\frac{2\pi}{n})\\
&\quad+V_{2b}\cos\phi_{2b}\sin(\delta_{2a}-\frac{\pi}{n})-N_{2b}\cos\frac{\pi}{n}=0\\
&\bullet\ T_{2b}\sin\alpha_{2b}+V_{2b}\sin\phi_{2b}-T_{2b}\sin\alpha_{2a}=0
\end{aligned}\right\}\quad(6)$$

The support reactions under prestressed conditions can also be determined using the following equations:

$$\left.\begin{aligned}
&\bullet\ X=\begin{bmatrix}B_2\cos\beta_2\cos\left(\gamma_{2\beta}-\frac{\pi}{n}\right)\\+T_{2b}\cos\alpha_{2b}\cos\left(\gamma_{2b}-\frac{\pi}{n}\right)\end{bmatrix}\\
&\bullet\ Y=\pm\begin{bmatrix}B_2\cos\beta_2\sin\left(\gamma_{2\beta}-\frac{\pi}{n}\right)\\-T_{2b}\cos\alpha_{2b}\sin\left(\gamma_{2b}-\frac{\pi}{n}\right)\end{bmatrix}
\end{aligned}\right\}\quad(7)$$

In conclusion, based on the node force equilibrium equations for a single substructure, formulas for calculating the internal forces in various types of cables and struts have been derived. These formulas are specifically applicable for determining the internal force distribution in the prestressed state of the ${}_{24}\bar{H}_{24\mathrm{III}}$ cable dome with a planar projection in the shape of a circle, while satisfying periodicity and symmetry conditions.

3. Parametric analysis of prestressed state

3.1. Structural design parameters

For the ${}_{24}\bar{H}_{24\mathrm{III}}$ cable dome with a span of L, inner ring opening size of L_0, spherical shell radius of R, rise height of f and structural thickness of h, the simplified half-space truss, considering periodicity and symmetry conditions, is shown in Fig. 3. The calculation formulas for the main geometric parameters are listed in Table 1.

The thickness h_i and length Δ_{ia}, Δ_{ib} of the cable dome are determined separately using the following equations (8) and (9). The thickness h represents the center thickness of the cable dome, while h_i varies linearly along the radial direction. ζ and η_i are dimensionless coefficients.

$$h_i=h\left(1\pm\xi\frac{r_i}{r}\right)\qquad i=(1,2)\quad(8)$$

$$\frac{\Delta_{ia}}{\Delta_{ib}}=\eta_i\quad(9)$$

As illustrated in Fig. 3, the arrangement schemes for the lower chord node i' of the structure includes three cases:

Case 1: The projected length of the two inner struts in the horizontal plane radial direction is 0, as shown in Fig. 3a.

Case 2: The projected length of the two inner struts in the horizontal plane radial direction is $\Delta_{ia}/2$, as shown in Fig. 3b.

Case 3: The projected length of the two inner struts in the horizontal plane radial direction is Δ_{ia}, as shown in Fig. 3c.

Based on the above, the primary design parameters for the form of the cable dome structure include the span-to-rise ratio, thickness-to-span ratio and the arrangement scheme for the lower chord nodes i'. Once these design parameters are established, the geometric configuration of the structure can be determined using the formulas provided in Table 1. Furthermore, the prestress distribution within the cable dome can be determined using equations (1) to (7).

Table 1
Formula for calculating the geometric dimensions of the $_{24}H_{24III}$ type cable dome (i=1, 2)

Length parameter	Angle parameters
$R = L^2/8_f + \frac{f}{2}$ $\quad r = R\sin\theta$	
$r_{ia} = R\sin\theta_{ia} = r_{(i+1)a} - (\Delta_{ia} + \Delta_{ib})$	
$r_{ib} = R\sin\theta_{ib} = r_{(i+1)a} - \Delta_{ib}$ $\quad r' = r_i = R\sin\theta_i$	
$s_{ia} = \sqrt{(r_{ib}\cos\frac{\pi}{n} - r_{ia})^2 + (r_{ib}\sin\frac{\pi}{n})^2}$	$\alpha_{ia} = \tan^{-1}(\frac{h_{ia}}{s_{ia}})$ $\quad \alpha_{ib} = \tan^{-1}(\frac{h_{ib}}{s_{ib}})$
$s_{ib} = \sqrt{(r_{(i+1)a}\cos\frac{\pi}{n} - r_{ib})^2 + (r_{(i+1)a}\sin\frac{\pi}{n})^2}$	$\varphi_{ia} = \tan^{-1}(\frac{h'_{ia}}{s'_{ia}})$ $\quad \varphi_{ib} = \tan^{-1}(\frac{h'_{ib}}{s'_{ib}})$
$s'_{ia} = \sqrt{(r_i - r_{ia}\cos\frac{\pi}{n})^2 + (r_{ia}\sin\frac{\pi}{n})^2}$	$\beta_i = \tan^{-1}(\frac{h'_i}{s'_i})$ $\quad \gamma_{ia} = \tan^{-1}(\frac{r_{ib}\sin\frac{\pi}{n}}{r_{ib}\cos\frac{\pi}{n} - r_{ia}})$
$s'_{ib} = \sqrt{(r_b\cos\frac{\pi}{n} - r_i)^2 + (r_{ib}\sin\frac{\pi}{n})^2}$	$\gamma_{ib} = \tan^{-1}(\frac{r_{(i+1)a}\sin\frac{\pi}{n}}{r_{(i+1)a}\cos\frac{\pi}{n} - r_{ib}})$ $\quad \delta_{ia} = \tan^{-1}(\frac{r_{ia}\sin\frac{\pi}{n}}{r_i - r_{ia}\cos\frac{\pi}{n}})$
$s'_i = \sqrt{(r_{(i+1)a}\cos\frac{\pi}{n} - r_i)^2 + (r_{(i+1)a}\sin\frac{\pi}{n})^2}$	$\delta_{ib} = \tan^{-1}(\frac{r_{ib}\sin\frac{2\pi}{n}}{r_{ib}\cos\frac{2\pi}{n} - r_i})$ $\quad \gamma_{i\beta} = \tan^{-1}(\frac{r_{(i+1)a}\sin\frac{\pi}{n}}{r_{(i+1)a}\cos\frac{\pi}{n} - r_i})$
$h_{ia} = R(\cos\theta_{ia} - \cos\theta_{ib})$ $\quad h_{ib} = R(\cos\theta_{ib} - \cos\theta_{(i+1)a})$	
$h'_{ia} = h_i + R(\cos\theta_{ia} - \cos\theta_i)$ $\quad h'_{ib} = h_i + R(\cos\theta_{ib} - \cos\theta_i)$	
$h'_i = h_i - R(\cos\theta_i - \cos\theta_{(i+1)a})$	

Note: h_{ia}, h_{ib}, h'_{ia}, h'_{ib}, h'_i represent the height of the upper chord cables, struts and diagonal cables respectively, S_{ia}, S_{ib}, S'_{ia}, S'_{ib}, S'_i represent the horizontal projected lengths of the upper chord cables, struts and diagonal cables respectively.

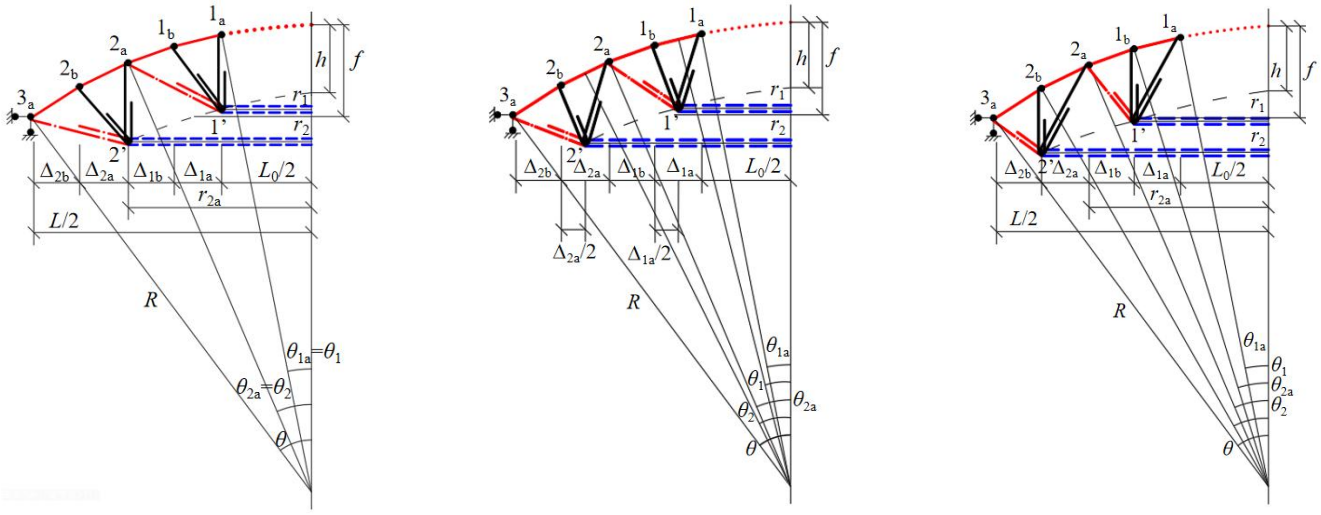

(a) Case 1 (b) Case2 (c) Case 3

Fig. 3 The arrangement schemes for the lower chord node *i*'

3.2. Parametric analysis example of prestress distribution

In the parametric analysis, the span-to-rise ratio was set to 0.08, 0.09 and 0.10, while the thickness-to-span ratio was set to 0.07, 0.08, 0.09 and 0.10. The parameter η was set to 1.0. The cable dome structure had a span (L) of 120 m, an inner ring opening diameter (L_0) of 40 m, and both Δ_{ia} and Δ_{ib} equal to 10 m. Under the relative prestress H_2 = 1.0, the prestressed cable dome structure's internal force distribution in cables and struts can be determined. Prestressed state analysis was implemented using a custom code developed on the Matlab platform, and the calculated results are shown in Table 2. Through comparison with the case study, the calculated results were found to be consistent with the results obtained from the second-order singular value decomposition method [19].

By observing the calculated results in Table 2, the following patterns can be summarized:

(1) When the span-to-rise ratio (f/L) and the thickness-to-span ratio (h/L) are equal for the cable dome, and the same lower chord node arrangement scheme is used, the internal forces in cables and struts exhibit geometrically equal patterns under prestressed conditions.

(2) Under prestressed state, the internal forces in cables and struts, including support reactions, increase linearly with an increasing thickness-to-span ratio. This indicates that as the structural stiffness increases, the internal forces in cables and struts also increase accordingly.

(3) Under prestressed state, the internal force distribution in the cables and struts of the outer ring of the cable dome structure is significantly greater than that of the inner ring, indicating that the structural stiffness is mainly contributed by the outer ring structure.

(4) Among the three lower chord node arrangement schemes, Case 1 is less affected by changes in the span-to-rise ratio and thickness-to-span ratio in terms of internal forces in cables and struts. Case 2 is relatively more sensitive, while Case 3 is the most sensitive to these changes.

Table 2
The distribution of prestress in the cable dome structure under changes in geometric parameters

Parameter	f/L	0.08				0.09				0.10			
	h/L	0.07	0.08	0.09	0.10	0.07	0.08	0.09	0.10	0.07	0.08	0.09	0.10
Case 1	H_2	1.00	1.00	1.00	1.00	1.00	1.00	1.00	1.00	1.00	1.00	1.00	1.00
	N_1	0.21	0.30	0.41	0.52	0.13	0.21	0.30	0.39	0.08	0.15	0.22	0.30
	N_{1a}	0.24	0.35	0.47	0.60	0.15	0.25	0.35	0.45	0.09	0.17	0.26	0.35
	N_{1b}	0.07	0.10	0.14	0.18	0.04	0.07	0.10	0.13	0.02	0.05	0.07	0.10
	T_{1a}	0.09	0.14	0.18	0.23	0.06	0.10	0.13	0.18	0.03	0.07	0.10	0.13
	T_{1b}	0.10	0.15	0.21	0.27	0.06	0.11	0.15	0.20	0.04	0.07	0.11	0.15
	V_{1a}	-0.01	-0.02	-0.02	-0.03	-0.01	-0.01	-0.02	-0.02	-0.01	-0.01	-0.02	-0.02
	V_{1b}	-0.01	-0.01	-0.02	-0.02	-0.01	-0.01	-0.02	-0.02	0.00	-0.01	-0.01	-0.02
	B_1	0.07	0.08	0.10	0.11	0.05	0.07	0.08	0.10	0.04	0.06	0.07	0.08
	H_1	0.15	0.18	0.20	0.22	0.11	0.15	0.18	0.20	0.08	0.12	0.15	0.17
	N_{2a}	0.20	0.28	0.36	0.40	0.14	0.21	0.28	0.35	0.09	0.15	0.21	0.28
	N_{2b}	0.24	0.34	0.44	0.54	0.16	0.25	0.33	0.43	0.10	0.17	0.25	0.33
	T_{2a}	0.23	0.31	0.40	0.49	0.16	0.24	0.31	0.39	0.10	0.17	0.24	0.31
	T_{2b}	0.26	0.37	0.49	0.60	0.18	0.28	0.37	0.47	0.11	0.20	0.28	0.37
	V_{2a}	-0.05	-0.07	-0.09	-0.11	-0.04	-0.06	-0.08	-0.10	-0.03	-0.05	-0.07	-0.09
	V_{2b}	-0.04	-0.06	-0.07	-0.08	-0.03	-0.05	-0.06	-0.07	-0.02	-0.04	-0.05	-0.06
	B_2	0.44	0.45	0.46	0.47	0.43	0.44	0.45	0.46	0.43	0.43	0.44	0.45
	X	0.64	0.73	0.83	0.93	0.56	0.65	0.73	0.82	0.50	0.58	0.65	0.73
	Y	-0.03	-0.08	-0.14	-0.20	0.02	-0.03	-0.08	-0.13	0.05	0.01	-0.04	-0.08
Case 2	H_2	1.00	1.00	1.00	1.00	1.00	1.00	1.00	1.00	1.00	1.00	1.00	1.00
	N_1	0.27	0.36	0.46	0.56	0.19	0.28	0.36	0.45	0.14	0.21	0.28	0.36
	N_{1a}	0.31	0.43	0.54	0.66	0.23	0.32	0.42	0.52	0.16	0.25	0.33	0.42
	N_{1b}	0.10	0.13	0.17	0.20	0.07	0.10	0.13	0.16	0.05	0.07	0.10	0.13
	T_{1a}	0.13	0.17	0.22	0.27	0.09	0.13	0.17	0.21	0.07	0.10	0.14	0.17
	T_{1b}	0.15	0.20	0.26	0.31	0.11	0.15	0.20	0.25	0.08	0.12	0.16	0.20
	V_{1a}	-0.02	-0.02	-0.03	-0.04	-0.02	-0.02	-0.03	-0.03	-0.01	-0.02	-0.02	-0.03
	V_{1b}	-0.01	-0.02	-0.02	-0.02	-0.01	-0.01	-0.02	-0.02	-0.01	-0.01	-0.02	-0.02
	B_1	0.07	0.08	0.09	0.10	0.06	0.07	0.08	0.09	0.05	0.06	0.07	0.08
	H_1	0.18	0.20	0.22	0.23	0.15	0.18	0.20	0.21	0.13	0.15	0.18	0.19
	N_{2a}	0.35	0.44	0.54	0.64	0.27	0.35	0.44	0.53	0.20	0.28	0.36	0.44
	N_{2b}	0.37	0.48	0.59	0.70	0.29	0.38	0.48	0.58	0.22	0.30	0.39	0.48
	T_{2a}	0.35	0.44	0.53	0.62	0.27	0.36	0.44	0.52	0.21	0.29	0.37	0.44
	T_{2b}	0.43	0.55	0.67	0.79	0.34	0.45	0.55	0.66	0.26	0.36	0.46	0.55
	V_{2a}	-0.09	-0.11	-0.13	-0.14	-0.08	-0.10	-0.12	-0.14	-0.07	-0.09	-0.11	-0.13
	V_{2b}	-0.07	-0.08	-0.09	-0.10	-0.06	-0.07	-0.08	-0.09	-0.05	-0.06	-0.07	-0.08
	B_2	0.42	0.42	0.43	0.44	0.42	0.42	0.43	0.44	0.42	0.42	0.43	0.44
	X	0.74	0.83	0.93	1.03	0.66	0.74	0.83	0.92	0.60	0.67	0.75	0.83
	Y	-0.08	-0.14	-0.20	-0.27	-0.03	-0.08	-0.14	-0.20	0.02	-0.04	-0.09	-0.14
Case 3	H_2	1.00	1.00	1.00	1.00	1.00	1.00	1.00	1.00	1.00	1.00	1.00	1.00
	N_1	0.33	0.42	0.52	0.62	0.26	0.34	0.42	0.51	0.20	0.27	0.35	0.42
	N_{1a}	0.39	0.50	0.62	0.73	0.31	0.40	0.50	0.60	0.24	0.33	0.41	0.50

Table 2
The distribution of prestress in the cable dome structure under changes in geometric parameters

Parameter	f/L	0.08				0.09				0.10			
	h/L	0.07	0.08	0.09	0.10	0.07	0.08	0.09	0.10	0.07	0.08	0.09	0.10
Case 3	N_{1b}	0.13	0.16	0.20	0.24	0.10	0.13	0.16	0.20	0.08	0.11	0.13	0.16
	T_{1a}	0.17	0.22	0.26	0.31	0.14	0.18	0.22	0.26	0.11	0.14	0.18	0.22
	T_{1b}	0.21	0.26	0.32	0.37	0.17	0.21	0.26	0.31	0.13	0.17	0.22	0.26
	V_{1a}	-0.03	-0.04	-0.04	-0.05	-0.03	-0.03	-0.04	-0.05	-0.02	-0.03	-0.04	-0.04
	V_{1b}	-0.02	-0.02	-0.03	-0.03	-0.02	-0.02	-0.02	-0.03	-0.01	-0.02	-0.02	-0.02
	B_1	0.07	0.08	0.08	0.09	0.06	0.07	0.08	0.09	0.06	0.06	0.07	0.08
	H_1	0.20	0.21	0.23	0.24	0.18	0.20	0.21	0.22	0.16	0.18	0.20	0.21
	N_{2a}	0.53	0.63	0.74	0.85	0.44	0.53	0.63	0.73	0.37	0.45	0.54	0.63
	N_{2b}	0.55	0.67	0.78	0.89	0.46	0.56	0.66	0.76	0.38	0.47	0.57	0.66
	T_{2a}	0.50	0.59	0.68	0.77	0.43	0.51	0.59	0.67	0.37	0.44	0.52	0.59
	T_{2b}	0.66	0.79	0.91	1.04	0.56	0.68	0.79	0.90	0.48	0.59	0.69	0.79
	V_{2a}	-0.15	-0.17	-0.18	-0.20	-0.14	-0.16	-0.18	-0.19	-0.13	-0.15	-0.17	-0.19
	V_{2b}	-0.10	-0.11	-0.12	-0.13	-0.10	-0.11	-0.12	-0.13	-0.09	-0.10	-0.11	-0.12
	B_2	0.39	0.39	0.40	0.41	0.39	0.40	0.41	0.42	0.40	0.40	0.41	0.42
	X	0.85	0.94	1.04	1.14	0.77	0.86	0.94	1.03	0.71	0.78	0.86	0.94
	Y	-0.15	-0.22	-0.29	-0.36	-0.09	-0.16	-0.22	-0.28	-0.05	-0.11	-0.16	-0.22

4. Structural dynamic characteristics analysis

4.1. Finite element model

In the finite element software Ansys, a numerical model with a span of 120 m was established. As an example, a set of parameters was chosen, which includes a span-to-rise ratio of 0.08, a thickness-to-span ratio of 0.10, and Case 1 of lower chord node arrangement scheme. The cable dome consists of two ring structures, with the inner ring structure having an opening diameter of 40 m. There are a total of 17 categories of components in the model. In the Ansys model, both cables and struts were simulated using the LINK180 element. Cables were defined as tension-only elements, while struts were defined as compression-only elements [20]. According to the initial prestress requirement, the cable cross-sections were prestressed to 20% of their breaking strength, while and the strut cross sections followed the aspect ratio design. For the cable, steel wire strands were used, and for the struts, hot-pressed seamless steel pipes were used. The material properties of these components can be found in Table 3. In the structural model, all nodes 3a in the outer ring were fully constrained as boundary conditions. The standard value for roof load is set to 0.5 kN/m^2, and it is applied by converting the distributed load into equivalent nodal loads using the SURF154 surface effect element for calculation. The structural model is depicted in Fig. 4. The initial prestress was applied through initial strains, and the levels of initial prestress and component cross-sectional parameters can be found in Table 4. The prestress mode was determined based on the values in Table 1. As shown in Table 4, the internal force distribution after the self-balancing of the finite element structural model matches the results of the prestressed state distribution, demonstrating the correctness of the established finite element model.

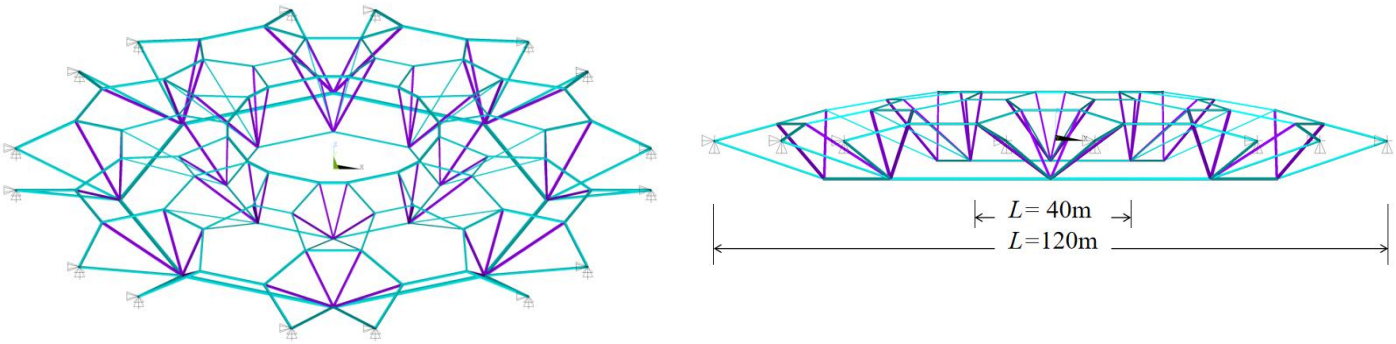

(a) 3D visualization of the numerical model (b) front view of the numerical model

Fig. 4 Numerical model of the $_{24}\bar{H}_{24\mathrm{III}}$ cable dome

Table 3
Material properties

Components	Yield strength (Mpa)	Poisson's ratio	Modulus of elasticity (Mpa)	Coefficient of linear expansion	Density (kg/mm^3)
cables	1860	0.3	1.95×10^5	1.36×10^{-5}	7.85×10^{-6}
struts	345	0.3	2.06×10^5	1.2×10^{-5}	7.85×10^{-6}

Table 4
Structural prestressing modes and member section parameters

Categorization	Components	Prestressed Mode	Self-equilibrating Internal Forces（kN）	Sectional Dimensions
Ridge cables	N_1	0.52	5235	Φ147
	N_{1a}	0.60	6030	Φ161
	N_{1b}	0.18	1760	Φ92
	N_{2a}	0.40	3962	Φ127
	N_{2b}	0.54	5448	Φ147
Diagonal cables	T_{1a}	0.23	2322	Φ80
	T_{1b}	0.27	2660	Φ107
	T_{2a}	0.49	4879	Φ147
	T_{2b}	0.60	5980	Φ155
Ring cables	B_1	0.11	1108	Φ92
	B_2	0.47	4699	Φ147
Sturts	H_1	0.22	2240	Φ80
	H_2	1.00	10000	Φ154
	V_{1a}	-0.03	-294	Φ254×14
	V_{1b}	-0.02	-231	Φ273×16
	V_{2a}	-0.11	-1082	Φ426×16
	V_{2b}	-0.08	-789	Φ427×15

4.2. Analysis of structural modal characteristics

The natural vibration characteristics are intrinsic mechanical properties of a structure that are closely related to its mass and stiffness. These characteristics not only reflect the stiffness of the structure but also directly influence the response to dynamic loads. They serve as an important basis for judging whether the distribution of structural stiffness and mass matches and is reasonable. Modal analysis includes two aspects: natural frequencies and mode shapes. The free vibration equation for each node are as follows:

$$[M]\{\ddot{u}\}+[C]\{\dot{u}\}+[K]\{u\}=0 \tag{10}$$

In the aforementioned equation, [M] represents the structural mass matrix, [C] represents the structural damping matrix, [K] represents the structural stiffness matrix, {F(t)} denotes the time-varying load function, $\{u\}$ is the nodal displacement vector, $\{\dot{u}\}$ is the nodal velocity vector, and $\{\ddot{u}\}$ is the nodal acceleration vector [15]. When conducting modal analysis, the influence of damping is not typically neglected. Therefore, the equation can be rewritten as follows:

$$[M]\{\ddot{u}\}+[K]\{u\}=0 \tag{11}$$

By performing a transformation on the equation, the generalized characteristic equation for the structure can be obtained as follows:

$$(K-\omega^2 M)\Phi=0 \tag{12}$$

In the equation, ω represents the structural natural frequencies, and Φ is the mode shape vector. The characteristic determinant of equation is given by:

$$\left|K-\omega^2 M\right|=0 \tag{13}$$

Solving the equation yields the n natural frequencies of the system denoted as $\omega_1 \le \omega_2 \le \ldots \le \omega_n$ and along with their corresponding mode shapes. In this study, the Block Lanczos method was employed for modal analysis, specifically considering the first 50 modes. The variation of natural frequencies is shown in Fig. 5. It is noteworthy that the first 10 natural frequencies of the structure exhibit proximity to each other, while the higher-order natural frequencies are more widely spaced. The fundamental frequency of the structure, measured at 1.0184 Hz, indicates that the structure has a relatively high stiffness. Due to the axial and central symmetry of the structure, the frequencies will appear in pairs with equal values.

From the data in Table 5, it can be observed that each pair of equal-frequency modes is essentially the same, except they are rotated 90° around the structure's central axis. As shown in Fig. 6, the modes for each order exhibit distinct characteristics. The 1st and 2nd modes are primarily dominated by vertical deformation in the inner ring, with horizontal displacement smaller than vertical displacement. The 3rd mode involves horizontal vibration, primarily characterized by circumferential deformation in the inner ring. In the 4th and 5th modes, vertical deformation dominates, with the point of maximum displacement shifting from the inner ring to the outer ring. Additionally, these modes exhibit significant horizontal displacement. The 6th and 7th modes are characterized by circumferential deformation in the outer ring, accompanied by vertical displacement. The 8th and 9th modes primarily exhibit vertical vibrations, with vertical deformation in the outer ring as the dominant feature. These modes also exhibit significant horizontal displacement. The 10th mode involves coupled deformation in both the circumferential and vertical directions, with slightly larger vertical displacement observed in the inner ring compared to horizontal displacement in the outer ring. Based on the analysis provided, it can be concluded that, for this cable dome configuration, the inner ring has lower stiffness compared to the outer ring, and the structural stiffness in the vertical direction is weaker than that in the circumferential direction.

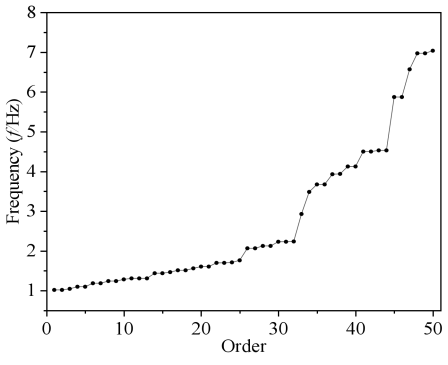

Fig. 5 The first 50 natural frequencies of the structure vs order numbers

Table 5
Material properties

Order	1、2	3	4、5	6、7	8、9	10
Frequency（Hz）	1.0184	1.0455	1.0991	1.1863	1.2417	1.2828

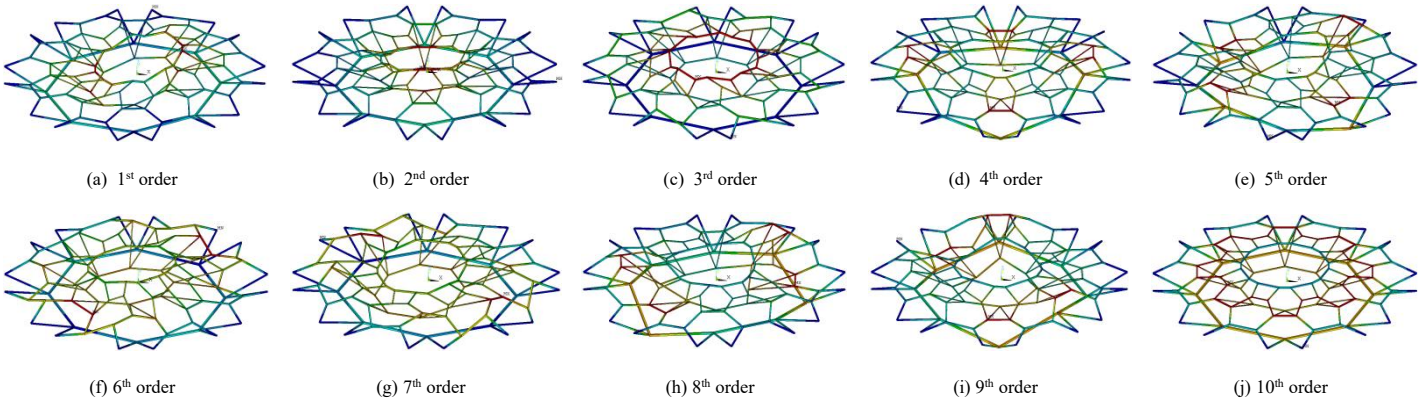

(a) 1st order (b) 2nd order (c) 3rd order (d) 4th order (e) 5th order

(f) 6th order (g) 7th order (h) 8th order (i) 9th order (j) 10th order

Fig. 6 The first 10 vibration modes of the structure

4.3. Parametric analysis of structural modal characteristics

The structural modal characteristics are closely related to factors such as the geometric configuration of the structure and the level of prestress. Therefore, it is essential to conduct a parametric analysis of the structural modal characteristics. To further investigate the influence of structural parameters on modal characteristics, several key structural parameters are selected, including the initial prestress level, span-to-rise ratio, thickness-to-span ratio and lower chord node arrangement scheme. Through parametric analysis, the impact of each parameter on the structural modal characteristics is explored.

4.3.1. Initial prestress level

To investigate the influence of the initial prestress level on the structural modal characteristics while keeping other parameters constant, the prestress levels are varied to be 0.5, 1.0, 1.5, and 2.0 times. Modal analysis is performed on the structure, and the resulting first 50 natural frequencies are shown in Fig. 6. From the figure, it is observed that, under different initial prestress levels, the trends in the first 50 natural frequencies of the structure remain generally consistent. The low-frequency modes are densely distributed, while the high-frequency modes are sparser and exhibit multiple jump points. As the initial prestress level increases, the natural frequencies of the structure also increase. The increase in low-frequency modes is more significant compared to the increase in high-frequency modes. Notably, when the prestress level changes from 0.5 times to 1.0 times, there is a significant increase in frequencies. However, as the prestress level changes from 1.0 times to 2.0 times, the rate of increase gradually decreases. This suggests that as the initial prestress level increases, the structural stiffness also increases. However, the rate of stiffness increase gradually decreases when the prestress level exceeds 1.0 times.

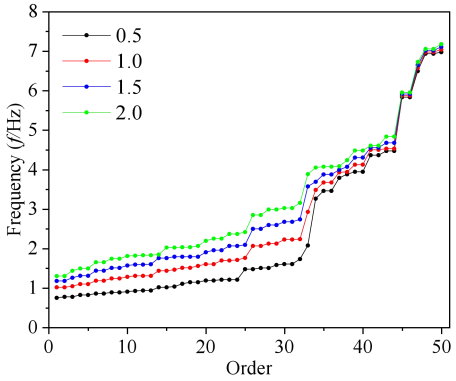

Fig. 6 The first 50 natural frequencies under different initial prestress level vs order numbers

4.3.2. Span-to-rise ratio

To explore the impact of the span-to-rise ratio on the structural natural frequencies while keeping other parameters constant, the structural model was analyzed with span-to-rise ratios of 0.07, 0.08, 0.09, and 0.10. The resulting first 50 natural frequencies of the structure are shown in Fig. 7 below. From the graph, it is observed that, for all four span-to-rise ratios, the overall trend of natural frequency variations is similar. The lower-order frequencies are denser, while the higher-order frequencies are sparser and exhibit multiple jump points. As the span-to-rise ratio increases, the natural frequencies decrease initially until around the 45th mode, after which they exhibit the opposite trend, increasing with a higher span-to-rise ratio. The span-to-rise ratio has a significant impact on the fundamental mode and lower-order frequencies, leading to changes in structural stiffness as the span-to-rise ratio increases.

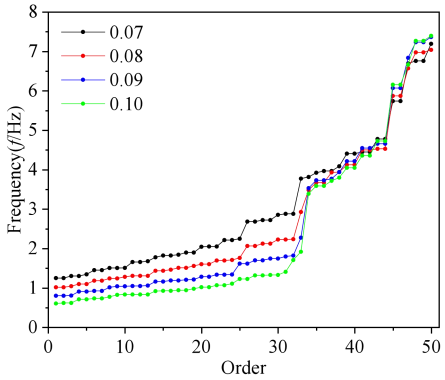

Fig. 7 The first 50 natural frequencies under different span-to-rise ratios vs order numbers

4.3.3. Thickness-to-span ratio

To investigate the impact of the thickness-to-span ratio on the structural natural frequencies while keeping other parameters constant, the structural model was analyzed with thickness-to-span ratios of 0.07, 0.08, 0.09 and 0.10. The resulting first 50 natural frequencies of the structure are shown in Fig. 8 below. From the figure, it is observed that, for all four thickness-to-span ratios, the overall trend of natural frequency variations is quite similar. The lower-order frequencies are denser, while the higher-order frequencies are sparser and exhibit multiple jump points. As the thickness-to-span ratio increases, the natural frequencies also increase. After the 45th mode, the natural frequencies of the three models with a thickness-to-span ratio greater than 0.08 become relatively close, indicating that the structural stiffness reaches its peak. An increase in the structural thickness-to-span ratio results in a corresponding increase in structural stiffness.

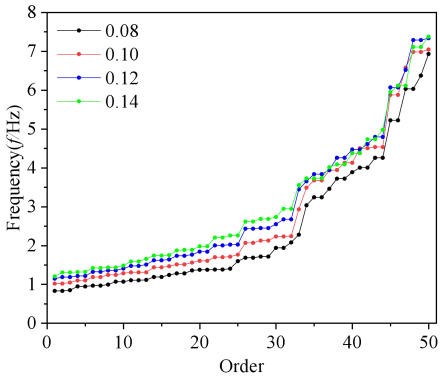

Fig. 8 The first 50 natural frequencies under different thickness-to-span ratios vs order numbers

4.4. Time history analysis of structural seismic

4.4.1. Selection and input of seismic waves

To understand the impact of seismic actions on this structure, this study

selected the El-Centro wave from the 1940 El Centro, California earthquake, which had a magnitude of 7.1, as the seismic load input. The numerical model employed in this section is the same as that in Section 4.1, with a damping ratio set to 0.02 [21]. The dynamic response of the structure under seismic loading was investigated. According to the guidelines outlined in the "Seismic Design Code for Buildings" Section 5.1.4, the analysis was conducted for high-intensity earthquake conditions in Seismic Design Category 8, with a maximum ground acceleration of 0.7 m/s² [22]. The El-Centro earthquake waveforms in three directions were adjusted to have peak accelerations of 0.7 m/s² in the X direction, 0.7 m/s² in the Y direction and -0.7 m/s² in the Z direction to meet the specific requirements. The acceleration time-history curves of the El-Centro earthquake waveforms for the first 30 seconds after adjustment are shown in Fig. 9.

The seismic response analysis of the structure was conducted using the dynamic time-history analysis method [14]. The structure's dynamic response was computed under one-dimensional, two-dimensional and three-dimensional seismic load inputs. The earthquake arrays used in the analysis are listed in Table 6. The seismic excitation factors were set to 1.0 and 0.65 for the two-dimensional seismic wave, and 1.0, 0.85, and 0.65 for the three-dimensional seismic wave.

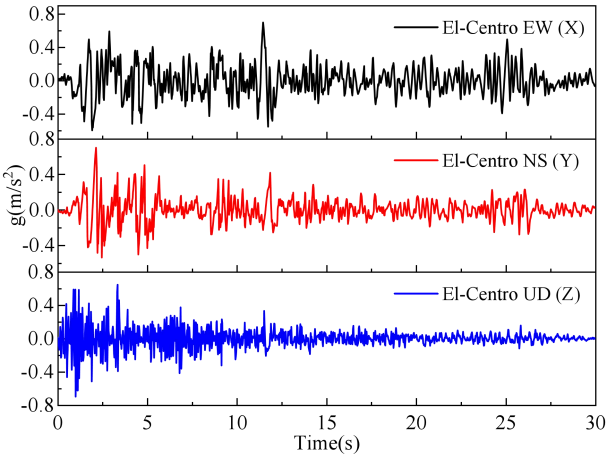

Fig. 9 The acceleration time-history curve for the first 30 s after amplitude adjustment of El-Centro seismic wave

Table 6
The excitation factors of each earthquake array

Arrays	X(EW)	Y(NS)	Z(U)
1D seismic wave	1.0	—	—
2D seismic wave	1.0	—	0.65
3D seismic wave	1.0	0.85	0.65

4.4.2. Internal force analysis

The calculation results of dynamic internal force coefficients for the structure under three different seismic arrays are shown in Table 7. Dynamic internal force coefficient refers to the ratio of the maximum internal force of a component during the time-varying internal force process to its initial internal force. Analyzing the data from Table 7, it can be concluded that the overall dynamic effect on component internal forces in the structure under seismic actions is not significant, with a maximum dynamic internal force coefficient of only 1.0031. In general, the internal forces of inner ring components exhibit a greater dynamic response to seismic actions compared to outer ring components. The dynamic response of internal forces induced by three-dimensional and two-dimensional seismic actions is significantly larger than that induced by one-dimensional seismic actions. Furthermore, the structural dynamic response to three-directional seismic actions is slightly greater than that to two-dimensional seismic actions.

Fig. 10 shows the time-history curves of the components that exhibit the most pronounced dynamic response under seismic actions among various types of components. During the analysis process, no tension cables exhibited any slackening phenomenon, and the distribution of dynamic responses coincided with the acceleration time-history curves of the seismic waves.

Table 7
The dynamic internal force coefficients of each component under different earthquake arrays

Components		Dynamic internal force coefficient of each component		
		1D	2D	3D
Ridge cables	N_1	1.00072	1.00260	1.00257
	N_{1a}	1.00285	1.00256	1.00256
	N_{1b}	1.00244	1.00291	1.00284
	N_{2a}	1.00230	1.00207	1.00207
	N_{2b}	1.00257	1.00229	1.00257
	T_{1a}	1.00235	1.00252	1.00254
	T_{1b}	1.00281	1.00277	1.00278
	T_{2a}	1.00243	1.00220	1.00237
	T_{2b}	1.00289	1.00263	1.00284
Diagonal cables	B_1	1.00215	1.00251	1.00295
	B_2	1.00217	1.00241	1.00259
Ring cables	H_1	1.00159	1.00191	1.00213
	H_2	1.00123	1.00187	1.00200
Struts	V_{1a}	1.00205	1.00218	1.00290
	V_{1b}	1.00297	1.00302	1.00310
	V_{2a}	1.00202	1.00214	1.00249
	V_{2b}	1.00217	1.00295	1.00227

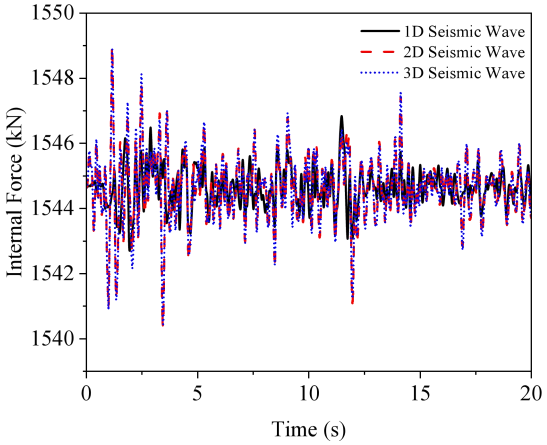

(a) The time-history curve of N_{1b}

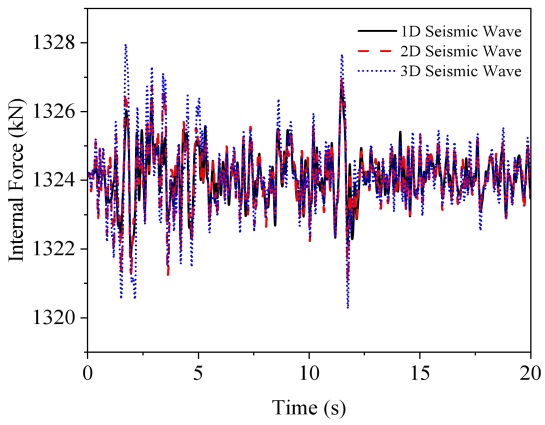

(b) The time-history curve of B_1

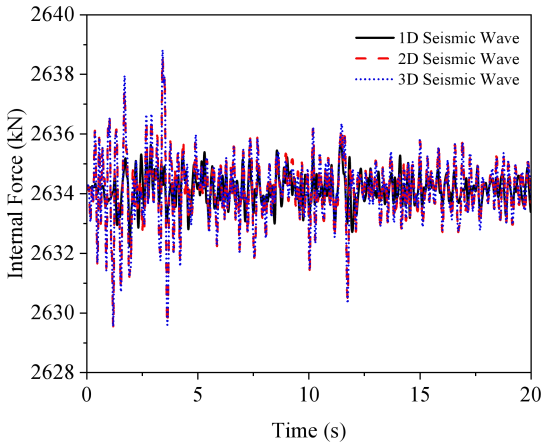

(c) The time-history curve of H_1

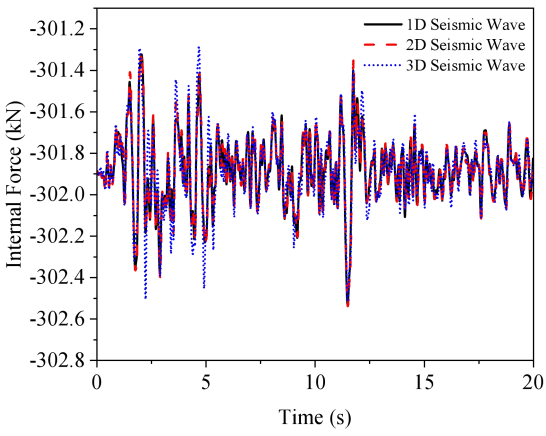

(d) The time-history curve of V_{1b}

Fig. 10 The time-history curve of internal forces in components under seismic loading

4.4.3. Deformation analysis

The seismic wave input direction and the substructure numbering for the cable dome structure are shown in Fig. 11. Along the X-axis, nodes are parallel to the one-dimensional horizontal seismic load direction, while along the Y-axis, nodes are perpendicular to the one-dimensional horizontal seismic load direction. Therefore, the maximum horizontal displacement in the X-direction occurs at nodes along the X-axis. Table 8 below presents the calculated dynamic displacement responses of various nodes in the cable dome structure under multi-dimensional seismic loads. Considering the horizontal symmetry of the structure in terms of height, the analysis of horizontal displacement primarily focuses on the X-direction.

Regarding the horizontal displacement of the structure, an analysis of the calculation results in Table 8 reveals that, due to the additional constant load acting only on the upper chord nodes, the X-direction horizontal displacement response at each upper chord node is greater under two- and three-dimensional seismic loads compared to one-dimensional seismic loads. Under two- and three- dimensional seismic loads, the dynamic responses are similar. For the lower chord nodes, under all three seismic arrays, the displacement dynamic responses are relatively close. The four braces converge at the lower chord node, providing sufficient lateral stiffness for the upper chord honeycomb cable grid. Therefore, the X-direction horizontal displacement dynamic response coefficients for all upper chord nodes are less than 1.10. The maximum displacement response coefficient is observed at inner ring lower chord node 1, with a coefficient of 1.54, which is significantly greater than the outer ring's coefficient of 1.03. This discrepancy is attributed to the lower pre-tension level of the inner ring cables, resulting in significantly lower radial stiffness for the inner ring. The time-history curves of horizontal displacement for the lower chord nodes are shown in Fig. 12.

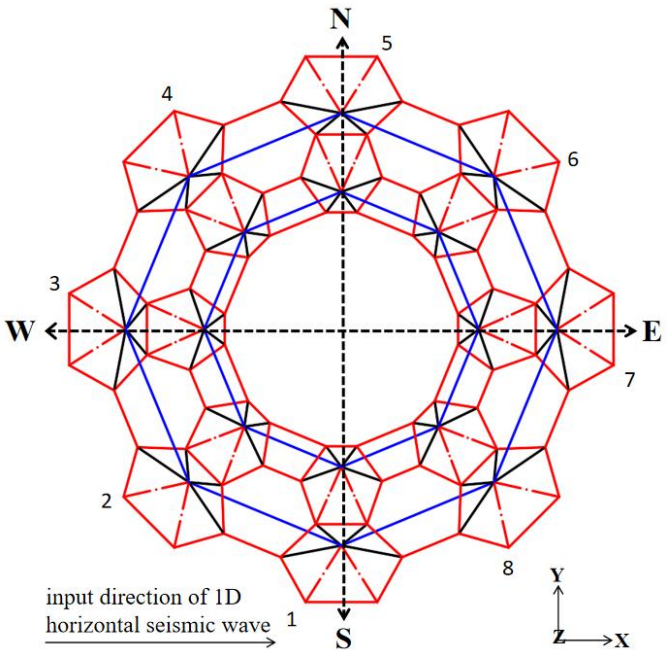

Fig. 11 Earthquake wave direction and substructure numbering

Table 8

The dynamic internal force coefficients of each component under different earthquake arrays

Node number		1_a			1_b			2_a			2_b			1’			2’		
Direction		1D	2D	3D	1D	2D	3D	1D	2D	3D	1D	2D	3D	1D	2D	3D	1D	2D	3D
U_x	U_{xmax}	6.50	6.53	6.52	7.82	7.86	8.00	7.53	7.57	7.56	7.17	7.20	7.21	4.83	4.85	4.86	12.55	12.57	12.58
	U_{x0}		6.06			7.45			7.01			6.96			3.15			12.27	
	U_{xmax}/U_{x0}	1.07	1.08	1.08	1.05	1.06	1.07	1.07	1.08	1.08	1.03	1.03	1.04	1.53	1.54	1.54	1.02	1.02	1.03
U_y	U_{ymax}	6.39	6.40	6.70	7.90	8.14	8.48	7.40	7.48	7.93	7.00	7.05	7.14	3.16	3.16	4.3	12.27	12.27	12.54
	U_{y0}		6.06			7.45			7.01			6.96			3.15			12.23	
	U_{ymax}/U_{y0}	1.05	1.06	1.11	1.06	1.09	1.14	1.06	1.07	1.13	1.01	1.01	1.03	1.00	1.00	1.37	1.00	1.00	1.03
U_z	U_{zmax}	91.90	92.10	92.37	81.65	81.77	82.94	57.03	57.18	57.56	39.61	39.64	40.15	91.05	91.63	92.12	56.32	56.36	56.71
	U_{z0}		-90.68			-81.19			-56.23			-39.23			-90.40			-55.43	
	U_{zmax}/U_{z0}	1.01	1.02	1.03	1.01	1.01	1.02	1.01	1.02	1.03	1.01	1.02	1.03	1.01	1.02	1.03	1.01	1.02	1.03

Note: U represents displacement, and subscripts with letters represent the direction of displacement. U_0 represents the initial load state displacement. The displacement dynamic response coefficient is the ratio of the maximum displacement in a certain direction to the initial load state displacement.

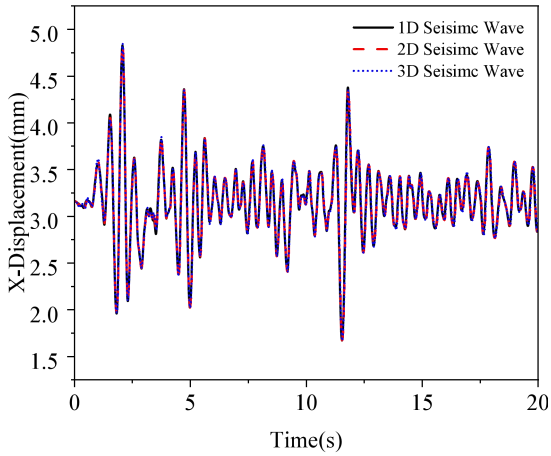

(a) The horizontal displacement time-history curve for lower chord node 1'-7

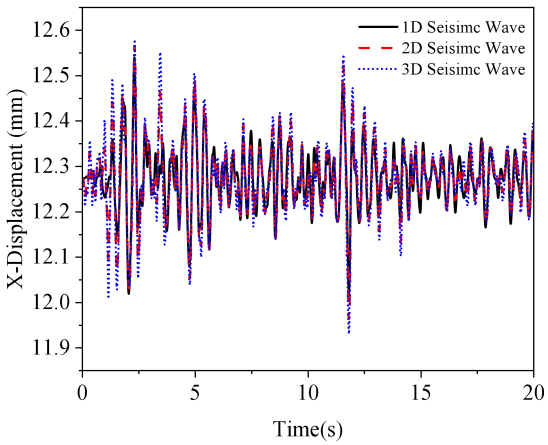

(b) The horizontal displacement time-history curve for lower chord node 2'-7

Fig. 12 The horizontal displacement time-history curve of lower chord nodes

Regarding the horizontal displacement of the structure, in seismic arrays 2 and 3, seismic waves were introduced in the Z-direction. Consequently, under two-dimensional and three-dimensional seismic loads, the vertical displacement dynamic response at various structural nodes is greater than that under one-dimensional loads. However, under one-dimensional and two-dimensional seismic loads, the dynamic response is similar. When comparing the results for upper chord nodes and lower chord nodes, it is evident that node loads have a relatively small impact on the Z-direction displacement of the nodes. When comparing the displacement values between inner and outer ring nodes, it can be observed that Z-direction seismic waves have a greater impact on the inner ring of the structure than the outer ring, indicating that the inner ring of the structure has lower stiffness than the outer ring. The time-history curves of vertical displacement for inner ring nodes are shown in Fig. 13, and the displacement fluctuations align with the acceleration time-history curves.

Overall, the dynamic response of the structure under seismic loads is relatively small. However, each type of components and nodes exhibits distinct dynamic responses to different seismic actions. The analysis results reflect the structural characteristics that are essential to consider when conducting dynamic load calculations and structural design for this cable dome structure. These findings are of significant importance.

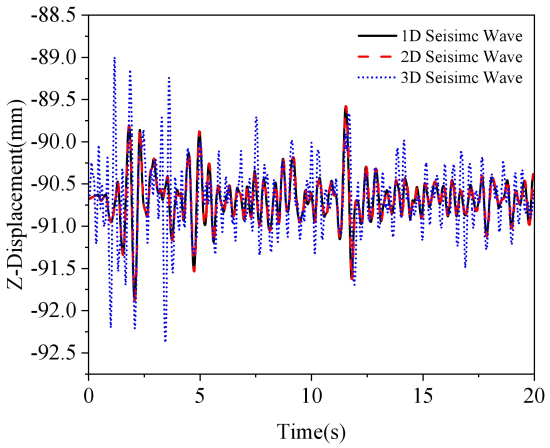

(a) The vertical displacement time-history curve for lower chord node 1_a-1

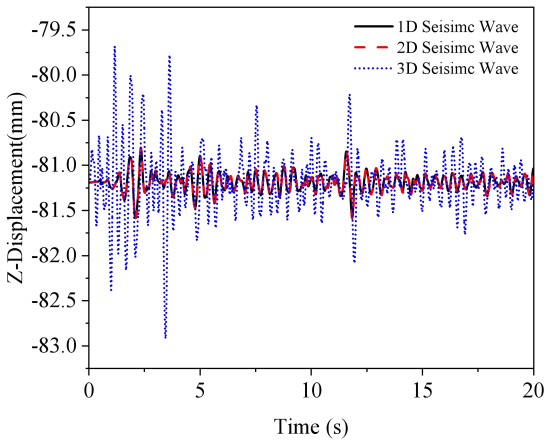

The vertical displacement time-history curve for lower chord node 1_b-1

Fig. 13 The vertical displacement time-history curve of inner ring nodes

5. Conclusions

This study focuses on the new form ${}_{24}\bar{H}_{24III}$ cable dome structure. Based on the node equilibrium theory, it derives general calculation formulas for the prestress state of the structure and the internal forces in the bars. Additionally, the study analyzes the distribution of prestress within the structure and how it changes with variations in structural parameters. Using a finite element numerical model with a span of 120 meters as an example, the study explores the impact of structural parameters on the structural vibration characteristics through modal analysis. Based on the modal analysis results, the study calculates the dynamic response of the components and critical nodes' displacements under multi-dimensional seismic loads using nonlinear dynamic analysis methods. These research findings provide valuable insights into the mechanical performance of the structure. The main conclusions of this paper are as follows:

(1) From the perspective of structural topology, the cable grid of the ${}_{24}\bar{H}_{24III}$ cable dome structure is uniformly distributed, making the structural design simple and efficient while minimizing the use of cables and struts. By tensioning the outer ring cables simultaneously, the structure can be pre-positioned, reducing the steps involved in tensioning during construction. This design approach can accommodate diverse architectural requirements while remaining cost-effective.

(2) The results of the prestressed state calculation example indicate that, the internal forces in the prestressed cables and struts of the structure are reasonably distributed, with the outer ring of the structure primarily governing the overall stiffness. Meanwhile, variations in the aspect ratio, height-to-span ratio and the arrangement of lower chord nodes have distinct effects on the distribution of internal forces in the cables and struts. Increasing the thickness-to-span ratio while moderately reducing the span-to-rise ratio can enhance the structural stiffness. However, this change would also lead to increased support reactions.

(3) The modal analysis results show that the fundamental frequency of the structure is 1.0184, indicating good stiffness. Due to the structural height symmetry, there is a distinct pattern in the resonant modes of the structure. These modes predominantly involve vertical deformations, suggesting that the vertical stiffness of the structure is comparatively weaker than the radial stiffness. Additionally, structural parameters have a noticeable impact on the resonant characteristics. Increasing the initial prestress level, reducing the span-to-rise ratio or increasing the thickness-to-span ratio can effectively enhance the structural stiffness.

(4) From the results of the seismic response calculations, the dynamic responses of various structural components and nodes do not significantly

differ from those under static loads. This indicates that the ${}_{24}\bar{H}_{24|||}$ cable dome structure, as a flexible system, demonstrates excellent seismic performance when reasonable structural parameters are selected under specific site conditions.

Acknowledgments

The work was financially supported by the National Natural Science Foundation of China (No. 52268031), which is gratefully acknowledged.

References

[1] Fuller, R.B. “Tensile-Integrity Structure”, U.S Patent, 3063521, 1962.
[2] Geiger, D.H., “The design and counstruction of two cable domes for Korean Olympics”, In Proceedings of the Membranes and Space Frames IASS Symposium, Osaka, Japan, 15–19, September, 1986.
[3] Geiger, D.H. “Roof structure”, U.S Patent, 4736553, 1998.
[4] Levy, M.P. “The Georgia dome and beyond achieving light weight-long span structure”, In Proceedings of the IASS-ASCE International Symposium, Atlanta, 560-562, 1994.
[5] Jian. Lu, S.D. Xue, X.Y. Li, et al., "Segmented Assembly Construction Forming Method Without Brackets of Spatial Cable-Truss Structure Without Inner Ring Cables", Advanced Steel Construction, 18(3), 687-698, 2022.
[6] X.F. Yuan, S.L. Dong, “New forms and initial prestress calculation of cable dome”, Engineering Mechanics, 22(2), 22-26, 2005.
[7] S.L. Dong, Z.H Wang, X.F. Yuan, “Static behavior analysis of a space structure combined of cable dome and single-layer lattice shell”, Journal of Building Structure, (03), 1-8, 2010.
[8] S.L. Dong, Y. Tu, “Configuration and prestress distribution of honeycomb-type cable dome with four struts”, Spatial Structures, (02), 3-12, 2018.
[9] S.L. Dong, Y. Tu, “Reserch on the system of honeycomb-type cable dome structures”, In Proceedings of the 18th National Symposium on Modern Structural Engineering, 7-12, 2018.
[10] S.L. Dong, H. Lv, Z.Q. Chen et al., “Structural form and initial prestress analysis on drum-shaped honeycomb-type cable with quad-strut layout”, Spatial Structures, 28(04), 3-15, 2022.
[11] Pellegrino S, Calladine C R. “Matrix analysis of statically and kinematically indeterminate frameworks”, International Journal of Solids and Structures, 22(4), 409-428, 1986.
[12] Pellegrino S, “Structural computation with the singular value decomposition of equilibrium matrix”, International Journal of Solids and Structures, 30(21), 3025-3035, 1993.
[13] X.F. Yuan, S.L. Dong, “The concept of integral feasible prestressing of cable dome structure and its application”, China Civil Engineering Journal, 34(2), 33-37, 2001.
[14] P.C. Li, “Nonlinear stability behaviour of cable-stiffened single-layer latticed shells under earthquakes”, International Journal of Structural Stability and Dynamics, 18(10), 1850117, 2018.
[15] Z.W. Lin, C. Zhang, J.C. Dong, et al., “Dynamic Response Analysis of Multiple Square Loops-String Dome under Seismic Excitation”, Symmetry, 13, 2062, 2021.
[16] H. Zhang, H. Lv, Z.Y. Zhu, et al., “Dynamic Response of the Component Failure of Drum-Shaped Honeycomb-Type III Cable Dome with Quad-Strut Layout”, Buildings, 13(8), 1894, 2023.
[17] C.Zhu, X.S Wu. “Reconstructing Dynamic Responses and Screening High-Precision Unmeasured Points for Geiger Cable Dome Structures”, Engineering Mechanics, 1-13, 2024.
[18] A.L Zhang, W. Wen, Y.X. Zhang, et al., “Static performance analysis of alternated cable dome with single and double brace struts”, Journal Of Vibration And Shock, 41(12), 321-330, 2022.
[19] X.F. Yuan, S.L. Dong, “The concept of integral feasible prestressing of cable dome structure and its application”, China Civil Engineering Journal, 34(2), 33-37, 2001.
[20] H.C. Liu, S.L. Dong, Y.D. Wang, “Structural morphological analysis and optimal design of a ribbed-type suspen-dome as stadium canopy with quad-strut layout and large central opening”, Journal of Building Structures, 44(9), 135-150, 2023.
[21] Z. Cao, S.D. Xue, X.S. Wang, “Selection of earthquake waves and values of damping ratio for space structures in aseismic analysis”, Spatial Structures, 14(3), 3-8, 2008.
[22] “Seismic Design Code for Buildings”, China Architecture Publishing & Media Co. Ltd, Beijing, 2010.

Advanced Steel Construction – Vol. 20 No. 1 (2024) 93–104
DOI:10.18057/IJASC.2024.20.1.10

AN INVESTIGATION ON THE EFFECT OF RANDOM PITTING CORROSION ON THE STRENGTH OF THE SUBSEA PIPELINE USING MONTE CARLO METHOD

Tong Lin [1] , Wei Huang [1,*] , Si-Wei Liu [2] and Rui Bai [1]

[1] *School of Civil Engineering, Sun Yat-Sen University, Guangzhou, China*

[2] *Department of Civil and Environmental Engineering, The Hong Kong Polytechnic University, Hung Hom, Kowloon, Hong Kong, China*

* (*Corresponding author: E-mail: huangw288@mail.sysu.edu.cn*)

ABSTRACT

Pitting corrosion is normally distributed randomly along the pipeline, which is the source of the uncertainty affecting the ultimate bearing capacity of the submarine pipelines. So the Monte Carlo method is employed to study the effect of pitting corrosion on the upheaval buckling behavior of the pipeline. A corroded pipeline model with randomly distributed pitting corrosion is utilized to captures the intricate realities of corrosion scenarios. Multiple corrosion models with distinct artificial patterns have been meticulously crafted. Additionally, a new pipeline element based on Euler-Bernoulli beam theory is extended considering corroded sections, pipe-soil interactions, axial load, initial imperfections, and other major factors. Moreover, the bearing capacity, vertical deformation and section stress of the pipeline under corrosion is discussed thoroughly, wherein a Newton- Raphson typed numerical analysis procedure is utilized for nonlinear analysis of the upheaval buckling of pipelines. The influence of corrosion parameters such as the corrosion depth, corrosion ratio and area loss ratio on mechanical properties of the submarine pipelines is further analyzed in detail. It's indicated that varying patterns of corrosion distribution, despite exhibiting identical corrosion parameters, can result in distinct reduction factors and vertical buckling displacements.

ARTICLE HISTORY

Received: 20 February 2024
Revised: 20 March 2024
Accepted: 20 March 2024

KEYWORDS

Monte Carlo method;
Corrosion;
Pipeline element;
Upheaval buckling;
Submarine pipelines

Copyright © 2024 by The Hong Kong Institute of Steel Construction. All rights reserved.

1. Introduction

Submarine pipelines are highly efficient in transporting oil and gas, also recognized as "lifeline engineering", as they play a similar role as human arteries. However, the complexity of the marine environment results in corrosion in steel pipelines, leading to pipeline failures and damage. The corrosion of pipelines not only compromises their structural integrity but also poses potentially harmful consequences for the surrounding marine environment. Pitting corrosion is a common form of localized corrosion that occurs due to inadequate cathodic protection or absence of pipeline coating. The phenomenon is characterized by the formation of small pits on the pipeline surface, which can grow in size and depth, leading to severe pipeline damage over time. Pitting damage, though diminutive in size, can trigger the stress concentration and expedite the onset of plasticity in metallic structural components. To mitigate such corrosion-related concerns, it's imperative to ensure a robust coating system and effective cathodic protection measures are in place. It's therefore imperative to remain vigilant and implement effective maintenance strategies to detect and preserve against such damages to ensure the durability and longevity of structures[1-3].

Submarine pipelines installed on uneven seabeds are prone to buckling when exposed to elevated temperature and pressure conditions. Thermal expansion and pressure increase can generate axial compression force that exceeds the pipeline's critical axial compression limit. This exceeds the stress and strain thresholds, potentially resulting in local buckling and decreased axial carrying capacity, which may even lead to fatigue and fracture[4,5]. It's essential to proactively mitigate such risks by applying adequate pipeline design methods and advanced modelling techniques to anticipate and prevent corrosion failure to safeguard the pipeline's functioning and longevity. When pipelines undergo corrosion, there is an increased risk of compromised structural integrity and strength, resulting in uncertainty regarding the estimation of burst pressure. Consequently, it is crucial to evaluate the impact of corrosion on the pipeline's buckling behavior. Nevertheless, the corrosion of pipelines is influenced by several factors such as the ocean environment, anti-corrosion effect, pipeline materials and manufacturing technology, stress level etc. Meanwhile, the specific feature and geometric parameter of pitting corrosion including the corrosion ratio, distribution, size and shape are of great variability, which leads to the uncertainties of its adverse effects on the performance of steel pipelines. There is a possibility of encountering challenges during the design and operation of submarine pipelines.

Pitting corrosion in pipelines is typically marked by the formation of circular cavities on the exterior of the compromised material. These cavities are typically assumed to be of uniform or random size, depth, and distribution throughout the pitted member [6]. The Pipeline Defect Assessment Manual (PDAM) offers a comprehensive overview of the techniques available for evaluating pipeline flaws, including corrosion. Additionally, it highlights a specific defect type and the associated factors that contribute to uncertainty in the modeling process for each assessment [7]. Netto [8] developed a numerical tool by creating oval corrosion pits defects for pipelines through the process of spark corrosion while the size and area of defects was specified, and the influence of corrosion defects on the collapse pressure of offshore pipelines was studied. Wang et al.[9] introduced random pitting defects into the outer surface of the pipeline by using 6% ferric chloride solution and found that the shape of pitting defects was cylindrical or semi-ellipsoid. It is said that the random geometric defects, amplitude of out-of-roundness and material properties would affect the collapse pressure significantly. Motta et al.[10] evaluated the failure pressure of corroded pipelines using nonlinear FE analyses of the manufactured defect models with constant or complex shape, dimension and configuration which were generated by PIPEFLAW. It is said that the conservative predictions would be obtained based on the semiempirical method. Mohd et al.[11] conducted a study on the residual strength properties of corroded subsea pipelines subjected to combined internal pressure and bending moment, taking into account the distinct characteristics (distribution, shape, and size) of the corrosion models. Nazaria et al.[12] used an idealized corrosion model in elliptical shape with 16 different corrosion geometries varied in depth, length and location along the tube aiming for predicting the ultimate strength and buckling behavior of locally damaged tubes. Ahn et al.[13] conducted compressive loading tests on steel tubes with two different types of artificially induced corrosion damage achieved by a mechanical process to examine the residual compressive strength and structure of locally corroded tubes. In reality, corrosion damage in pipelines is frequently more intricate than idealized models assume, as they postulate a uniform distribution of corrosion pits. While these simplified models may offer some insights into the underlying mechanisms of corrosion, they tend to overestimate the pipeline's strength under the same level of corrosion scenarios in reality. Therefore, the utilization of models that accurately replicate the dispersion of pitting corrosion is imperative, along with a thorough examination of the potential mechanisms of pipeline failure across varying corrosion scenarios [3]. Those equations derived from specific corroded models or actual corroded members should be examined for applicability in practical use. This is owing to the lack of consideration of the uncertainties associated with the various features of pitting corrosion, as evenly corroded surfaces with uniform corrosion dimensions are rare in reality [14, 15]. The presence of uncertainties in the corrosion features of pipelines can lead to variations in their ultimate strength. To accurately determine the remaining strength of corroded components, it is necessary to employ simulation technologies that can replicate the real-world conditions of the pipelines. Without such simulations, it is difficult to draw general conclusions about the strength of corroded components under different loading scenarios, as the impact of corrosion can vary greatly depending on the specific materials,

conditions, and geometries involved [16].

The present study aims to examine the impact of various corrosion parameters, including distribution, shape, and size, on the ultimate strength of submarine pipelines exposed to severe corrosive environments [6, 17-21]. Chen et al.[17] presented an efficient algorithm to determine the deterioration of the bearing cpacitys of I-Section steel members with random corrosion. Silva et al.[18] conducted a study on the diverse forms of corrosion, examining the influence of a random distribution of corrosion thickness on the ultimate strength of an unstiffened rectangular steel plate. Wang et al.[19] analyzed the failure mechanism and degradation of ultimate strength of the plated steel structure caused by the random pitting corrosion. A numerical study was carried out on tubular members of diverse slenderness ratios with pitting corrosion on the surface along the length and hoop to clarify the pitting effect on ultimate strength [6]. Ben et al.[20] applied Separable Monte Carlo (SMC) for randomly sampling the sets of input parameters of the Limit State Function (LSF) for the purpose of estimating the failure probability of corroded pipelines.

Pipelines play a critical role in transportation of oil and gas products in the subsea environment [22-25]. Owing to the unpredictable nature of pitting distribution and the intricate variations in material properties, considerable uncertainty persists regarding the impact of corrosion on the bearing capacity of pipelines. Hence, the aim of this research is to utilize the Monte Carlo method to investigate the upheaval buckling of submarine pipelines that are influenced by pitting corrosion, considering its stochastic distribution. A new pipeline element based on the Euler-Bernoulli beam theory to investigate the impact of pitting corrosion on submarine pipelines, including its random distribution across the cross-section, length, and circumference of the pipeline. A detailed explanation of how to employ these effects into the pipeline element is presented in detail. It is essential to consider the impact of pitting corrosion on the pipeline's overall bearing capacity as it significantly affects its performance. This paper is structured as follows, Section 2 explains the submarine pipeline model considering the pitting corrosion in detail. Utilizing the Monte Carlo method, a significant number of corrosion sections are randomly produced and organized to accurately replicate the dispersal pattern of pitting corrosion across both the longitudinal length and the circumferential perimeter of the pipeline surface. Section 3 provides a detailed description of the computational methods employed for determining the pertinent parameters of corroded submarine pipelines. The sections were discretized, and the geometric parameters were computed in accordance with the pertinent section model. Section 4 presents the flowchart of buckling analysis of the corroded pipeline. Sections 5 to 7 offer a detailed exposition on the determination of the bearing capacity, vertical deformation, and stress of corroded pipelines. The buckling behavior of pipelines affected by corrosion is discussed extensively. Moreover, parameter analysis that examines how the size and type of corrosion affects the buckling deformation as various pipeline types is presented. The concluding remarks are subsequently summarized.

2. Corrosion modelling of the pipeline

In our previous works, a new pipeline element based on the Euler-Bernoulli beam theory designed for pipeline buckling analysis has been proposed [26-28]. Compared to the traditional method that utilizes Winkler-type springs to account for soil-pipeline interaction, it has been demonstrated that the method we proposed is more efficient. This advantage becomes more apparent when using the Monte Carlo method, as it requires the design and execution of numerous cases. By considering the corrosion distribution across the cross-section, length, and circumference of the pipeline, section properties can be determined. This part provides a detailed explanation of how pitting corrosion is distributed on the pipeline.

In most conditions, features of pitting corrosion are randomly distributed in steel pipelines due to the harsh ocean environment. Regardless of the shape of the pits, corrosion at the sectional level results in a decrease in the thickness of the section. Fig.1 shows the generation of the corrosion model of a pipeline cross section. The circular hollow section of the pipeline can be described using two variables i.e. wall thickness *t* and diameter *D*.

Divide the pipeline cross section into *n* small segments with the same radian θ. Those corroded segments will be chosen by random, and the thickness of the corroded segments t_r will be expressed as,

$$t_r = t - t_d \tag{1}$$

where *t* is the wall thick of the pipeline, t_d is the corrosion depth of the chosen segment, which is randomly distributed in reality.

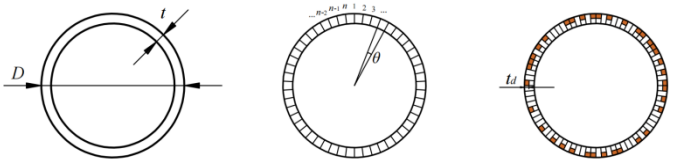

Fig. 1 The generation of the corrosion on a pipeline cross section

The total number of corroded segments n_c can be expressed as,

$$n_c = n\rho_{CR} \tag{2}$$

where n_c denotes the number of segment and ρ_{CR} is the corrosion ratio which represents the proportion of corroded segments to the total number of intact segments within a given section.

Thus, the area loss ratio of the section (DOPs) can be deduced,

$$\text{DOPs} = \frac{A_c}{A} = \frac{0.5\theta t_d(D - t_d)}{(D - t)\pi t} n\rho_{CR} \tag{3}$$

where A and A_c are the original area and corroded area of the cross section. DOPs indicates the pitting intensity of the cross section.

In Monte Carlo simulation, all corrosion sections are arranged along the length of the pipeline, so pitting corrosion is distributed on the surface of the pipe along the length and circumferential direction of the pipeline. In other words, the pipeline is divided into *m* small segments with the same length *l* along the pipeline axis, where *m* also means the number of runs for the Monte Carlo simulation, as shown in Fig. 2. It is important to note that the cross-section of the pipeline can be subdivided into numerous extremely small cross-sectional segments, each with a negligible volume. These corrosion segments are randomly distributed and combined, resulting in the formation of pitting corrosion, the volume and shape of which are inherently unpredictable so as to captures the intricate realities of corrosion scenarios.

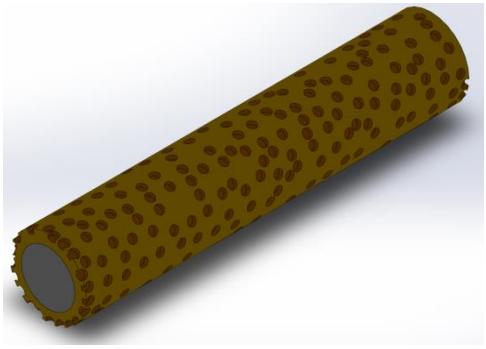

(a) A pipe with random pitting corrosion

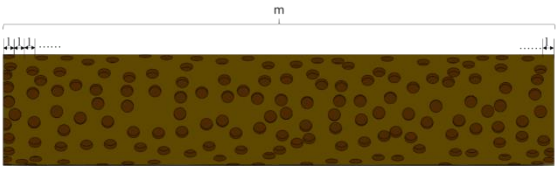

(b) The dimension of pitting corrosion

Fig. 2 Pipeline model with corrosion

The degree of degradation (DOD) is introduced to describe the deterioration of the pipeline, which can be expressed as,

$$\text{DOD} = \frac{V - V_r}{V} \tag{4}$$

where V and Vr are the original volume and remaining volume of the pipeline, which can be obtained by[29],

$$V = (D - t)\pi t L \tag{5}$$

$$V_r = [(D-t)\pi t - 0.5\theta t_d(D-t_d)n\rho_{CR}]L \quad (6)$$

$$\mathrm{DOD} = \frac{0.5\theta t_d(D-t_d)n\rho_{CR}L}{(D-t)\pi tL} \quad (7)$$

3. Bearing capacity and relevant parameters

3.1. Bearing capacity

The bearing cpacity of steel pipelines are discussed in this section. To assess the pipeline's structural integrity, axial compression force *P* is applied uniformly to both ends. It should be noted that both ends of the pipelines are fixed when estimating the bearing capacity of the pipelines under axial compression. Subsequently, the external load is incrementally increased until the stress concentration at a designated cross-sectional point achieves the yield strength. This approach allows for an accurate assessment of the pipeline's resistance to failure under compressive loads. When the yield strength is reached, the pressurization is stopped and the maximum pressure applied is collected as the bearing capacity. Global buckling of pipelines can be approximately considered as a column-type response, given the restricted deformation of their cross-sections. As a result, the Euler buckling approach is a suitable method to analyze their buckling behavior [23, 30]. The criteria for pipeline failure pressure in the commonly used evaluation criteria at home and abroad can be summarized into two categories: two failure criteria based on stress and strain [2]. The evaluation criteria commonly utilized domestically and internationally for pipeline failure pressure can be categorized into two principal branches: stress-based and strain-based failure criteria[31]. In engineering practice, however, the deformation of pipeline sections is frequently constrained by various factors, including material strength, manufacturing processes, and operational environments. Consequently, the degree of deformation is typically limited, making the stress-based failure criterion the prevailing approach for assessing the bearing capacity of pipelines with corrosion defects. Therefore, this study opts to employ the stress-based failure criterion for calculating the load-bearing capacity of pipelines with corrosion defects.

The yield strength is a commonly used evaluation index for the mechanical properties of solid materials, representing the practical limit of the material's use. When stress surpasses the yield limit, plastic deformation occurs, leading to a sudden increase in strain and eventual failure of the materia. According to ASME B31.4-2022 [32], the longitudinal stress from pressure and external loadings in unrestrained pipe is calculated by,

$$S_L = \frac{P_i D}{40t} + \frac{iM}{Z} + \frac{F_a}{A} = \frac{P_i D}{40t} + \frac{F_a}{A} + \frac{My_{max}}{I} \le 0.54S_y \quad (8)$$

where, A is the section area, M is the bending moment across the nominal pipe cross section due to weight or seismic inertia loading, y_{max} is the maximum distance to axis on the section, S_y is the specified minimum yield strength of pipeline material, F_a is the axial force, P_i is the internal design gage pressure, Z is the section modulus of the pipeline, i is the component stress intensification in plane of loading, limited by $0.75i \ge 1$. For straight pipe, i=1.0.

The bearing cpacity P_B of the steel pipeline under compression can be expressed as,

$$P_B = AS_L \quad (9)$$

3.2. Relevant geometrical parameters

In order to calculate the bearing capacity in Eq. (8), the pertinent section parameters of the pipeline should be confirmed firstly. Due to the randomness of corroded sections, their area, centroid coordinates, and moment of inertia must be calculated using a fiber model. In this model, each unit of the section is treated as a fiber, with its centroid coordinates and area calculated and stored as small fiber blocks. By integrating all of these fiber blocks, the full fiber model information for the entire corroded section can be obtained, which includes the section area *A*, the centroid coordinate (Y_0, Z_0) and the moment of inertia *I*. A coordinate system *yoz* is established to describe the position of each node, where the centroid of the cross-section is *o*, as shown in Fig. 3. According to the equations above, the section area *A*, centroid coordinates (Y_0, Z_0) and the moment of inertia *I* are key parameters for the computation of bearing cpacity of corroded section. They are given by,

$$t_{ri} = \begin{cases} t & \text{(uncorroded)} \\ t - t_d & \text{(corroded)} \end{cases} \quad (10)$$

$$R_i = \frac{D}{2} - t + \frac{t_{ri}(1.5D - 3t + 2t_{ri})}{3(D - 2t + t_{ri})} \quad (11)$$

$$A_i = 0.5\theta t_{ri}(D - 2t + t_{ri}) \quad (12)$$

$$A = \sum_{i=1}^{n} A_i \quad (13)$$

$$Y_0 = \sum_{i=1}^{n} Y_i A_i / A = \sum_{i=1}^{n} R_i \sin\phi_i A_i / A \quad (14)$$

$$Z_0 = \sum_{i=1}^{n} Z_i A_i / A = \sum_{i=1}^{n} R_i \cos\phi_i A_i / A \quad (15)$$

$$I_y = \int (Z_i - Z_0)^2 dA = \frac{\theta}{2}\sum_{i=1}^{n} (R_i \sin\phi_i - Z_0)^2 t_{ri}(D - 2t + t_{ri}) \quad (16)$$

$$I_z = \int (Y_i - Y_0)^2 dA = \frac{\theta}{2}\sum_{i=1}^{n} (R_i \cos\phi_i - Y_0)^2 t_{ri}(D - 2t + t_{ri}) \quad (17)$$

where: I_y and I_z are the *y*- and *z*- moment of inertial of the asymmetric section after corrosion. R_i denotes the length from the left node of i_{th} segment on the cross section to the center *o*, while ϕ_i denotes the angle between the line and *y* axis, as shown in Fig. 4.

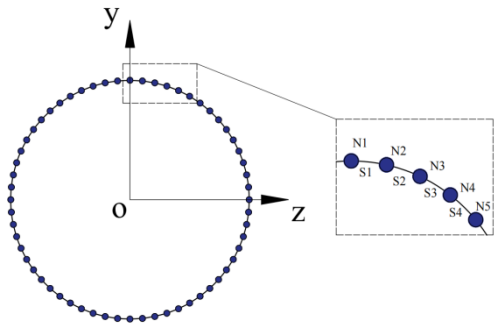

Fig. 3 Corroded section division and the number

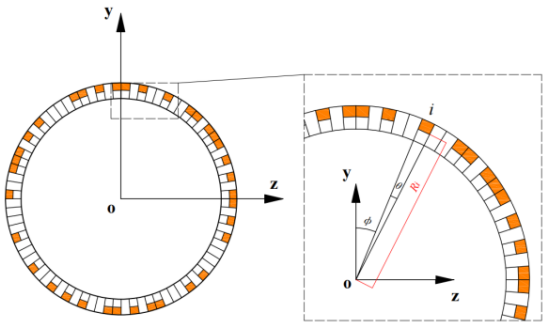

Fig. 4 Segments on the corroded section

4. Flowchart of buckling analysis

The detailed flowchart of how to perform the buckling analysis is presented in Fig. 5. The section is divided into *n* segments, and the central angle of each unit is θ. The number of corroded pieces n_c can be calculated based on Eq. (2). Several ϕ_i $(i = 1, 2, 3 \ldots n)$ locating the positions of corroded pieces are

generated randomly, which guarantees the random properties of pitting corrosions. When the pits and section parameters are obtained for *m* cases, the buckling analysis based on the Newton-Raphson iteration procedure is carried out. The internal pressure and external hydrostatic pressure of the pipeline are expressed by the pressure difference. The vector sum of the pipeline internal pressure, external hydrostatic pressure and the external load applying at both ends of the pipeline element is named as external forces, which can be seen in Fig.5. The python program stops running and records the utmost permissible loading pressure as the pipeline's bearing capacity when the normal stress on a section of the pipeline exceeds its yield strength, indicating that the pipeline is damaged and can no longer withstand the compressed pressure.

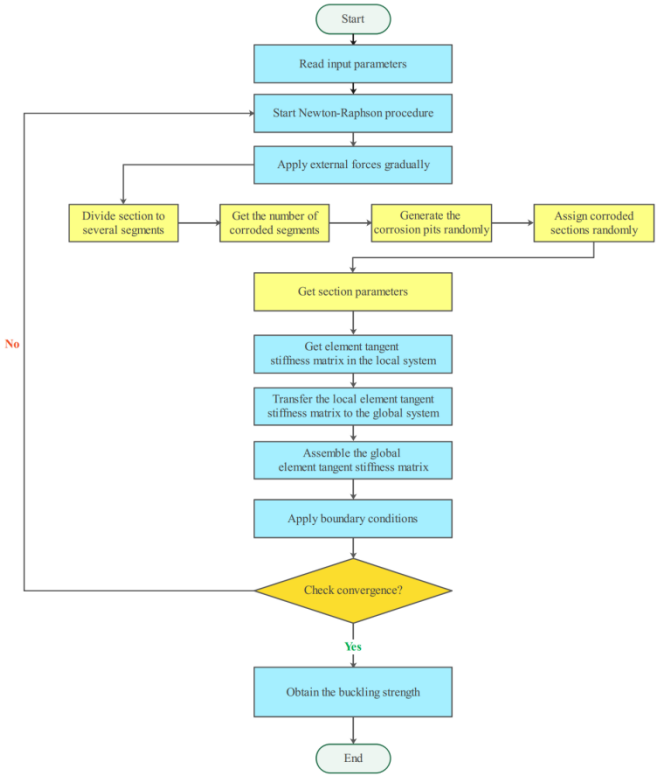

Fig. 5 Flow chart of the Monte Carlo simulation procedure

5. Monte Carlo simulation

5.1. Design parameters of the pipeline

The basic information of section's size, corrosion ratio, corrosion depth and segments are shown in Table 1.

Table 1
Design parameters for the pipeline and corrosion

Description	Paramete	Value	Unit
Diameter	D	323.9	mm
Thickness	t	14.3	mm
Pipeline length	L	100	m
Number of segments	n	360	-
Mesh size	θ	1	◦
Corrosion ratio	ρ_{CR}	50	%
Corrosion depth	t_d	2.86	mm
Initial imperfection length	L_{Y0}	20	m
Initial imperfection amplitude	V_{m0}	0.2	m
Young's module	E	206	GPa
Yield strength	S_y	450	MPa
Length coefficient	k	1	-
Total number of pipeline element	n_{ele}	300	-

The pipelines are fabricated by an API 5L X65 PSL2 steel and both ends of the pipelines are assumed fixed, the initial imperfection of the pipeline can be determined by the following equation,

$$V_0(X) = \frac{V_{m0}}{2}[1 + cos(\frac{2\pi}{L_{Y0}})], \quad -\frac{L_{Y0}}{2} < X < \frac{L_{Y0}}{2} \tag{18}$$

where, V_{m0} is the maximum initial imperfection amplitude about *Y*- axis, as shown in Fig. 6; L_{Y0} is the vertical initial imperfection length. The pipeline is assumed to be placed in a trench on a semi-rigid seabed and covered with backfill soil. The sum weight of the trench backfills and the pipeline is 1.5 kN/m and the vertical soil-pipeline interaction can be obtained and presented in Fig. 7. The axial friction between the pipeline and the foundation is ignored. The specific parameters of the damaged pipeline model are shown in the Table 1. 2000, 4000, 6000, 8000 and 10000 kN load are divided into 100, 1000, 2500 and 5000 parts and applied on both ends of the pipeline element. The step length and bearing capacity of each test are recorded in Table 2. Arrange the bearing capacity in Table 2 into Table 3 according to the load step and record the the run time of the program of different load steps. For different applied loads, when the same step size is set, the calculation results are basically similar. When the step length is in the range of 4 ~ 6 kN, the absolute value of the relative error between the bearing capacity and the high-precision result is less than 0.5%, which is acceptable. Indeed, the computation time for all scenarios remains minimal, with the longest duration being less than 16 minutes. Therefore, the step length can be taken as 4 ~ 6 kN in the case studies in the following sections.

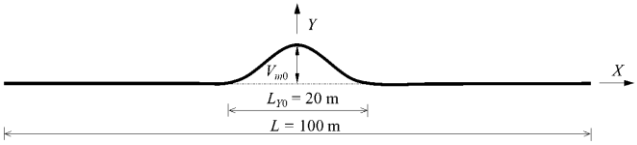

Fig. 6 Initial vertical configuration of the pipeline

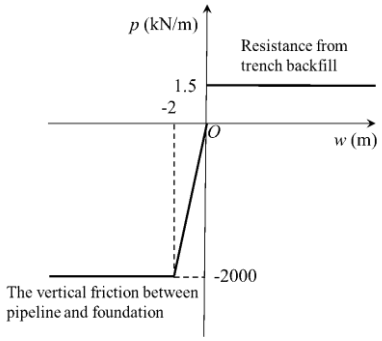

Fig. 7 Pipe-soil interaction

5.2. Run time assessment of Monte Carlo simulation

Monte Carlo method is conducted to simulate a naturally corroded pipeline, and numerous cases are needed to be carried out. To establish the relationship between the Monte Carlo simulation outcomes (bearing capacity) and the number of runs, investigations on bearing capacity, number of runs, and pipeline slenderness are necessary. The basic information of section's size, corrosion ratio, corrosion depth and segments are kept the same with Section 5.1. The Monte Carlo simulation is then performed several times for each type of pipeline according to different slenderness of the pipeline. Slenderness is the ratio of the pipeline length to the radius of rotation of the pipeline Section. For the uncorroded pipelines, it is given by,

$$\lambda = \mu\frac{L}{R_{gr}} = \mu\frac{L}{\sqrt{I/A}} = \mu\frac{4L}{\sqrt{D^2 + d^2}} \tag{19}$$

where, μ is the length factor, for pipeline with both ends fixed, μ=0.5; R_{gr} is the radius of gyration of the Section; *d* is the inner diameter of the pipeline. The slenderness is determined according to the size of the pipeline before being corroded and the estimated bearing capacity is documented accordingly.

Table 4 presents the bearing capacity of 9 pipelines with length of 30m,

50m, 100m, 150m, 200m, 250m, 300m, 400m and 500m at different random times and record the results with random times of 50, 100, 300, 500 and 1000 respectively. Fig. 8 shows that the bearing capacity of the pipeline decreases as the slenderness increases. For pipelines with slenderness of 245.7, 409.5, 819.0, 1228.5 and below, the bearing capacity decreases rapidly as the pipeline length increases. For pipelines with the slenderness of 1638.0, 2047.5, 2457.0, 3276.0, 4095.0 and above, the bearing capacity is limited by length of the pipeline. In this scenario, as the slenderness (pipeline length) increases further, the reduction in bearing capacity of the pipeline gradually stabilizes, ultimately resulting in a consistent and reliable bearing capacity value.This significant effect on the buckling behavior due to the pipeline length was also found by other researchers [24]. One of their results shows that, for long pipelines, if the pipeline length is greater than the critical length, the increase of pipeline length has negligible effect on the analysis results. As the area loss rate of the section remains constant in each turn, the resulting maximum and minimum bearing capacities should also be consistent across different runs. The calculated results of cases with a run count of 1000 were used as reference values. Upon achieving a run count of 300, the relative error between the pipeline's bearing capacity and the reference value remains consistently below 2%. To ensure efficient computation and avoid unnecessary delays, we have elected to limit the number of random iterations to a range of 300 to 500 runs in the scenarios outlined below.

Table 2
Loading condition of the pipeline with corrosion

Load step	100		1000		2500		5000	
Member load (kN)	Step length (m)	Bearing capacity (kN)	Step length (m)	Bearing capacity (kN)	Step length (m)	Bearing capacity (kN)	Step length (m)	Bearing capacity (kN)
2000	20	1140	2	1138	0.8	1137.6	0.4	1138.4
4000	40	1160	4	1140	1.6	1137.6	0.8	1137.6
6000	60	1140	6	1140	2.4	1140.0	1.2	1135.2
8000	80	1120	8	1144	3.2	1139.2	1.6	1139.2
10000	100	1200	10	1140	4.0	1136.0	2.0	1140.0

Table 3
Run time and relative error of different load steps

Load step (kN)	Run time (min)	Relative error (%)	Load step (kN)	Run time (min)	Relative error (%)
100	<0.5	5.411	4.0	16	0.141
80	<1	1.620	3.2	22	0.070
60	<1	0.141	2.4	31	0.141
40	<1	1.897	2.0	55	0.035
20	<2	0.141	1.6	98	0.070
10	<5	0.141	1.2	122	0.281
8	<7	0.492	0.8	190	0.070
6	<8	0.141	0.4	360	0.000

Table 4
The pipeline bearing capacity related to run time of Monte Carlo simulation

Run count		50		100		300		500		1000	
Length (m)	Slenderness	Bearing capacity (kN)	Relative error (%)	Bearing capacity (kN)	Relative error (%)	Bearing capacity (kN)	Relative error (%)	Bearing capacity (kN)	Relative error (%)	Bearing capacity (kN)	Relative error (%)
30	245.7	1494	4.96	1560	0.76	1572	0.00	1560	0.76	1572	0.00
50	409.5	1326	0.00	1332	0.45	1326	0.00	1326	0.00	50	409.5
100	819.0	1140	0.00	1140	0.00	1140	0.00	1140	0.00	100	819.0
150	1228.5	1056	1.68	1080	0.56	1080	0.56	1080	0.56	150	1228.5
200	1638.0	1026	1.72	1050	0.57	1044	0.00	1044	0.00	200	1638.0
250	2047.5	1050	2.34	1032	0.58	1026	0.00	1026	0.00	250	2047.5
300	2457.0	1008	0.60	1020	1.80	1014	1.20	1002	0.00	300	2457.0
400	3276.0	1020	1.80	1008	0.60	1002	0.00	1002	0.00	400	3276.0
500	4095.0	1002	1.21	1020	3.03	990	0.00	990	0.00	990	0.00

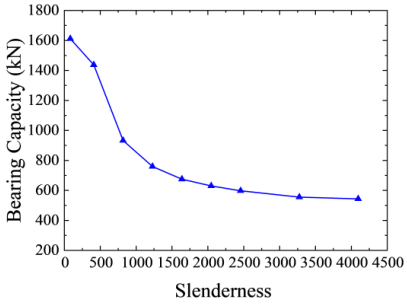

Fig. 8 The bearing capacity of pipelines with different slenderness

5.3. Bearing capacity of specified corrosion models

Monte Carlo Simulation constructs models of potential outcomes by utilizing probability distributions, like the uniform or normal distribution, to account for variables that have inherent uncertainty. This enables the prediction of a range of results based on estimated values. Although two pipeline models may have the same size, corrosion ratio, corrosion depth, and other corrosion-related parameters, they are essentially distinct models because of the different corrosion pitting layout. In order to figure out the difference of the bearing capacity of pipelines caused by the randomness of corrosion distribution, six different corrosion patterns are artificially designed, as shown in Fig. 9. In Type *a*, the regularly distributed corrosion pattern is assumed, in which the section is symmetrical about both vertical and transverse axes. In Types *b* and *c*, the

corrosion only distributes at the left half and right half, respectively. In Type *d* and *e*, the corrosion only distributes at the top half and bottom half, respectively. In Type *f*, an irregularly distributed corrosion pattern is adopted. The basic information of section's size, corrosion ratio, corrosion depth and segments are shown in Table 5. The area loss ratios of the sections with different corrosion patterns are all 81.37%. Table 6 presents the bearing capacity of six types of pipelines. The distribution of corrosion in a pipeline plays a crucial role in determining its buckling bearing capacity, which can vary considerably.

In particular, Types *d* and *e* tend to have the smallest buckling bearing capacity. By analyzing corrosion distribution, we can identify the most dangerous types and take necessary measures to avoid them in practical engineering, reducing the risk of damage.

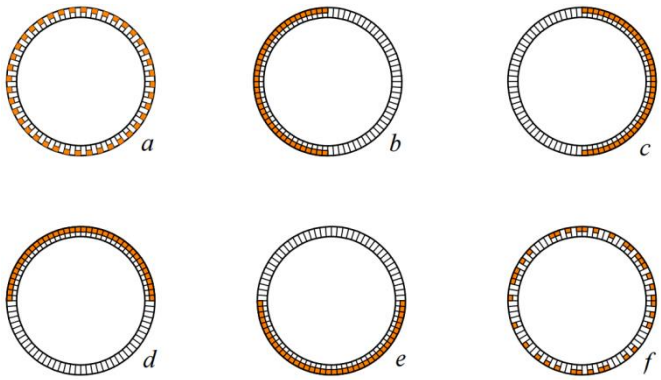

Fig. 9 Specified corrosion models

Table 5
Design parameters for the pipeline and corrosion

Description	Paramete	Value	Unit
Diameter	D	200	mm
Thickness	t	30	mm
Pipeline length	L	100	m
Number of segments	n	360	-
Mesh size	θ	1	◦
Corrosion ratio	ρ_{CR}	50	%
Corrosion depth	t_d	10	mm
Initial imperfection length	L_{Y0}	20	m
Initial imperfection amplitude	V_{m0}	0.2	m
Young's module	E	206	GPa
Yield strength	S_y	450	MPa
Length coefficient	k	1	-
Total number of pipeline element	n_{ele}	300	-

Table 6
Bearing capacity of different corrosion type

Corrosion type	*a*	*b*	*c*	*d*	*e*	*f*
Bearing capacity (kN)	1044	1032	1032	1020	1026	1044

5.4. The influence of the maximum wheelbase of the section

According to the equations in Section 3.1, the maximum wheelbase on the section y_{max} is an important parameter when calculating the section coefficient W_Z, and its size directly affects the normal stress of the section. However, since numerous corroded sections are distributed along the length of the pipeline, the section parameters of each pipeline element are different and uncertain. Meanwhile, the value of y_{max} for corroded pipelines is not defined in the relevant specifications. In other words, the section coefficient W_Z of each piping element is also indeterminate, reflecting the real-world conditions. To assess the impact of uncertainty in W_Z on the calculated magnitude of normal stress in a given section, a comprehensive case study was undertaken.

Five pipeline section models with different sizes are designed and the corroded levels of these sections are unified. The specific parameters of these corroded pipeline models are the same with Section 5.3. In the pipeline element program, the y_{max} value is taken as $D/2$ and $D/2$-t_d respectively, which represents the maximum wheelbase of the section before and after corrosion. The bearing capacity of these corroded pipelines of each case is recorded in Table 7. Take the minimum bearing capacity of all the cases as the reference, the relative error of each case compared with the reference value can be obtained. At the same time, the bearing capacity of these five pipelines with intact section (no corrosion) is also presented.

It can be seen from Table 7 that as the thickness-diameter ratio of the pipeline decreases, the relative error of the bearing capacity of the pipeline caused by the value of y_{max} gradually decreases. The difference between the calculation results of the corroded pipeline model and the non-corroded pipeline model is gradually becoming smaller. For the corroded pipeline with thicker wall, when y_{max} equals $D/2$, the bearing capacity of the pipeline is the smallest among all the cases. Compared with the bearing capacity of the non-corroded pipeline in the same size, the bearing capacity of pipeline buckling obtained for two different values of wheelbase of cross-section is obviously different.

In the following studies, the value of y_{max} are considered as $D/2$ and $D/2$-t_d separately, and the pipeline bearing capacity under two maximum wheelbase values are referred as low value and high value. For the thin-walled pipelines, the relative errors between the bearing capacity of the corroded pipeline and the uncorroded one are smaller than that of thick wall pipelines. When the pipeline wall is thin and the thickness-diameter ratio is relatively small, the bearing capacity is determined mainly by its size. Slight corrosion has little effect on the bearing capacity of the pipeline, so the difference of pipeline bearing capacity before and after the corrosion shrinks.

6. Buckling bearing capacity assessment

This section aims at examining the distinct impact of varying parameters of corrosion on pipeline bearing capacity, while also comparing the effects of corrosion on pipelines of different sizes. Three pipeline sections with different sizes were selected according to ASME specifications, and their related parameters are presented in the Table 8. The pipeline element is limited to static analysis at present and does not involve dynamic analysis. Therefore, hydrodynamics cannot be considered temporarily. The pipelines are all single-walled in this paper. This method is not applicable for the buckling analysis of PIPs or piggyback pipelines at present. The thickness-diameter ratio of three kinds of pipelines is, Type 3> Type 1> Type 2. As vital parameters related to corrosion, the corrosion depth and corrosion ratio are set as variables. The corresponding DOPs are also presented to reflect the overall effect of corrosion on the bearing capacity of pipeline. The corrosion depth of the pipeline section varies between 20%, 40%, 60%, and 80% of its original thickness. Concurrently, the corrosion ratio fluctuates between 0.2, 0.4, 0.6, and 0.8 of the total number of elements comprising the pipeline section. It should be noted that the corrosion depth ratio is the ratio of corrosion depth to the original thickness of the section. Both high and low values of the bearing capacity are presented respectively in Tables 9 and 10. The specific parameters of these corroded pipeline models are consistent with Section 5.3.

Table 8
Design parameters for the pipeline section model

Parameters	Type 1	Type 2	Type 3
D (mm)	323.9	323.9	168.3
t (mm)	14.3	12.7	14.3
Thickness-diameter ratio (%)	4.41	3.92	8.50

6.1. Relationship between the bearing capacity and corrosion depth

This section details the impact of corrosion depth on the bearing capacity of pipelines, given a specific corrosion ratio. It illustrates the relationship between the two factors and how they interact. The relationships between the bearing capacity and corrosion depth for each section are presented in Figs. 10 and 11. As the corrosion depth and ratio increase, a noticeable decline in the bearing capacity of all three pipeline types is observed.

The relationship between bearing capacity and corrosion depth is nonlinear. As the corrosion ratio escalates, the gradient of the bearing capacity-corrosion depth ratio curve experiences a marked increase, signifying a heightened influence of corrosion depth on the pipeline's bearing capacity. Additionally, as corrosion depth intensifies, the disparity between the high and low bearing

capacity values widens. Notably, at reduced levels of corrosion, the discrepancy between the high and low bearing capacities is more pronounced compared to higher corrosion rates. This observation indicates greater uncertainty in the pipeline's bearing capacity when corrosion rates are relatively low.

Fig. 11 illustrates the correlation between bearing capacity and corrosion depth across various corrosion ratios. For Type 3, the slope of the bearing capacity-corrosion depth ratio curve is the least among the three types, regardless of whether the values are low or high. Furthermore, when the corrosion ratio is substantial, the curve of Type 1 exhibits a steeper incline compared to Type 2.

Table 7
Bearing capacity of corrosion type with different y_{max}

Corroded section model			$y_{max} = D/2$, $t = t$		$y_{max} = D/2 - t_d$, $t = t_r$		uncorroded		Thickness diameter ratio
Diameter (mm)	Thickness (mm)	Corrosion depth (mm)	Bearing capacity (kN)	Relative error (%)	Bearing capacity (kN)	Relative error (%)	Bearing capacity (kN)	Relative error (%)	—
150	30	10	642	0.00	744	15.89	846	31.78	0.2
200	30	10	954	0.00	1044	9.43	1206	26.42	0.15
200	20	10	654	0.00	690	5.50	882	34.86	0.1
400	10	3	1092	0.00	1098	0.55	1266	15.93	0.025
500	10	3	1464	0.00	1470	0.41	1710	16.80	0.02

Table 9
Design parameters of the corrosion and the high value of bearing capacity for the pipelines

Type 1				Type 2				Type 3			
t_d (mm)	ρ_{CR}	DOPs (%)	Bearing capacity (kN)	t_d (mm)	ρ_{CR}	DOPs (%)	Bearing capacity (kN)	t_d (mm)	ρ_{CR}	DOPs (%)	Bearing capacity (kN)
0.00	0	0.00	1248	0.00	0	0.00	1140	0.00	0	0.00	552
2.86	0.2	2.38	1200	2.54	0.2	2.37	1098	2.86	0.2	2.46	528
5.72	0.2	4.71	1146	5.08	0.2	4.70	1050	5.72	0.2	4.84	504
8.58	0.2	7.00	1092	7.62	0.2	6.99	990	8.58	0.2	7.13	480
11.44	0.2	9.25	996	10.16	0.2	9.24	912	11.44	0.2	9.34	450
2.86	0.4	4.75	1152	2.54	0.4	4.73	1056	2.86	0.4	4.92	528
5.72	0.4	9.42	1062	5.08	0.4	9.39	972	5.72	0.4	9.68	462
8.58	0.4	14.00	960	7.62	0.4	13.98	882	8.58	0.4	14.26	420
11.44	0.4	18.50	852	10.16	0.4	18.48	768	11.44	0.4	18.68	378
2.86	0.6	7.13	1110	2.54	0.6	7.10	1020	2.86	0.6	7.39	480
5.72	0.6	14.13	978	5.08	0.6	14.10	894	5.72	0.6	14.52	420
8.58	0.6	21.01	846	7.62	0.6	21.00	762	8.58	0.6	21.39	360
11.44	0.6	27.76	672	10.16	0.6	27.73	630	11.44	0.6	28.01	312
2.86	0.8	9.51	1068	2.54	0.8	9.47	978	2.86	0.8	9.85	462
5.72	0.8	18.84	888	5.08	0.8	18.78	810	5.72	0.8	19.36	378
8.58	0.8	28.01	696	7.62	0.8	27.95	642	8.58	0.8	28.52	312
11.44	0.8	37.01	510	10.16	0.8	36.97	474	11.44	0.8	37.35	246

Table 10
Design parameters of the corrosion and the low value of bearing capacity for the pipelines

Type 1				Type 2				Type 3			
t_d (mm)	ρ_{CR}	DOPs (%)	Bearing capacity (kN)	t_d (mm)	ρ_{CR}	DOPs (%)	Bearing capacity (kN)	t_d (mm)	ρ_{CR}	DOPs (%)	Bearing capacity (kN)
0.00	0	0.00	1248	0.00	0	0.00	1140	0.00	0	0.00	552
2.86	0.2	2.38	1206	2.54	0.2	2.37	1104	2.86	0.2	2.46	540
5.72	0.2	4.71	1164	5.08	0.2	4.70	1068	5.72	0.2	4.84	522
8.58	0.2	7.00	1116	7.62	0.2	6.99	1014	8.58	0.2	7.13	510
11.44	0.2	9.25	1032	10.16	0.2	9.24	936	11.44	0.2	9.34	486
2.86	0.4	4.75	1206	2.54	0.4	4.73	1062	2.86	0.4	4.92	516
5.72	0.4	9.42	1074	5.08	0.4	9.39	984	5.72	0.4	9.68	474
8.58	0.4	14.00	984	7.62	0.4	14.00	888	8.58	0.4	14.30	444
11.44	0.4	18.50	870	10.16	0.4	18.48	792	11.44	0.4	18.68	396
2.86	0.6	7.13	1116	2.54	0.6	7.10	1020	2.86	0.6	7.39	492
5.72	0.6	14.10	984	5.08	0.6	14.10	900	5.72	0.6	14.50	432
8.58	0.6	21.00	858	7.62	0.6	21.00	786	8.58	0.6	21.40	378
11.44	0.6	27.76	702	10.16	0.6	27.73	642	11.44	0.6	28.01	324
2.86	0.8	9.51	1074	2.54	0.8	9.47	984	2.86	0.8	9.85	468
5.72	0.8	18.84	894	5.08	0.8	18.78	822	5.72	0.8	19.36	390
8.58	0.8	28.01	720	7.62	0.8	27.95	660	8.58	0.8	28.52	318
11.44	0.8	37.01	528	10.16	0.8	36.97	492	11.44	0.8	37.35	252

The result suggests that in pipelines composed of various sections, the bearing capacity of the pipelines is increasingly affected by the depth of corrosion as the thickness-diameter ratio decreases. Notably, when the pipeline's thickness-diameter ratio is comparable, thicker walled pipelines are more susceptible to the influence of corrosion depth, particularly under conditions of high corrosion ratios. It can be seen in Fig. 11 that, for pipeline Type 3, which boasts a thicker thickness-diameter ratio compared to the other two pipelines, exhibits a substantial variance in its bearing capacity between its high and low values. It is indicated that the value of y_{max} significantly influences the pipeline's bearing capacity when considering the impact of corrosion depth.

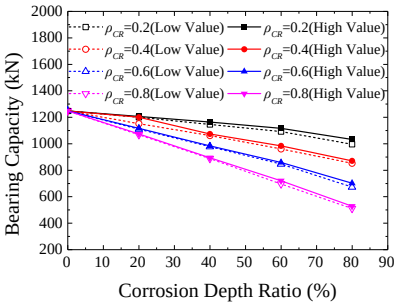

(a) Type 1

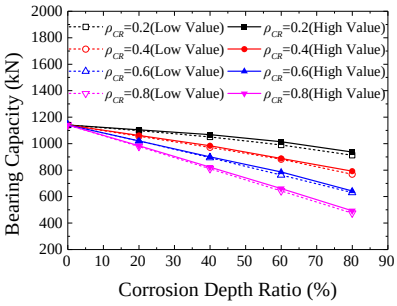

(b) Type 2

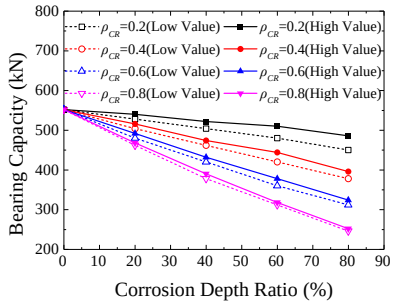

(c) Type 3

Fig. 10 The bearing capacity of three types of pipelines

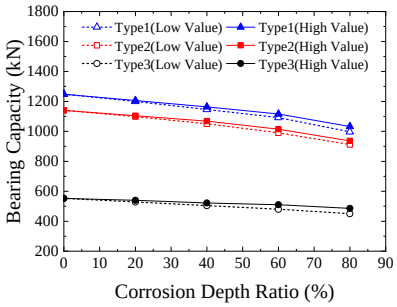

(a) Corrosion Ratio = 0.2

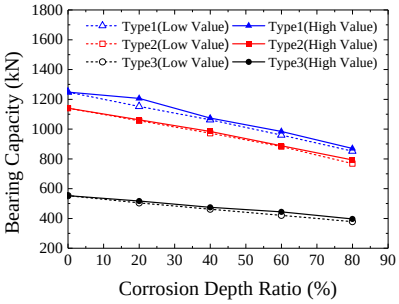

(b) Corrosion Ratio = 0.4

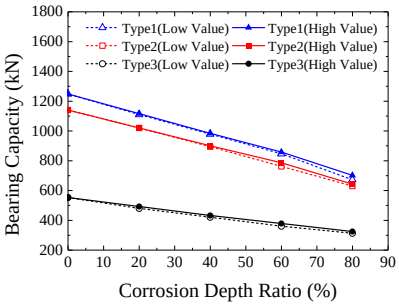

(c) Corrosion Ratio = 0.6

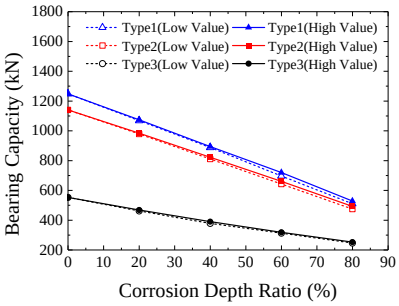

(d) Corrosion Ratio = 0.8

Fig. 11 The relationship between bearing capacity and corrosion depth

6.2. Relationship between bearing capacity and corrosion ratio

The objective of this section is to undertake a comprehensive examination of the impact exerted by the corrosion ratio on the bearing capacity of pipelines, with the corrosion depth remaining constant throughout the analysis. Fig. 12 exhibits the trend of the bearing capacity variations in three distinct pipeline types with respect to escalating corrosion ratios. As shown in Fig. 12, all three types of pipelines exhibit a decline in their bearing capacity as the corrosion ratios rise. Additionally, as the corrosion depth ratio escalates, the nonlinearity of the bearing capacity-corrosion ratio curve becomes increasingly apparent, and the slop of the curve experiences a marked increase. These observations underscore the influence of corrosion ratio on pipeline bearing capacity, particularly at deeper corrosion depths. As the corrosion ratio increases, the gap between the high and low values of pipeline bearing capacity tends to narrow. Moreover, pipelines with higher corrosion depth rates exhibit a more substantial dispersion in their bearing capacity values compared to those with lower corrosion depth rates. It can be inferred that pipelines with a lower corrosion depth ratio tend to possess a bearing capacity that is less predictable.

The relationship between the bearing capacity and the corrosion ratio for different pipeline's corrosion ratio can be seen in Fig. 13. The slope of the bearing capacity-corrosion ratio curve for Type 3 pipelines is the least steep. In contrast, Types 1 and 2 exhibit a more rapid decline in bearing capacity with increasing corrosion ratio. Furthermore, a noticeable impact of the corrosion depth ratio on the trend is observed. As the corrosion depth ratio increases, the rate of change in the curve slope among the three types of pipelines follows the order: Type 1 > Type 2 > Type 3.

The result reveals that for pipelines with a reduced thickness-diameter ratio, the influence of the corrosion ratio on the bearing capacity becomes more pronounced. Specifically, under conditions of elevated corrosion depth ratios, the thicker-walled pipelines exhibit a greater sensitivity to the corrosion ratio, particularly when the thickness-diameter ratios of the pipelines are comparable. Furthermore, it is observed that across all three types of pipelines, the disparity between the high and low values of bearing capacity remains minimal. This

suggests that the influence of y_{max} on the relationship between bearing capacity and corrosion ratio is negligible.

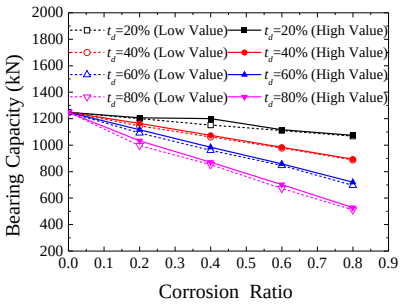

(a) Type 1

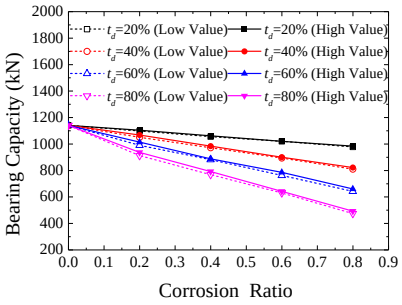

(b) Type 2

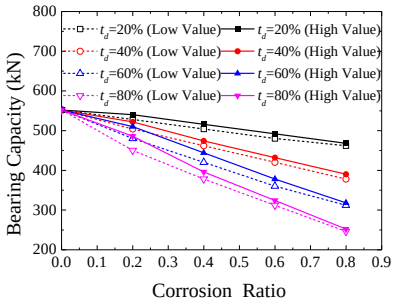

(c) Type 3

Fig. 12 The bearing capacity of three types of pipelines

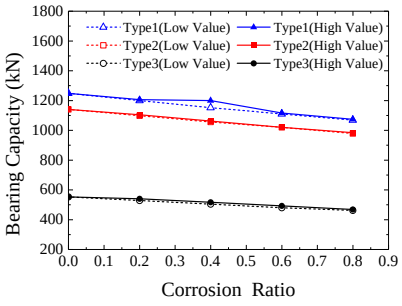

(a) Corrosion Depth Ratio = 20%

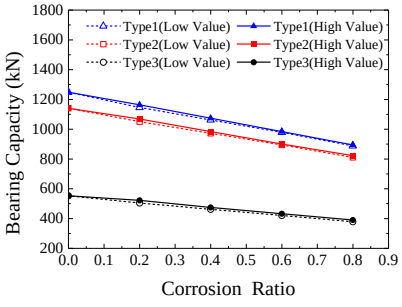

(b) Corrosion Depth Ratio = 40%

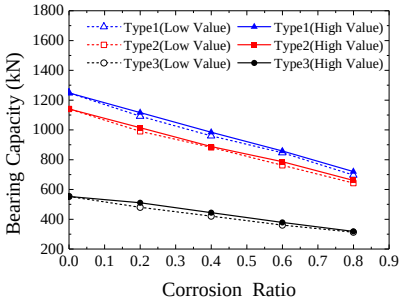

(c) Corrosion Depth Ratio = 60%

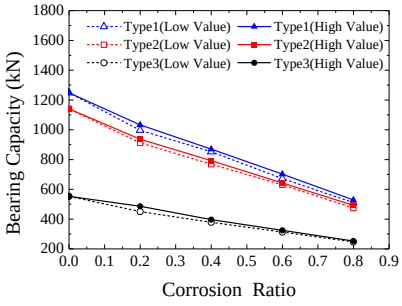

(d) Corrosion Depth Ratio = 80%

Fig. 13 The relationship between bearing capacity and the corrosion ratio

6.3. Relationship between bearing capacity and corrosion DOPs

This section aims at investigating the relationship between the pipeline's bearing capacity and the area loss ratio. Fig. 14 reveals that the bearing capacity of all three pipeline types diminishes as the DOPs increase. Moreover, the bearing capacity-DOPs curve exhibits great nonlinearity. Notably, the bearing capacity-DOPs curve of Type 3 pipeline exhibits the least variation in slope compared to Type 1 and Type 2, which display comparable patterns.

Meanwhile, it is evident that despite the proximity of area loss ratios, slight variations in bearing capacity for identical sections may occur. This variance is more pronounced in Types 1 and 2, whereas for Type 3, the fluctuations in the curve are minimal. To delve deeper into the uncertainty of pipeline bearing capacity under a specific area loss ratio, multiple scenarios with comparable DOPs values have been considered, as detailed in Tables 9 and 10. The ratio comparing the bearing capacity of a corroded pipeline to that of an intact pipeline serves as the benchmark, referred to as the reduction factor. Both the upper and lower bounds of the reduction factor, along with the maximum relative errors among various sets of reduction factors, have been computed and are presented in Table 11.

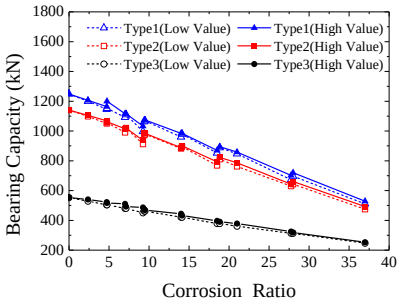

Fig. 14 Relationship between bearing capacity and DOPs

Table 11 reveals a significant variation in pipeline bearing capacity, even for identical cross-sections and area loss ratios. This variation is attributed to the combined effects of different corrosion ratio and depth. Notably, a combination of reduced corrosion depth with elevated corrosion ratio results in a more considerable reduction factor. Conversely, a scenario with deeper corrosion coupled with a lower corrosion ratio leads to a less pronounced reduction factor. These findings underscore the inadequacy of solely relying on area loss ratio to assess pipeline bearing capacity. Furthermore, they underscore the impact of corrosion on the unpredictability of pipeline bearing capacity, offering a distinct perspective on this aspect.

Upon analyzing the reduction factors across Type 1, 2, and 3 pipelines, it was evident that Types 1 and 2 exhibited significantly higher maximum relative

errors in their reduction factors compared to Type 3. Notably, pipelines of Types 1 and 2 with a smaller thickness-diameter ratio tended to possess increased uncertainty in terms of their bearing capacity when exposed to corrosion. Conversely, pipelines of Type 3 maintained consistent reduction factors in both high and low values.

Table 11 reveals that, with identical section and area loss ratios, the bearing capacity of pipelines is profoundly influenced by the intricate relationship between corrosion ratio and depth. Notably, a combination of shallow corrosion depth and high corrosion ratio results in a more pronounced reduction factor. Conversely, deeper corrosion coupled with a lower corrosion ratio leads to a less significant reduction factor. These observations underscore the inadequacy of solely relying on area loss ratio to assess pipeline bearing capacity. Furthermore, they underscore the impact of corrosion on the unpredictability of pipeline bearing capacity from a distinct perspective. When comparing the reduction factors among Type 1, 2, and 3 pipelines, it is evident that Type 1 and 2 pipelines exhibit significantly higher maximum relative errors in their reduction factors compared to Type 3. Specifically, pipelines of Types 1 and 2 with a smaller thickness-diameter ratio appear to exhibit greater uncertainty in their bearing capacity when subjected to corrosion. Conversely, Type 3 pipelines maintain consistent reduction factors across both high and low values, indicating a more reliable performance under corrosion conditions.

Table 11
The bearing capacity of 3 types of pipelines with similar DOPS

Section type	DOPs (%)	ρ_{CR}	t_d (mm)	Reduction factor (L)	Maximum relative error (%)	Reduction factor (H)	Maximum relative error (%)
	9.25	0.2	11.44	0.798		0.827	
Type 1	9.42	0.4	5.72	0.851	6.44	0.861	4.11
	9.51	0.8	2.86	0.856		0.861	
	9.24	0.2	10.16	0.800		0.821	
Type 2	9.39	0.4	5.08	0.853	6.63	0.863	3.64
	9.47	0.8	2.54	0.855		0.863	
	9.34	0.2	11.44	0.815		0.880	
Type 3	9.68	0.4	5.72	0.837	2.70	0.859	2.38
	9.85	0.8	2.86	0.837		0.848	

Table 12 presents a compilation of three distinct sets of reduction factors, each corresponding to different section types but maintaining identical DOPs, corrosion ratios, and corrosion depth ratios. The results reveal that, despite the uniformity in corrosion parameters and DOPs, there exists a noteworthy disparity in the reduction factors among the various section types. This observation underscores the limitations of solely relying on DOPs as a metric for assessing the bearing capacity of pipelines impacted by corrosion. Notably, the maximum relative error among these reduction factors can reach up to 8.3%, and there is no consistent pattern in the relationship between the reduction factors of the three section types. This implies that the section type alone is not a determinant of the magnitude of the reduction factor.

Table 12
The bearing capacity of different type of pipeline with similar DOP

DOPs (%)	ρ_{CR}	Corrosion depth ratio (%)	Section type	Reduction factor (L)	Maximum relative error (%)	Reduction factor (H)	Maximum relative error (%)
			Type 1	0.769		0.788	
14	0.4	60	Type 2	0.774	1.71	0.779	3.21
			Type 3	0.761		0.804	
			Type 1	0.678		0.688	
21	0.6	60	Type 2	0.668	3.99	0.689	0.58
			Type 3	0.652		0.685	
			Type 1	0.409		0.423	
37	0.8	80	Type 2	0.416	8.30	0.432	5.79
			Type 3	0.446		0.457	

7. Buckling deformation and stress

The section presents the global deformation, mid-span displacement and maximum stress of the section. The parameters of the pipeline are kept the same with Section 6, corrosion ratios 0.4 and 0.8, and corrosion depth ratios 40% and 80% are taken into account.

7.1. Global deformation

Fig. 15 depicts the global deformation of pipelines affected by corrosion. Given the minimal variance in vertical deformation between high and low values, only the peak vertical deformation is presented. Furthermore, the global vertical deformation of the identical type of pipeline without corrosion in the process of loading to the maximum bearing capacity is also shown in the figure as a reference. As evident from Fig. 15, as the corrosion ratio and depth increase, the pipeline's vertical deformation decreases. Concurrently, with the progression of corrosion, both the vertical deformation and the length of vertical buckling exhibit a decrease. Notably, Type 3 exhibits the largest vertical displacement, followed by Type 1, with Type 2 exhibiting the smallest displacement. It is indicated that, under specific corrosion conditions, a pipeline with a higher thickness-diameter ratio experiences more severe vertical deformation. Additionally, while the DOPs of pipelines under conditions of ρ_{CR} = 0.4, t_d = 80% and ρ_{CR} = 0.8, t_d = 40% exhibit similar trends, there are significant differences in vertical deformation for Type 1 and Type 2 pipelines between these conditions, whereas for Type 3, the difference can be neglected.

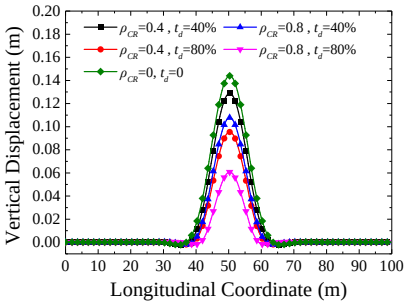

(a) Type 1

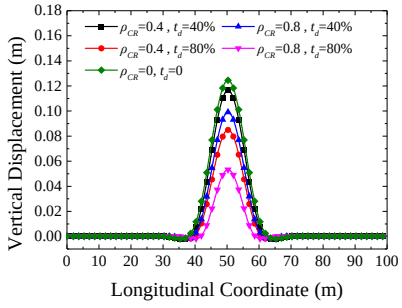

(b) Type 2

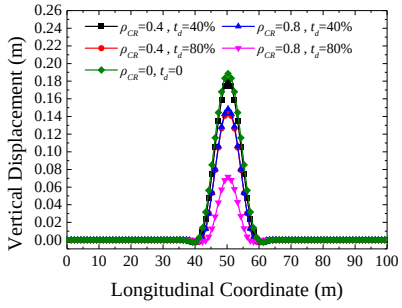

(c) Type 3

Fig. 15 The vertical deformation of the pipelines with different corrosion parameters

7.2. Vertical displacement at the midpoint

The vertical deformation at the midpoint of the pipeline exhibits a minor difference between high and low values, which is rational given the limited influence of y_{max} on the vertical deformation at the midpoint. Thus, only the high value of the vertical deformation is presented. Fig. 16 illustrates the increase in vertical displacement at the pipeline midpoint with increasing imposed load. With constant corrosion parameters, the curves exhibit a distinct nonlinearity, indicating that as external loads gradually increase and pipeline deformation accelerates, the rate of vertical displacement growth at the midpoint progressively rises. Additionally, the vertical displacement at the midpoint of

the pipeline diminishes as the corrosion ratio and corrosion depth increase, consistent with the global vertical deformation of the pipeline. Moreover, the slopes of the curves steepen correspondingly with the growth of the corrosion ratio or corrosion depth. It means that, with the aggravation of pipeline corrosion, the growth rate of vertical displacement at the midpoint increases significantly with the imposed load. Moreover, since the DOPs of the pipeline at ρ_{CR} = 0.4, t_d = 80% and ρ_{CR} = 0.8, t_d = 40% are nearly identical, resulting in similar slopes for these two curves.This supports the inference that as DOPs increase, the rate of vertical displacement growth at the midpoint responds significantly to external loads. The observed correlation between the vertical displacement at the midpoint and vertical deformation of the three pipeline types confirms that thicker sections of the pipeline exhibit more pronounced vertical deformation compared to thinner sections under comparable constant parameter conditions.

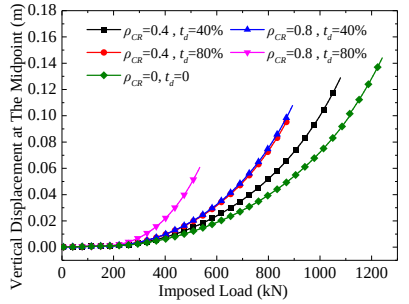

(a) Type 1

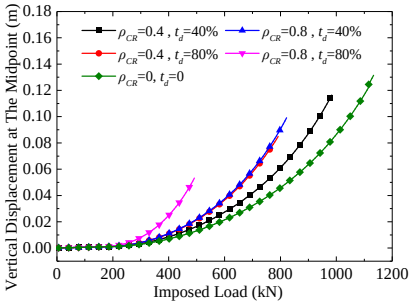

(b) Type 2

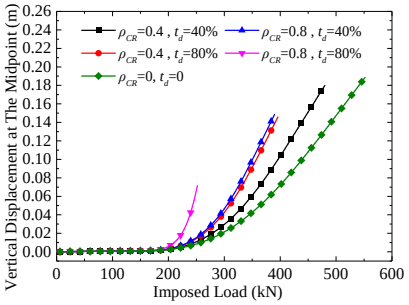

(c) Type 3

Fig. 16 The vertical displacement at the midpoint with different corrosion parameters

7.3. Stress at the midpoint

A graphical representation of the normal stress variations within the cross-section at the pipeline's midpoint, corresponding to different loading stages, is depicted in Fig. 17. Additionally, a reference value of 0.54S_y is included as the upper limit for longitudinal stress. Under imposed loads, both the stress and vertical displacement at the pipeline's midpoint exhibit comparable patterns of variation.

The stress at the midpoint of the pipeline diminishes as the corrosion ratio and depth increase. Furthermore, the slopes of the curves also increase with the corrosion ratio (corrosion depth). Moreover, when subjected to imposed loads, the stress growth rate at the midpoint experiences a notable acceleration with the elevation of DOPs. This suggests that the rate at which stress accumulates at the midpoint remarkably amplifies with the progression of pipeline corrosion. Nevertheless,the vertical displacement change at the same point exceeds the stress variation during the application of external loads, suggesting that the rate of stress accumulation at the midpoint rises steadily with the persistent imposition of external loads. Although the stresses at the midpoint are comparable among the three pipeline types, Type 3 exhibits the highest rate of stress accumulation at the midpoint, followed by Type 2, with Type 1 showing a relatively lower increase rate. Therefore, it seems that the thickness-diameter ratio of the pipeline section does not largely affect the connection between corrosion and stress at the midpoint.

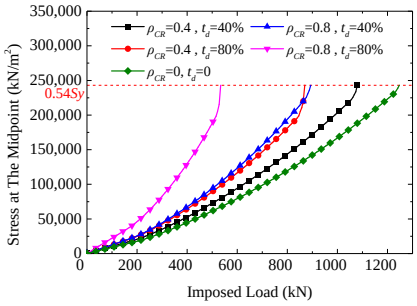

(a) Type 1

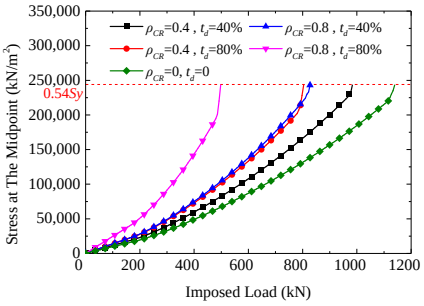

(b) Type 2

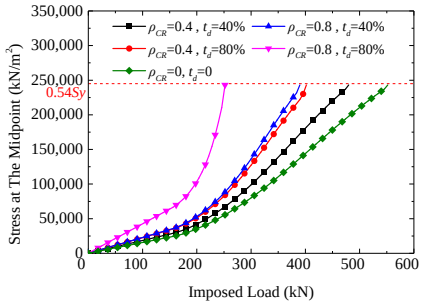

(c) Type 3

Fig. 17 The stress at the midpoint of pipelines with different corrosion parameters

8. Conclusions

By implementing Monte Carlo method, a corrosion-inclusive model of a submarine pipeline was developed to perform a numerical analysis regarding pipeline buckling considerations. The findings of this study serve as the foundation for a quantitative assessment of the pipelines' bearing capacity. Based on the previously established pipeline element, the newly introduced element demonstrates significant efficiency advantages when dealing with numerous cases that require analysis. Without the employment of highly efficient numerical models, it would be unfeasible to carry out the multi-factorial parametric studies. In order to investigate how the corrosion features affect the bearing capacity of the pipelines, a series of pitting corrosion are designed and randomly distributed across the cross sections of the pipelines. A comprehensive analysis has been conducted to assess the impact of diverse corrosion parameters, including corrosion depth, corrosion ratio, and area loss ratio, on the mechanical characteristics of pipelines. The examination encompassed key properties such as bearing capacity, buckling deformation, and stress. The findings can be summarized as follows:

- As the corrosion depth (corrosion ratio) increases, its impact on the pipelines bearing capacity becomes more increasingly significant. Even slight corrosion enhance the unpredictability of the pipeline’ s bearing capacity. With the aggravation of the corrosion, the buckling displacement and stress at the midpoint of the pipeline accelerate under applied loads, indicating accelerated deformation. Besides, pitting corrosion has a more substantial influence on the magnitude of upheaval buckling deformation than the buckling length. Evaluating the bearing

capacity of a corroded pipeline solely based on single corrosion parameter is inadequate. Minor variations in corrosion ratio and depth can lead to slight differences in the bearing capacity and buckling displacement of a specific section, especially at similar area loss ratio of the section (DOPs).The combination of substantial corrosion depth with a relatively low corrosion ratio often results in a more minor reduction in the reduction factor. Furthermore, different types of sections, even with identical corrosion parameters, can exhibit varying reduction factors and vertical buckling displacements.

- The bearing capacity of the pipeline decreases as the slenderness increases and then gradually stabilizes. When assessing the buckling bearing capacity of a corroded pipeline, it is crucial to note that the section coefficient W_Z for corroded pipelines is not clearly defined in relevant specifications. To capture the uncertainty of its bearing capacity, it is necessary to consider both values of y_{max}: $D/2$ and $D/2$- t_d. Although the effect of y_{max} on the bearing capacity and buckling deformation is limited by the impact of corrosion ratio, its influence on corrosion depth remains significant. Furthermore, the buckling bearing capacity of a pipeline can vary significantly depending on corrosion distribution. Among various corrosion models with identical area loss ratios, pipelines exhibiting regular and random corrosion patterns exhibit similar bearing capacities while the corrosion concentration in the top or bottom half of the pipeline cross-section should be avoided, as this leads to the lowest buckling bearing capacity.
- This method is applicable for corrosion analysis of both thin and thick-walled pipelines. For pipelines with varying cross-sections, a reduced thickness-to-diameter ratio leads to heightened uncertainty regarding the structural integrity of the pipeline, considering both corrosion depth and corrosion ratio. Among pipelines with similar thickness-to-diameter ratios, those with thicker walls are more vulnerable to the effects of high-level corrosion, either in terms of corrosion depth or corrosion ratio. Conversely, pipeline sections with a larger thickness-to-diameter ratio may exhibit more pronounced vertical buckling displacement under certain corrosion conditions, whereas the thickness-diameter ratio has limited impact on the relationship between corrosion and stress at the midpoint.

Acknowledgement

The corresponding author would like to express his gratitude to the Natural Science Foundation of Guangdong Province (No. 2021A1515011734), Guangdong Basic and Applied Basic Research Foundation (No. 2022B1515250002), and the third author would like to express his gratitude to the National Science Foundation, China through the project (Grant No. 52008410) and the Hong Kong SAR Government on the project Second-order direct analysis for the design of steel members with irregular cross-sections (PolyU 15203121/22E).

References

[1] Cai, J., Jiang, X. L., Lodewijks, G., 2017. Residual ultimate strength of off- shore metallic pipelines with structural damage–a literature review. Ships and Offshore Structures 12 (8), 1037–1055.

[2] Galgoul, N. S., Lupinacci Massa, A. L., Claro, C. u. A., 2004. A discussion on how internal pressure is treated in offshore pipeline design. In: Inter- national Pipeline Conference. Vol. 41766. pp. 1887–1890.

[3] Wang, R. H., Shenoi, R. A., 2019. Experimental and numerical study on ultimate strength of steel tubular members with pitting corrosion damage. Marine Structures 64, 124–137.

[4] Chen, Z. H., Yang, J. G., Wang, Z. k., 2020. Numerical study on upheaval buckling for surface laid subsea pipelines with topographic step imperfec- tion. Applied Ocean Research 101, 102232.

[5] Det Norske Veritas, 2018. Global buckling of submarine pipelines. DNV-RP- F110, Oslo, Norway.

[6] Wang, R. H., Guo, H. C., Shenoi, R. A., 2020. Compressive strength of tubular members with localized pitting damage considering variation of corrosion features. Marine Structures 73, 102805.

[7] Cosham, A., Hopkins, P., 2004. The assessment of corrosion in pipelines– guidance in the pipeline defect assessment manual (PDAM). In: Pipeline pigging and integrity management conference, Amsterdam, The Nether- lands. pp. 17–18.

[8] Netto, T. A., 2009. On the effect of narrow and long corrosion defects on the collapse pressure of pipelines. Applied ocean research 31 (2), 75–81.

[9] Wang, H., Yu, Y., Yu, J., Duan, J., Zhang, Y., Li, Z., Wang, C., 2018a.Effect of 3d random pitting defects on the collapse pressure of pipepart i: Experiment. Thin-Walled Structures 129, 512–526.

[10] Motta, R. S., Cabral, H. L., Afonso, S. M., Willmersdorf, R. B., Bouchon- neau, N., Lyra, P. R., de Andrade, E. Q., 2017. Comparative studies for failure pressure prediction of corroded pipelines. Engineering Failure Anal- ysis 81, 178–192.

[11] Mohd, M. H., Lee, B. J., Cui, Y., Paik, J. K., 2015. Residual strength of cor- roded subsea pipelines subject to combined internal pressure and bending moment. Ships and offshore Structures 10 (5), 554–564.

[12] Nazaria, M., Khedmati, M. R., Khalaj, A. F., 2014. A numerical investi- gation into ultimate strength and buckling behavior of locally corroded steel tubular members. Latin American Journal of Solids and Structures 11, 1063–1076.

[13] Ahn, J. H., Choi, W. R., Jeon, S. H., Kim, S. H., Kim, I. T., 2016. Residual compressive strength of inclined steel tubular members with local corro- sion. Applied Ocean Research 59, 498–509.

[14] Melchers, R. E., 2005a. Statistical characterization of pitting corrosion part 1: Data analysis. Corrosion 61 (07).

[15] Melchers, R. E., 2005b. Statistical characterization of pitting corrosionpart 2: Probabilistic modeling for maximum pit depth. Corrosion 61 (8), 766–777.

[16] Yamamoto, N., 2008. Probabilistic model of pitting corrosion and the simula- tion of pitted corroded condition. In: International Conference on Offshore Mechanics and Arctic Engineering. Vol. 48197. pp. 527–534.

[17] Chen, L., Liu, S. W., Zhang, J. Z., Yam, M. C. H., 2022. Efficient algorithm for elastic buckling of corroded i-section steel members with monte carlo simulation. Thin-Walled Structures 175, 109216.

[18] Silva, J. E., Garbatov, Y., Soares, C. G., 2013. Ultimate strength assess- ment of rectangular steel plates subjected to a random localised corrosion degradation. Engineering Structures 52, 295–305.

[19] Wang, R., Shenoi, R. A., Sobey, A., 2018b. Ultimate strength assessment of plated steel structures with random pitting corrosion damage. Journal of Constructional Steel Research 143, 331–342.

[20] Ben Seghier, M. e. A., Bettayeb, M., Correia, J., De Jesus, A., Cal¸cada, R., 2018. Structural reliability of corroded pipeline using the so-called separa- ble monte carlo method. The Journal of Strain Analysis for Engineering Design 53 (8), 730–737.

[21] Caleyo, F., Vel´azquez, J., Valor, A., Hallen, J. M., 2009. Probability distri- bution of pitting corrosion depth and rate in underground pipelines: A monte carlo study. Corrosion Science 51 (9), 1925–1934.

[22] Wu, X., Lu, H., Wu, S., 2015. Stress analysis of parallel oil and gas steel pipelines in inclined tunnels. SpringerPlus 4 (1), 1–25.

[23] Khakimov, A., 2018. Interaction of pipeline instabilities. In: AIP Conference Proceedings. Vol. 2053. AIP Publishing LLC, p. 030025.

[24] Liu, R., Li, C. F., 2018. Determinate dimension of numerical simulation model in submarine pipeline global buckling analysis. Ocean Engineering 152, 26–35.

[25] Ma, H. H., Li, B. E., 2023. CFD-CGDEM coupling model for scour process simulation of submarine pipelines. Ocean Engineering 271, 113789.

[26] Ning, J., Lin, T., Liu, S., Bai, R., Huang, W., 2023. Three-dimensional pipeline element formulation for global buckling analysis of submarine pipelines with sleeper. Marine Structures 90, 103428.

[27] Ning, J. H., Liu, S. W., Lin, T., Huang, W., 2022. Pipeline elemen- t for upheaval buckling analysis of submarine pipelines with geometric- imperfections under high temperature high pressure. Ocean Engineering 264, 112456.

[28] Ning, J. H., Liu, S. W., Wan, J. H., Huang, W., 2021. Line-element for- mulation for upheaval buckling analysis of buried subsea pipelines due to thermal expansion. Advanced Steel Construction 17 (2), 210–220.

[29] Mateus, A. F., Witz, J. A., 1998. On the post-buckling of corroded steel plates used in marine structures. RINA Trans 140, 165–183.

[30] Cumming, G., Rathbone, A., 2010. Euler buckling of idealised horizontal pipeline imperfections. In: International Conference on Offshore Mechanics and Arctic Engineering. Vol. 49132. pp. 293–300.

[31] Markov, E. V., Pulnikov, S. A., Sysoev, Y. S., Kazakova, N. V., 2018. The convergence rate of the euler model for the deformed state when calculating the longitudinal bending. International Journal of Civil Engineering and Technology 9 (10), 1974–1979.

[32] American National Standards Institute, 2022. Pipeline transportation sys- tems for liquid hydrocarbons and other liquids. American Society of Me- chanical Engineers.